

Measurement of Muon Neutrino
Charged Current Single π^0 Production
on Hydrocarbon using MINERvA

A dissertation submitted by

Ozgur Altinok

in partial fulfillment of the requirements for the degree of

Doctor of Philosophy

in

Physics

Tufts University

May 2017

Advisor: Prof. W. Anthony Mann

Abstract

A sample of charged-current single pion production events for the semi-exclusive channel $\nu_\mu + \text{CH} \rightarrow \mu^- \pi^0 + \text{nucleon(s)}$ has been obtained using neutrino exposures of the MINERvA detector. Differential cross sections for muon momentum, muon production angle, pion momentum, pion production angle, and four-momentum transfer square Q^2 are reported and are compared to a GENIE-based simulation. The cross section versus neutrino energy is also reported. The effects of pion final-state interactions on these cross sections are investigated. The effect of baryon resonance suppression at low Q^2 is examined and an event re-weight used by two previous experiments is shown to improve the data versus simulation agreement. The differential cross sections for Q^2 for $E_\nu < 4.0$ GeV and $E_\nu \geq 4.0$ GeV are examined and the shapes of these distributions are compared to those from the experiment's $\bar{\nu}_\mu\text{-CC}(\pi^0)$ measurement. The polarization of the $p\pi^0$ system is measured and compared to the simulation predictions. The hadronic invariant mass W distribution is examined for evidence of resonance content, and a search is reported for evidence of a two-particle two-hole (2p2h) contribution. All of the differential cross-section measurements of this Thesis are compared with published MINERvA measurements for $\nu_\mu\text{-CC}(\pi^+)$ and $\bar{\nu}_\mu\text{-CC}(\pi^0)$ processes.

Dedicated to my wife Esra.

Acknowledgments

Prof. Anthony Mann has my deepest gratitude for being my mentor during my doctoral research. He is an excellent experimental physicist and a great teacher. He answered all my naive physics, math, statistics, and english grammar questions with an endless patience. I have become a better experimental physicist with his guidance.

My studies provided me with an opportunity to be a part of an exceptional group of scientists. The Tufts Neutrino Group provided me with unlimited resources to build my skills and complete my PhD. I would like to thank especially Prof. Hugh Gallagher for offering many clever insights about my research. Prof. Jack Schneps carefully proof read my thesis and spotted many mistakes, I am glad for his kind help. Dr. Joao Coelho, Dr. Trung Le, and Dr. Jeremy Wolcott have made enormous contributions to my research. I greatly appreciate their help.

I would like to thank to all members of the MINERvA Collaboration for carefully double-checking my results and providing useful suggestions. I have special thanks to Prof. Steve Dytman for agreeing to be a committee member for my thesis defense and also making valuable contribution to my analysis in all stages.

During my six years of PhD study, I have made a lot of good friends in the Department of Physics. Especially I would to thank to my best friends Travis and Jon for our conversations during lunch and coffee breaks.

I cannot thank enough my wife Esra. She is the reason for everything in my life. She encouraged me for starting a PhD in the USA and I am grateful that I followed her in 2011. I will always love you, thank you for being my partner in life.

I find myself very lucky to be surrounded by wonderful people. I am grateful for

Erman for mentoring me to become a better software developer, with his guidance the quality of my research and my future career improved greatly. I would like to thank all of my friends for making my life better. Life is beautiful with many good friends: Sezin, Antonis, Damla B., Dave, Burcak, Cagatay, Damla A., Kagan, Ayse, Ali, Sinem, Ozan, Ozlem B., Mustafa, Ozlem N., and Paul.

Last but not least, I would like to thank to my mom, dad and sister for supporting me for my whole life.

Contents

Contents	ix
List of Tables	xiv
List of Figures	xviii
1 Overview of Neutrino-induced Single Pion Production	1
1.1 Introduction	3
1.2 Charged current single pion production	5
1.2.1 CC single pion production through baryon resonances	6
1.2.2 CC single pion production through deep inelastic scattering	8
1.3 Review of previous experiments reporting charged current single π^0 production	9
1.4 Review of neutrino oscillations	11
1.4.1 Three flavor neutrino oscillations	14
2 The NuMI Neutrino Beam at Fermilab	19
2.1 The NuMI beam	21
2.2 The proton beam	21
2.3 The neutrino beam	22
2.4 NuMI beam flux	25
3 The MINERvA Detector	29
3.1 Detector overview	31

3.2	Active tracker modules	33
3.3	Electromagnetic and hadronic calorimeter modules	34
3.4	Optical system	36
3.4.1	Scintillator planes	36
3.4.2	Wavelength shifting fibers	36
3.4.3	Photomultiplier tubes and optical boxes	37
3.5	MINOS near detector	38
3.6	Solid nuclear target modules	39
3.7	Water target	42
4	Signal Definition and Event Selection	45
4.1	Analysis overview	47
4.2	Simulation software	48
4.3	Refinements to the simulation software	51
4.4	Signal definition	52
4.5	Kinematic behavior of signal events	54
4.6	Event selections	58
4.6.1	Time slicing	59
4.6.2	Vertex requirements	59
4.6.3	Muon selections	60
4.6.4	Proton selections	60
4.6.5	Neutral pion selections	61
4.6.6	Michel electron selections	65
4.6.7	Event kinematic selections	66
4.7	Analysis purity and efficiency	66
5	Event Reconstruction	69
5.1	Muon and proton reconstruction	71
5.1.1	Track reconstruction	71
5.1.1.1	Clustering	71
5.1.1.2	Tracking	72

5.1.2	Muon identification and momentum measurement	73
5.1.3	Proton identification and momentum measurement	75
5.2	Neutral pion reconstruction	78
5.2.1	Pre-reconstruction	80
5.2.2	Reconstruction	82
5.2.3	Post-reconstruction	84
5.2.4	Electromagnetic energy calibration	86
5.3	Event kinematics	89
5.3.1	Neutrino energy	89
5.3.2	Distributions of Q^2 and W	97
6	Background Classifications and Background Constraints	99
6.1	Background classifications	101
6.1.1	Background classification: Pion multiplicity	101
6.1.2	Background classification: Neutral pion multiplicity	103
6.1.3	Background classification: Major background sources	105
6.2	Sideband fit and background constraints	107
7	Determination of Differential Cross Sections of the Signal Channel	115
7.1	Differential cross-section calculation	117
7.2	Background subtraction	118
7.3	Unfolding	120
7.4	Efficiency correction	127
7.5	Flux, target number and bin width normalizations	129
7.6	Closure Tests	131
8	Systematic Uncertainties	133
8.1	Detector response uncertainties	136
8.1.1	Relative contributions of the detector response uncertainties to the total systematic error	141
8.2	Uncertainties inherent to the neutrino interaction model	141

8.3	Final state interaction model uncertainties	142
8.4	Neutrino beam flux uncertainties	143
8.5	Other uncertainties	144
8.6	Total systematic uncertainties	144
9	Cross Section Measurements for Charged Current Single π^0 Production	147
9.1	Single particle differential cross sections	149
9.1.1	Muon momentum	149
9.1.2	Muon production angle	151
9.1.3	Pion momentum and kinetic energy	152
9.1.4	Pion production angle	154
9.2	Cross-section results for interaction kinematics	156
9.2.1	Differential cross section for Q^2	156
9.2.2	Total cross section versus neutrino energy	158
9.3	Results comparison with nominal GENIE simulations	159
9.4	Effects from pion final-state interactions	161
9.5	Results comparison with MiniBooNE ν_μ -CC (π^0) measurement	169
10	Comparisons with CC Pion Production Measurements in MIN-ERvA	171
10.1	Definitions for the samples used in the comparison	173
10.2	Model comparisons	174
10.3	Comparisons of systematic uncertainties	183
10.4	Comparisons of component processes	185
10.5	Comparisons of pion FSI channels	191
11	Physics of Charged Current Single Pion Production	197
11.1	Suppression of baryon resonances at low Q^2	199
11.2	Q^2 distribution dependence on different E_ν ranges	203
11.3	Distributions for Δ^+ (1232) enriched sample	207

11.3.1	Proton-Pion invariant mass distribution	207
11.3.2	Polarization in the Δ^+ (1232) region	208
11.4	Distribution of hadronic invariant mass	212
11.4.1	Data versus Simulation disagreement	212
11.4.2	Decomposition of W by interaction type	213
11.5	Search for M_A^{RES} value	217
11.6	Search for 2p2h contribution to single pion production	218
12	Conclusions	223
12.1	Cross-section measurements for ν_μ -CC (π^0)	225
12.2	Comparisons with ν_μ -CC (π^+) and $\bar{\nu}_\mu$ -CC (π^0)	226
12.3	Physics of ν_μ -CC (π^0) sample	227
A	MINERvA Collaboration	229
B	Tables for the Cross-Section Measurements	231
B.1	Muon momentum	232
B.2	Muon production angle	233
B.3	Pion momentum	234
B.4	Pion kinetic energy	235
B.5	Pion production angle	236
B.6	Four-momentum transfer square Q^2	237
B.7	Neutrino energy	238
C	Brief History of Neutrinos	239
C.1	Neutrino oscillation experiments	241
	Bibliography	245

List of Tables

1.1	Three-flavor oscillation parameters.	17
3.1	Elemental composition of scintillator strips and constructed planes by mass percentage.	34
3.2	Properties of the Hamamatsu H8804MOD-2 multi-anode photomultiplier tube.	38
3.3	Hamamatsu H8804MOD-2 multi-anode photomultiplier tube operating characteristics at 25 °C.	38
3.4	Passive target location, thickness and mass.	41
4.1	Particle interaction models used in GENIE v2.8.2.	50
4.2	Bubble chamber data versus GENIE comparisons for non-resonant single pion channels.	52
4.3	Signal composition based on the GENIE event record.	55
4.4	Dimensions of reconstruction and fiducial volumes.	60
4.5	Detector mass, number of carbon atoms and nucleons inside the fiducial volume.	60
4.6	Michel-electron search distances for various topological locations in an event.	66
4.7	Purity and efficiency of the sample after each event selection.	67
5.1	Summary of variables used in Bethe-Bloch equation.	77
5.2	Recovery of signal events from events with one-shower candidate.	85
5.3	Recovery of signal events from events with three-shower candidates.	86

6.1	Estimated percentages for backgrounds classified according to the number of pions in the final state.	102
6.2	Estimated percentages for backgrounds classified according to the number of pions in the final state for 1-track and 2+ tracks events.	103
6.3	Percentages of background events based on the number of π^0 's in the final state for selected events.	104
6.4	Percentages of background events based on the number of π^0 's in the final state for events with 1-track and 2+ tracks.	105
6.5	Background events and their percentage contributions.	106
6.6	Percentage contributions of background event categories, subdivided according to the number of final-state tracks.	107
6.7	Event types of the MC components for the sideband fit.	109
6.8	Data and simulation statistics for each sideband.	109
6.9	Statistics for background types for each sideband.	110
6.10	Fit performance represented as the total χ^2 and χ^2/dof	110
6.11	Background weights and their uncertainties, according to the sideband fit.	110
7.1	Summary of variables used in the differential cross-section calculation.	117
7.2	Number of estimated signal and background events in data.	118
7.3	Number of unfolding iterations for each cross-section variable.	124
8.1	Muon tracking efficiency and uncertainties.	137
8.2	Proton tracking efficiencies and uncertainties.	137
8.3	Estimated uncertainty of the material thickness inside the MINERvA detector's tracking region.	138
8.4	Michel electron detection efficiencies and uncertainties.	140
8.5	GENIE $\pm 1\sigma$ systematic uncertainties for the parameters used in cross-section models.	142
8.6	GENIE $\pm 1\sigma$ systematic uncertainties for the parameters used in final state interaction models.	143

10.1	Signal definitions for samples obtained in channels ν_μ -CC (π^+), $\bar{\nu}_\mu$ -CC (π^0) , and ν_μ -CC (π^0)	173
11.1	Fit parameters for the low- Q^2 suppression function.	199
11.2	Slopes of $d\sigma/dQ^2$ for ν_μ -CC (π^0) and $\bar{\nu}_\mu$ -CC (π^0) samples.	204
11.3	Mass and full width of the Δ^+ (1232) resonance from best fit and PDG database.	214
11.4	Data and simulation shape-fit results for the Δ^+ (1232) resonance and the other baryon resonances.	217
B.1	Results for the muon momentum differential cross-section measurement.	232
B.2	Bin-by-bin systematic uncertainties on muon momentum differential cross- section measurement.	232
B.3	Results for the muon production angle differential cross-section measure- ment.	233
B.4	Bin-by-bin systematic uncertainties on muon production angle differential cross-section measurement.	233
B.5	Results for the pion momentum differential cross-section measurement. . .	234
B.6	Bin-by-bin systematic uncertainties on pion momentum differential cross- section measurement.	234
B.7	Results for the pion kinetic energy differential cross-section measurement.	235
B.8	Bin-by-bin systematic uncertainties on pion kinetic energy differential cross-section measurement.	235
B.9	Results for the pion production angle differential cross-section measurement.	236
B.10	Bin-by-bin systematic uncertainties on pion production angle differential cross-section measurement.	236
B.11	Results for the four-momentum transfer square Q^2 differential cross-section measurement.	237
B.12	Bin-by-bin systematic uncertainties on four-momentum transfer squared Q^2 differential cross-section measurement.	237
B.13	Results for the neutrino energy cross-section measurement.	238

B.14 Bin-by-bin systematic uncertainties on neutrino energy cross-section measurement.	238
--	-----

List of Figures

1.1	Total neutrino per nucleon charged-current cross sections for the three main interaction processes.	3
1.2	Reaction decomposition based on the number of pions for the NOvA Experiment.	4
1.3	Appearance probability for electron neutrino as a function of neutrino energy for DUNE and T2K neutrino oscillation experiments.	5
1.4	Nucleon-pion invariant-mass $M(N\pi)$ distributions for the final states $p\pi^+$, $p\pi^0$, and $n\pi^+$	10
1.5	Nucleon-pion invariant mass distributions for $p\pi^0$ and $n\pi^+$ channels.	11
1.6	Nucleon-pion invariant mass distributions for ν_μ -CC (π) and $\bar{\nu}_\mu$ -CC (π) reactions.	12
1.7	“Normal” and “Inverted” neutrino mass spectra.	15
2.1	Fermilab accelerator complex.	22
2.2	Low-energy run period for MINERvA experiment.	23
2.3	Diagram of the magnetic field and the force applied to a positively charged particle by the horn.	24
2.4	Schematic of the NuMI beam.	24
2.5	Low energy target with front half of Horn 1.	26
2.6	Hadron trajectories through the two horns.	27
3.1	Side view of the MINERvA detector.	32
3.2	Front view of a single detector module.	33

3.3	Three different plane orientations in the MINERvA Detector.	34
3.4	MINERvA scintillator strips.	36
3.5	Components of the optical boxes used in the MINERvA detector.	39
3.6	Transverse view of the MINOS near detector.	40
3.7	Upstream and downstream regions of the MINOS near detector as seen from top.	40
3.8	Orientation of the nuclear targets looking downstream.	41
3.9	Orientation of the nuclear target region along the beam line axis.	43
3.10	Schematic drawing of the MINERvA water target.	43
4.1	Feynman diagram of the neutrino interaction: $\nu_\mu + n \rightarrow \mu^- + p + \pi^0$	47
4.2	Signal definition based on out-of-nucleus particle content.	53
4.3	True neutrino energy for selected events according to GENIE.	57
4.4	Distribution of Q^2 calculated using the true neutrino and muon kinemat- ics.	58
4.5	Hadronic invariant mass W calculated using the true neutrino and muon kinematics.	58
4.6	Time profile of the hits within a NuMI beam spill.	59
4.7	Apothems for reconstruction and fiducial volumes.	61
4.8	Proton Score based on the log likelihood ratio (LLR) for dE/dx profile.	62
4.9	Event selection for the leading-photon conversion length.	64
4.10	Distribution of $[N(\text{Background}) - N(\text{Signal})]$ for $\cos\theta_{\gamma\gamma}$ versus $E_1 + E_2$	64
4.11	Event selection for the π^0 invariant mass.	65
5.1	Residual of fitted positions along a track relative to measured cluster positions for a rock muon sample.	73
5.2	Magnetic field map of the MINOS near detector looking from the down- stream direction.	75
5.3	Fractional residual errors for muon momentum and production angle.	76
5.4	Simulated proton and pion dE/dx profile compared to Bethe-Bloch.	78

5.5	Performance of the log likelihood ratio (LLR) method for separating the protons and pions.	79
5.6	Fractional residual errors for proton momentum and production angle.	80
5.7	Event display for candidate signal event (2021/23/449).	81
5.8	Event display for candidate signal event (2037/17/4807).	81
5.9	Event display for candidate signal event (2204/11/453).	82
5.10	Schematic view of cluster direction pointing towards the vertex.	83
5.11	Schematic for grouping of clusters based on their direction.	83
5.12	Number of shower candidates found by the Angle Scan algorithm.	84
5.13	Photon total cross section as a function of energy in carbon.	87
5.14	Energy-dependent calibration weight in the tracker region.	88
5.15	Energy-dependent calibration weight in the tracker region shown over a large visible energy range.	89
5.16	Energy-independent calibration weight in the ECAL region.	90
5.17	Fractional residual errors for the π^0 momentum and angle.	91
5.18	Distributions of reconstructed muon energy.	91
5.19	Distributions of reconstructed neutral pion energy.	92
5.20	Distributions of reconstructed proton energy.	93
5.21	Distributions of vertex energy.	94
5.22	Distribution of extra energy coming from rejected clusters during π^0 reconstruction.	94
5.23	Distribution of extra energy coming from muon non-tracked clusters.	95
5.24	Distribution of extra energy coming from leftover clusters.	95
5.25	Distributions of the total extra energy included in the neutrino energy estimation.	96
5.26	Neutrino energy distributions for events without a reconstructed proton.	96
5.27	Neutrino energy distributions for events with at least one reconstructed proton.	97
5.28	Neutrino energy distributions for all events.	97
5.29	Q^2 distribution for all selected events.	98

5.30	W distribution for all events.	98
6.1	Background percentages based on the number of pions in the final state.	102
6.2	Background percentages for events with 1-Track and 2+ Tracks.	103
6.3	Background percentages based on the number of neutral pions in the final state.	104
6.4	Background percentages based on the number of neutral pions in the final state for events with 1-Track and 2+ Tracks.	105
6.5	Background percentages based on the three major background types.	106
6.6	Background percentages based on the three major background types for events with 1-Track and 2+ Tracks.	107
6.7	Data and MC $\gamma\gamma$ invariant mass distributions.	111
6.8	Data and MC $\gamma\gamma$ invariant mass distributions in Michel sideband.	112
6.9	Data and MC $\gamma\gamma$ invariant mass distributions in pID sideband.	113
7.1	Data and POT-normalized MC distributions for the π^0 invariant mass.	119
7.2	Data and POT-normalized MC distributions for muon momentum.	119
7.3	Background-subtracted distributions of muon momentum for the data and the simulation.	120
7.4	Migration matrices for muon momentum and production angle.	121
7.5	Migration matrix for pion momentum and kinetic energy.	122
7.6	Migration matrix for the pion production angle.	122
7.7	Migration matrices for Q^2 (left) and neutrino energy (right).	123
7.8	Unfolding study plots for muon momentum for each bin after each iteration.	124
7.9	Total unfolding study plots for muon momentum after each iteration.	125
7.10	Unfolding study plots for π^0 momentum for each bin after each iteration.	125
7.11	Total unfolding study plots for π^0 momentum after each iteration.	126
7.12	Muon momentum distributions before and after unfolding.	126
7.13	Pion momentum distributions before and after unfolding.	127
7.14	True muon momentum distributions for signal events.	128
7.15	Efficiency curve for muon momentum.	128

7.16	Muon momentum distributions before and after the efficiency-correction.	129
7.17	The neutrino flux distribution used in this analysis.	130
7.18	Differential cross section of the signal channel for muon momentum.	130
7.19	Muon momentum closure test plots.	132
8.1	Data and Monte Carlo distributions for $m_{\gamma\gamma}$	139
9.1	Muon momentum differential cross-section measurement.	150
9.2	Total fractional uncertainty on the muon momentum cross-section measurement.	150
9.3	Muon production angle differential cross-section measurement.	151
9.4	Total fractional uncertainty on the muon production angle cross-section measurement.	152
9.5	Differential cross-section measurements for pion momentum and kinetic energy.	153
9.6	Total fractional uncertainty on the pion momentum and pion kinetic energy cross-section measurements.	154
9.7	Pion production angle differential cross-section measurement.	155
9.8	Total fractional uncertainty on the pion production angle cross-section measurement.	155
9.9	Differential cross-section versus Q^2 for data and simulation.	157
9.10	Total fractional uncertainty on the Q^2 cross-section measurement.	157
9.11	Total cross-section measurement for neutrino energy.	158
9.12	Total fractional uncertainty on the neutrino energy cross-section measurement.	159
9.13	Differential cross-section measurements for muon production angle and Q^2 using the tuned GENIE and the nominal GENIE.	160
9.14	Ratio of tuned GENIE and nominal GENIE differential cross-section measurements for muon production angle and Q^2 .	161
9.15	Differential cross-section measurements for muon momentum and pion momentum using the tuned GENIE and the nominal GENIE.	161

9.16	Final state interaction types converting signal events to background events.	163
9.17	Final state interaction types converting background events to signal events.	163
9.18	Pion momentum differential cross section with and without FSI modeling and with break-out of FSI processes.	164
9.19	Pion production angle differential cross section with and without FSI modeling and with break-out of FSI processes.	166
9.20	Differential cross sections for muon momentum and production angle with and without FSI modeling.	167
9.21	Cross sections for Q^2 and neutrino energy with and without FSI modeling.	168
9.22	The $d\sigma/dQ^2$ distributions for the ν_μ -CC (π^0) channel in MINERvA and MiniBooNE.	170
9.23	The $d\sigma/dP_{\pi^0}$ measurements for the ν_μ -CC (π^0) channel in MINERvA and MiniBooNE.	170
10.1	Differential cross sections for muon momenta of the samples ν_μ -CC (π^+), $\bar{\nu}_\mu$ -CC (π^0), and ν_μ -CC (π^0).	175
10.2	Differential cross sections for the muon production angle for the samples ν_μ -CC (π^+), $\bar{\nu}_\mu$ -CC (π^0), and ν_μ -CC (π^0).	176
10.3	Differential cross sections for the pion kinetic energy for the samples ν_μ -CC (π^+), $\bar{\nu}_\mu$ -CC (π^0), and ν_μ -CC (π^0).	178
10.4	Differential cross sections for the pion production angle for the samples ν_μ -CC (π^+), $\bar{\nu}_\mu$ -CC (π^0), and ν_μ -CC (π^0).	179
10.5	Differential cross sections for four-momentum transfer squared Q^2 for the samples ν_μ -CC (π^+), $\bar{\nu}_\mu$ -CC (π^0), and ν_μ -CC (π^0).	180
10.6	Cross sections as a function of neutrino energy E_ν for the samples ν_μ -CC (π^+), $\bar{\nu}_\mu$ -CC (π^0), and ν_μ -CC (π^0).	182
10.7	Total fractional uncertainties for $d\sigma/dP_\mu$ for the samples ν_μ -CC (π^+), $\bar{\nu}_\mu$ -CC (π^0), and ν_μ -CC (π^0).	184
10.8	Reaction compositions for $d\sigma/dP_\mu$ for the samples ν_μ -CC (π^+), $\bar{\nu}_\mu$ -CC (π^0), and ν_μ -CC (π^0).	187

10.9	Reaction compositions for $d\sigma/d\theta_\mu$ for the samples $\nu_\mu\text{-CC}(\pi^+)$, $\bar{\nu}_\mu\text{-CC}(\pi^0)$, and $\nu_\mu\text{-CC}(\pi^0)$	188
10.10	Reaction compositions for $d\sigma/dQ^2$ for the samples $\nu_\mu\text{-CC}(\pi^+)$, $\bar{\nu}_\mu\text{-CC}(\pi^0)$, and $\nu_\mu\text{-CC}(\pi^0)$	189
10.11	Reaction compositions for cross section as a function of neutrino energy for the samples $\nu_\mu\text{-CC}(\pi^+)$, $\bar{\nu}_\mu\text{-CC}(\pi^0)$, and $\nu_\mu\text{-CC}(\pi^0)$	190
10.12	FSI decompositions for $d\sigma/dQ^2$ for the samples $\nu_\mu\text{-CC}(\pi^+)$, $\bar{\nu}_\mu\text{-CC}(\pi^0)$, and $\nu_\mu\text{-CC}(\pi^0)$	192
10.13	FSI decompositions for $d\sigma/dT_\pi$ for $\nu_\mu\text{-CC}(\pi^+)$ and $\nu_\mu\text{-CC}(\pi^0)$	193
10.14	FSI decompositions for $d\sigma/dP_{\pi^0}$ for $\bar{\nu}_\mu\text{-CC}(\pi^0)$ and $\nu_\mu\text{-CC}(\pi^0)$	195
10.15	FSI decompositions for $d\sigma/d\theta_{\pi^0}$ for $\bar{\nu}_\mu\text{-CC}(\pi^0)$ and $\nu_\mu\text{-CC}(\pi^0)$	196
11.1	Q^2 -dependent weight function applied to all charged CC-RES events.	200
11.2	Differential cross-section measurements for Q^2 and muon production an- gle with and without the CC-RES suppression factor.	201
11.3	Cross sections for muon momentum and for neutrino energy with and without the CC-RES suppression factor.	201
11.4	Cross sections for pion momentum and for production angle with and without the CC-RES suppression factor.	202
11.5	Vector and axial-vector contributions to $d\sigma/dQ^2$ for $E_\nu = 2$ GeV and $E_\nu = 6$ GeV.	203
11.6	The $d\sigma/dQ^2$ distributions for the $4 \leq E_\nu < 10$ GeV range for $\nu_\mu\text{-CC}(\pi^0)$ and $\bar{\nu}_\mu\text{-CC}(\pi^0)$ samples.	205
11.7	The $d\sigma/dQ^2$ distributions for the $1.5 \leq E_\nu < 4$ GeV range for the $\nu_\mu\text{-CC}(\pi^0)$ and $\bar{\nu}_\mu\text{-CC}(\pi^0)$ samples.	206
11.8	Proton-pion invariant mass for the data and the simulation.	207
11.9	Coordinate system used for $p\pi$ polarization calculations.	208
11.10	The $\cos(\theta)$ distribution for the data and the simulation for each interac- tion type.	209
11.11	Fitted $\cos(\theta)$ distribution for the data.	210

11.12	Angle ϕ distribution for the data and the simulation.	210
11.13	Fitted angle ϕ distribution for the data.	211
11.14	Hadronic invariant mass distributions for the data and for the simulation.	212
11.15	Hadronic invariant mass distributions for the background subtracted data and for the simulation prediction to signal events.	213
11.16	W distribution for Δ^+ (1232) resonance events and the relativistic Breit- Wigner fit to the shape of the distribution.	214
11.17	Shape fit of the W distributions for other baryon resonances and non- resonant events.	215
11.18	Simulation prediction for the W distribution and the total shape fit result.	216
11.19	W distribution shape fit for the data.	216
11.20	The Q^2 differential cross sections for nominal M_A^{RES} and for best fit M_A^{RES} .	218
11.21	Double differential 2p2h cross section $d\sigma/dT_\mu d\cos\theta_\mu$ at $E_\nu = 3$ GeV. . .	219
11.22	Data and simulation distributions for muon kinetic energy versus cosine of the muon production angle.	220
11.23	Double differential 2p2h cross section $d\sigma/dq_0 dq_3$ at $E_\nu = 3$ GeV.	221
11.24	Data-minus-simulation distribution for energy transfer versus three-momentum transfer.	221
C.1	Electron energy spectrum for beta decay of carbon-14.	240
C.2	Production of atmospheric neutrinos by cosmic-ray interactions.	242

Chapter 1

Overview of Neutrino-induced Single Pion Production

1.1 Introduction

The results of early solar and atmospheric neutrino oscillation experiments were so important that the Nobel Prize in Physics 2015 was awarded jointly to Takaaki Kajita and Arthur B. McDonald "for the discovery of neutrino oscillations, which shows that neutrinos have mass" [1, 2]. Proving the neutrinos have mass opened up a new set of questions such as "What is the mass hierarchy?", and "What is the relationship between the mass eigenstates and the flavor states?". If neutrinos are massive then neutrino mixing is described by PMNS matrix that contains three Euler rotation angles and one complex phase. This complex phase is CP violation in neutrino sector. To answer these questions and measure δ_{CP} in neutrino sector, different accelerator-based neutrino oscillation experiments have been designed. The neutrino charged-current (CC) interaction processes (quasielastic scattering (QE), baryon resonance production (RES), and deep inelastic scattering (DIS)) for different neutrino energies in T2K [3], NOvA [4] and the planned DUNE [5] neutrino oscillation experiments are shown in Fig. 1.1. All three neutrino oscillation experiments have sensitivity to different neutrino energy ranges.

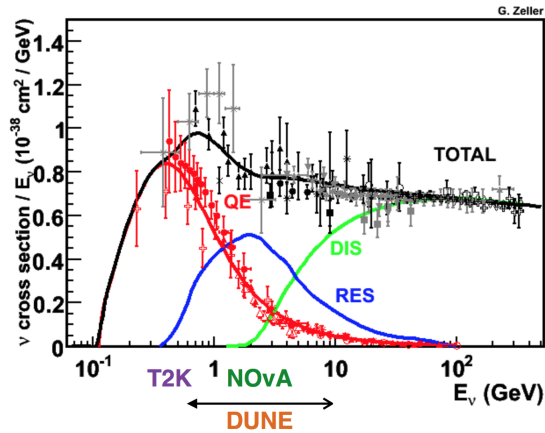


FIG. 1.1: Total neutrino per nucleon charged-current cross sections for the three main interaction processes. The NOvA and DUNE experiments have large event rates from RES and DIS processes. From Refs. [6, 7].

Charged-current pion production through baryon resonances and deep inelastic scattering have large rates in the NOvA and DUNE neutrino oscillation experiments.

A more detailed reaction decomposition based on the number of pions in the final state for the NOvA experiment is shown in Fig 1.2. Charged-current single pion production is the dominant process in the NOvA experiment followed by quasielastic-like interactions. It is important to determine the absolute CC single-pion cross sections in order to accurately predict the event rates and neutrino energy distributing in these oscillation experiments.

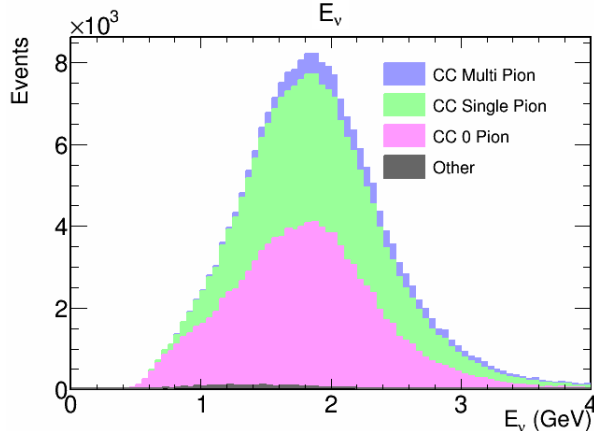


FIG. 1.2: Reaction decomposition based on the number of pions for the NOvA Experiment. The CC single pion production is the leading process type followed by quasielastic-like reactions.

The basic phenomena of neutrino oscillations can be illustrated by a two-flavor oscillations example. Consider “atmospheric” $\nu_\mu \rightarrow \nu_\tau$ oscillations. The ν_τ appearance probability (in an initial ν_μ beam) is given by

$$P_{\nu_\mu \rightarrow \nu_\tau} = \sin^2(2\theta) \sin^2\left(\frac{(m_3^2 - m_2^2) c^4 L}{4\hbar c E_\nu}\right). \quad (1.1)$$

A derivation is given in Sec. 1.4.

As seen in Eq. (1.1) the distance over neutrino energy ratio (L/E_ν) is the crucial variable for neutrino oscillations. Since the distance L is fixed in accelerator and reactor-based long baseline neutrino oscillation experiments, the requirement of accuracy falls to E_ν . Electron neutrino appearance probabilities, $P(\nu_\mu \rightarrow \nu_e)$, as a function of neutrino energy for DUNE and T2K experiments are given in Fig. 1.3. The baseline, L , for DUNE is 1300 km and for T2K is 295 km. To be able to make conclusions for the value of δ_{CP} and mass hierarchy, the neutrino energies must be

known within 100 MeV for DUNE and 50 MeV for T2K [8]. Thus, the measurements on CC (π) reactions play an important role in obtaining accurate predictions of the oscillated spectrum as a function of E_ν .

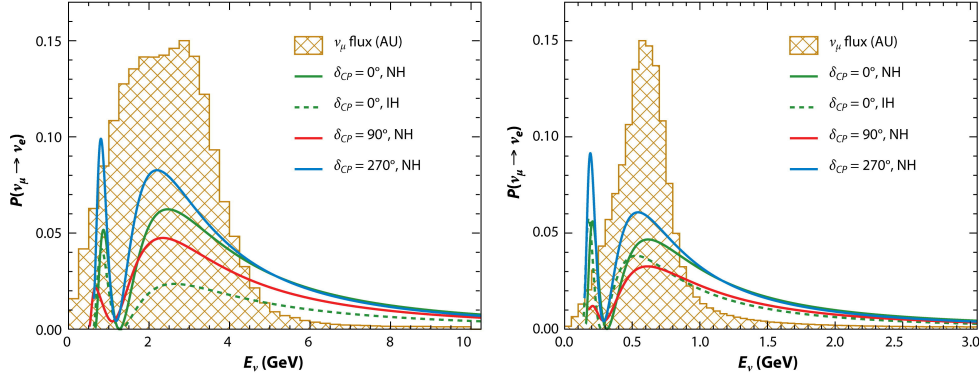


FIG. 1.3: Appearance probability for electron neutrino as a function of neutrino energy for DUNE (left) and T2K (right) neutrino oscillation experiments. The appearance probability for different δ_{CP} values and mass hierarchies (Normal Hierarchy (NH) and Inverted Hierarchy (IH)) are given. To make a precise measurements the neutrino energies have to be known within 100 MeV for DUNE and 50 MeV for T2K. From Refs. [9].

Furthermore, the measurements on CC (π) reactions improve the simulation predictions that are used in neutrino oscillation experiments. Precise measurements of CC (π) reactions provide insights into many physics processes. For example, the simulation models for the intranuclear scattering effects (or Final state Interactions = FSI), can be improved by analyzing the CC (π) scattering on different nuclei.

1.2 Charged current single pion production

A neutrino interaction can produce a pion through three different processes. One process proceeds through resonance production, in which the neutrino excites the struck nucleon to a baryon resonance states, which decays to a nucleon and a pion in $\sim 10^{-23}$ seconds. Another process is deep inelastic scattering (DIS), in which the neutrino interacts with one of the quarks inside the nucleon and the quark then hadronizes to form one or multiple pions. The pion production from a nucleon not involving a resonance, commonly called nonresonant processes and treated as

a subsample of the DIS processes for hadronic invariant mass W less than 2 GeV. A third process is coherent pion production from nuclei, an electroweak process in which a pion is created from neutrino-nucleus interaction where the target nucleus remains unchanged in its ground state after the scattering.

1.2.1 CC single pion production through baryon resonances

Many of the neutrino generators including GENIE use the Rein-Sehgal [10] phenomenology to predict the baryon resonance production. According to this formalism, the production cross section of a single resonance with mass M and negligible width is given by

$$\frac{d\sigma}{dq^2 d\nu} = \frac{G_F^2}{4\pi^2} \left(\frac{-q^2}{|\vec{q}|^2} \right) \kappa (u^2 \sigma_L + v^2 \sigma_R + 2uv\sigma_s) \delta(W - M) \quad (1.2)$$

where G_F^2 is the Fermi constant, q is the four-momentum transfer ($q_\nu - q_\mu$), ν is the energy transfer ($E_\nu - E_\mu$), $|\vec{q}|$ is the three-momentum transfer ($|\vec{q}_\nu - \vec{q}_\mu|$), and W is the hadronic invariant mass. The kinematic quantities u , v , and κ are

$$\begin{aligned} u &= \frac{E_\nu + E_l + |\vec{q}|}{2E_\nu}, \\ v &= \frac{E_\nu + E_l - |\vec{q}|}{2E_\nu}, \\ \kappa &= \frac{M^2 - m_N^2}{2m_N^2}, \end{aligned}$$

where E_ν is the initial neutrino energy, E_l is the final state lepton energy, and m_N is the nucleon mass. The σ_L , σ_R , and σ_s are the partial helicity cross sections for an intermediate vector boson of left-handed, right-handed and zero helicity respectively. The helicity cross sections are calculated using the Feynman-Kislinger-Ravndal (FKR) model [11], which represents the basic quark-quark interactions with a relativistic harmonic oscillator.

The narrow width approximation $\delta(W - M)$ can be replaced for resonances with a finite width Γ by a Breit-Wigner factor given by

$$\delta(W - M) \rightarrow \frac{1}{2\pi} \frac{\Gamma}{(W - M)^2 + \frac{\Gamma^2}{4}}. \quad (1.3)$$

The total cross section is obtained by integrating Eq. (1.2) within the bounds $W_{min} \leq W \leq W_{max}$ and $|q^2|_{min} \leq |q^2| \leq |q^2|_{max}$, whose limits are given by

$$\begin{aligned} W_{min} &= m_N + m_\pi, \\ W_{max} &= \sqrt{s} = \sqrt{2m_N E_\nu + m_N^2}, \\ |q^2|_{min} &= 0, \\ |q^2|_{max} &= \frac{(s - m_N^2)(s - W^2)}{s}. \end{aligned}$$

The measured cross section is different from the cross section of a single isolated resonance. In the measured cross section the nearby resonances will overlap and interfere to produce the same final state. The interference occurs only for identical final states with same orbital angular momentum and spin. As an example for the interfering resonances, the $\nu n \rightarrow \mu^- p \pi^0$ channel will be described.

The first step is to obtain the isospin amplitudes for the $\nu n \rightarrow \mu^- p \pi^0$ channel. The isospin state $|I, I_z\rangle$ for proton is $|\frac{1}{2}, +\frac{1}{2}\rangle$ and the isospin state for the neutral pion is $|1, 0\rangle$. Thus, there are two possible isospin states for the $p\pi^0$ final state: $A_3^{CC} = |\frac{3}{2}, +\frac{1}{2}\rangle$ and $A_1^{CC} = |\frac{1}{2}, +\frac{1}{2}\rangle$. Using the specific Clebsch-Gordon coefficients for the whole transition sequence given in Ref. [12] the total amplitude $A^{CC}(p\pi^0)$ is written as

$$\text{Ampl}(\nu n \rightarrow \mu^- p \pi^0) = A^{CC}(p\pi^0) = \frac{2}{3} (A_3^{CC} - A_1^{CC}). \quad (1.4)$$

Here, the A_3^{CC} is dominated by isospin $\frac{3}{2}$ resonances, while A_1^{CC} is dominated by isospin $\frac{1}{2}$ resonances. In the Rein-Sehgal paper [10], the charged-current amplitudes are given by

$$\begin{aligned}\sqrt{2}A_3^{CC} &= \sqrt{3}\sum_{I=\frac{3}{2}}a^{CC}(\mathbb{N}_3^{*+}), \\ \frac{2}{3}A_1^{CC} &= \sqrt{\frac{1}{3}}\sum_{I=\frac{1}{2}}a^{CC}(\mathbb{N}_1^{*+}),\end{aligned}$$

where $\mathbb{N}_{3,1}^{*+}$ represents positively charged resonances of isospin $\frac{3}{2}$ or $\frac{1}{2}$. Thus the total amplitude for $A^{CC}(p\pi^0)$ can be written as

$$A^{CC}(p\pi^0) = \sqrt{\frac{2}{3}}\sum_{I=\frac{3}{2}}a^{CC}(\mathbb{N}_3^{*+}) - \sqrt{\frac{1}{3}}\sum_{I=\frac{1}{2}}a^{CC}(\mathbb{N}_1^{*+}) \quad (1.5)$$

Since only the resonances with the same spin and the same orbital angular momentum are allowed to interfere, the resonance $P_{33}(1232)$ can interfere with the resonance $P_{13}(1740)$, however it cannot interfere with $P_{11}(1450)$ or $D_{33}(1730)$. Consequently, $|A^{CC}(p\pi^0)|^2$ can be calculated with interfering resonances having a central mass up-to 2 GeV by the following equation:

$$\begin{aligned}|A^{CC}(p\pi^0)|^2 &= \left| \sqrt{\frac{2}{3}}\sum_{I=\frac{3}{2}}a^{CC}(S_{31}^+) - \sqrt{\frac{1}{3}}\sum_{I=\frac{1}{2}}a^{CC}(S_{11}^+) \right|^2 \\ &+ \sum_{j=1,3} \left| \sqrt{\frac{2}{3}}\sum_{I=\frac{3}{2}}a^{CC}(P_{3j}^+) - \sqrt{\frac{1}{3}}\sum_{I=\frac{1}{2}}a^{CC}(P_{1j}^+) \right|^2 \\ &+ \sum_{j=3,5} \left| \sqrt{\frac{2}{3}}\sum_{I=\frac{3}{2}}a^{CC}(D_{3j}^+) - \sqrt{\frac{1}{3}}\sum_{I=\frac{1}{2}}a^{CC}(D_{1j}^+) \right|^2 \\ &+ \sum_{j=5,7} \left| \sqrt{\frac{2}{3}}\sum_{I=\frac{3}{2}}a^{CC}(F_{3j}^+) - \sqrt{\frac{1}{3}}\sum_{I=\frac{1}{2}}a^{CC}(F_{1j}^+) \right|^2.\end{aligned}$$

1.2.2 CC single pion production through deep inelastic scattering

The cross section for neutrino-nucleon scattering can be expressed using structure functions as follows:

$$\frac{d^2\sigma^{\nu N}}{dx dy} = \frac{G_F^2 s}{2\pi} \left[y^2 x F_1^{\nu N}(x, Q^2) + (1-y) F_2^{\nu N}(x, Q^2) + y \left(1 - \frac{y}{2}\right) x F_3^{\nu N}(x, Q^2) \right] \quad (1.6)$$

where, x and y are dimensionless kinematic variables defined as $x = \frac{Q^2}{2m_N \nu}$ and $y = \left(\frac{2m_N}{s-m_N^2}\right) \nu$.

The structure functions $F_1^{\nu N}(x, Q^2)$, $F_2^{\nu N}(x, Q^2)$, and $F_3^{\nu N}(x, Q^2)$ are functions of parton distribution functions (PDFs) and they describe the quark composition of the nucleon. The structure functions are the experimental observables of DIS interactions and can be obtained from global fits to various data sets at very high energies [13, 14, 15].

1.3 Review of previous experiments reporting charged current single π^0 production

There are two measurements by S. J. Barish *et al.* in 1976 [16] and by G. M. Radecky *et al.* in 1982 [17] using the Argonne National Laboratory's (ANL) 12-ft deuterium-filled bubble chamber [18]. Both measurements limited the neutrino energy to <1.5 GeV and reported distributions for the nucleon-pion invariant mass $M(N\pi)$ and the four-momentum transfer square Q^2 for all CC (π) reactions.

T. Kitagaki *et al.* in 1986 [19] reported measurements for all CC (π) reactions using Brookhaven National Laboratory's (BNL) 7-ft deuterium-filled bubble chamber. The experiment used a wide-band neutrino beam with an average energy of 1.6 GeV. The nucleon-pion invariant mass distributions for all CC (π) channels are shown in Fig. 1.4. In the $p\pi^+$ channel the $\Delta^{++}(1232)$ peak is dominant and no other resonance structure is observed. However, in the $p\pi^0$ and $n\pi^+$ channels, in addition to the $\Delta^+(1232)$ peak, a broad $N\pi$ -mass distribution ranging up-to 2.5 GeV is observed.

The SKAT collaboration in 1989 [20] reported cross-section measurements of single pion measurements for charged current neutrino and anti-neutrino interactions.

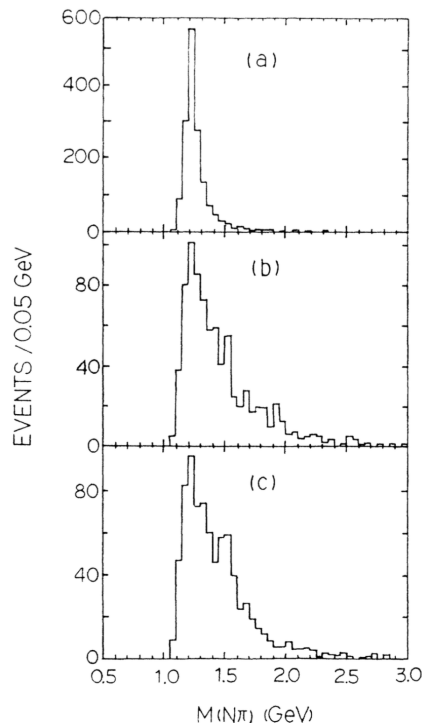


FIG. 1.4: Nucleon-pion invariant-mass $M(N\pi)$ distributions for the final states $p\pi^+$ (a), $p\pi^0$ (b), and $n\pi^+$ (c). The $\Delta(1232)$ resonance is dominant in all cases. The $N\pi$ invariant-mass distributions for $p\pi^0$ and $n\pi^+$ channels have higher-mass events extending up-to 2.5 GeV. From Ref. [19].

The experiment used a heavy liquid bubble chamber exposed to the wide band neutrino and antineutrino beam of the Serpukhov U70 accelerator. The neutrino and anti-neutrino beam energies ranged between 3 and 30 GeV. The nucleon-pion invariant mass distributions for $p\pi^0$ and $n\pi^+$ channels are given in Fig. 1.5. After the $W < 2.0$ GeV requirement, the $p\pi^0$ sample has 165 candidates and the $n\pi^+$ sample has 76 candidates. The $\Delta(1232)$ resonance is not apparent in the distributions and both samples have contributions from higher W regions.

Deuterium bubble chamber measurements for ν_μ -CC(π) and $\bar{\nu}_\mu$ -CC(π) reactions were reported by D. Allasia *et al.* in 1990 [21]. The experiment used high energy beams with an average energy of 54 GeV for neutrinos and 40 GeV for anti-neutrinos. The nucleon-pion invariant mass distributions for all charged current single pion production from neutrino and anti-neutrino interactions are shown in Fig 1.6. In the pure isospin $I = \frac{3}{2}$ final states ($p\pi^+$ and $n\pi^-$) the $\Delta(1232)$ peak is dominant

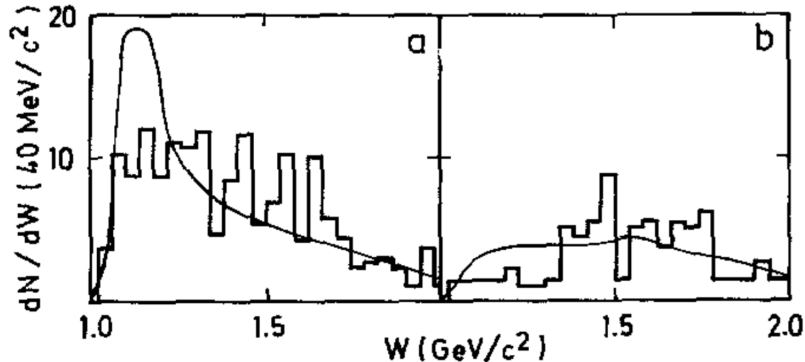


FIG. 1.5: Nucleon-pion invariant mass distributions for $p\pi^0$ (a) and $n\pi^+$ (b) channels. The solid black line represents the simulation prediction. In the $p\pi^0$ channel the $\Delta(1232)$ resonance is superimposed and the higher W region is included. In the $n\pi^+$ sample there is a flat contribution over the whole W range. From Ref. [20].

and there are small contributions from other states. However, in other channels ($p\pi^-$, $p\pi^0$ and $n\pi^+$), there is evidence for contributions from higher-mass states.

1.4 Review of neutrino oscillations

Neutrino induced CC single-pion production measurements are important for neutrino oscillation experiments. Thus, a short review of neutrino oscillation phenomenology and latest neutrino oscillation parameters are provided in this section.

Experiments have shown that the neutrinos can convert from one flavor state to another. For example, the $\nu_\mu \rightarrow \nu_\tau$ oscillation was observed by the OPERA Collaboration [22]. The OPERA experiment directly observed tau leptons at interaction vertices initiated by a ν_μ neutrino beam that originated from 730 km away.

The neutrino oscillation formalism is basically the quantum mechanics of superposition mixed states and involves two distinct sets of basis states. The mechanism is based on the fact that neutrino flavor eigenstates (ν_e, ν_μ, ν_τ) can be represented by orthogonal linear combinations of mass eigenstates (ν_1, ν_2, ν_3) - the mass basis. Similarly mass eigenstates can be represented by orthogonal linear combinations of flavor eigenstates - the flavor basis.

To illustrate the neutrino oscillation mechanism, we restrict the discussion to only

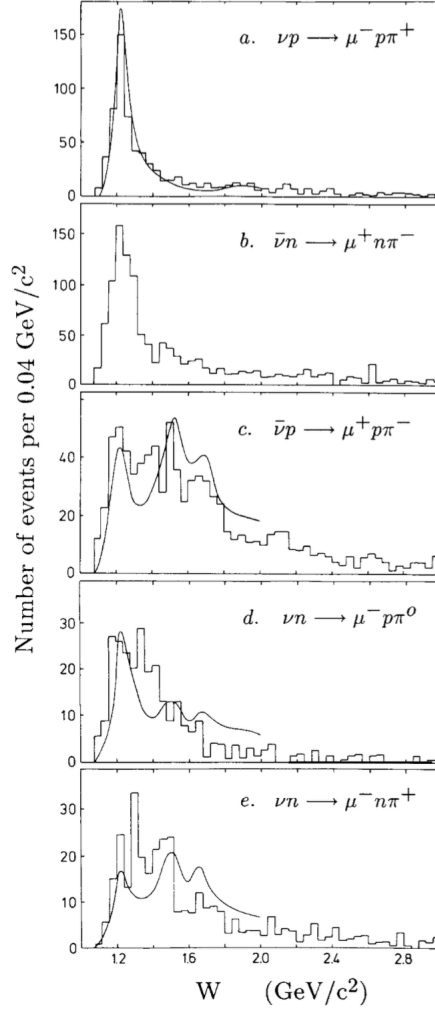


FIG. 1.6: Nucleon-pion invariant mass distributions for ν_μ -CC(π) and $\bar{\nu}_\mu$ -CC(π) reactions. The solid curves represent the predictions of Rein-Sehgal [10]. In the $p\pi^+$ and $n\pi^-$ final states the $\Delta(1232)$ peak is dominant. However in the other channels there are contributions from higher W regions. From Ref. [21].

two neutrino flavors (ν_μ, ν_τ) and calculate the probability that the muon neutrino has converted into a tau neutrino after a time t .

With two neutrino flavor states (ν_μ, ν_τ), there are two mass states (ν_2, ν_3). The relation between the flavor eigenstates and mass eigenstates is

$$\begin{pmatrix} \nu_\mu \\ \nu_\tau \end{pmatrix} = \begin{pmatrix} \cos \theta & \sin \theta \\ -\sin \theta & \cos \theta \end{pmatrix} \begin{pmatrix} \nu_2 \\ \nu_3 \end{pmatrix} \quad (1.7)$$

Using the mixing matrix the flavor eigenstates (ν_μ, ν_τ) can be represented in terms

of (ν_2, ν_3) as the following:

$$\begin{aligned} |\nu_\mu\rangle &= \cos\theta |\nu_2\rangle + \sin\theta |\nu_3\rangle, \\ |\nu_\tau\rangle &= -\sin\theta |\nu_2\rangle + \cos\theta |\nu_3\rangle. \end{aligned}$$

According to the effective wave equation, the mass eigenstates evolve in time as

$$|\nu_2(t)\rangle = e^{-iE_2t/\hbar} |\nu_2(0)\rangle \quad \text{and} \quad |\nu_3(t)\rangle = e^{-iE_3t/\hbar} |\nu_3(0)\rangle \quad (1.8)$$

which leads to

$$\begin{aligned} |\nu_\mu(t)\rangle &= \cos\theta |\nu_2(t)\rangle + \sin\theta |\nu_3(t)\rangle \\ &= \cos\theta e^{-iE_2t/\hbar} |\nu_2(0)\rangle + \sin\theta e^{-iE_3t/\hbar} |\nu_3(0)\rangle. \end{aligned}$$

Then the probability amplitude for observing a ν_τ after a time t is

$$\begin{aligned} \langle \nu_\tau | \nu_\mu(t) \rangle &= -\sin\theta \cos\theta e^{-iE_2t/\hbar} \langle \nu_2(0) | \nu_2(0) \rangle + \sin\theta \cos\theta e^{-iE_3t/\hbar} \langle \nu_3(0) | \nu_3(0) \rangle \\ &= \sin\theta \cos\theta \left(e^{-iE_3t/\hbar} - e^{-iE_2t/\hbar} \right). \end{aligned}$$

The probability that the muon neutrino has converted into a tau neutrino, after a time t is

$$\begin{aligned} |\langle \nu_\tau | \nu_\mu(t) \rangle|^2 &= (\sin\theta \cos\theta)^2 \left(e^{-iE_3t/\hbar} - e^{-iE_2t/\hbar} \right) \left(e^{iE_3t/\hbar} - e^{iE_2t/\hbar} \right) \\ &= \frac{\sin^2(2\theta)}{4} \left(1 - e^{i(E_3-E_2)t/\hbar} - e^{-i(E_3-E_2)t/\hbar} + 1 \right) \\ &= \frac{\sin^2(2\theta)}{4} \left(2 - 2 \cos \frac{(E_3 - E_2)t}{\hbar} \right) \\ &= \frac{\sin^2(2\theta)}{4} 4 \sin^2 \left(\frac{E_3 - E_2}{2\hbar} t \right), \end{aligned}$$

which reduces to

$$P_{\nu_\mu \rightarrow \nu_\tau} = \sin^2(2\theta) \sin^2 \left(\frac{E_3 - E_2}{2\hbar} t \right). \quad (1.9)$$

Equation 1.9 shows why the process is called oscillations: ν_μ will convert to ν_τ , and then back again, sinusoidally. [23]

In the probability equation (Eq. (1.9)) the energies of the neutrino mass states cannot be directly measured. The mass eigenstates are ν_2 and ν_3 , with masses m_2 and m_3 . Using the relativistic energy formula ($E^2 = |\vec{p}|^2 c^2 + m^2 c^4$), the energy difference can be approximately written as:

$$E_3 - E_2 \approx \frac{m_3^2 c^3 - m_2^2 c^3}{2|\vec{p}|} \approx \frac{(m_3^2 - m_2^2)}{2E_\nu} c^4 \quad (1.10)$$

Using Eq. (1.10) the Eq. (1.9) can be written

$$P_{\nu_\mu \rightarrow \nu_\tau} = \sin^2(2\theta) \sin^2\left(\frac{(m_3^2 - m_2^2) c^4 L}{4\hbar c E_\nu}\right) \quad (1.11)$$

where $L \approx ct$ is the distance traveled.

Notice that the ratio L/E_ν is the only variable quantity in the neutrino oscillation probability. Thus the neutrino energy, E_ν , and the distance from the neutrino source, L , are the key variables of a neutrino oscillation experiment. Equation 1.11 shows that the neutrino oscillations are only sensitive to differences in (the squares of) neutrino masses.

1.4.1 Three flavor neutrino oscillations

The Standard Model contains three flavors of neutrinos each of which is associated with one of the three fermion families, and so current experiments are measuring oscillations among three flavor states. In three flavor oscillation mechanism there are three mass splittings,

$$\Delta m_{21}^2 = m_2^2 - m_1^2$$

$$\Delta m_{32}^2 = m_3^2 - m_2^2$$

$$\Delta m_{31}^2 = m_3^2 - m_1^2$$

where only two of them are independent ($\Delta m_{31}^2 = \Delta m_{21}^2 + \Delta m_{32}^2$). From the oscillation measurements it is known that one splitting is very small, and the other two relatively large. By convention ν_1 and ν_2 label the pair closely-spaced in mass (with $m_2 > m_1$), and ν_3 has a distinctly different mass. This structure is somewhat similar to the charged lepton case where e^- and μ^- are fairly close in mass, but the τ^- is much higher. However, in the neutrino case it is not known whether ν_3 is heavier than the other two or not, consequently two different mass spectra are possible as shown in Fig. 1.7.

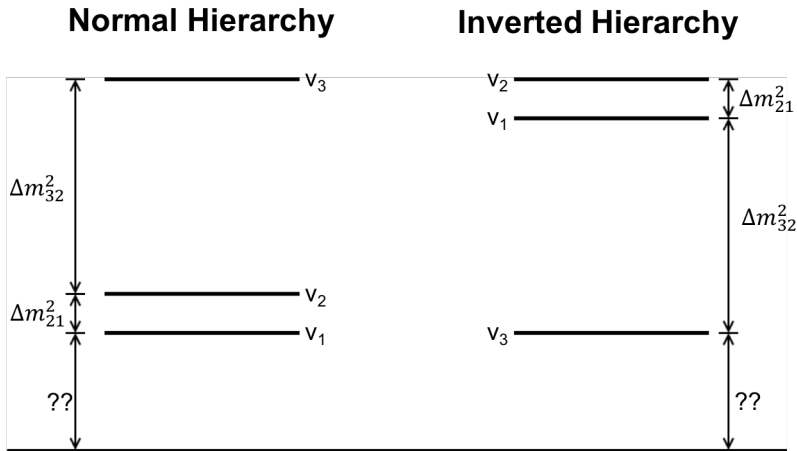


FIG. 1.7: “Normal” and “Inverted” neutrino mass spectra

As mentioned previously, neutrino oscillation experiments are only sensitive to differences in neutrino masses squared, and the global analysis of variety of measurements for these are provided in Table 1.1. Figure 1.7 provides no information on the absolute value of neutrino masses. At present it is known from tritium β decay experiments that the mass of the lightest neutrino is less than about 2 eV [24].

Determining the mass hierarchy requires a multi-parameter fit using all neutrino oscillation parameters. The other neutrino oscillation parameters are three mixing angles (θ_{12} , θ_{23} , θ_{13}) and one CP-violating phase. These parameters appear in the mixing matrix U which couples mass eigenstates with flavor eigenstates.

For three flavors the mixing matrix is more complicated;

$$\begin{pmatrix} \nu_e \\ \nu_\mu \\ \nu_\tau \end{pmatrix} = \begin{pmatrix} U_{e1} & U_{e2} & U_{e3} \\ U_{\mu1} & U_{\mu2} & U_{\mu3} \\ U_{\tau1} & U_{\tau2} & U_{\tau3} \end{pmatrix} \begin{pmatrix} \nu_1 \\ \nu_2 \\ \nu_3 \end{pmatrix} \quad (1.12)$$

For three flavors the mixing matrix U can be expressed using three different mixing angles $(\theta_{12}, \theta_{23}, \theta_{13})$ and one CP-violating phase (δ_{CP}) as follows:

$$U = \begin{pmatrix} c_{12}c_{13} & s_{12}c_{13} & s_{13}e^{-i\delta_{CP}} \\ -s_{12}c_{23} - c_{12}s_{23}s_{13}e^{i\delta_{CP}} & c_{12}c_{23} - s_{12}s_{23}s_{13}e^{i\delta_{CP}} & s_{23}c_{13} \\ s_{12}s_{23} - c_{12}c_{23}s_{13}e^{i\delta_{CP}} & -c_{12}s_{23} - s_{12}c_{23}s_{13}e^{i\delta_{CP}} & c_{23}c_{13} \end{pmatrix} \quad (1.13)$$

where $c_{ij} \equiv \cos \theta_{ij}$, $s_{ij} \equiv \sin \theta_{ij}$, δ_{CP} is the CP-violating phase.

The mixing matrix U is known as Pontecorvo-Maki-Nakagava-Sakata (PMNS) matrix. It can be parametrized using three different Euler rotation matrices;

$$U = R_1 R_2 R_3 \quad (1.14)$$

where

$$R_1(\theta_{23}) = \begin{pmatrix} 1 & 0 & 0 \\ 0 & c_{23} & s_{23} \\ 0 & -s_{23} & c_{23} \end{pmatrix} \quad R_3(\theta_{12}) = \begin{pmatrix} c_{12} & s_{12} & 0 \\ -s_{12} & c_{12} & 0 \\ 0 & 0 & 1 \end{pmatrix}$$

$$R_2(\theta_{13}, \delta_{CP}) = \begin{pmatrix} c_{13} & 0 & s_{13}e^{-i\delta_{CP}} \\ 0 & 1 & 0 \\ -s_{13}e^{i\delta_{CP}} & 0 & c_{13} \end{pmatrix}$$

The experimentally measured values for this parametrization lead to the following classifications: The mixing angle θ_{23} and the mass difference term Δm_{32}^2 are associated with atmospheric neutrino oscillations. The mixing angle θ_{13} is associated with ν_e flavor appearance and it is the term closely linked to the CP-violating phase δ_{CP} . Finally, the mixing angle θ_{12} and the mass difference term Δm_{21}^2 are associated with solar neutrino oscillations, due to its association with solar neutrino oscillation the mass difference term Δm_{21}^2 is also known as solar mass difference $\Delta m_{\odot}^2 = \Delta m_{21}^2$.

M.C. Gonzalez-Garcia, Michele Maltoni and Thomas Schwetz collected data from all neutrino oscillation experiments and carried out a global fit for all neutrino oscillation parameters. Their fit results for mixing angles and the mass squared differences are shown in Table 1.1.

	Normal Mass Hierarchy		Inverted Mass Hierarchy	
	bfp $\pm 1\sigma$	3σ range	bfp $\pm 1\sigma$	3σ range
$\sin^2 \theta_{12}$	$0.306^{+0.012}_{-0.012}$	$0.271 \rightarrow 0.345$	$0.306^{+0.012}_{-0.012}$	$0.271 \rightarrow 0.345$
$\theta_{12}/$	$33.56^{+0.77}_{-0.75}$	$31.38 \rightarrow 35.99$	$33.56^{+0.77}_{-0.75}$	$31.38 \rightarrow 35.99$
$\sin^2 \theta_{23}$	$0.441^{+0.027}_{-0.021}$	$0.385 \rightarrow 0.635$	$0.587^{+0.020}_{-0.024}$	$0.393 \rightarrow 0.640$
$\theta_{23}/$	$41.6^{+1.5}_{-1.2}$	$38.4 \rightarrow 52.8$	$50.0^{+1.1}_{-1.4}$	$38.8 \rightarrow 53.1$
$\sin^2 \theta_{13}$	$0.02166^{+0.00075}_{-0.00075}$	$0.01934 \rightarrow 0.02392$	$0.02179^{+0.00076}_{-0.00076}$	$0.01953 \rightarrow 0.02408$
$\theta_{13}/$	$8.46^{+0.15}_{-0.15}$	$7.99 \rightarrow 8.90$	$8.49^{+0.15}_{-0.15}$	$8.03 \rightarrow 8.93$
$\delta_{CP}/$	261^{+51}_{-59}	$0 \rightarrow 360$	277^{+40}_{-46}	$145 \rightarrow 391$
$\frac{\Delta m_{21}^2}{10^{-5} eV^2}$	$7.50^{+0.19}_{-0.17}$	$7.03 \rightarrow 8.09$	$7.50^{+0.19}_{-0.17}$	$7.03 \rightarrow 8.09$
$\frac{\Delta m_{3\ell}^2}{10^{-3} eV^2}$	$+2.524^{+0.039}_{-0.040}$	$+2.407 \rightarrow +2.643$	$-2.514^{+0.038}_{-0.041}$	$-2.635 \rightarrow -2.399$

TABLE 1.1: Three-flavor oscillation parameters from a fit to global data as of November 2016. The numbers in the 1st (2nd) column were obtained assuming Normal Mass Hierarchy(NO) (Inverted Mass Hierarchy(IO)). Note that $\Delta m_{3\ell}^2 \equiv \Delta m_{31}^2 > 0$ for NO and $\Delta m_{3\ell}^2 \equiv \Delta m_{32}^2 < 0$ for IO. From Refs. [25, 26].

Chapter 2

The NuMI Neutrino Beam at Fermilab

2.1 The NuMI beam

The Neutrinos at the Main Injector (NuMI) neutrino beam [27] was initially built at Fermilab to provide neutrinos for MINOS, a long-baseline neutrino oscillation experiment. The NuMI beam facility has now been used by many experiments, namely: MINOS [28], MINOS+ [29], MINERvA [30], ArgoNeuT [31], and NOvA [4].

The NuMI beam facility produces neutrinos by steering a proton beam onto a narrow graphite target. The produced hadrons are then magnetically focused in the forward direction and are directed into a decay pipe where most of the mesons decay into neutrinos (or antineutrinos) and charged leptons. The resulting neutrino beam reaches the MINERvA detector and the MINOS Near Detector at locations that are approximately 1.04 km downstream of the NuMI target. Then it continues further north through the Earth's crust, encounters the MINOS Far Detector 734 km away in the Soudan Mine in Minnesota, and finally exits the Earth 12 km further north [32]. The NuMI Beam is described below: Section 2.2 describes the initial proton beam created by the Fermilab Main Injector, and Sec. 2.3 describes the neutrino beam production after the protons have collided with the graphite target.

2.2 The proton beam

The NuMI beam is presently the world's most intense neutrino beam and is produced by the 120 GeV protons extracted from the Fermilab Main Injector. A layout of the accelerator complex at Fermilab is shown in Fig. 2.1 [33]. Protons are accelerated to 120 GeV in three stages: Firstly, protons originate as H^+ ions in the Linac which accelerates them to 400 MeV, then they are accelerated to 8 GeV by the Booster. The Booster batches are transported to the Main Injector, which accelerates protons to 120 GeV. The circumference of the Main Injector is seven times the circumference of the Booster. Consequently the Main Injector can accommodate storage and acceleration of six Booster batches [32]. Finally 120 GeV protons are extracted and transported 350 m to the NuMI target. The steered protons collide

with a 1 meter long graphite target, creating the initial particles for the neutrino beam. The total number of protons on target (P.O.T.) for the MINERvA low-energy (LE) run for muon neutrinos, which corresponds to the data set used in this analysis, is 3.33×10^{20} . Figure 2.2 shows the data-taking periods for ν_μ and $\bar{\nu}_\mu$ for whole low energy exposure of the MINERvA detector.

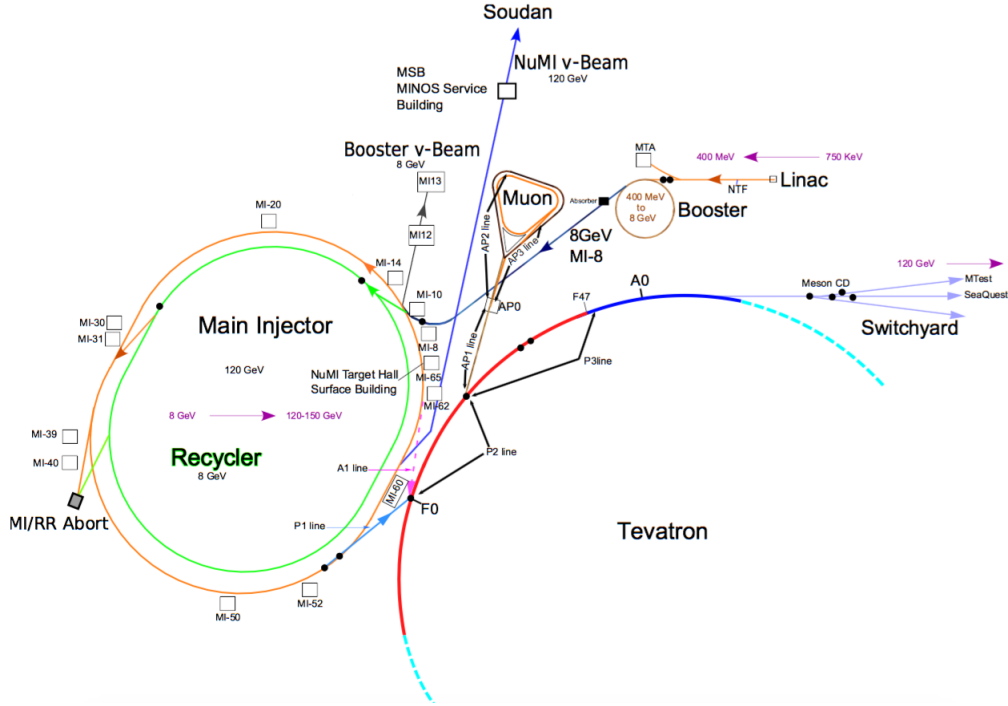


FIG. 2.1: Fermilab accelerator complex. The proton accelerator cycle for the NuMI Beam starts with the Linac and is followed by the Booster and then the Main Injector. From Ref. [32].

2.3 The neutrino beam

Protons colliding with the graphite target produce hadrons, mostly pions (π^\pm) and kaons (K^\pm, K^0). The positive mesons (π^+, K^+) are focused by two magnetic horns and then they enter to a 675 m long decay volume. The horns apply a charge sign selection to focus hadrons of one or the other charge sign. For example, if a neutrino beam is being created, the positively charged mesons are focused towards the beam axis and negatively charged mesons are deflected away. Figure 2.3 shows a diagram of the magnetic field and the force applied to a positively charged particle by the

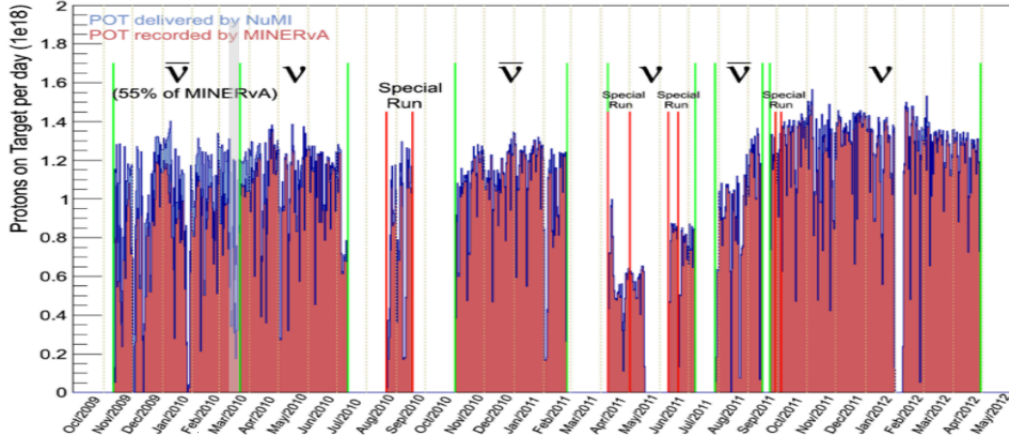


FIG. 2.2: Low-energy run period for MINERvA experiment. The total POT for ν_μ running is 3.33×10^{20} and for $\bar{\nu}_\mu$ running is 2.01×10^{20} . The MINERvA detector live time during this period was 97.2%. From Ref. [33]

horn. In the figure a current I flows into the page on the inner cylinder and returns back from the outer cylinder. Due to this closed current loop there are no magnetic fields inside or outside of the horn. The magnetic field \vec{B} between the two cylinders is calculated according to Ampere's Law as given in Eq. (2.1).

$$\oint \vec{B} \cdot d\vec{s} = \mu I_{enc} \quad (2.1)$$

where μ is the magnetic permeability and I_{enc} is the current enclosed by the loop. The magnetic force \vec{F} on a charged particle due to the magnetic field \vec{B} is the Lorentz force whose equation is

$$\vec{F} = q\vec{v} \times \vec{B} \quad (2.2)$$

where q is the charge of the particle and \vec{v} is the velocity vector of the particle.

This horn configuration focuses the positively charged particles back to the beam line and diverts the negatively charged particles away from the beam line. Since there is no magnetic field inside the inner cylinder, the particles moving near the beam line center are not affected by the magnetic focusing.

The focused π^+ and K^+ mesons decay via the following modes to create the neutrino beam;

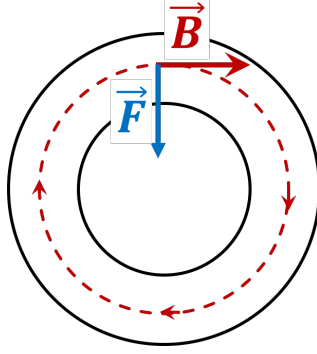


FIG. 2.3: Diagram of the magnetic field and the force applied to a positively charged particle by the horn. A current I flows into the page on the inner cylinder and returns back from the outer cylinder. The current on the inner cylinder creates a magnetic field in the clockwise direction shown as the dashed red line. Due to this magnetic field a force \vec{F} is applied to the positively charged particles traveling into the page. The sign of the \vec{F} is opposite for negatively charged particles.

$$\pi^+ \rightarrow \mu^+ + \nu_\mu$$

$$K^+ \rightarrow \mu^+ + \nu_\mu$$

There is also a 6% $\bar{\nu}_\mu$ component coming from the decay of negative hadrons (π^- , K^-) and 1% contamination of ($\nu_e + \bar{\nu}_e$) due to the subdominant electronic decay mode of K^+ hadrons, decays of K^0 particles, and decays of tertiary muons [32, 34]. The schematic of the NuMI beam is shown in Fig. 2.4.

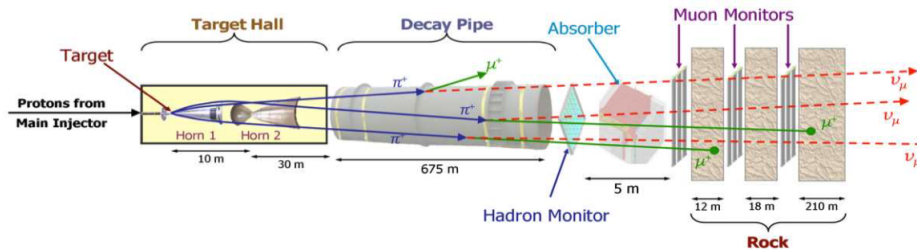


FIG. 2.4: Schematic of the NuMI beam. The individual components of the NuMI beam (not to scale) are shown together with the relevant dimensions. All the important elements are shown, including the target, the horns, the decay pipe, the hadron absorber, and the so-called muon shield which consists of the dolomite rock upstream of the MINOS Near and MINERvA Detectors. From Ref. [32].

A hadron monitor is located at the end of the decay pipe, just in front of the 5

m thick steel absorber, to record the profile of the residual hadrons. These residual hadrons are attenuated to a negligible number by the absorber. In order to measure the residual muon flux, three muon monitors are positioned inside the rock just downstream of the absorber. The 240 m of rock following the absorber stops the remaining muons in the beam [32]. At a distance of 240 m further downstream, the neutrino beam enters a cavern that houses the MINERvA and MINOS Near detectors.

2.4 NuMI beam flux

The neutrino beam flux is proportional to the flux of the secondary hadrons produced from the collision of protons with the graphite target. The produced hadrons are focused by two magnetic horns, Horn 1 and Horn 2, which are located in the “Target Hall” as seen in Fig. 2.4. The horns significantly increase the hadron flux in the desired energy range and provide flexibility in choosing that energy.

The target-to-horn distance is adjustable and the separation between the two horns can also be changed. The design accommodates three potential Horn 2 positions of 10 m, 23 m, and 37 m downstream from the zero position (taken to be the upstream end of Horn 1), corresponding to low, medium and high neutrino energy respectively, coupled with appropriate target movement upstream. Figure 2.5 shows a schematic of the 95 cm graphite target inserted into Horn 1 for the low energy configuration used in the MINERvA experiment [32]. Data collected by the MINERvA detector for this analysis used the same horn configuration.

Hadrons that move along the beam axis traverse the magnetic focusing undeflected. However, the mesons produced in the target have a transverse momentum spectrum that peaks at approximately 0.35 GeV/c, which means a large fraction of the mesons will not be moving along the beam axis.

Charged mesons that are well-focused by the first horn are generally not affected by the second horn. However particles that are either over- or under-focused by the first horn, are usually brought into better focus by the second horn. In other words,

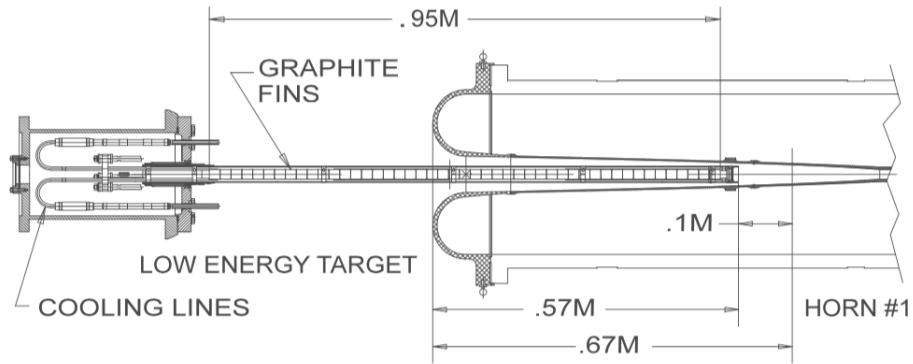


FIG. 2.5: Low energy target with front half of Horn 1. The target is shown retracted by 10 cm upstream from the maximal design insertion. This corresponds to the nominal low energy beam configuration in which the MINERvA low energy (LE) data was taken. From Ref. [32].

the charged mesons are brought into alignment with the beam direction. This two horn system increases the efficiency of the focusing system by about 50%. Different initial production angles with trajectories through the horns are illustrated in Fig. 2.6 [32].

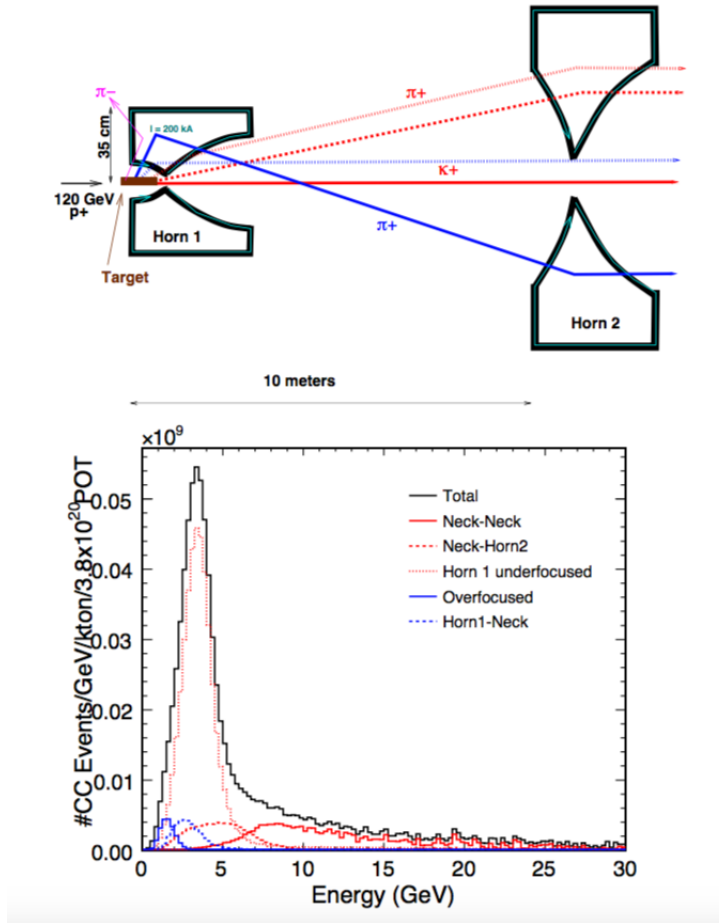


FIG. 2.6: Hadron trajectories through the two horns. The top diagram illustrates possible trajectories through the two NuMI horns. Hadrons that are under-focused or over-focused by the first horn are further focused by the second horn. The bottom graph illustrates the composition of the low energy NuMI spectrum from the different hadron trajectory classes through the horns. From Ref. [32].

Chapter 3

The MINERvA Detector

3.1 Detector overview

The MINERvA detector is designed to have the following functionality: 1) Resolve multi-particle final states; 2) track low energy charged particles; 3) contain electromagnetic showers; 4) contain high-energy (up to at least 10 GeV) final states; 5) resolve multiple interactions in a single beam spill; and 6) include targets with a wide range of nucleon number, A , to enable studies of the nuclear dependence of neutrino interactions.

In order to resolve multi-particle final states with low energy thresholds, the core of the detector must be fully active and have good spatial resolution. This region of the detector is called the “Active tracker”. Full containment of events requires that the active region be surrounded with electromagnetic calorimetry (ECAL) and hadronic calorimetry (HCAL). The details of the tracker and the calorimeters are discussed in Secs. 3.2 and 3.3.

Ideally, charge identification would be included by adding a magnetic field. However, this is impractical for the main detector for reasons of cost. In any case most of the charged current muons escape the detector. By placing MINERvA immediately upstream of the MINOS near detector, charge and energy measurements of forward-going muons can be made. Details of the MINOS detector utilization in MINERvA measurements are presented in Sec. 3.5.

A schematic side view of the detector is shown in Fig. 3.1 where the beam direction is from left to right. An illustrative charged-current neutrino interaction is shown inside the detector. Neutrino reactions in the rock upstream of the detector hall can produce hadrons and muons. A “veto wall” (visible in Fig. 3.1) upstream of the main detector shields against lower energy hadrons from the rock and tags the muons (referred to as “rock muons”), which can traverse all or part of the downstream detector. The veto wall consists of a 5 cm thick steel plate, a 1.9 cm thick plane of scintillator, a 2.5 cm thick steel plate, and a second plane of 1.9 cm thick scintillator [35].

The MINERvA detector is composed of 120 modules suspended vertically and

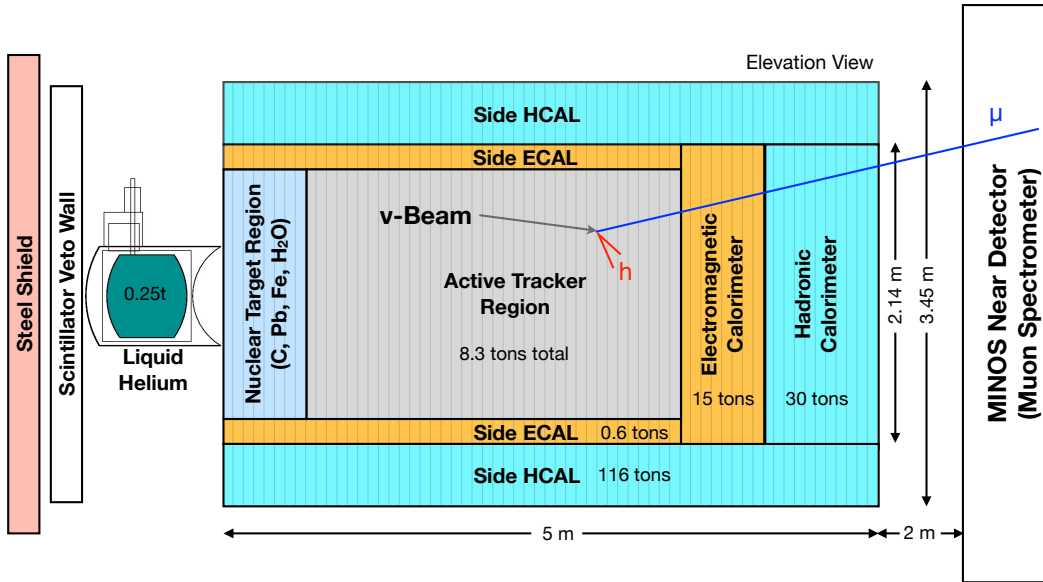


FIG. 3.1: Side view of the MINERvA detector showing the nuclear target, the tracker and the surrounding electromagnetic and hadronic calorimeter regions. From Ref. [35].

stacked along the beam direction. All MINERvA modules are in the shape of a regular hexagon and 2 planes of scintillator are mounted in one frame. A schematic front view of a single module in the active tracker is shown in Fig. 3.2. There are four basic types of modules: Tracking modules, electromagnetic calorimeter modules, hadronic calorimeter modules, and passive nuclear targets. There are three orientations of strips in the tracking planes, offset by 60° from each other, which enable the three-dimensional reconstruction of tracks. The 60° offset fits naturally with the hexagonal transverse cross section of the detector.

The MINERvA coordinate system is defined such that the z -axis is horizontal and points downstream along the central axis of the detector, the y -axis points upward, and the x -axis is horizontal pointing to beam left as viewed looking downstream, with the $x - y$ origin at the center of the detector. In this system the neutrino-beam central axis is in the $y - z$ plane and points downward at 3.37° [35].

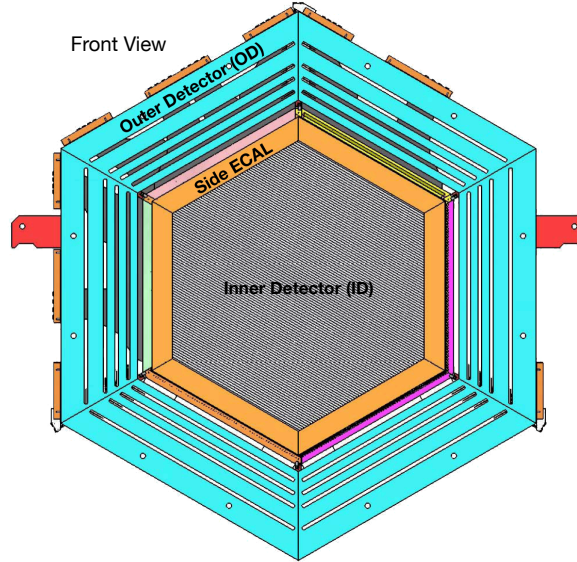


FIG. 3.2: Front view of a single detector module. The active region composed of scintillator is labeled “Inner Detector (ID)”. The region labelled “Side ECAL” is the electromagnetic calorimetry surrounding the tracker region. The Side ECAL is also surrounded by steel plates. The configuration functions as an HCAL; it is labelled “Outer Detector (ID)”. From Ref. [35].

3.2 Active tracker modules

The active tracking region is composed entirely of scintillator extrusions, and it serves as the primary fiducial volume for this analysis. That is, it is required that the event vertex be inside the active tracker region. The active tracker region has low density scintillator material ($\rho = 1.043 \pm 0.002$) g/cm³ for precise tracking. The fine sampling structure ensures that low energy ($E < 100$ MeV) particles can be tracked inside the detector [35].

In the MINERvA detector there are three different plane orientations, referred to as X-planes, U-planes or V-planes according to the coordinate in the MINERvA system. The X-planes have scintillator strips aligned vertically. The U- and V-planes are rotated 60° counterclockwise and clockwise from the X-planes in the x–y plane, respectively. Plane views can be seen in Fig. 3.3.

Three different views are used to avoid ambiguities with reconstructed hit associations that can occur when multiple tracks traverse two orthogonal planes. Each tracking and electromagnetic calorimeter module has one X-plane, and either a U-

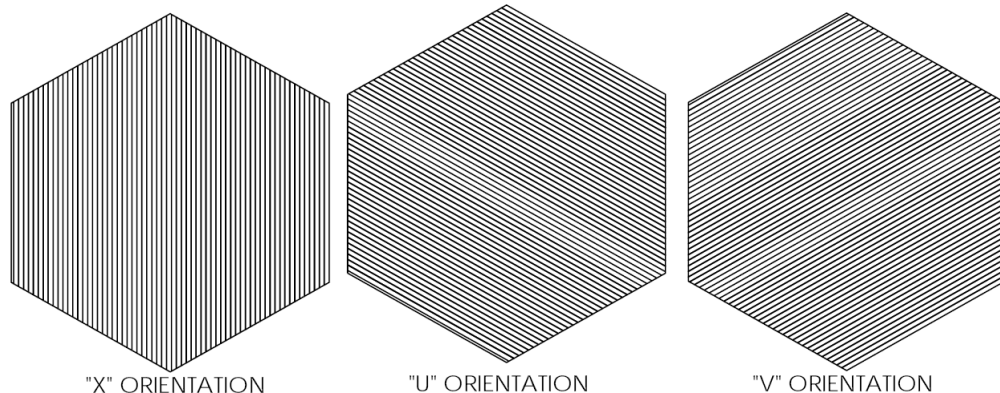


FIG. 3.3: Three different plane orientations in the MINERvA detector. From Ref. [36].

or a V-plane, with modules alternating between a UX and a VX structure with the X-planes always located downstream of the U- or V-planes. For example, an eight-plane setup (4 modules) will have the plane sequence UX VX UX VX.

Since the analysis requires that the neutrino interaction occur inside the active tracker region, the elemental composition of the tracking modules is important for the measurement. The elemental composition of the strips and assembled tracker scintillator planes is given in Table 3.1. There is some uncertainty in the composition of the coated strips due to the uncertainty in the coating thickness, which is estimated to have a relative uncertainty of about 10%. [35]

Component	H(%)	C(%)	O(%)	Al(%)	Si(%)	Cl(%)	Ti(%)
Strip	7.59	91.9	0.51	-	-	-	0.77
Plane	7.42	87.6	3.18	0.26	0.27	0.55	0.69

TABLE 3.1: Elemental composition of scintillator strips and constructed planes by mass percentage. The main elements are carbon and hydrogen for the low density scintillator material. The other elements such as Al, Si, Cl, and Ti are included in the coating material. From Ref. [35].

3.3 Electromagnetic and hadronic calorimeter modules

An Electromagnetic Calorimeter (ECAL) module has a structure that is similar to a central tracking module, the only difference is that the ECAL module has an additional 0.2 cm thick sheet of lead covering the entire scintillator plane. The

additional lead ($Z = 82$) dramatically increases the cross section of electromagnetic interactions due to the high atomic number (number of protons). The lead sheets on the upstream end of the planes ensure that each plane of ECAL has a lead absorber upstream of it. By having the same scintillator plane configuration as the active tracker, the ECAL enables directional measurement for photon and electron particles while providing excellent energy resolution for these particles. There are 10 modules in the ECAL region of the detector; they can be seen in Fig. 3.1. As shown in Figs. 3.1 and 3.2, each central tracking module is surrounded with an ECAL structure called the “Side ECAL”. The Side ECAL structure is obtained by attaching a 0.2 cm thick lead sheet on the outermost 15 cm of each central tracking module. The thickness of the lead sheets used for the electromagnetic calorimetry modules were measured using an ultrasonic device to determine the variation in thickness along the length of the sheet. The thickness of the lead sheets varies at the 5% level [35].

The Hadronic Calorimeter (HCAL) modules are also similar to central tracking modules. The HCAL modules consist of one scintillator plane instead of two and each scintillator plane is attached to a 2.54 cm (1 inch) thick hexagonal steel plane. Steel made from iron ($^{56}_{26}\text{Fe}$) is a good absorber for nuclear interactions because of its high density of nucleons and short radiation length. Steel is also preferred in HCAL designs due to its structural integrity and relatively low cost. Since there is only one scintillator plane attached to each module, they are inserted into the detector with a repeating pattern of X V X U [35]. There are 20 HCAL modules which can be seen in Fig. 3.1. The “Side HCAL” or “Outer Detector (OD)” visible in Fig. 3.2 is also constructed with steel plates. It serves as the HCAL around the detector, improving the containment of the events. The Side HCAL is instrumented with four strips of scintillator interleaved into the steel.

3.4 Optical system

3.4.1 Scintillator planes

Each tracking module consists of two scintillator planes and each scintillator plane is composed of 127 stacked triangular single scintillator strips. A green wavelength shifting (WLS) fiber running through the center of the strips provides signal read-out. The scintillator strips are triangular in cross section with a height of 17 ± 0.5 mm and a width of 33 ± 0.5 mm. Figure 3.4 shows the cross section of a single scintillator strip and three scintillators stacked as a part of a tracker plane. The scintillator strips are made from polystyrene pellets (Dow Styron 663 W) doped with 1% (by weight) 2,5-diphenyloxazole (PPO) and 0.03% (by weight) 1,4-bis (5-phenyloxazol-2-yl)benzene (POPOP). This scintillator composition was previously utilized in the scintillator strips of the MINOS experiment [37].

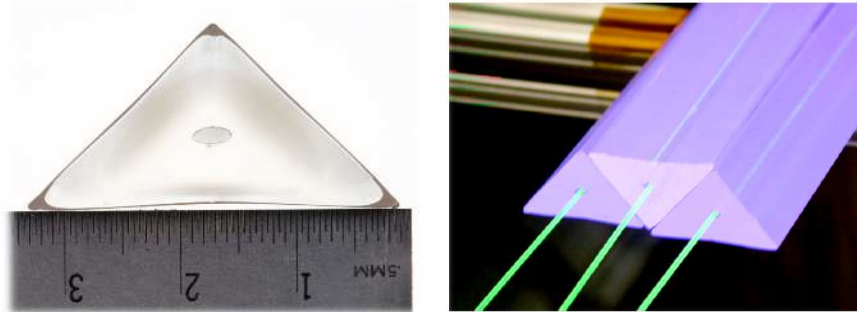


FIG. 3.4: MINERvA scintillator strips are triangular in cross section (left) and range from 122 cm to 245 cm in length. Planes are built by stacking the triangular strips as shown in the righthand figure. This configuration ensures that any charged particle traversing the plane creates a scintillation signal in a minimum of two strips. From Ref. [35].

3.4.2 Wavelength shifting fibers

The scintillator strips are read out by 1.2 mm diameter, 175 ppm ^{11}Y doped, ^{35}S , multicladd wavelength shifting (WLS) fibers produced by the Kuraray corporation [35]. Figure 3.4 shows the strips positioned inside a scintillator plane emitting green light.

MINERvA reads out only one end of its WLS fibers. To maximize light collection, the unread end of each fiber is “mirrored”. The procedure for preparing mirrored fiber ends consists of three steps: First, the end to be mirrored is polished using a technique called “ice-polishing” [38]. Then a 2500 Å thick reflective coating of 99.999% pure aluminum is applied and finally another protective layer of Red Spot UV Epoxy is applied to the mirrors. After this process the average mirror reflectivity is measured to be $83 \pm 7\%$ [35].

3.4.3 Photomultiplier tubes and optical boxes

The multi-anode photomultiplier tube (PMT) model number H8804MOD-2 manufactured by Hamamatsu Photonics is used as the MINERvA detector’s signal readout photosensor. That specific model has a timing resolution better than ~ 5 ns, which is required for distinguishing overlapping events within a single spill of the NuMI beamline and for measuring time-of-flight and decay times of charged mesons created in neutrino interactions [35]. It is essentially the same PMT as was used by MINOS [39].

The H8804MOD-2 PMT has an 8×8 array of pixels laid out on a $2 \text{ cm} \times 2 \text{ cm}$ grid, i.e. 64 pixels per PMT with each pixel having an effective size of $2 \times 2 \text{ mm}^2$. The general properties of the H8804MOD-2 PMT are listed in Table 3.2 and the operating characteristics provided by the manufacturer are given in Table 3.3 [35]. The PMTs for the detector are required to have a minimum quantum efficiency of 12% at 520 nm and a maximum-to-minimum pixel gain ratio less than three. A total of 507 PMTs are used in the fully instrumented detector [35].

Each PMT requires an enclosure to shield outside light and magnetic field. For this purpose each PMT is housed in an individual light-tight cylindrical enclosure made of 2.36 mm thick steel. Figure 3.5 shows all the optical components and the steel cylindrical enclosure.

Parameter	Description/value
Spectral response	300-650 nm
Peak wavelength	420 nm
Photocathode material	Bialkali
Photocathode minimum effective area	18×18 mm ²
Window material	Borosilicate glass
Dynode structure	Metal channel dynodes
Number of stages	12
Weight	30 g
Operating ambient temperature	-30-50 °C
Average anode current	0.1 mA

TABLE 3.2: Properties of the Hamamatsu H8804MOD-2 multi-anode photomultiplier tube. From Ref. [35].

Parameter	Min.	Typically	Max.	Unit
Luminous (2856 K) cathode sensitivity	60	70	-	μA/lm
Quantum efficiency at 420 nm	-	20	-	%
Anode dark current	-	2	20	nA
Anode pulse rise time	-	1.4	-	ns
Electron transit time	-	8.8	-	ns
Pulse linearity ±2%	-	30	-	mA

TABLE 3.3: Hamamatsu H8804MOD-2 multi-anode photomultiplier tube operating characteristics at 25 °C. From Ref. [35].

3.5 MINOS near detector

The MINOS near detector is positioned 2.1 m downstream of the MINERvA detector in the NuMI beamline. The MINOS near detector is used to measure momentum and charge of the muons that exit the MINERvA detector. Only forward-going ($\theta_\mu < 25^\circ$) energetic muons can be captured and analyzed with the MINOS detector.

The MINOS near detector is a tracking calorimeter composed of planes of magnetized iron and plastic scintillator with a total mass of 1 kTon. It uses a toroidal magnetic field with an average strength of 1.3 T to measure particle momentum and charge from the curvature of the particle track. The near detector consists of 282 steel plates, which are 2.54 cm thick. Only 152 of the plates are instrumented with 1 cm thick scintillator planes. The scintillator planes are made of 4.1 cm wide strips oriented $\pm 45^\circ$ with respect to the vertical and alternating $\pm 90^\circ$ in successive planes [35]. A schematic transverse view of the MINOS near detector is shown in Fig. 3.6

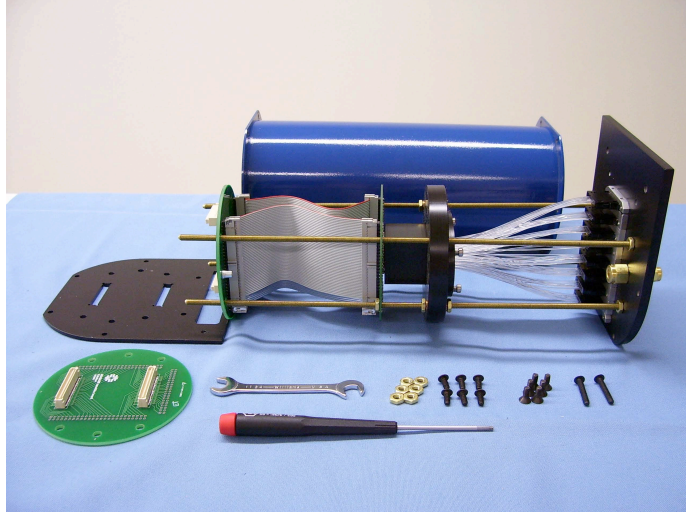


FIG. 3.5: Components of the optical boxes used in the MINERvA detector. The cylindrical enclosure (blue box) shields the optical elements from outside light and magnetic field. From Ref. [35].

[40].

The MINOS near detector has two regions (upstream and downstream regions), shown in Fig. 3.7 [40]. The upstream region is designed for fine sampling and it contains 120 planes. In this region each partially instrumented scintillator plane (or fully instrumented scintillator plane for every fifth plane) is followed by a steel plane. The surface area of partially instrumented and fully instrumented scintillator planes can be seen in Fig. 3.6. The downstream region has 162 planes and serves as the muon spectrometer. The downstream region has no partially instrumented planes and every fifth plane has full scintillator coverage [35].

3.6 Solid nuclear target modules

There are five layers of passive targets at the most upstream part of the MINERvA detector which enable the study of neutrino interactions on different nuclei. These passive targets are separated by four tracking modules to optimize the vertex and particle reconstruction for events originating inside the target modules. The five targets have different element compositions with different thicknesses. The thinner targets are included in order to study specific neutrino interactions with low mo-

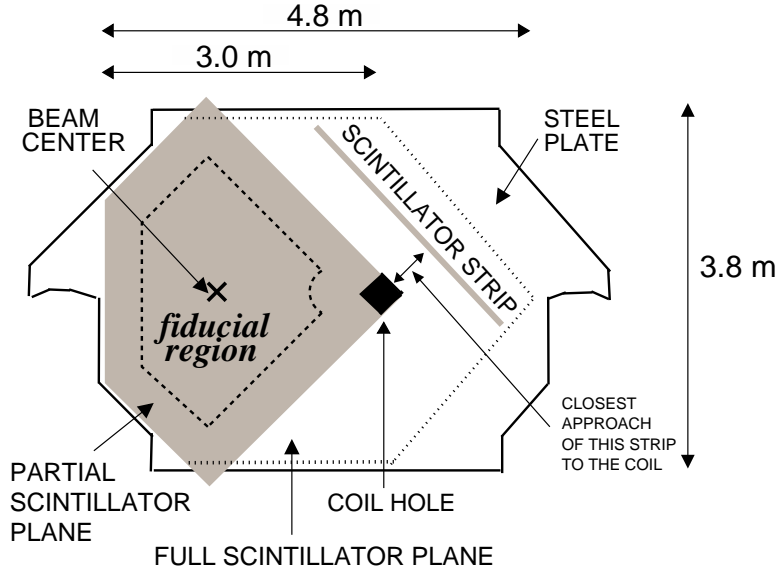


FIG. 3.6: Transverse view of the MINOS near detector. The outline of a partially instrumented scintillator plane is shown as shaded area and the outline of a fully instrumented scintillator plane is shown with the dotted line. The fiducial region defined in this figure is the fiducial region for the MINOS experiment itself. The drawing is not to scale. From Ref. [35].

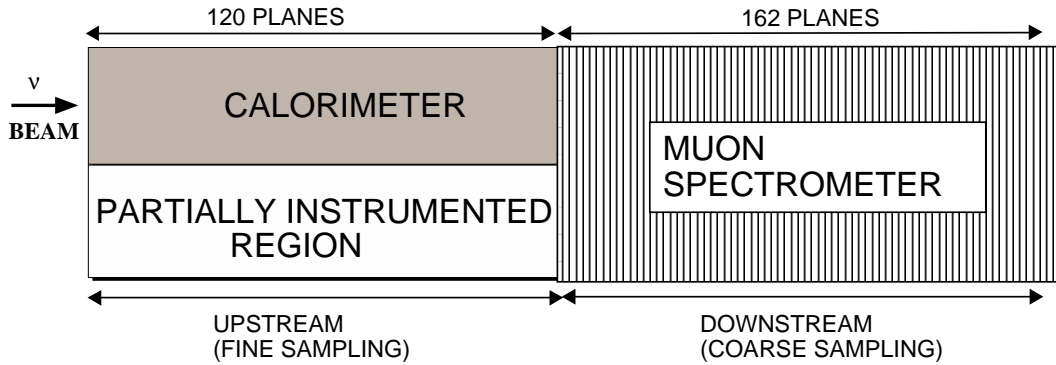


FIG. 3.7: Upstream and downstream regions of the MINOS near detector as seen from top. The drawing is not to scale. From Ref. [35].

momentum final-state particles which are normally absorbed inside the thicker targets.

Four of the targets contain different materials with different orientations designed to minimize the effect of acceptance differences for different regions of the detector. Target 4 is the only passive target containing pure lead and it functions as an upstream electromagnetic calorimeter. Targets 1, 2, and 5 are mixed steel and lead, in which the steel plate section is larger than the lead plate section, with the dividing line 20.5 cm from the plane center. Target 3 is composed of graphite, iron and steel.

The graphite covers half the area of the hexagon, the steel one-third, and the lead one-sixth [35].

The location, thickness and mass of the material composition of the targets is given in Table 3.4. The orientation of the planes, as viewed looking downstream, is shown in Fig. 3.8. The orientation of the planes along the axis of the beam line is shown in Fig. 3.9. The Water target listed in Table 3.4, is described in Sec. 3.7.

Target	Material	z-Location (cm)	Thickness (cm)	Mass (kg)
1	$^{56}_{26}\text{Fe}$	452.5	2.567 ± 0.006	492
1	$^{208}_{82}\text{Pb}$	452.5	2.578 ± 0.012	437
2	$^{56}_{26}\text{Fe}$	470.2	2.563 ± 0.006	492
2	$^{208}_{82}\text{Pb}$	470.2	2.581 ± 0.016	437
3	$^{56}_{26}\text{Fe}$	492.3	2.573 ± 0.004	238
3	$^{208}_{82}\text{Pb}$	492.3	2.563 ± 0.004	170
3	$^{12}_6\text{C}$	492.3	7.620 ± 0.005	258
Water	Water	528.4	17-24	627
4	$^{208}_{82}\text{Pb}$	564.5	0.795 ± 0.005	340
5	$^{56}_{26}\text{Fe}$	577.8	1.289 ± 0.006	227
5	$^{208}_{82}\text{Pb}$	577.8	1.317 ± 0.007	204

TABLE 3.4: Passive target location, thickness and mass. The mass is for the entire plate of target material. The location of the planes is given in the MINERvA coordinate system. From Ref. [35] .

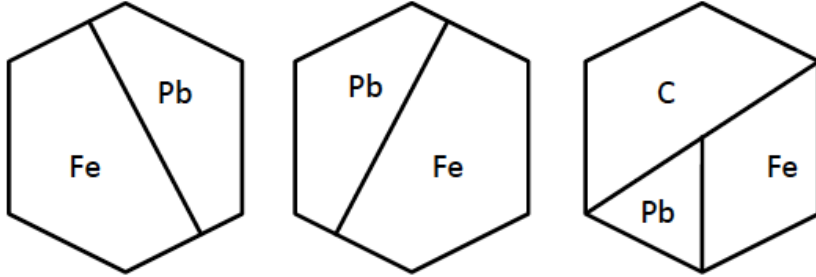


FIG. 3.8: Orientation of the nuclear targets looking downstream. Targets 1 and 5 have the leftmost orientation, target 2 has the middle orientation, and target 3 the rightmost orientation. From Ref. [35].

3.7 Water target

The MINERvA detector includes a water target between solid targets 3 and 4 as shown in Fig. 3.9. This target enables MINERvA to obtain cross-section measurements that are of interest to water Cherenkov detectors such as Super-Kamiokande (used by T2K).

The water target consists of a circular steel frame with a diameter slightly larger than the MINERvA inner detector size as shown in Fig. 3.10 [35]. The location, thickness and mass of the water target is given in Table 3.4. When the target is filled, the lower part expands more than the upper part, and it is not possible to access the entire target in order to make precise measurements [35]. The shape of the water target is estimated via a finite element analysis and the estimated thickness varies from about 17 cm at the edge of the fiducial region¹ to 24 cm at the thickest part. The water target chemical composition by mass is 88.5% O and 11.1% H with negligible amounts of C and N [35].

¹The fiducial area for the targets is defined by a hexagon with an 85 cm apothem.

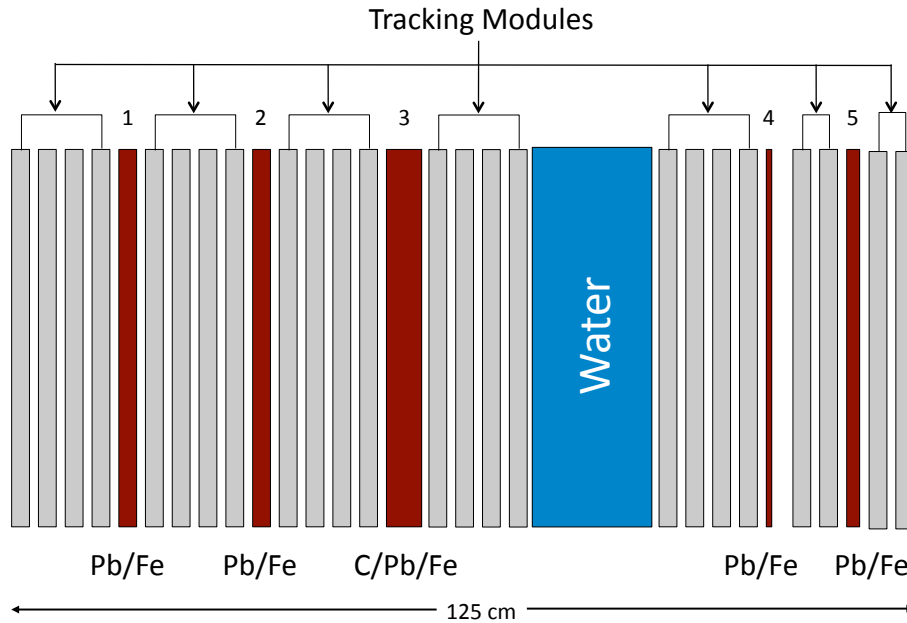


FIG. 3.9: Orientation of the nuclear target region along the beam line axis. The thinner targets are located downstream and the thicker targets are located upstream. Each target is preceded by four tracking modules for accurate vertex reconstruction except for the final thin Pb/Fe target, which is preceded by only two modules. From Ref. [35].

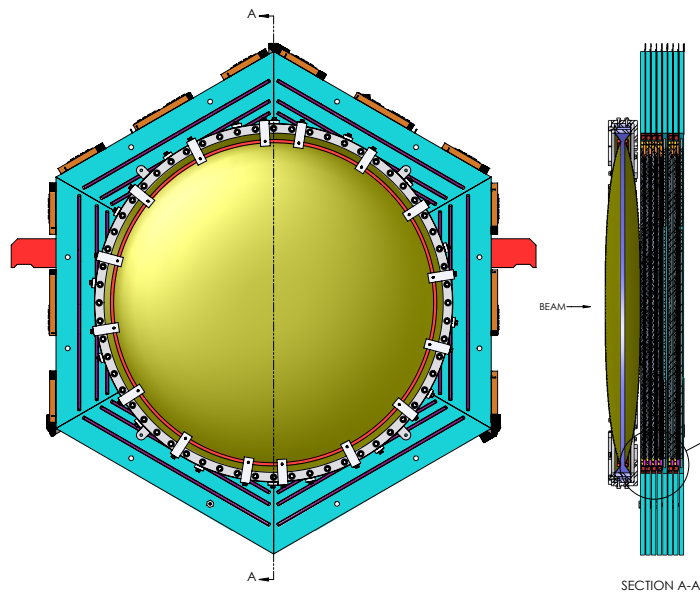


FIG. 3.10: Schematic drawing of the MINERvA water target, showing front view and side view of the center section. From Ref. [35].

Chapter 4

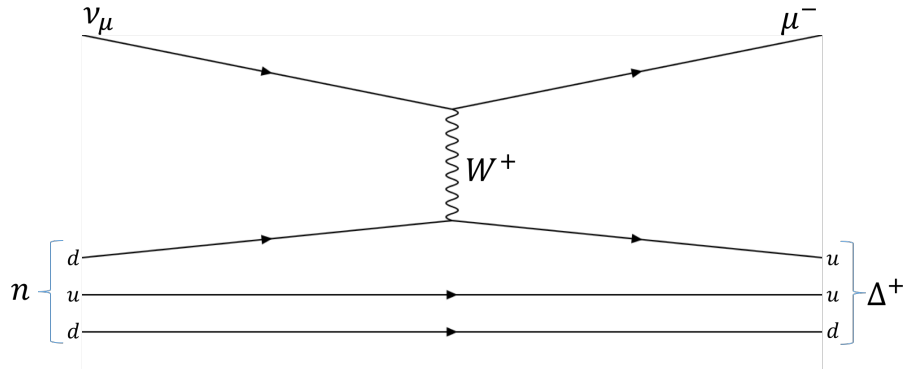
Signal Definition and Event Selection

4.1 Analysis overview

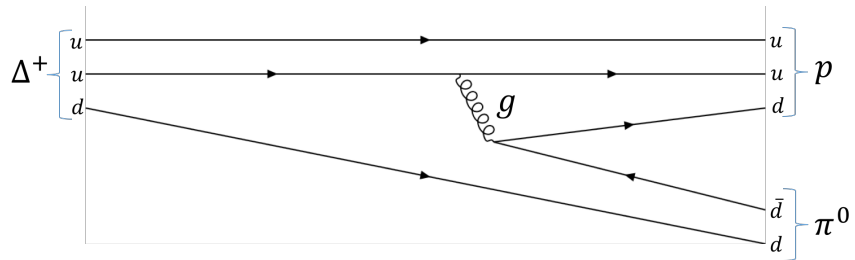
This Thesis presents a measurement of muon-neutrino charged-current(CC) single π^0 production on a hydrocarbon target. The analysis focuses on an exclusive neutrino interaction channel whose final-state particles are a muon and a neutral pion together with any number of protons and neutrons. The reaction equation is

$$\nu_\mu + \text{CH} \rightarrow \mu^- + \pi^0 + X \text{ (nucleons)} \quad (4.1)$$

where most of the reactions involve target neutrons ($\nu_\mu + n$) bound within carbon nuclei. Feynman diagrams for neutrino-induced single pion production resulting from production and decay of the Δ^+ (1232) resonance are as follows:



(a) Feynman diagram for neutrino-induced Δ^+ (1232) resonance: $\nu_\mu + n \rightarrow \mu^- + \Delta^+$



(b) Feynman diagram for Δ^+ decay: $\Delta^+ \rightarrow p + \pi^0$

FIG. 4.1: Feynman diagram of the neutrino interaction: $\nu_\mu + n \rightarrow \mu^- + p + \pi^0$. The diagrams shown here depict neutrino-induced single pion production proceeding via production of the Δ^+ (1232) resonance. In Fig. (a), charged current neutrino interaction excites the target neutron to Δ^+ ; in Fig. (b) the Δ^+ decays to a proton and a neutral pion. The Δ^+ lifetime is of the order of $\sim 10^{-23}$ seconds and cannot be detected as a track [41].

The signal definition and procedures of the analysis are given in Sec. 4.4. A

set of event selections is optimized in order to be able identify the $\nu_\mu + \text{CH} \rightarrow \mu^- + \pi^0 + (p)$ reaction with relatively high purity and efficiency; details of these selections are given in Sec. 4.6. The analysis uses a variety of methods to reconstruct each final-state particle inside the MINERvA detector. Reconstruction methods for the relevant particle types are given in Secs. 5.1 and 5.2. Upon completion of particle reconstruction, the neutrino energy is estimated based on the final-state particle energies and the extra energy that is not used by particle reconstruction. The details of neutrino energy estimation and Q^2 and W^2 calculations are given in Sec. 5.3. Background classifications for the final selected sample and sideband studies are presented in Secs. 6.1 and 6.2.

The analysis requires that the final-state muon and the neutral pion be reconstructed. However, the absence of low-energy proton reconstruction is acceptable. In other words, the muon and neutral pion are the final-state particles that are required in the final sample. For this reason this analysis has two different set of events: Single-track plus two gamma events in which the muon is the only track reconstructed, and two-track plus two gamma events in which at least one proton track is successfully reconstructed in addition to the muon track.

4.2 Simulation software

The analysis requires validated simulation software to provide guidance to the data measurement. The simulation software should be able to provide estimations of backgrounds and detector acceptance effects. MINERvA uses the GENIE neutrino event generator [42] to simulate the neutrino interactions. The GENIE event record for a simulated neutrino interaction contains all of the generated truth information for final-state particles and the interaction kinematics. The final-state particles generated by GENIE are propagated (in simulation) in the MINERvA detector by the code GEANT4 [43]. The GENIE version 2.8.4 [44] and GEANT4 version geant4-09-4-patch-02[45] are used in this analysis.

GENIE simulates a neutrino interaction based upon world measurements, parti-

cle phenomenology, and the NuMI flux, then outputs an event record which contains detailed information about the interaction. The GENIE event record provides information about the neutrino interaction type such as charged current (CC) or neutral current (NC), about the interaction channel such as quasielastic (QE), baryon resonance (RES), or deep inelastic scattering (DIS), and about the interaction kinematics such as the four-momentum transfer, Q^2 and the hadronic invariant mass W . In addition to interaction details, the event record contains the identities and kinematics of all the particles involved in the interaction. Importantly, the GENIE event record provides a record of intranuclear scatterings of created particles in the neutrino interaction. The intranuclear scatterings are referred to as “final state interactions (FSI)”.

The two most important physics processes in this analysis are pion production through baryon resonance and pion production through deep inelastic scattering (DIS). For baryon resonance production, GENIE uses the Rein and Sehgal model without interference between neighboring resonances [10], and for deep inelastic scattering GENIE uses a model by Bodek and Yang [15]. The nuclear medium in GENIE is simulated by the relativistic Fermi gas model that is modified in order to include short range nucleon–nucleon correlations [46].

Realistic simulation software must include detailed final state interaction (FSI) models for accurately estimating the neutrino interaction cross sections. The neutrino interaction occurring inside a nucleus creates the final-state particles inside the nuclear medium. The particles originally created in the neutrino interaction may undergo intranuclear scatterings losing some or all of their energies. More importantly for this analysis, pions created inside the nucleus may undergo a charge exchange or may be absorbed inside the nucleus. All of these final state interactions inside the nucleus depend on hadron interaction cross sections and must be predicted accurately by the simulation software. Especially the π^0 FSI modeling heavily depends on simulations due to the absence of π^0 -nucleus scattering experiments. The π^0 FSI models rely on isospin symmetry and pion charge exchange data. For the simulation of final state interactions GENIE uses an effective cascade model [47]. Table 4.1

summarizes the physical models used in GENIE that are important for this analysis.

Process	Model in GENIE
Baryon Resonance	Rein and Sehgal [10]
Deep Inelastic Scattering	Bodek-Yang [15]
Nuclear Media	Modified Relativistic Fermi Gas [46]
Final State Interactions	Effective Cascade [47]

TABLE 4.1: Particle interaction models used in GENIE v2.8.2.

The GENIE output for final-state particles kinematics after FSI is the input to GEANT4. GEANT4 propagates particles through the MINERvA detector in discrete steps. In each step, it calculates the energy deposited in the detector due to ionization and radiation based on the particle type. After each step, GEANT4 uses interaction models to determine whether any of the particles interacted in the detector. If an interaction occurs, GEANT4 produces the outgoing particles according to the interaction model.

If a simulated particle exits the MINERvA detector and points toward the MINOS detector, then GEANT3 [48] is used as the simulation of particle propagation in the MINOS near detector, as developed by the MINOS collaboration. Similar to GEANT4, GEANT3 simulates particle energy loss, interactions, and decays in the MINOS detector.

Details of the simulated neutrino interactions can be studied by using the GENIE event record. By evaluating the event record, each event can be identified as signal or a specific background. Background events generated in the simulation provide an estimate for the number of background events in the real data. On the other hand, the GEANT4 simulation can be used to optimize the reconstruction algorithms to identify particle trajectories. In addition, since the true energy of each particle in the simulation is known, the MINERvA detector can be calibrated based on the GEANT4 results and the energies of particles can be estimated in data. Combining all particle energies and other energies in the detector, the neutrino energy can be estimated and compared to the true neutrino energy.

As indicated above, robust simulation software is highly useful for understanding

the real data. Likewise, precise data measurements can help to improve the existing simulation software. In experimental high energy physics, simulation software is continually being updated based upon new information provided by data analyses.

4.3 Refinements to the simulation software

The simulation predictions from GENIE are improved by introducing new event weights based on other published studies. In the nominal GENIE, the angular spectrum of the Δ decay is isotropic. In this analysis GENIE predictions are reweighted such that the Δ decay angular anisotropy is 50% of the Rein and Sehgal prediction. This reweight is based on the MINERvA charged pion results and only affects the Δ^{++} resonance channel [49].

Another event reweight is applied to the GENIE prediction for single pion non-resonant production. A study by P. Rodrigues *et al.* [50] reanalyzed deuterium bubble chamber data from Argonne National Laboratory's (ANL) 12 ft bubble chamber [18] and Brookhaven National Laboratory's (BNL) 7 ft bubble chamber [19]. In the latter paper, Q^2 and E_ν distributions from ANL and BNL data are renormalized using CCQE event rates with a method described in Ref. [51]. Datasets for three different single pion production channels are renormalized for the fits: $\nu_\mu p \rightarrow \mu^- p \pi^+$, $\nu_\mu n \rightarrow \mu^- p \pi^0$, and $\nu_\mu n \rightarrow \mu^- n \pi^+$. A fit to all three channels is applied to find the best GENIE renormalization for resonant and non-resonant single pion production. This study indicates that the resonant normalization is consistent with the GENIE nominal while the non-resonant normalization should be reduced. The fit results for each channel are given in Table 4.2. As seen from the Table, the fit results significantly reduce the χ^2 in the $\nu_\mu n \rightarrow \mu^- n \pi^+$ channel; however, no major improvement in χ^2 is observed for the other two channels. Thus, in this analysis an event weight equal to 0.43 is applied to GENIE predictions for non-resonant $\nu_\mu n \rightarrow \mu^- n \pi^+$ events.

The GENIE version used in this analysis does not include a physical model for neutrino interactions with two nucleons producing two holes (2p2h) in the nuclear medium. Consequently, a new set of simulation events based on a model by Nieves

Channel	Dataset	Nominal χ^2	Best Fit χ^2	<i>d.o.f.</i>
$\nu_\mu n \rightarrow \mu^- n \pi^+$	ANL Q^2	44.0	32.2	18
	ANL E_ν	45.3	33.0	7
	BNL Q^2	84.6	31.3	19
	BNL E_ν	265.6	59.6	11
$\nu_\mu p \rightarrow \mu^- p \pi^+$	ANL Q^2	6.6	9.5	18
	ANL E_ν	16.3	10.6	7
	BNL Q^2	15.3	23.0	19
	BNL E_ν	15.3	5.6	7
$\nu n \rightarrow \mu^- p \pi^0$	ANL Q^2	24.5	21.3	18
	ANL E_ν	19.8	16.1	7
	BNL Q^2	46.7	46.4	19
	BNL E_ν	31.1	35.6	10

TABLE 4.2: Bubble chamber data versus GENIE comparisons for non-resonant single pion channels. From Ref. [50].

et al. [52, 53] for 2p2h reactions that produce QE-like final states are included in the analysis. This data set is adjusted to match with MINERvA data and also includes the RPA (random phase approximation) model for short range nucleon-nucleon correlations [54]. Since the included 2p2h simulation applies only to QE-like events, the effect on the cross-section measurements is small.

4.4 Signal definition

The analysis seeks to isolate the specific neutrino interaction given in Eq. (4.1). The signal definition necessarily includes global experimental effects to ensure that the defined signal can be measured. For instance, the event vertex must occur inside the MINERvA detector. Importantly, only particles that are exiting the nucleus can be used in the signal definition. For example, suppose that a single π^0 is created in the neutrino interaction, but then by intranuclear scattering, the π^0 becomes absorbed in the nucleus and creates no visible signature in the detector. In such a case detecting that π^0 is impossible, and so it is impossible to treat such events as signal. On the other hand, a π^+ created in the neutrino interaction can charge exchange to a π^0 via intranuclear scattering and the π^0 can exit the nucleus. In this case, the π^0 will be detected in the detector and the event will appear as a signal. For these reasons, the

signal definition uses the final-state particle content as it emerges out of the nucleus. Figure 4.2 gives examples of FSI inside nuclei and indicates the effect upon the signal definition.

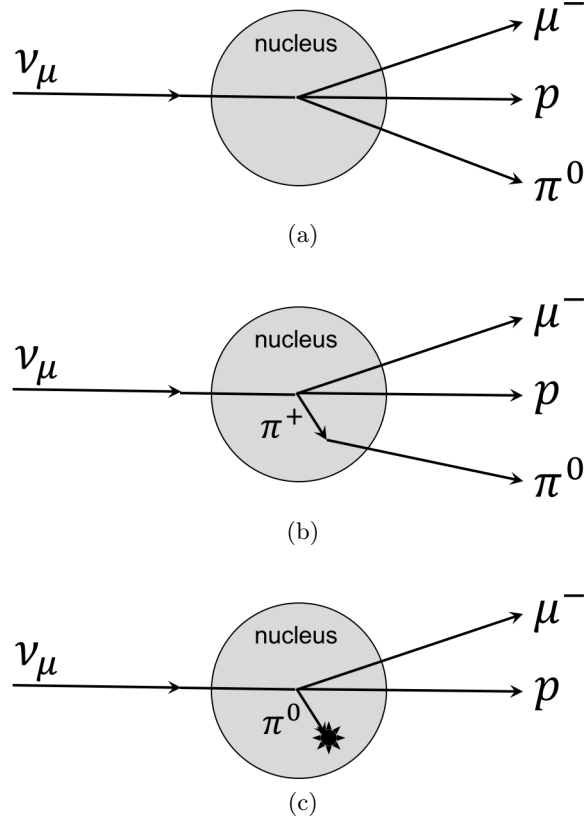


FIG. 4.2: Signal definition based on out-of-nucleus particle content. In diagram (a), a π^0 created in the neutrino interaction exits the nucleus. In diagram (b), a π^+ is created in the neutrino interaction, however it charge-exchanges inside the nucleus and a π^0 is detected in the detector. In diagram (c), a π^0 is created in the neutrino interaction and is then absorbed in the nucleus. According to the out-of-nucleus particle content, (a) and (b) are denoted as signal and (c) as a background event.

Based on the above considerations, the analysis signal definition requires the following statements to be true:

- The interaction must be a muon-neutrino charged current (CC ν_μ) reaction.
- The interaction vertex is located inside the MINERvA fiducial volume whose definition is given in Sec. 4.6.
- The muon angle with respect to the incoming neutrino is less than 25 degrees.

- The out-of-nucleus particle content cannot include any particle other than a single π^0 , protons, neutrons and a muon.
- The neutrino energy is limited to between 1.5 GeV and 20 GeV.
- The hadronic invariant mass W must be less than 1.8 GeV.

A GENIE simulation containing 4.8×10^7 neutrino interactions (events) is used (P.O.T.= 2.22×10^{21}). From this sample the events that have a vertex inside the MINERvA fiducial volume comprise 26.1% of the generated sample. Events that occur outside of the MINERvA fiducial volume are not considered further. The percentages given hereafter are based on the number of events with an interaction vertex inside the MINERvA detector.

Using the signal definition, 2.9% of the Monte Carlo (MC) events are denoted as signal. Starting with a sample with 2.9% purity (number of signal events over total number of events), strong event selections are required to achieve a purity greater than 45% in the final sample. Similarly, event selections must be optimized to keep as much signal as possible. The signal purity and reconstruction efficiency are discussed in Sec. 4.7.

Although the out-of-nucleus particle content is used to tag an event as signal, it is useful to study the event record for the history of the signal events. From the event record it is possible to determine the true interaction type and the true particle identities that are created in the neutrino interaction (before FSI). Table 4.3 shows the signal event composition based on the GENIE event record.

As mentioned previously, FSI inside the nucleus may convert a non-signal event to a signal. For instance, the 1.5% of quasielastic events marked as signal are the result of FSI creating a π^0 inside the nucleus.

4.5 Kinematic behavior of signal events

The four-momentum-transfer squared, Q^2 , and the hadronic invariant mass, W , for each event are calculated using the neutrino and muon kinematics. The true Q^2

Interaction Type	Definition	Percent
Quasielastic	Only nucleons created in neutrino interaction	1.5
$\Delta(1232)$ Resonance	Resonance Excitation in neutrino interaction	48.3
N(1535) Resonance		8.5
N(1520) Resonance		8.7
Other Resonances		11.1
Non-Resonance Background	Non-resonance pion production	20.7
DIS	Deep inelastic scattering	0.5
2p2h	Valencia 2p2h model	0.7

TABLE 4.3: Signal composition based on the GENIE event record. Note that baryon resonance production (rows 2 through 5) accounts for 76.6% of the signal events.

and W provided by the GENIE event record are difficult to reconstruct using the observable quantities. For this reason, true Q^2 and true W are calculated using the true quantities of lepton kinematics and neutrino energy, instead of using the values directly from the GENIE event record. The calculated true Q^2 and W are referred as “true experimental” Q^2 and W resulting from the calculations based on the observables. The true experimental Q^2 and W are also called post-FSI Q^2 and W , representing physical parameters that are closer to the measurements in this analysis.

The squared four-momentum transfer from the leptonic sector to the hadronic sector, Q^2 , is derived as follows:

$$\begin{aligned}
\mathbf{q} &= \mathbf{P}_\nu - \mathbf{P}_\mu \\
\mathbf{q}^2 &= (\mathbf{P}_\nu - \mathbf{P}_\mu)^2 \\
\mathbf{q}^2 &= \mathbf{P}_\nu^2 + \mathbf{P}_\mu^2 - 2\mathbf{P}_\nu\mathbf{P}_\mu
\end{aligned}$$

where \mathbf{q} , \mathbf{P}_ν , \mathbf{P}_μ are four-momenta and $\mathbf{P}_\nu\mathbf{P}_\mu$ is the four-momentum contraction. Calculating \mathbf{P}_ν^2 and \mathbf{P}_μ^2 gives

$$\mathbf{q}^2 = m_\nu^2 + m_\mu^2 - 2\mathbf{P}_\nu\mathbf{P}_\mu. \tag{4.2}$$

The neutrino mass in Eq. (4.2) can be neglected. The 4-vector dot product ($\mathbf{P}_\nu\mathbf{P}_\mu$) calculated with the assumption $m_\nu \approx 0$, gives

$$\begin{aligned}
\mathbf{P}_\nu \mathbf{P}_\mu &= E_\nu E_\mu - \vec{p}_\nu \cdot \vec{p}_\mu \\
&= E_\nu E_\mu - p_\nu p_\mu \cos \theta_{\nu\mu} \\
&= E_\nu E_\mu - E_\nu p_\mu \cos \theta_{\nu\mu} \\
&= E_\nu (E_\mu - p_\mu \cos \theta_{\nu\mu})
\end{aligned}$$

Rewriting Eq. (4.2) gives,

$$\mathbf{q}^2 = m_\mu^2 - 2E_\nu (E_\mu - p_\mu \cos \theta_{\nu\mu}) \quad (4.3)$$

It is standard practice to define $Q^2 = -q^2$. Then Eq. (4.3) can be written

$$Q^2 = 2E_\nu (E_\mu - p_\mu \cos \theta_{\mu\nu}) - m_\mu^2 \quad (4.4)$$

where $\theta_{\mu\nu}$ is the angle between muon and neutrino, and m_μ is the muon rest mass.

The invariant hadronic mass, W can be calculated using the relativistic energy formula $E^2 = |\vec{p}|^2 + m_0^2$:

$$W^2 = E_{had}^2 - |\vec{p}_{had}|^2 \quad (4.5)$$

where E_{had} and \vec{p}_{had} are the total energy and momentum of the hadronic sector. Assuming that the target nucleon is at rest, the total energy of the hadronic sector E_{had} can be calculated using conservation of energy:

$$E_{had} = E_\nu + m_N - E_\mu. \quad (4.6)$$

Similarly, using conservation of momentum and the assumption that the incident nucleon is at rest ($\vec{p}_N = (0, 0, 0)$), \vec{p}_{had} can be calculated as

$$\vec{p}_{had} = \vec{p}_\nu - \vec{p}_\mu. \quad (4.7)$$

After inserting Eqs. (4.6) and (4.7) into Eq. (4.5), W^2 becomes

$$\begin{aligned}
W^2 &= ((E_\nu - E_\mu) + m_N)^2 - (\vec{p}_\nu - \vec{p}_\mu)^2 \\
&= m_N^2 + 2(E_\nu - E_\mu)m_N + (E_\nu - E_\mu)^2 - (\vec{p}_\nu - \vec{p}_\mu)^2.
\end{aligned}$$

Representing $(E_\nu - E_\mu)^2 - (\vec{p}_\nu - \vec{p}_\mu)^2$ as $(\mathbf{P}_\nu - \mathbf{P}_\mu)^2$ and using the definition for $\mathbf{q}^2 = (\mathbf{P}_\nu - \mathbf{P}_\mu)^2$, W^2 can be written as

$$W^2 = m_N^2 + 2(E_\nu - E_\mu)m_N + \mathbf{q}^2. \quad (4.8)$$

Rewriting Eq. (4.8) using $Q^2 = -q^2$, the final form of W^2 can be represented as

$$W^2 = m_N^2 + 2m_N(E_\nu - E_\mu) - Q^2; \quad (4.9)$$

where m_N is the nucleon mass.

The true neutrino energy distribution for signal events is given in Fig. 4.3. The neutrino energy distribution based on GENIE simulation has the shape of the NuMI flux shown in Fig. 2.6; the distribution peaks at 3.5 GeV. The distributions for the true experimental Q^2 and W are given in the Figs. 4.4, and 4.5. In all of the distributions the signal composition is based on the GENIE event record and the percentage of each interaction type is given in Table 4.3.

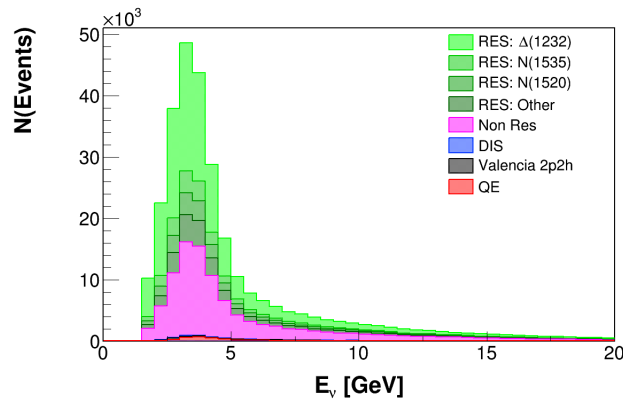


FIG. 4.3: True neutrino energy for selected events according to GENIE. The signal definition requirement on neutrino energy, $1.5 \text{ GeV} < E_\nu < 20 \text{ GeV}$, is visible on the plot.

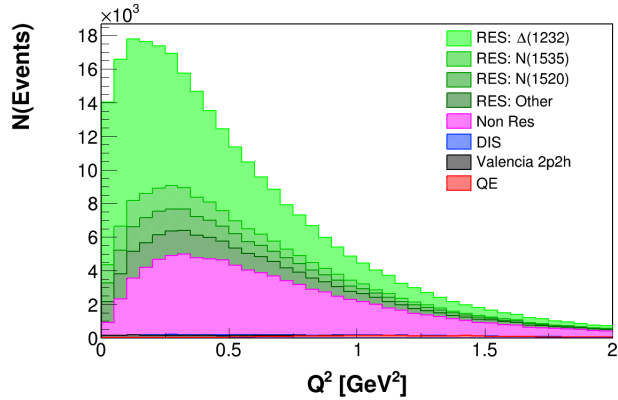


FIG. 4.4: Distribution of Q^2 calculated using the true neutrino and muon kinematics. Note that no event selection is made on Q^2 , however selection is made on W which is related to Q^2 , as indicated by Eq. (4.9) .

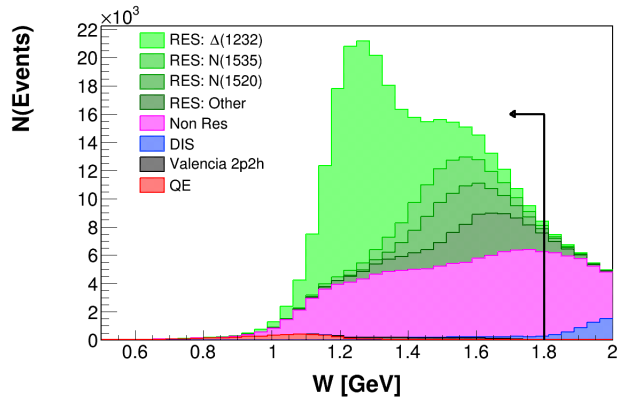


FIG. 4.5: Hadronic invariant mass W calculated using the true neutrino and muon kinematics. As indicated with the black arrow, events with W less than 1.8 GeV are considered to be signal. The $W > 1.8$ GeV region contains a small number of resonance events and is mostly dominated by non-resonant background.

4.6 Event selections

To identify the events of the signal channel Eq. (4.1), a set of event selections is applied to the complete data set. The event selections can be grouped as follows: Time slicing, vertex requirements, muon identification, proton identification, π^0 identification, Michel electron search and kinematics selections.

4.6.1 Time slicing

Hits within a gate are bunched into smaller time windows called time slices. A time slicing algorithm analyzes all hits in the gate and groups hits according to their time. Then each time slice is analyzed differently and low energy time slices are rejected. The time slicing algorithm groups the hits that triggered the PMT and sorts them by calibrated time. The time is calibrated to the center of the scintillator strip. The algorithm groups the hits into a single time slice based on the number of photoelectrons triggered by that hit. Each time slice begins with a hit of at least 10 photoelectrons and ends with a hit of less than 10 photoelectrons [55]. Figure 4.6 shows the time slicing in a single NuMI beam spill.

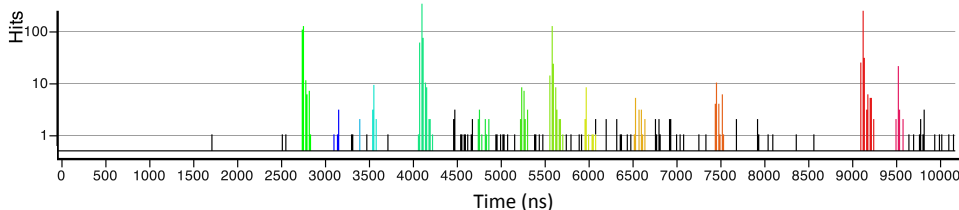


FIG. 4.6: Time profile of the hits within a NuMI beam spill. Each group of hits having a specific color are hits within the same time slice. A time slice is typically 150 nanoseconds in duration. From Ref. [35].

4.6.2 Vertex requirements

The event vertex is required to be inside the MINERvA detector. There are two vertex location requirements that are applied to each event sequentially. Initially, the vertex position is estimated based on the muon track start point inside the MINERvA detector, then the vertex position is refitted by adding the short tracks around the initial vertex position. In order to have a valid result for the second vertex position determination, the short tracker algorithm requires that the initial vertex location must be inside the “reconstruction volume”. Therefore, the first location-based constraint removes events having a vertex outside of the reconstruction volume. The short tracker algorithm is used to create short tracks and refit the vertex location before the fiducial volume check. The dimensions for the reconstruction volume are

given in Table 4.4. The second location constraint is applied to the refitted vertex position; it removes events with a vertex outside of the fiducial volume whose dimensions are also given in Table 4.4. The detector mass, number of carbon atoms and nucleons inside the fiducial volume are given in Table 4.5. Apothems of reconstruction and fiducial volume selections are shown on a MINERvA plane in Fig. 4.7. (An apothem is the distance between the center of the hexagon to the midpoint of a side.)

	Apothem [mm]	Upstream Z [mm]	Downstream Z [mm]
Reconstruction Volume	1000.0	5810.0	8600.0
Fiducial Volume	850.0	5991.37	8363.92

TABLE 4.4: Dimensions of reconstruction and fiducial volumes.

Detector Mass	Number of Carbon Atoms	Number of Nucleons
5.27×10^6 g	2.34×10^{29}	3.17×10^{30}

TABLE 4.5: Detector mass, number of carbon atoms and nucleons inside the fiducial volume.

4.6.3 Muon selections

The selected events are required to have a muon track that intersects the MINOS near detector, enabling a momentum and charge measurement. This requirement removes all muons with $\theta_\mu > 25$ degrees. After charge identification, events initiated by $\bar{\nu}_\mu$ (yielding μ^+ tracks) are removed.

4.6.4 Proton selections

Proton selections are applied when there is at least one short track in the event. In cases when there are multiple short tracks, all short tracks must pass the proton selections. The first requirement is that the track ionization dE/dx is compatible with a proton or charged pion hypothesis. If the dE/dx profile of the track does not agree with a proton or pion hypothesis, the event is removed. In some cases a four-momentum estimation for the short track cannot be obtained; in such a case

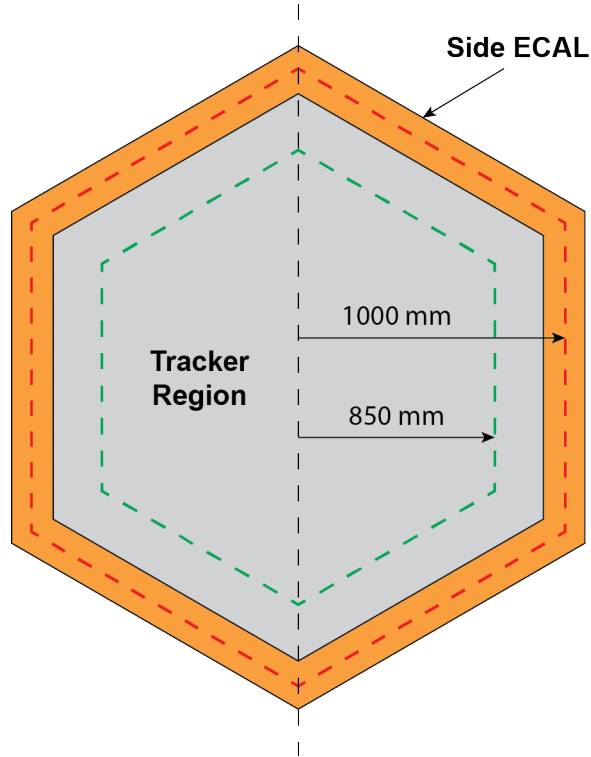


FIG. 4.7: Apothems (dark arrows) for reconstruction (outer dashed border) and fiducial (inner dashed border) volume selections drawn on a MINERvA plane.

the event is removed. Finally, all short tracks in the event must have a high proton score, indicating that the track is more likely to be a proton than a pion. For the proton score estimation, the dE/dx profile of the track is compared to the proton dE/dx profile based on MC simulations [56]. The score is calculated based on the Log Likelihood Ratio (LLR). If the Log Likelihood Ratio is high, the track is more likely to be a proton. Figure 4.8 shows the selection applied for the proton score. A very conservative event selection is used for the proton score in order to save as many signal events as possible for the final sample. Only the events with a proton score LLR lower than -10 are removed. Details of this method are given in Sec. 5.1.3.

4.6.5 Neutral pion selections

Pion selections are applied to all events both before and after the π^0 reconstruction. There is a pre-filter selection used before π^0 reconstruction. The pre-filter selection checks the available unused energy inside the detector after the muon and proton

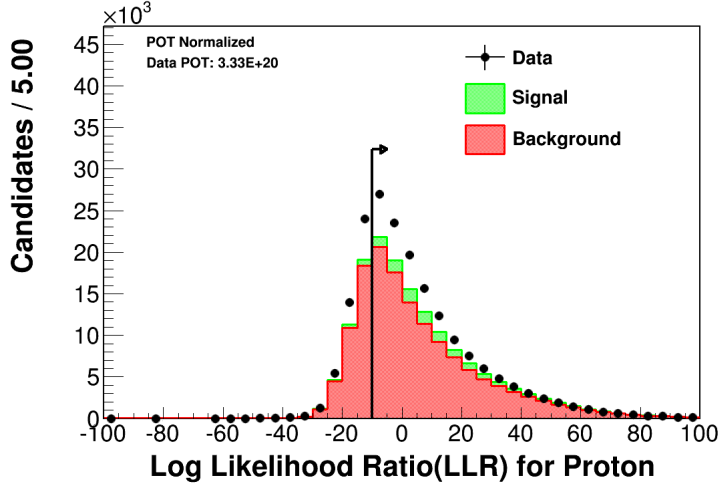


FIG. 4.8: Proton Score based on the log likelihood ratio (LLR) for dE/dx profile. Events having a proton score greater than -10 are selected for the final sample.

reconstructions, and removes events in three different conditions. Firstly, events are removed if the visible energy in the nuclear targets is greater than 20 MeV. This analysis uses neutrino interactions in the tracker region only; activity in the nuclear targets is likely due to a neutrino interaction on a nuclear target or due to a rock muon. Rock muons are created inside the earth, upstream of the detector by the NuMI beam. They must be removed in this analysis. Secondly, events are removed if the unused visible energy in the MINERvA detector (Tracker, ECAL and HCAL) is less than 50 MeV. It is not possible to obtain meaningful results from the π^0 reconstruction algorithm for the events having unused energy less than 50 MeV. (Available energy is much lower than the π^0 rest mass of 135 MeV). Finally, events are also removed if the unused visible energy in the MINERvA detector is more than 2500 MeV. Such events are not likely to have a single π^0 in the final state. This specific selection removes most of the multi-pion DIS background events.

If an event satisfies all of the pre-filter selections, further quality selections are applied after the π^0 reconstruction. It is required that the π^0 reconstruction algorithm finds exactly two electromagnetic (EM) showers reconstructed inside the MINERvA detector. This event selection uses the $\pi^0 \rightarrow 2\gamma$ decay channel whose decay fraction is 98.82%. There is a shower direction selection applied to all events with two EM

showers. It is required that for both EM showers it is possible to fit a straight line using the shower clusters and the interaction vertex. This line defines the direction of the initial photon. Similar to the situation for proton tracks, in some rare cases the four-momentum estimation for the EM showers can fail, and in such cases the event is removed. Events that survive to this point have two EM showers with momentum and direction estimates.

An event is removed if the conversion distance for the leading photon (the more energetic photon) is too close to the vertex. It is required that an event have a minimum 14 cm conversion distance from the event vertex. This selection ensures that non-tracked charged particle hits close to the vertex are not considered as EM showers. There is no constraint on the conversion distance of the secondary photon. Figure 4.9 shows the effect of selection on the leading photon conversion length.

The photon energies and opening angle are used to calculate the π^0 invariant mass. The 2D distribution of total photon energies ($E_1 + E_2$) and cosine of the opening angle ($\cos \theta_{\gamma\gamma}$) is examined and, it is observed that there is a region which is background-dominated (visible in Fig. 4.10). All events that have total photon energy less than 400 MeV and additionally have cosine of the opening angle greater than 0.95, are removed.

Finally the π^0 invariant mass, which is calculated from the photon energies and cosine of the opening angle as shown in Eq. (4.10), is required to be in the range $60 \text{ MeV} < m_{\gamma\gamma} < 200 \text{ MeV}$. Figure 4.11, shows the π^0 invariant mass event selection.

$$\begin{aligned}
 m_{\gamma\gamma}^2 &= (E_{\gamma_1} + E_{\gamma_2})^2 - (\vec{p}_{\gamma_1} + \vec{p}_{\gamma_2})^2 \\
 &= (E_{\gamma_1}^2 + E_{\gamma_2}^2 + 2E_{\gamma_1}E_{\gamma_2}) - (E_{\gamma_1}^2 + E_{\gamma_2}^2 + 2E_{\gamma_1}E_{\gamma_2} \cos \theta_{\gamma\gamma}) \\
 &= 2E_{\gamma_1}E_{\gamma_2} - 2E_{\gamma_1}E_{\gamma_2} \cos \theta_{\gamma\gamma} \\
 &= 2E_{\gamma_1}E_{\gamma_2} (1 - \cos \theta_{\gamma\gamma}),
 \end{aligned}$$

$$m_{\gamma\gamma} = \sqrt{2E_{\gamma_1}E_{\gamma_2} (1 - \cos \theta_{\gamma\gamma})}. \quad (4.10)$$

Here, E_γ is the energy of the photon, and $\theta_{\gamma\gamma}$ is the decay opening angle for the photon pair.

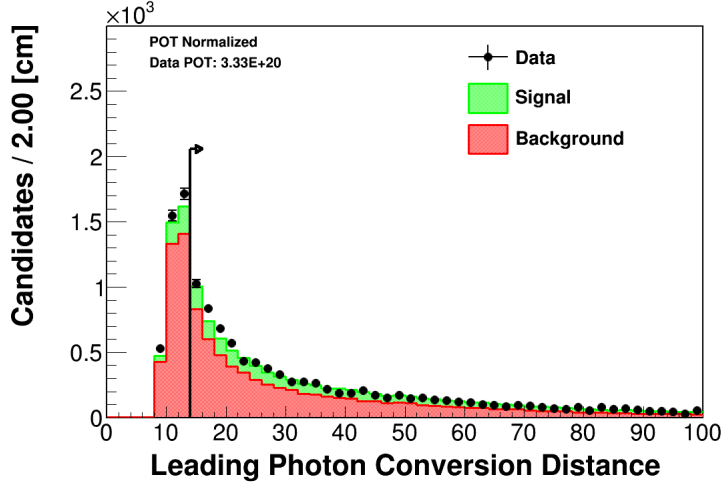


FIG. 4.9: Event selection for the leading-photon conversion length. The leading photon shower in an event is required to have a conversion distance higher than 14 cm from the event vertex.

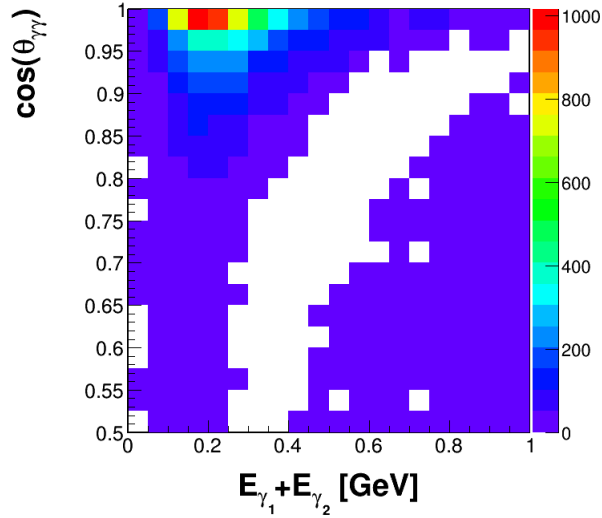


FIG. 4.10: Distribution of $[N(\text{Background}) - N(\text{Signal})]$ for $\cos\theta_{\gamma\gamma}$ versus $E_1 + E_2$. All the events with total photon energy less than 0.4 GeV and with cosine of the opening angle greater than 0.95 are removed. The removed events are clustered at the top left corner of the 2D distribution.

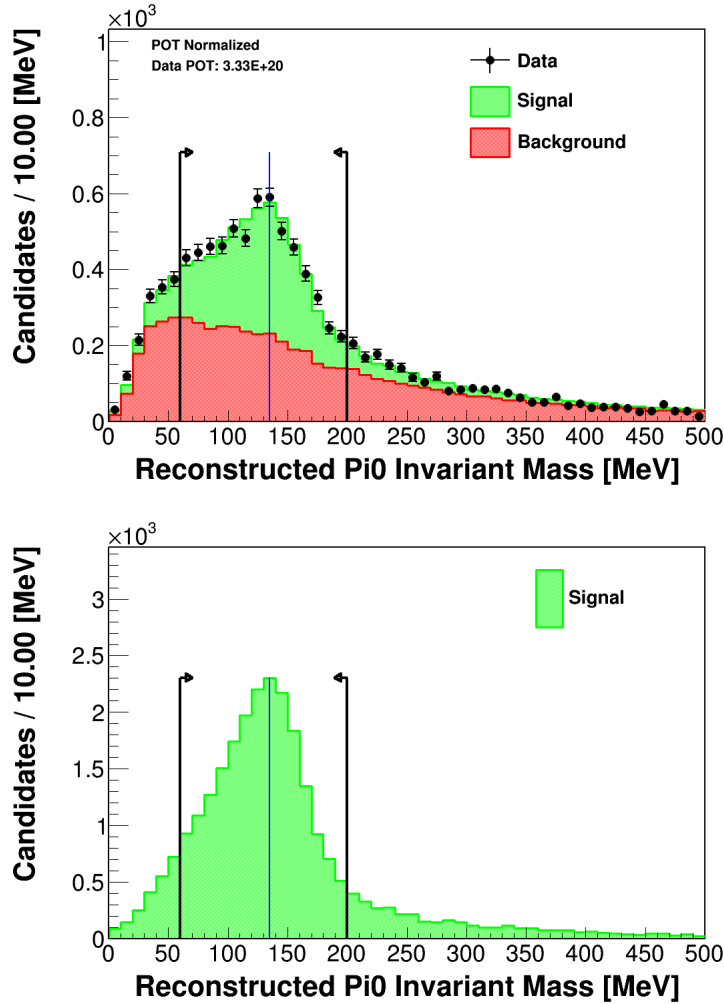


FIG. 4.11: Event selection for the π^0 invariant mass. The top plot shows the data versus MC comparison in which the MC events are categorized by event type. The bottom plot, shows only the MC signal events. On both plots the blue line shows the nominal π^0 mass.

4.6.6 Michel electron selections

It is necessary to remove all events that have a π^+ in the final state. A π^+ stopping inside the detector decays into μ^+ and ν_μ , then the μ^+ after a mean life of $2.2 \mu\text{s}$, decays into a positron and two neutrinos. The positron-initiated shower is referred to as a Michel electron. The detection method for Michel electrons is to look for an energy deposition in a later time slice. Michel electrons are searched for around primary vertices in order to locate any short pions that decayed in the vertex vicinity. A search volume whose dimensions are given in Table 4.6 is used around the vertex

point. The motivation for increasing the transverse search distance is to detect transversely going pions which do not get tracked. The Michel electrons are also searched for at the end of each track. If a track has multiple components due to scattering, then a Michel electron is searched for around each end point. Finally, the beginning and end points of both EM showers are searched for Michel electrons. This is an effective selection that identifies π^+ particles that are not tracked in the detector.

	Transverse [mm]	Longitudinal [mm]
Vertex	1000	125
Track End Point	175	125
Secondary Track End Point	175	125
Shower End Points	175	125

TABLE 4.6: Michel-electron search distances for various topological locations in an event.

4.6.7 Event kinematic selections

In the signal definition of this analysis the neutrino energy is limited to $1.5 \text{ GeV} < E_\nu < 20 \text{ GeV}$. This limit is also applied to the reconstructed neutrino energy. The motivation for the lower bound is to ensure good acceptance for MINOS matched muons, and the motivation for the higher bound is to remove events that are unlikely to be CC single-pion production. The analysis signal definition also includes a 1.8 GeV upper bound for the hadronic invariant mass W . The motivation for this limit is to isolate final states that are dominated by resonance events. Events having W above 1.8 GeV are mostly CC DIS events.

4.7 Analysis purity and efficiency

The purity of the sample is defined as the fraction of the number of signal events to the number of total events in that sample $\left(Purity = \frac{N(\text{Signal})}{N(\text{Total Events})}\right)$. Similarly, the efficiency of the sample is defined as the fraction of the number of signal events in the current sample to the number of all signal events $\left(Efficiency(All) = \frac{N(\text{Signal})}{N(\text{All Signal})}\right)$.

Table 4.7 lists the purity and efficiency of the sample after each event selection. Since this analysis uses events that have only MINOS matched muons, the efficiency is also calculated as $\left(Efficiency(MINOS) = \frac{N(\text{Signal})}{N(\text{Signal}) \text{ with MINOS match}} \right)$.

Selection	Purity	Efficiency	
		All	MINOS
Vertex in Fiducial Volume and MINOS Matched μ^-	6.1%	49.5%	100.0%
Muon Angle	6.1%	49.5%	99.9%
Michel: Vertex	7.0%	48.7%	98.3%
Michel: Track End Point	7.6%	48.0%	97.0%
Michel: Sec. Track End Point	7.6%	48.0%	96.9%
Short Track: No Particle	7.7%	48.0%	96.9%
Short Track: No Proton	7.8%	46.5%	94.0%
Short Track: Bad Proton Reco	7.8%	45.9%	92.7%
Short Track: Proton Score Low	9.2%	39.1%	78.9%
PreFilter Pi0	12.5%	35.6%	71.9%
No Two EM Showers	22.6%	22.5%	45.4%
Shower Direction Bad	23.4%	16.6%	33.5%
Pi0 Reconstruction Bad	23.2%	14.4%	29.0%
Michel: Shower	25.4%	13.9%	28.0%
Leading Photon Distance Low	29.7%	12.3%	24.9%
Secondary Photon Distance Low	29.7%	12.3%	24.9%
Showers Low E_{Total} and Small $\theta_{\gamma\gamma}$	31.3%	11.8%	23.9%
$1.5 \text{ GeV} < E_\nu < 20 \text{ GeV}$	33.7%	11.7%	23.7%
$W < 1.8 \text{ GeV}$	38.8%	10.9%	22.1%
π^0 Invariant Mass	50.7%	8.4%	17.0%

TABLE 4.7: Purity and efficiency of the sample after each event selection. The purity and efficiency of the sample are calculated only for the events that have a vertex inside the fiducial volume and a muon track reconstructed inside the MINOS near detector. The final purity of the final sample is 50.7%. The reconstruction efficiency of the signal events with respect to all signal events is 8.4% and the efficiency with respect to signal events that have a MINOS matched muon track is 17.0%.

Chapter 5

Event Reconstruction

5.1 Muon and proton reconstruction

Every charged particle creates “hits” (energy depositions in scintillator) inside the MINERvA detector while it traverses the scintillator strips. Track-based reconstruction algorithms are used to collect hits and to form 3D tracks where the start and end position of the tracks are known. The track-based reconstruction algorithms are specifically designed to reconstruct muon and hadron (proton and pion) tracks. The particle identification, however, is not a part of track reconstruction [57]. Once a track is reconstructed, other algorithms are used to determine the particle type and to attach particle information to the track.

The reconstruction of muon and proton tracks within the MINERvA scintillator tracker proceeds in the same way, however the MINOS near detector is used for muon momentum and charge measurement. In this Section, the track-based algorithms and particle identification inside the MINERvA detector are discussed.

5.1.1 Track reconstruction

The track reconstruction has three stages: First, hits within a gate are bunched into smaller time windows called time slices; this stage is called “Time Slicing” and was described in Sec. 4.6.1. Then, the hits per time slice are spatially grouped into objects called clusters; this stage is called “Clustering”. Finally, the clusters are fitted to straight lines to get the particle tracks; this stage is called “Tracking”. [58]

5.1.1.1 Clustering

A cluster is a collection of neighboring hits in a time slice that are in the same plane. Clusters are classified topologically according to the number and energies of the hits that they contain. Each cluster has a position and time. The position is the energy-weighted position of the hits contained in the cluster, and the time is the time of the highest energy hit [55]. The cluster classifications are the following: Clusters having a hit sum of very low energy are called “low-activity” clusters. If the average energy of each hit in the cluster is between 1 MeV and 8 MeV and no hit has an energy

greater than 12 MeV, then the clusters are called “trackable”. However, clusters that have a hit with a very high energy, are referred to as “heavily ionizing”. Finally, if a cluster has a broad hit distribution or double-peaked distributions in a time slice, then the clusters are called “superclusters” or “shower-like” clusters. [59]

5.1.1.2 Tracking

A track is a reconstructed object representing the charged particle’s trajectory through the MINERvA detector. The number of tracks associated with a single particle trajectory can be more than one. If a particle scatters inside the detector and changes its direction, the particle trajectory is represented by multiple linked tracks. Compared to the muons, the hadrons which propagate through the MINERvA detector are far more likely to require multiple tracks.

Tracking is done in a single time slice by multiple pattern recognition algorithms. A master event-building algorithm systematically applies the various track pattern recognitions to find muon and hadron tracks. It associates groups of tracks with common vertices, using a Kalman filter fit [60] to reconstruct the best position for the vertex.

The first step in formation of a track is to form track seeds out of trackable and heavily ionizing clusters. The track seeds are grouped by views (X, U, or V module) and consist of three consecutive clusters in the same view. A track seed must satisfy the following criteria: There can be only one cluster in a given scintillator plane; the clusters of a track seed must be in consecutive scintillator planes; and the clusters must satisfy a fit to a two-dimensional straight line in two views. If the algorithm merges two track seeds into a candidate track, it will attempt to merge additional seeds to the candidate using the same criteria. In order to avoid the potentially confusing influence of heavy vertex activity, the merging procedure starts from the downstream end of the detector and stops at the event vertex [55, 58].

The next step of the tracking algorithm is to combine track candidates from different views into 3D track objects. This is achieved by two sub-algorithms, namely two-view and three-view tracking algorithms. The track candidates that contain only

one seed with a polar angle greater than 60° are rejected by both of the algorithms. As described in Ref. [55] “Such track candidates typically correspond to random energy deposits that happen to fit a straight line.”. The three-view tracking algorithm requires 3 hits from each view corresponding to at least 11 planes. An example for the shortest plane configuration for three-view tracking can be the following: VXUXVXUXVXU. However, the looser two-view tracking is able to form tracks that traverse as few as 4 planes [58, 55, 59].

All tracks are fit by a Kalman filter fit routine [60] that includes multiple scattering [61]. Each cluster on the track receives a three-dimensional position and direction from the fit. Figure 5.1 shows the tracking position resolution after the fit. The fit is used to add additional clusters to the track by searching nearby planes in which the track does not contain a cluster. If an extra cluster is found, then the extra cluster is added to the track.

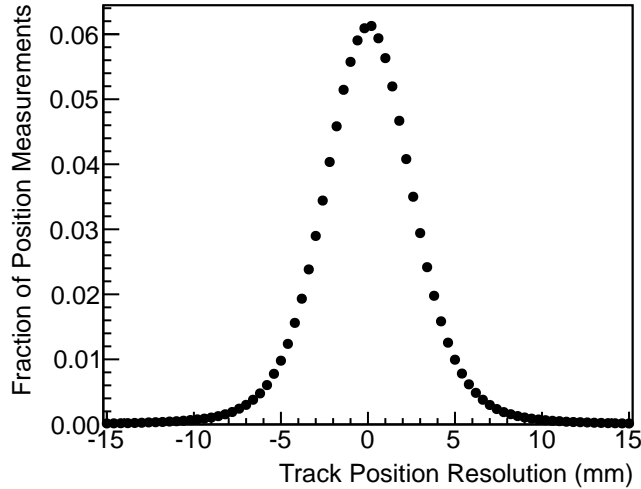


FIG. 5.1: Residual of fitted positions along a track relative to measured cluster positions for a rock muon sample. The resolution is 3 mm. From Ref. [35].

5.1.2 Muon identification and momentum measurement

It is extremely rare for a charged hadron to travel through the ECAL and HCAL without stopping or interacting. Consequently, a muon can be identified as a non-

interacting track that exits the detector. Since the MINERvA detector is not magnetized, it is not possible to measure the momentum or charge of the exiting muons. These quantities are measured by requiring the muon to be reconstructed in the MINOS near detector.

MINOS track matching

Before measuring the momentum and charge of the muon, a match must be found between a track exiting the MINERvA detector and a track entering the MINOS near detector. The matching is done in two ways. First, the MINOS track is projected to the last active MINERvA plane, and the MINERvA track is projected to the first active MINOS plane. The difference between the projection and the other track's activity in the plane must be less than 40 cm in both cases in order to make a match. If this fails to yield a match, then the point of closest approach along the projection is used. This latter criterion is helpful in cases where the muon scattered in the passive material between the two detectors [55]. Additionally, the tracks in the two detectors must occur within 200 ns of each other.

Charge and momentum measurement

The magnetic field in the MINOS near detector deflects muon tracks according to their charge via the Lorentz force ($\vec{F} = \pm e (\vec{v} \times \vec{B})$). In the MINOS near detector, the magnetic field lines follow concentric, nearly circular loops around the coil as shown in Fig. 5.2. In this magnetic field configuration a negatively charged particle traveling along the detector Z-axis experiences a Lorentz force directed toward the coil, and a positively charged particle is deflected away from the coil. The direction of the curvature determines the charge of the muon track.

The momentum of a muon is measured in two different ways: by range-to-stopping and by curvature. Low-energy and small-angle muons stop inside the MINOS detector and the momentum is measured by integrating the track range through the detector material and using range tables [63]. The uncertainty of this measurement is 2%, which includes uncertainties of the MC geometry simulation, of

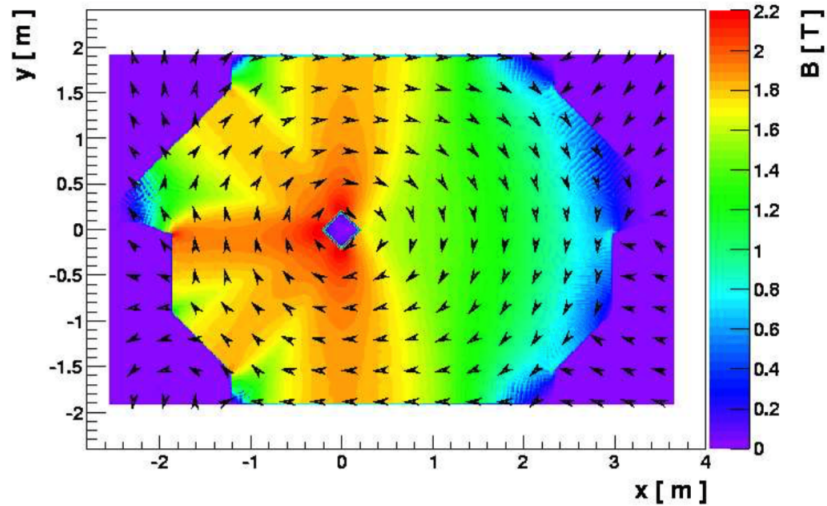


FIG. 5.2: Magnetic field map of the MINOS near detector looking from the downstream direction. The detector has toroidal magnetic field geometry with an average field strength of around 1.2 T. Black arrows indicate the direction of the magnetic field lines. From Ref. [62].

the detector mass, and errors in the track finding [62]. For exiting muons the curvature of the track is used to measure the muon momentum. A track fitter algorithm is used to measure the muon momentum by minimizing the differences between actual track hits and the estimated muon trajectory through the detector in the presence of the magnetic field [64]. For the final momentum estimation the ionization energy lost inside the MINERvA detector is included in the measurement.

Muon variables are the most accurately measured quantities in this analysis. Figure 5.3 shows the fractional residual errors ($\frac{reconstructed - true}{true}$) for muon momentum and angle with respect to the beam.

5.1.3 Proton identification and momentum measurement

Charged hadrons are identified as the non-muon tracks at the primary vertex. The fitted track has the direction of the hadron but it does not include the identification and momentum estimate. The energy loss (dE/dx) profile of the track is used to separate protons from charged pions. The rate that charged particles lose energy in matter is given by the Bethe-Bloch equation [41],

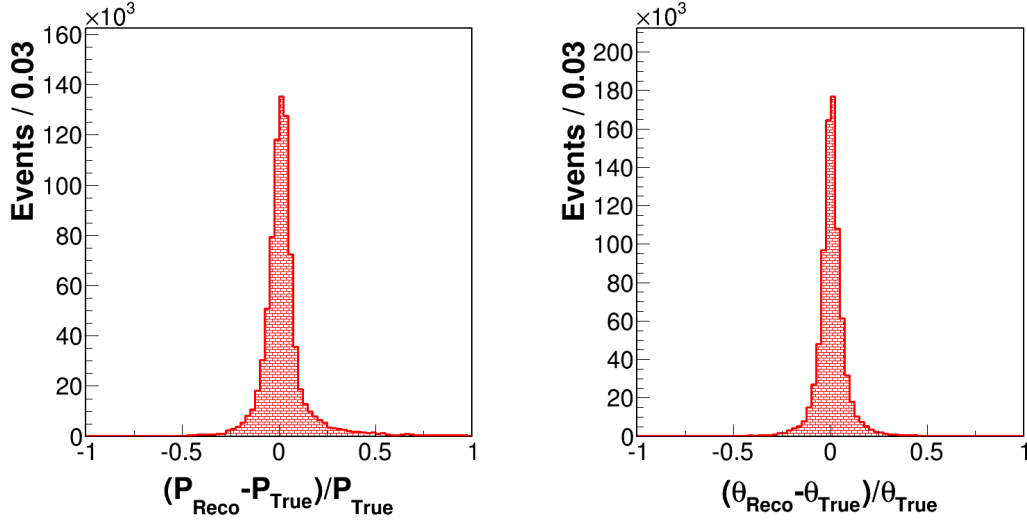


FIG. 5.3: Fractional residual errors for muon momentum (left) and production angle (right). Muon momentum and angle are the most accurately measured variables in this analysis. Both distributions have a mean at zero, symmetrical shapes and short tails on both sides. Full width at half maximum (FWHM) for the muon momentum fractional error is 0.10 and for the muon angle fractional error is 0.08.

$$-\left\langle \frac{dE}{dx} \right\rangle = K z^2 \frac{Z}{A} \frac{1}{\beta^2} \left[\frac{1}{2} \ln \frac{2m_e c^2 \beta^2 \gamma^2 W_{max}}{I^2} - \beta^2 - \frac{\delta(\beta\gamma)}{2} \right], \quad (5.1)$$

where W_{max} is the maximum energy transfer in a single collision, and the other variables are defined in Table 5.1.

The Bethe-Bloch equation describes the mean rate of energy loss in the region $0.1 \lesssim \beta\gamma \lesssim 1000$ for intermediate-Z materials with an accuracy of a few percent. The velocity of the particle at the lower limit is comparable to atomic electron velocities and radiative effects begin to be important at the upper limit. Figure 5.4 compares the energy loss profile of a simulated proton and simulated pion to the profiles predicted by the Bethe-Bloch equation.

The momentum measurement is done by finding the best fit for the dE/dx profile for each track under proton and pion hypotheses. The best fit for the dE/dx profile for the track is constrained to be consistent with the range of the track, and the fit returns two different momentum estimations based on the proton and pion hypotheses. In this analysis, the track is assumed to be a proton and the momentum estimation based on the proton hypothesis is used.

Symbol	Definition	Units or Value
β	v/c	
γ	$(1 - \beta^2)^{-1/2}$	
K	$4\pi N_A r_e^2 m_e c^2$	$0.307 \text{ g}^{-1}\text{cm}^2$
r_e	Classical electron radius	2.818 fm
N_A	Avogadro constant	$6.022 \times 10^{23} \text{ mol}^{-1}$
z	Charge of incident particle	
Z	Atomic number	
A	Atomic mass	g mol^{-1}
$m_e c^2$	Electron mass $\times c^2$	0.511 MeV
I	Mean excitation energy	eV
$\delta(\beta\gamma)$	Density effect correction to ionization energy loss	

TABLE 5.1: Summary of variables used in Bethe-Bloch equation. From Ref. [65].

For the separation between proton and pion the Neyman-Pearson Lemma [66], a method based on the likelihood ratio of the two hypotheses, is used. In the proton-pion likelihood case the ratio is

$$R = \frac{\prod_{clusters} P(E_{cluster}|p)}{\prod_{clusters} P(E_{cluster}|\pi)} \quad (5.2)$$

The log likelihood ratio used for the proton-pion separation corresponds to the following

$$\log R = \sum_{clusters} [\log P(E_{cluster}|p) - \log P(E_{cluster}|\pi)] \quad (5.3)$$

This details of the method are described in Ref. [56]. Since the Log Likelihood Ratio (LLR) depends on the cluster energies along the track, the method excels in fully tracked particle trajectories. Calculations of the log likelihood ratio of the partially tracked trajectories have less information, which leads to a poor LLR score estimation. The separation performance of the log likelihood ratio method is shown in Fig. 5.5. As seen from the figure, the LLR method is more successful identifying the particle ID for fully tracked particle trajectories. The event selection based on the log likelihood ratio parameter is shown in Fig. 4.8. The fractional residual errors for proton momentum and angle are given in Fig. 5.6.

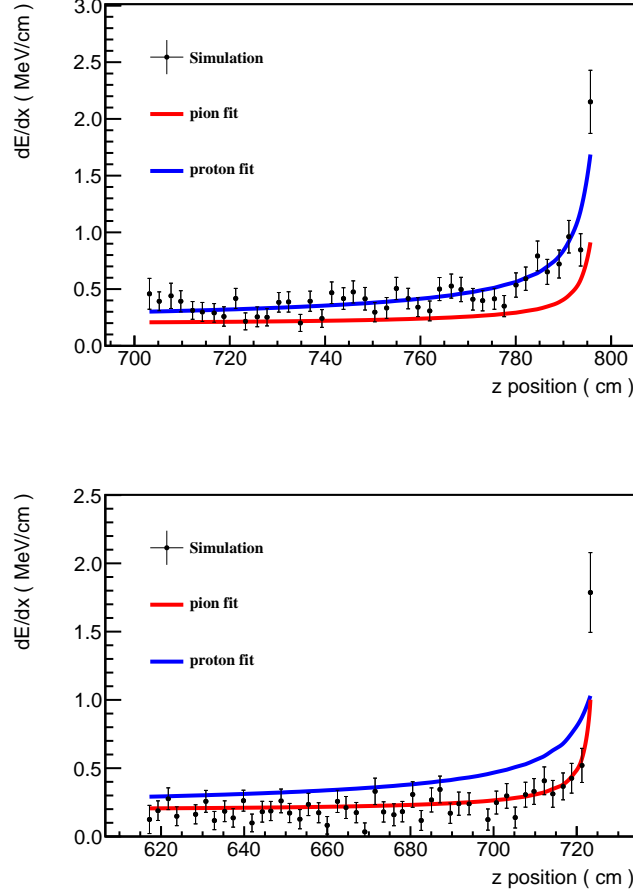


FIG. 5.4: Simulated proton (top) and pion (bottom) dE/dx profile compared to Bethe-Bloch (solid curves). The simulation dE/dx profile for a proton (top, blue curve versus simulation) and for a pion (bottom, red curve versus simulation) matches Bethe-Bloch equation results. From Ref. [35]

5.2 Neutral pion reconstruction

The neutral pion decays into two gamma rays ($\pi^0 \rightarrow 2\gamma$) via the electromagnetic interaction on a time scale of about 10^{-17} seconds. The photons produce energetic electron-positron pairs through gamma conversion ($\gamma \rightarrow e^- + e^+$) and the resulting electrons lose energy through bremsstrahlung ($e^- \rightarrow e^- + \gamma$), creating additional photons which produce more electron-positron pairs. The resulting cascade is called an electromagnetic shower [67].

The neutral pion reconstruction algorithm is designed to identify and measure

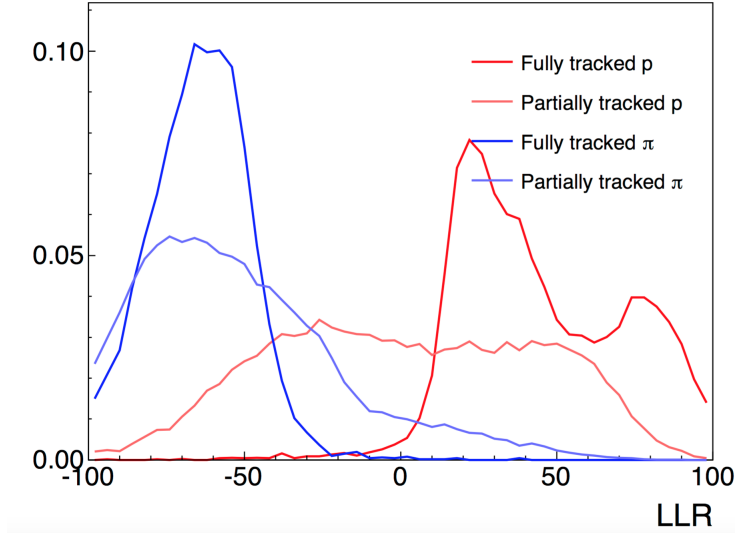


FIG. 5.5: Performance of the log likelihood ratio (LLR) method for separating the protons and pions. In both proton and pion cases the LLR score is more reliable if the particle trajectory is fully tracked. From Ref. [56].

the energy and direction of the two electromagnetic showers coming from the π^0 decay. Figures 5.7, 5.8, and 5.9 show candidate signal events inside the MINERvA detector. In all of the event displays, the long track exiting the back of the detector is the muon, and the short track connected to the event vertex is the proton. The two EM shower-like objects pointing to the vertex are the candidate gammas from a $\pi^0 \rightarrow 2\gamma$ decay. In standard notation the leading (more energetic) gamma is denoted as γ_1 and secondary (less energetic) gamma is denoted as γ_2 .

The π^0 reconstruction algorithm proceeds in three stages. The first stage is the pre-reconstruction stage, in which the unused clusters are analyzed and the clusters to be used during the reconstruction stage are selected. The second stage is the reconstruction stage, in which an algorithm referred to as “Angle Scan” is used to detect individual shower-like objects and to measure their energy and direction. The final stage is post-reconstruction, in which the quality of found shower-like objects are checked and the π^0 four-momentum is calculated.

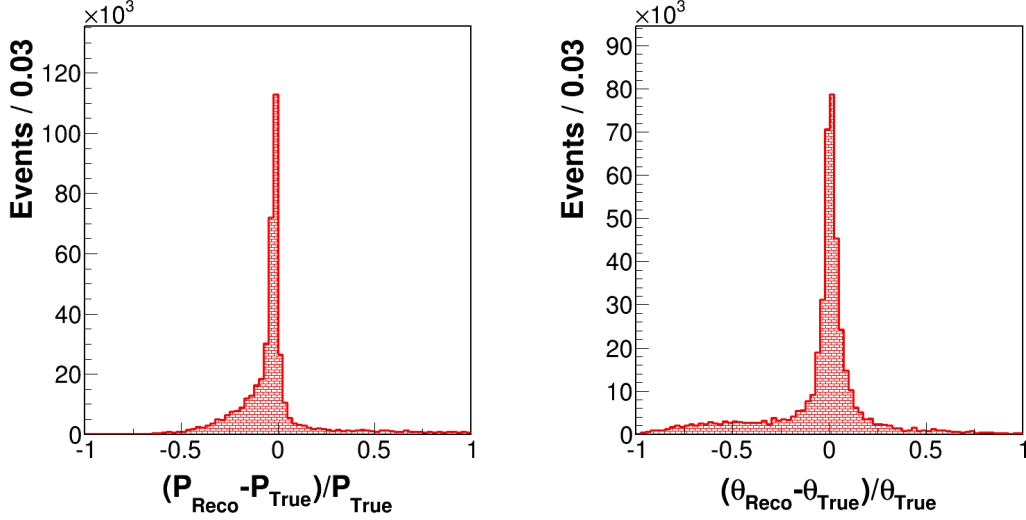


FIG. 5.6: Fractional residual errors for proton momentum (left) and production angle (right). The fractional residual error means for both momentum and angle are located at zero. However, the shape of the momentum distribution is asymmetrical and is shifted towards the negative side. The asymmetrical shape is due to the partially tracked protons. Partial proton tracks leads to a lower estimated momentum due to missing clusters. Also, the proton angle distribution has long tails on both sides. These tails are due to partially tracked protons which have a poor direction estimate. Full width at half maximum (FWHM) for the proton momentum fractional error is 0.03 and for the proton angle fractional error it is 0.05.

5.2.1 Pre-reconstruction

The Pre-Reconstruction stage of the π^0 reconstruction analyzes unused clusters and decides which clusters will be used during the reconstruction stage. The unused clusters are the non-tracked clusters. The tracked clusters are already used to form tracks as described in Sec. 5.1 and these tracks are used during muon and proton reconstruction. The first step in the pre-reconstruction stage is to decide whether an event contains a π^0 candidate or not. For this task all unused clusters are collected and the total visible energy in different sub-detectors of the MINERvA detector are calculated. Then the following visible energy requirements are applied: $E_{vis}^{Target} < 20$ MeV, $E_{vis}^{Tracker} + E_{vis}^{ECAL} + E_{vis}^{HCAL} > 50$ MeV, $E_{vis}^{Tracker} + E_{vis}^{ECAL} + E_{vis}^{HCAL} < 2500$ MeV. The details of these selections are described in Sec. 4.6.

The second step is the selection of clusters to be used during the reconstruction stage. For this task, the following requirements are applied to each cluster: Firstly,

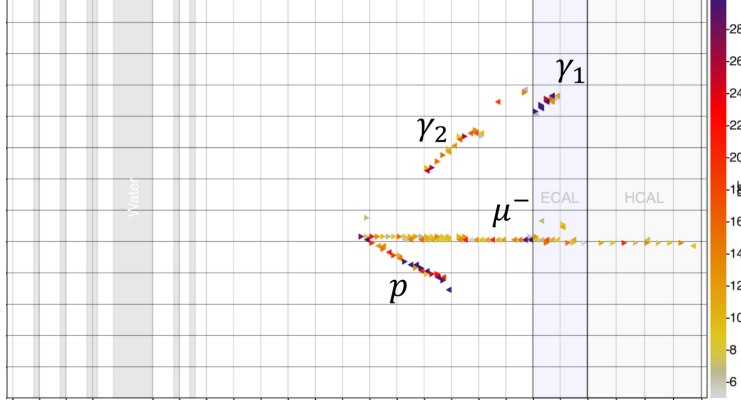


FIG. 5.7: Event display for a candidate signal event (2021/23/449). The color scale shows the number of photo-electrons of the clusters, for clusters having at least five photo-electrons. The leading shower measured energy $E_\gamma = 618.2$ MeV contained inside the ECAL, and the second shower, converted within the scintillator tracker, measured energy $E_\gamma = 139.7$ MeV. The clusters within the ECAL have more photo-electrons than the clusters inside the Tracker region.

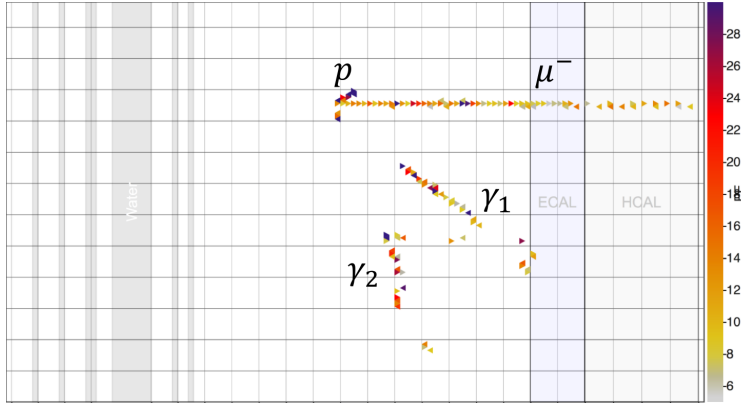


FIG. 5.8: Event display for a candidate signal event (2037/17/4807). Both showers are contained in the Tracker region of the detector. Measured energies for the showers are $E_{\gamma_1} = 393.6$ MeV and $E_{\gamma_2} = 298.1$ MeV. In addition to the short proton track near the vertex there is additional vertex activity. Depending on the source of the vertex activity this event can be a signal or a background.

the time difference between the cluster and muon track must be less than 25 ns. This selection ensures that only clusters that are in the same time slice with the muon track are used in π^0 reconstruction. Secondly, the charge of the cluster, which is defined as number of photo-electrons divided by number of hits inside the cluster, must be greater than 3. This selection removes “low-activity” clusters that might be due to cross-talk. Finally, the clusters in the HCAL are removed, because these clusters are most likely created by neutrons, not EM showers. If all three conditions

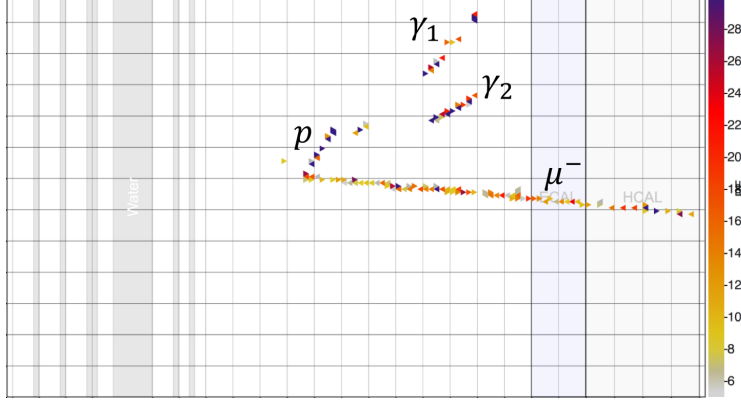


FIG. 5.9: Event display for a candidate signal event (2204/11/453). Both showers are contained in the Tracker region and the measured energies are $E_{\gamma_1} = 416.7$ MeV and $E_{\gamma_2} = 223.2$ MeV. There is additional activity near the end point of the proton track. That activity is most probably due to the γ_1 undergoing a Compton scattering. The actual shower development of γ_1 starts more downstream. The π^0 reconstruction algorithm is designed to contain all the clusters having the same angle from the vertex. Consequently, the energy loss due to Compton scattering for γ_1 is included in the measured energy.

are satisfied, the cluster is saved as a usable cluster. Once all the usable clusters are selected, the reconstruction stage is started.

5.2.2 Reconstruction

The Angle Scan algorithm is used to reconstruct two EM showers coming from the $\pi^0 \rightarrow 2\gamma$ decay. This algorithm groups clusters that fall within a conical region starting at the event vertex. The groups of clusters are stored as blobs. The Angle Scan algorithm assumes that every cluster has a direction pointing towards the vertex. Using this assumption a 1D histogram based on the angle of the cluster with respect to the z-axis is filled. Each cluster is associated with the angle between the cluster direction and the z-axis as illustrated in Fig. 5.10.

The cluster angles are loaded into a 1D histogram where each cluster entry is weighted by the number of photo-electrons of the cluster. The histogram is used to identify discrete shower-like structures in the event. The histogram is scanned bin-by-bin in search of isolated and continuous distributions representing EM showers. Figure 5.11 illustrates the process. Two isolated distributions (Group 1 and Group

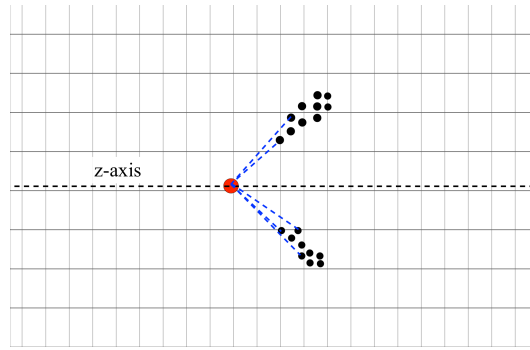


FIG. 5.10: Schematic view of cluster direction pointing towards the vertex. The red circle represents the event vertex, and each black circle represents a single cluster. The dotted lines relates clusters to the event vertex. The angle of the cluster is defined relative to the z-axis.

2), correspond to the two clusters shown in the event display. After identifying groups and their bin limits (minimum and maximum angles), all clusters that fall inside of a conical region defined by the minimum and maximum angle are grouped. In Fig. 5.11, Group 1 (bottom shower) and Group 2 (top shower) are reconstructed with all the clusters inside the conical regions. Note that the conical shape allows the inclusion of all clusters in the main direction regardless of gaps in the showers (as in Group 1) [68]

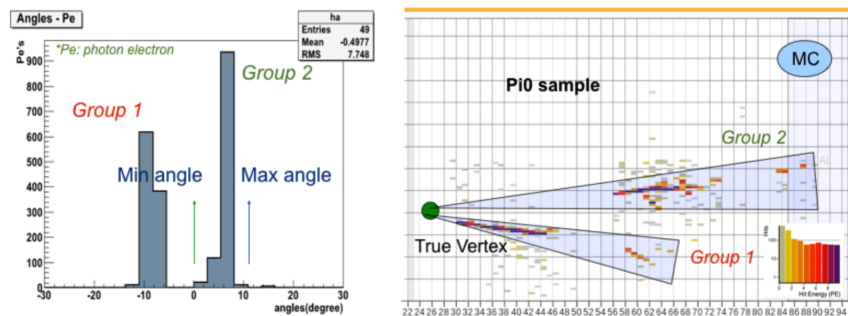


FIG. 5.11: Schematic for grouping of clusters based on their direction. Left: 1D Histogram filled by cluster angles. The X-axis gives the angle of the clusters, and the Y-axis shows the photo-electron deposition of each cluster. Right: Event display of the identified groups. Each group is located inside a conical region starting from the event vertex. From Ref. [68].

Recall that, the MINERvA detector has 3 different views (X, U, V). The Angle Scan algorithm scans cluster angles in the X-view to identify groups of clusters

falling in a single conical region. Once the grouping is done in the X-view, the algorithm reorganizes the clusters inside each group with an increasing z position. Then, using the z position and direction of each cluster, the U-view and V-view clusters are added to the corresponding groups. At the end of merging all X-view, U-view and V-view clusters, shower-like objects called blobs are formed and these blobs are further analyzed in the post-reconstruction stage.

5.2.3 Post-reconstruction

Since the π^0 reconstruction algorithm is designed to detect $\pi^0 \rightarrow 2\gamma$ decay, exactly two distinct shower-like objects are required. Therefore, in the post-reconstruction stage, the first thing that is checked is the number of found shower candidates by the Angle Scan algorithm. Figure 5.12, shows the number of shower candidates found by the algorithm.

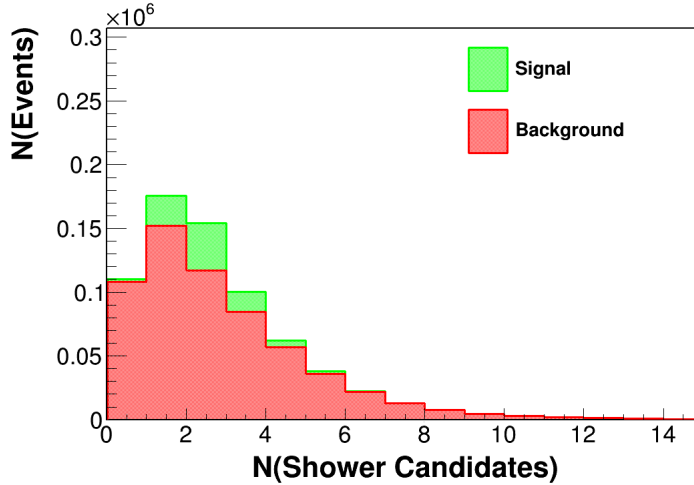


FIG. 5.12: Number of shower candidates found by the Angle Scan algorithm. The number of signal events is greatest for events with two-shower candidates. The events with one-shower and three-shower candidates also contain significant numbers of signal events. However, the events with zero and more than three shower candidates are mostly background.

Since the events with one-shower and three-shower candidates contains significant numbers of signal events, they deserve special treatment. For this Thesis, new methods were developed to recover one- and three-shower events. The goal is to

isolate two different showers from events having one or three shower candidates. For events with one-shower candidates, the first approach is to reduce the scanning angle. The scanning angle is the bin size of the cluster angle histogram described in the previous section. The default scanning angle is 4 degrees and if the Angle Scan algorithm finds only one shower in the event with the default scanning angle, the algorithm is run again with a scanning angle of 2 degrees. If this smaller angle does not resolve two different showers from a single shower, the second approach is to change the start-search view. As described in the previous Section, the Angle Scan algorithm uses the X-view to group clusters. If the clusters are aligned in the X-view, all of them will be in the same group and there will be a single shower-like object at the end. However, if the cluster grouping starts in the U view, and if the clusters are separated in the U-view, then it is possible to create two different groups. Similarly if the X-view and U-view searches give only one shower, then a V-view search is tried. If one of these methods can recover two showers from an event with one shower candidate, the event is kept; otherwise, the event is rejected. The performance of these methods is summarized in Table 5.2. As seen from the Table, 9.61% of single-shower events can be recovered as two-shower signal events.

	N(Signal)	Percent	N(Background)	Percent
Recovered: Small Angle	821	6.75%	676	1.19%
Recovered: Search U-view	194	1.59%	278	0.49%
Recovered: Search V- View	154	1.27%	212	0.37%
Total Recovered	1169	9.61%	1166	2.06%

TABLE 5.2: Recovery of signal events from events with one-shower candidate. Percentages are based on the total number of signal events (12,169) and background events (56,653) in the simulation sample.

The main objective of the post-reconstruction stage is to estimate the shower direction. For this task, a straight line is fitted using the positions of each cluster in the shower and the event vertex. If a straight line fit is successful, then the direction of the line is accepted as the direction of the shower. If the fit procedure fails, the shower is not used.

The shower direction check method is useful to recover signal events from events

with three shower candidates. The direction of all three showers are checked assuming that they point towards the event vertex, and the showers with bad directions are rejected. If there are two showers after the direction check, the event is kept; otherwise, it is rejected. The performance of the direction check on events with three-shower candidates is given in Table 5.3. As the Table shows, 21.4% of the three-shower events are recovered as two-shower signal events by this method.

	N(Signal)	Percent	N(Background)	Percent
Recovered: Direction	1735	21.4%	3099	11.2%

TABLE 5.3: Recovery of signal events from events with three-shower candidate. Percentages are based on the total number of signal events (8,128) and background events (27,669) in the simulation sample.

5.2.4 Electromagnetic energy calibration

After the three stages of the π^0 reconstruction algorithm, two shower-like objects pointing towards the event vertex are obtained. The next step is to estimate the EM shower energies. In this study, an energy-dependent calibration is used to calculate the calibrated energy of the EM showers.

The EM shower energy calibration depends on the Z values of the active and passive materials, and on the shower energy as well. Figure 5.13 shows the photon total cross sections as a function of energy in carbon. In this analysis, most of the EM showers come from $\pi^0 \rightarrow 2\gamma$ decay and have an energy range between 50 MeV and 1 GeV. As shown in the Figure, for photon energies between 1 MeV and 1 GeV, Compton scattering (σ_{incoh}) and pair production (κ_N) contribute to the total cross section almost equally. The lower the shower energy, the more probable it is to have soft shower particles from Compton scattering in the detector.

In order to determine the calibrated energy of the EM showers, a study is performed using MC truth information. The visible energy (deposited energy) of the shower and its relation to the true energy of the shower is studied. The calibration weight is calculated as the ratio of true energy over visible energy, $k_{cal} = E_{true}/E_{visible}$. In this analysis an energy-dependent calibration weight is used. As

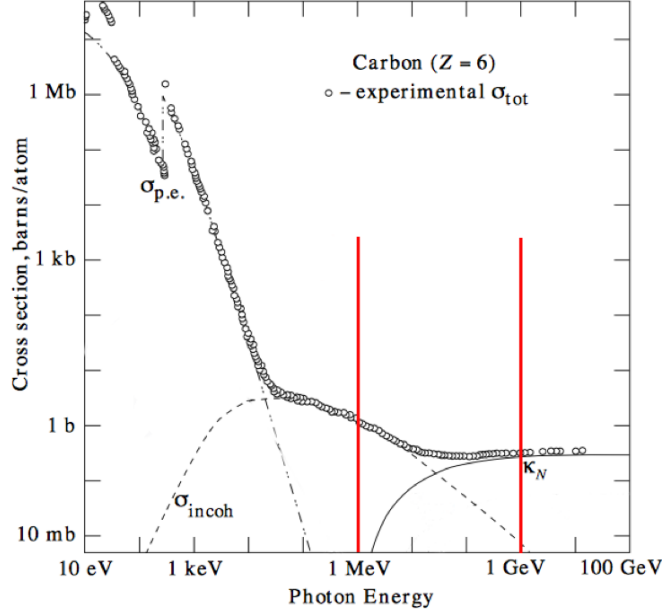


FIG. 5.13: Photon total cross section as a function of energy in carbon. The plot shows the total cross section and the individual photon interaction cross sections, namely the photoelectric effect ($\sigma_{p.e.}$), Compton scattering (σ_{incoh}), and pair production (κ_N). The red lines define the range of shower energies observed in this analysis. From Ref. [41].

explained above, lower photon energies are more likely to create soft shower particles from Compton scattering. The soft shower particles tend to leave less visible energy inside the longitudinally segmented MINERvA detector. Thus showers with low visible energy require a different calibration weight than showers with higher visible energy. The energy-dependent calibration weight deduced for the tracker region of the detector is shown in Fig. 5.14. The calibration weight k_{cal} , is larger at lower visible energies; it decreases as the visible energy increases. The red dotted line in Fig. 5.14 shows the calibration constant used in other MINERvA analyses for photons having energies greater than 1 GeV [69]. The Half Width at Half Maximum (HWHM) error bars in Fig. 5.14 represent the width of the distribution of $E_{true}/E_{visible}$. To calculate the HWHM, the showers are grouped according to their visible energies, and the distribution of $E_{true}/E_{visible}$ is studied in each group. The visible energy groups used are: $0 \text{ MeV} \leq E_\gamma \leq 50 \text{ MeV}$, $50 \text{ MeV} \leq E_\gamma \leq 100 \text{ MeV}$, $100 \text{ MeV} \leq E_\gamma \leq 150 \text{ MeV}$, $150 \text{ MeV} \leq E_\gamma \leq 200 \text{ MeV}$, $200 \text{ MeV} \leq E_\gamma \leq 300 \text{ MeV}$.

The HWHM value becomes smaller with increasing visible energy.

A straight line fit is used to define the relation between the calibration weight and the visible energy. The slope of the line is negative, and so the ratio decreases with increasing visible energy. The value of the energy-dependent calibration weight is constructed to converge with the well-studied energy calibration constant used in other MINERvA analyses [69]. Figure 5.15 shows the visible energy versus $E_{true}/E_{visible}$ ratio over the visible energy range relevant to MINERvA. The calibration weight is taken to be energy-independent for photons of energies greater than 697 MeV.

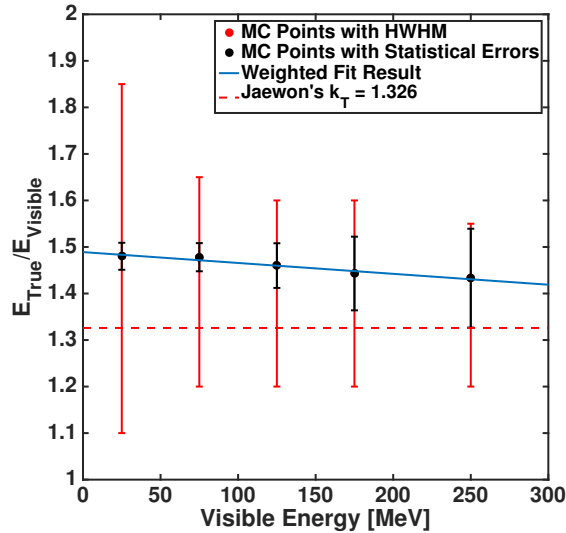


FIG. 5.14: Energy-dependent calibration weight in the tracker region. As visible energy increases the HWHM (red error bars) get smaller, but the statistical errors (black error bars) increases.

The contribution of Compton scattering in lead is not as large as in carbon, therefore, it is not expected that an energy-dependent calibration weight is appropriate for the ECAL region. In order to find the calibration weight for the ECAL region, the calibration study was repeated and an energy-independent constant was found, which is slightly greater than the EM energy calibration constant used in other MINERvA analyses with photon energies greater than 1 GeV [69, 70]. Figure 5.16 shows the results based on shower energies inside the ECAL region. As can be seen, the relation between the calibration weight k_{cal} and the visible energy stays

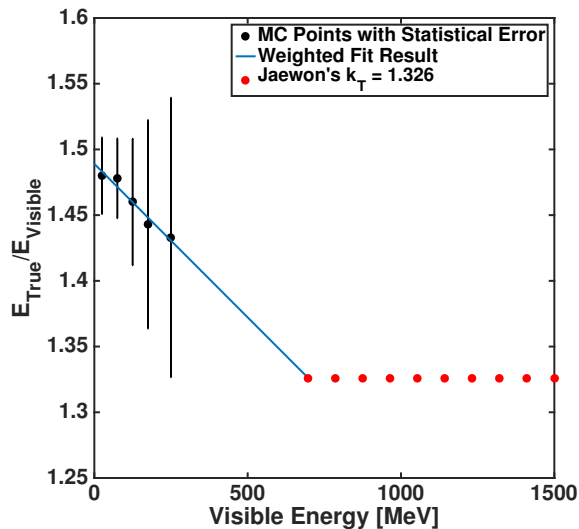


FIG. 5.15: Energy-dependent calibration weight in the tracker region shown over a large visible energy range. The calibration constant is set to the default EM calibration constant ($k_T = 1.326$) used in other MINERvA analyses for visible energies greater than 697 MeV.

constant.

The energies of the showers are estimated using the tracker and ECAL calibrations, then the π^0 four-momentum is calculated. Figure 5.17 shows the fractional residual errors ($\frac{reconstructed - true}{true}$) for π^0 momentum and angle. Even with the improved calibration methods, the fractional residual error on the π^0 momentum is large. However, the π^0 direction estimate is accurate.

5.3 Event kinematics

5.3.1 Neutrino energy

The neutrino energy estimation includes all final-state particle energies as well as the vertex activity energy and any extra energy not included in the particle reconstructions. In this analysis the neutrino energy is estimated as

$$E_\nu = E_\mu + E_\pi + \sum T_p + E_{vertex} + E_{extra} \quad (5.4)$$

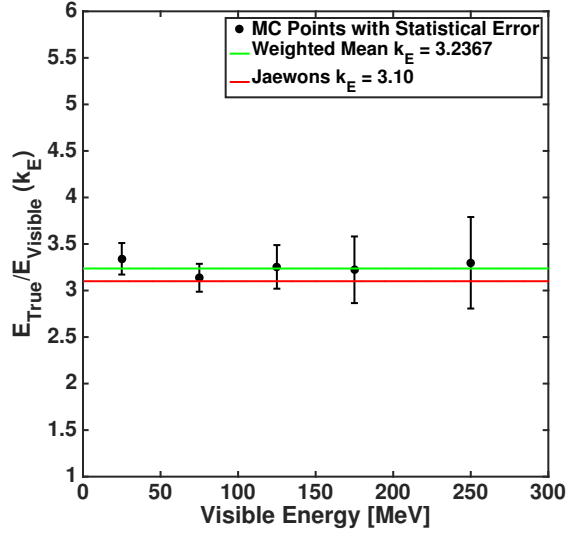


FIG. 5.16: Energy-independent calibration weight in the ECAL region. The red line represents the calibration constant used in Jaewon Park’s analysis [69] with photon energies greater than 1 GeV.

where T_p is the kinetic energy of a single proton, E_{vertex} is the vertex energy and E_{extra} is the extra energy leftover after the reconstruction. The details of each component are discussed below.

Final-state particle energies

The final-state particle energies are calculated during their individual reconstructions. In this investigation every event has a single muon and a single π^0 ; however, the number of reconstructed protons in the final state can vary. For events with one or more protons, all reconstructed proton kinetic energies are included in the neutrino energy estimation. In the case of no-proton events, the kinetic energy of a short proton (not reconstructed proton) may appear in E_{vertex} as shown in Fig. 5.21.

Figures 5.18, 5.19, and 5.20 show the data versus simulation comparisons for particle energies and the (reconstructed - truth) energy distributions for the final-state muons, π^0 ’s and protons respectively. In each plot, the data points have statistical errors only. The E_μ estimation provides the dominant contribution ($\sim 1 - 10$ GeV)

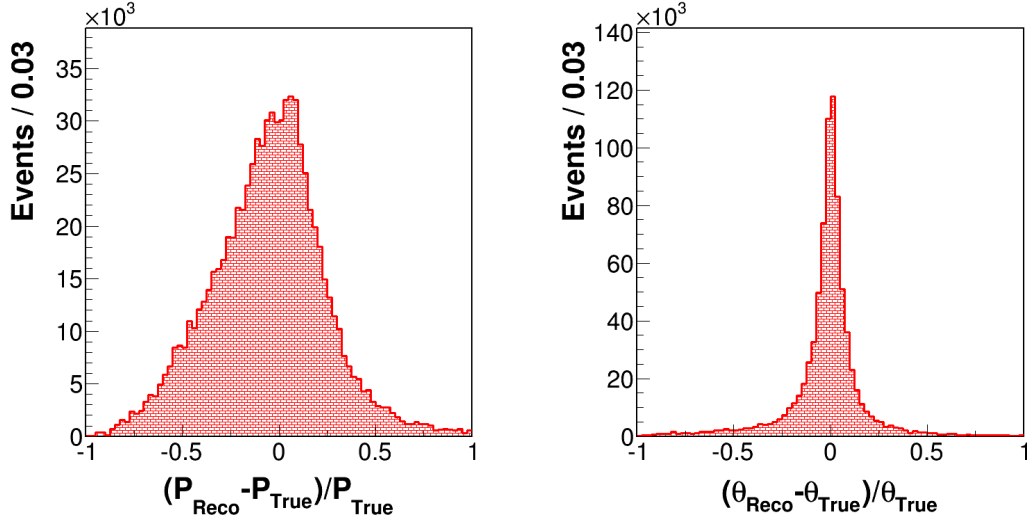


FIG. 5.17: Fractional residual errors for π^0 momentum (left) and angle (right). Both distributions are centered at zero and have a symmetrical shape. Full width at half maximum (FWHM) for the π^0 momentum fractional error is 0.5 and for the π^0 angle fractional error it is 0.08.

to the E_ν estimate. The $E_{Reco} - E_{True}$ distribution for proton energy has long tails especially on the negative side, due to partially reconstructed proton tracks. The long tail on the negative side is also visible in the fractional residual error on proton momentum in Fig. 5.6.

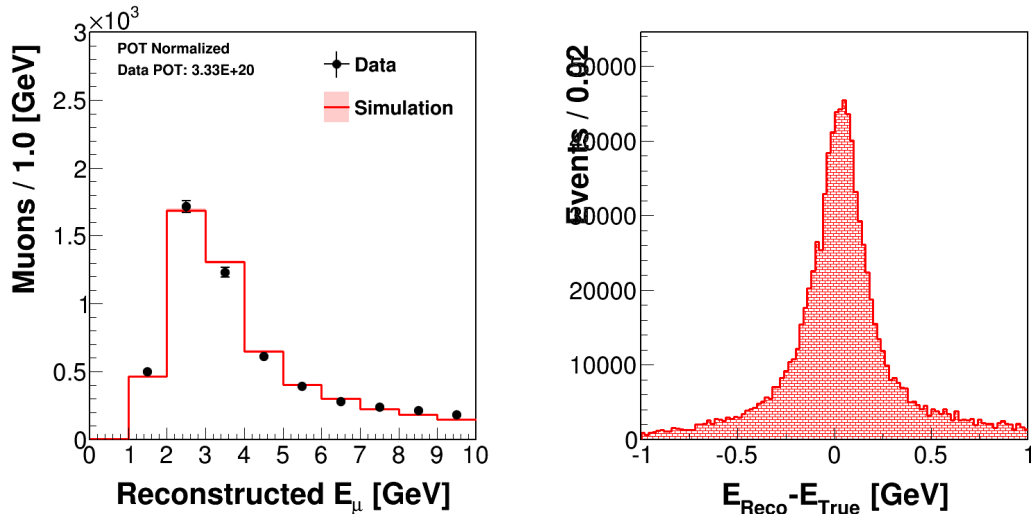


FIG. 5.18: Data and MC distributions for reconstructed muon energy (left), $E_{reco} - E_{true}$ distribution for MC (right). The data versus simulation agreement is good and the FWHM of the $E_{reco} - E_{true}$ distribution is ~ 0.24 GeV.

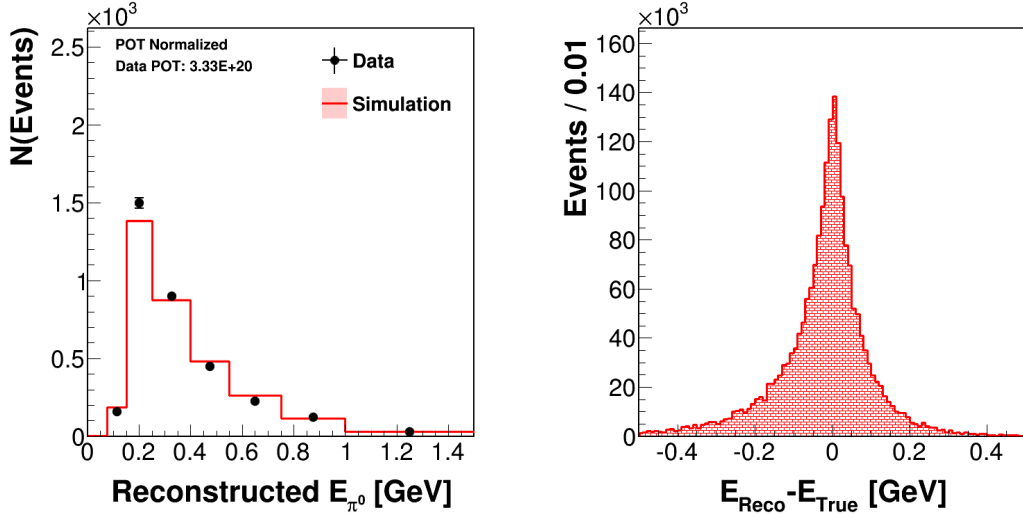


FIG. 5.19: Data and MC distributions for reconstructed neutral pion energy (left), $E_{\text{reco}} - E_{\text{true}}$ distribution for MC (right). There is a data versus simulation disagreement in which data prefers more low energy pions than the simulation. The FWHM of the $E_{\text{reco}} - E_{\text{true}}$ distribution is ~ 0.08 GeV.

Vertex energy

Vertex energy is estimated using an imaginary sphere with 90 mm radius centered at the event vertex. The unused hits inside the sphere are selected and their energies are estimated using a calibration based on inclusive hadron production. Only unused hits are used to avoid double-counting. The vertex energy has different distributions depending on the presence of reconstructed protons. Figure 5.21 shows the vertex energy data versus simulation comparisons for events with and without reconstructed protons.

Extra energy

Extra energy has three different individual sources. One extra energy source arises with the clusters rejected during π^0 reconstruction as described in Sec. 5.2.1. The extra energy is calculated using only the the low-activity clusters and the remote clusters inside HCAL. Clusters rejected because they were out of time with the muon track are not used for extra energy. A second source is the extra muon energy, arising with the clusters located close to the muon track but not used by the tracking

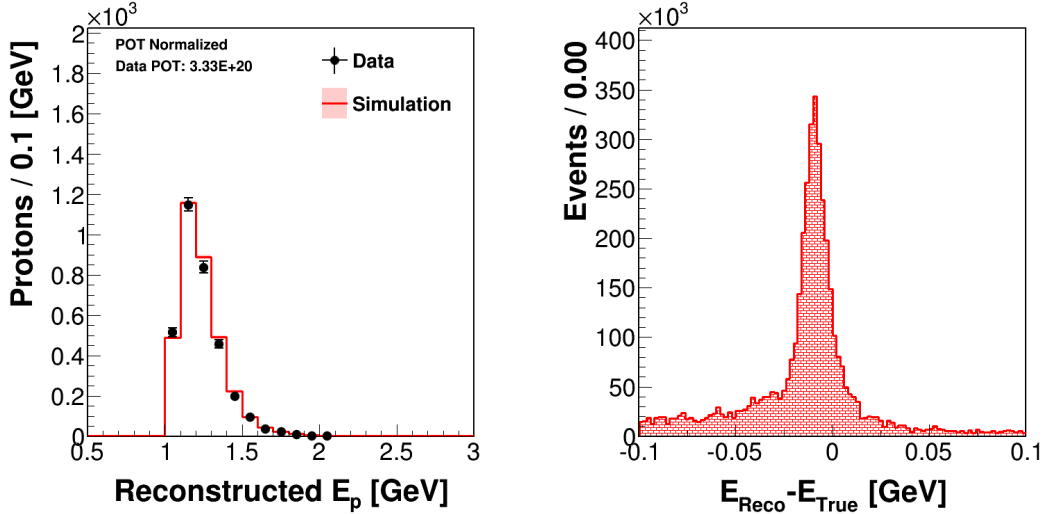


FIG. 5.20: Data and MC distributions for reconstructed proton energy (left), $E_{\text{reco}} - E_{\text{true}}$ distribution for MC (right). Note that, in the neutrino energy estimation the proton kinetic energies are used. Plots for proton energy comparisons are shown here for consistency with other final-state particle energy plots. The data versus simulation agreement is good. The FWHM of the $E_{\text{reco}} - E_{\text{true}}$ distribution is ~ 0.01 GeV.

algorithm. The third component of the extra energy is the leftover energy, which includes all other clusters not used in any of the particle reconstructions. The leftover clusters are collected by using an imaginary sphere with a radius 300 mm centered at the event vertex.

The effect of a reconstructed proton on extra energy has also been examined; however no change in the extra energy distributions is observed. Figures 5.22, 5.23, and 5.24 show the extra energy distributions for each extra energy source, for events with and without reconstructed protons. Figure 5.25 shows the total extra energy which is included in the neutrino estimation for events with and without reconstructed protons.

Neutrino energy estimation

Once the component contributions for the neutrino energy are calculated, the actual neutrino energy is estimated by adding them up as in Eq. (5.4). The effect of the presence or absence of a reconstructed proton on the neutrino energy estimation has

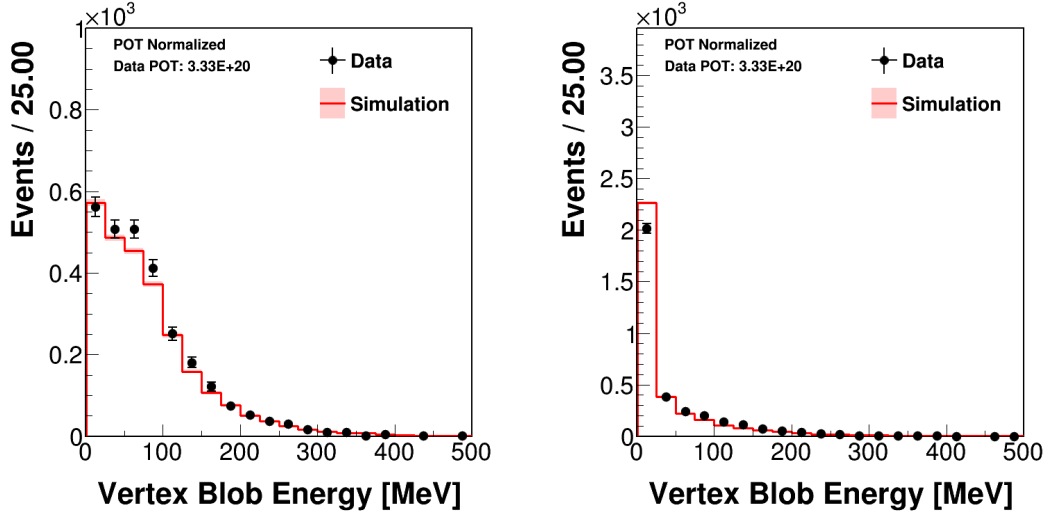


FIG. 5.21: Distributions of vertex energy. Vertex blob energy changes dramatically if an event has a reconstructed proton. Plot (a) shows the non-reconstructed proton energy that appears as vertex blob energy. Plot (b) shows that the vertex blob energy is greatly reduced in the presence of the reconstructed protons.

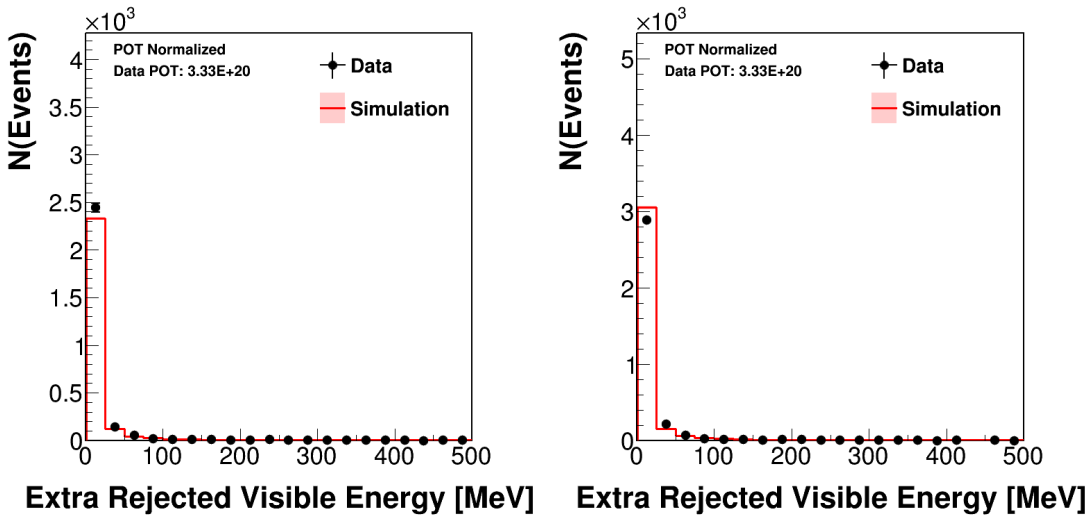


FIG. 5.22: Distribution of extra energy coming from rejected clusters during π^0 reconstruction. Plot (a) shows the events without a reconstructed proton; and plot (b) shows the events with at least one reconstructed proton. Both (a) and (b) have the same shape and are reasonably well described by the GENIE simulation.

been studied and it is concluded that there is no dramatic effect on the quality of the neutrino energy estimation. The study suggests that the vertex and extra energy collection methods do indeed include nearly all of the cluster energies which are not used in proton reconstruction. Figures 5.26 and 5.27 show the neutrino energy

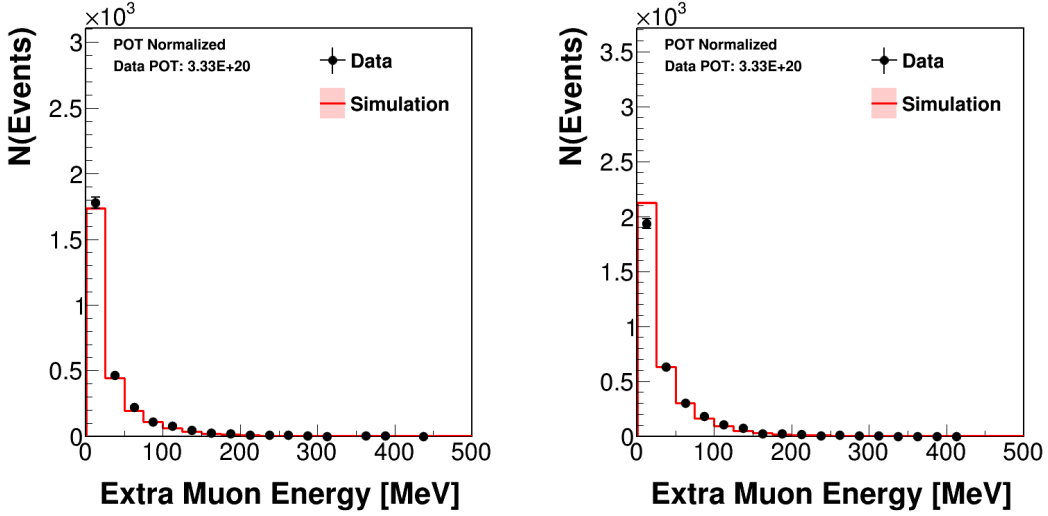


FIG. 5.23: Distribution of extra energy coming from muon non-tracked clusters. Plot (a) shows the events without a reconstructed proton; and plot (b) shows the events with at least one reconstructed proton. Both (a) and (b) have the same shape and are reasonably well described by the GENIE simulation.

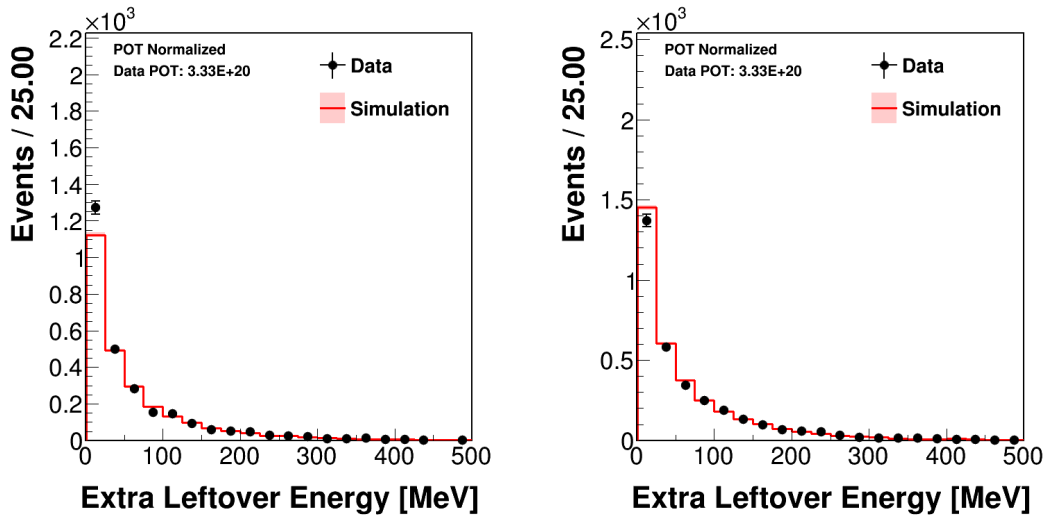


FIG. 5.24: Distribution of extra energy coming from leftover clusters. Plot (a) shows the events without a reconstructed proton; and plot (b) shows the events with at least one reconstructed proton. Both (a) and (b) have a similar shape and are reasonably well described by the GENIE simulation.

distributions for events with and without reconstructed protons. Figure 5.28 shows the neutrino energy distributions for all events.

Accurately estimating neutrino energy is crucial in any cross-section measurement. In this analysis the neutrino energy $E_{reco} - E_{truth}$ distribution (Fig. 5.28) has

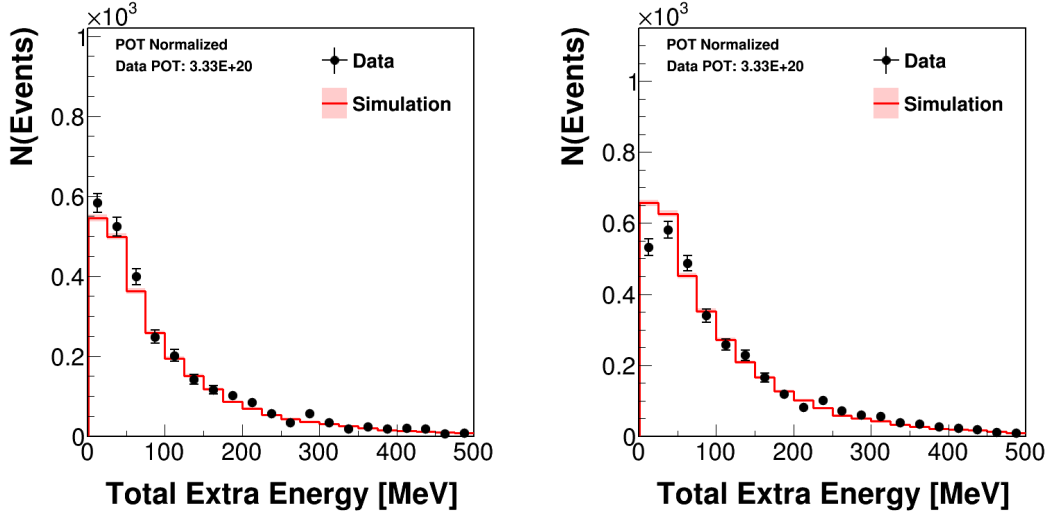


FIG. 5.25: Distributions of the total extra energy included in the neutrino energy estimation. Plot (a) shows the distributions for events without a reconstructed proton; plot (b) shows the distributions for events with at least one reconstructed proton. Distributions (a) and (b) have similar shapes and are reasonably well described by the GENIE simulation.

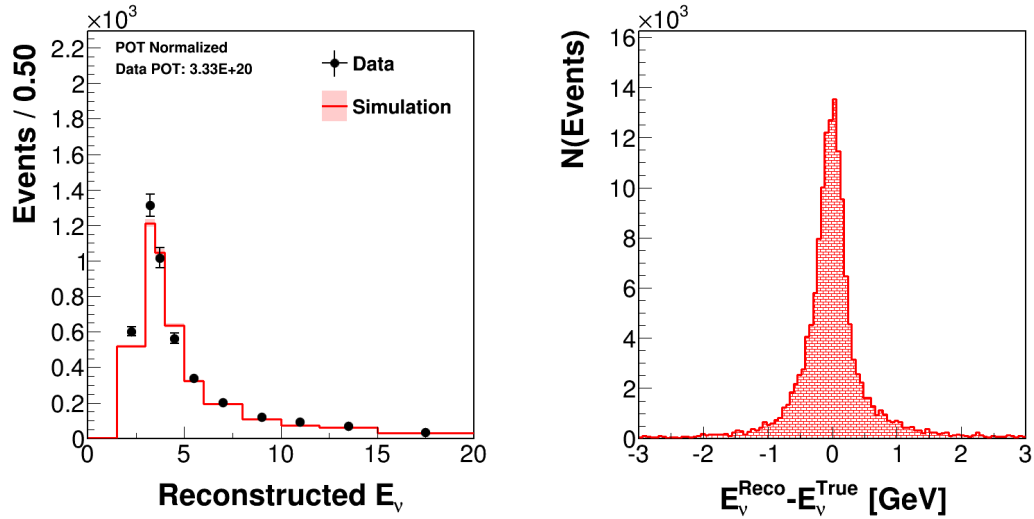


FIG. 5.26: Neutrino energy distributions for events without a reconstructed proton. The FWHM of the $E_{reco} - E_{true}$ distribution is 0.36 GeV.

a half width at half maximum of 0.21 GeV, and for an average neutrino energy of 3.5 GeV the uncertainty amounts to 6%.

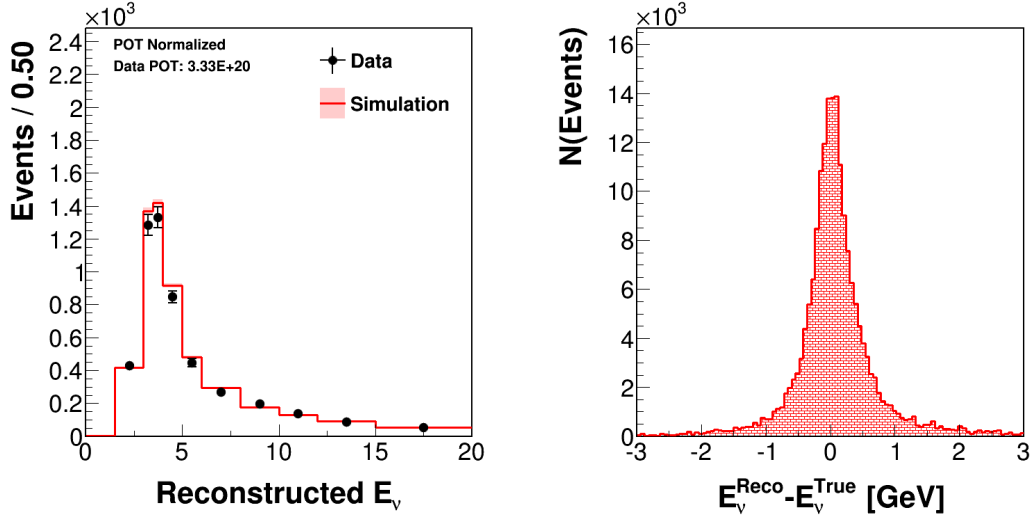


FIG. 5.27: Neutrino energy distributions for events with at least one reconstructed proton. The FWHM of the $E_{reco} - E_{true}$ distribution is 0.48 GeV.

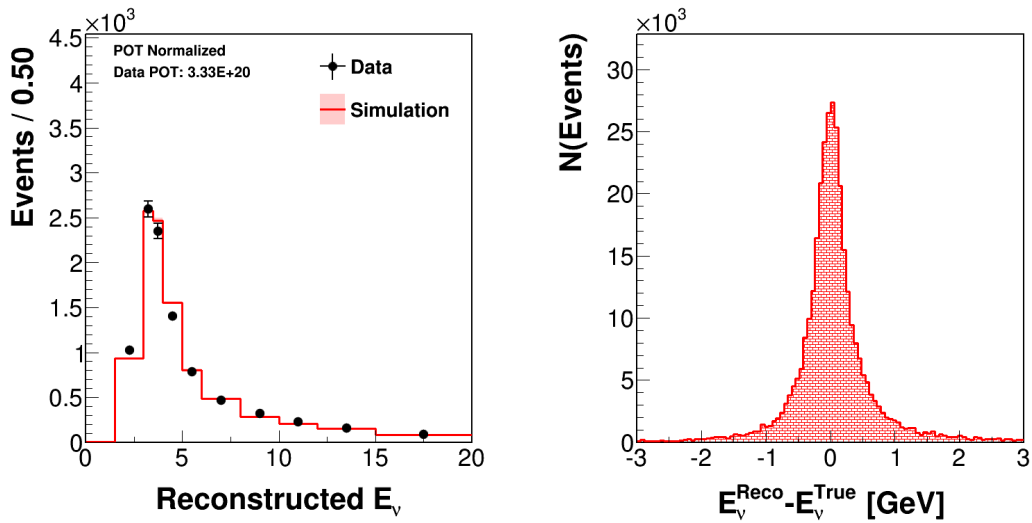


FIG. 5.28: Neutrino energy distributions for all events. The FWHM of the $E_{reco} - E_{true}$ distribution is 0.42 GeV.

5.3.2 Distributions of Q^2 and W

The variables Q^2 and W^2 are calculated using the estimated neutrino energy and the measured muon kinematics using the formulas of Eqs. (4.4) and (4.9) respectively. The data versus simulation and (reconstructed - truth) distributions are shown in Figs. 5.29, and 5.30. In the lowest Q^2 bin $Q^2 < 0.1 \text{ GeV}^2$, the data is 76% of the simulation prediction; also for the higher Q^2 region the data is greater than

the simulation prediction. The discrepancy between data and simulation in the W distribution suggests that W is over-predicted in the simulation by 20 MeV. The study for determining the shift amount in the simulation is reported in Sec. 11.4.1.

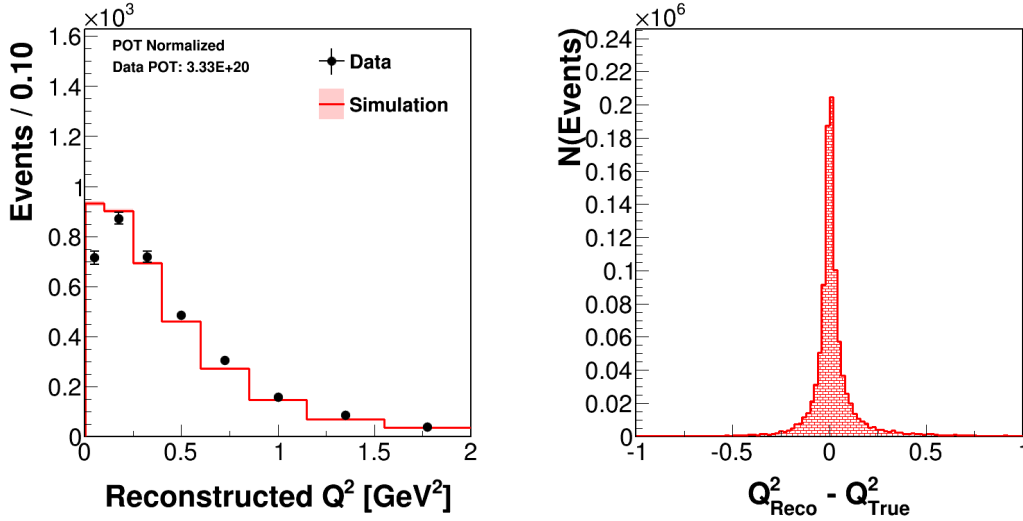


FIG. 5.29: Q^2 distribution for all selected events. The Q^2 distribution of data shows a fall off in the lowest bin $Q^2 < 0.1 \text{ GeV}^2$ that is not predicted by the MC. The FWHM of the $Q^2_{\text{reco}} - Q^2_{\text{true}}$ distribution is 0.02 GeV^2 .

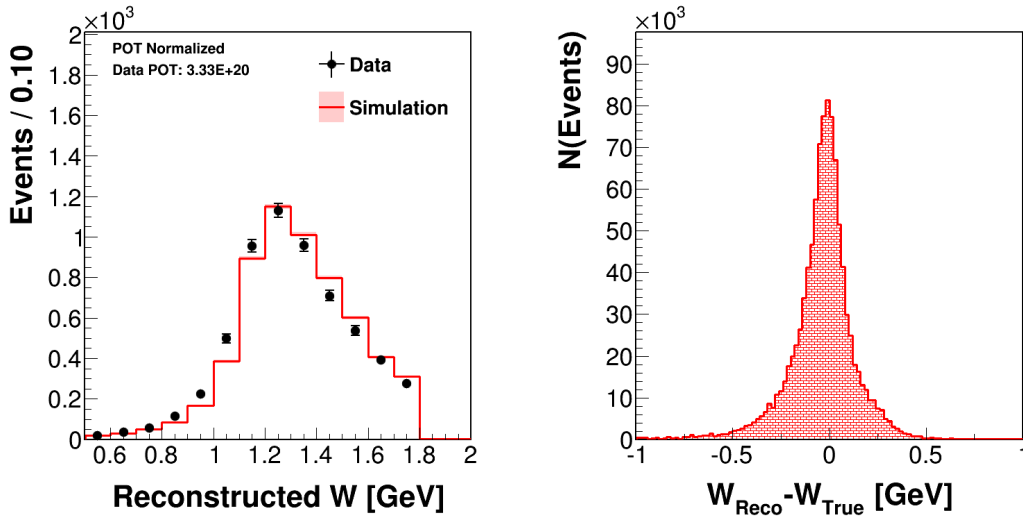


FIG. 5.30: W distribution for all events. The $W < 1.8 \text{ GeV}$ selection in signal definition is indicated on plot (a). The W distribution of the data appears to be shifted towards lower W relative to the MC prediction. The FWHM of the $W_{\text{reco}} - W_{\text{true}}$ distribution is 0.18 GeV .

Chapter 6

Background Classifications and Background Constraints

6.1 Background classifications

The background events for this analysis have been classified in three different ways: According to the pion multiplicity of the final state, according to the number of neutral pions in the final state, and major background sources.

6.1.1 Background classification: Pion multiplicity

The first way of classifying background events is according to the number of pions in the final state. However for the relatively small numbers of neutral current and antineutrino background events the number of pions in final state is not counted; rather, these reactions are assigned to their own categories. Charged current events having no mesons in the final state are classified as “QE-like”. Events having one charged pion in the final state are categorized in two different ways. If the charged pion has undergone charge exchange inside the detector to become a neutral pion, the event is classified as “Single Charged Pion Charge-Exchange”. However, if the single pion in the event has not undergone charge exchange in the detector, the event is classified as “Single Charged Pion”. Events having two pions in the final state are classified in two different ways. If there is at least one neutral pion in the final state, then the event is classified as “Double Pion with π^0 ”. However, if an event has two charged pions in the final state, the event is classified as “Double Pion without π^0 ”. Similarly, the events having multiple (2+) pions in the final state are classified in two different ways. If there is at least one neutral pion in the final state, then the event is classified as “Multi Pion with π^0 ”. However, if the event has multiple charged pions without any neutral pion in final state, the event is classified as “Multi Pion without π^0 ”. If the event does not belong to any of these categories it is categorized as “Other”, for example charged current events having a particle in their final state other than nucleons and pions. Table 6.1 lists the percentages for each category and Fig. 6.1 shows the background percentages using pie charts. Single pion channels are the dominant background, comprising the 44.1% of the total background. Two-pion channels contribute 18.6% to the background, while the multi-pion channels

contribute only 3.1%. The zero-pion contribution (QE-like) to the total background is 21.4%.

Background Type	Percentages
QE-like	21.4%
Single Charged Pion	32.7%
Single Charged Pion Charge-Exchange	11.4%
Double Pion with π^0	15.5%
Double Pion without π^0	3.1%
Multi Pion with π^0	2.4%
Multi Pion without π^0	0.7%
Neutral Current	0.1%
Anti Neutrino	1.8%
Other	11.0%
Total	100%

TABLE 6.1: Estimated percentages for backgrounds classified according to the number of pions in the final state.

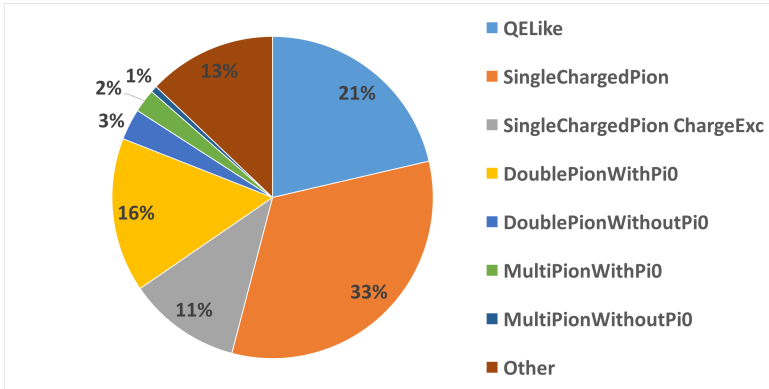


FIG. 6.1: Background percentages based on the number of pions in the final state. Leading background types are Single Charged Pion and QE-like.

Correlations are observed with events having or not having a reconstructed short track with a high proton score. When there is no reconstructed short track, the single charged pion background type increases; this is because there is no short track candidate to apply a particle score event selection, which is a method successfully detecting a charged pion. Table 6.2 lists the number of events and percentages for events with 1-track (muon track only) versus 2+ tracks (muon track + short tracks) events, and Fig. 6.2 shows the background percentages using pie charts.

Background Type	1-Track Percentages	2+ Tracks Percentages
QE-like	24.4%	19.1%
Single Charged Pion	37.3%	29.3%
Single Charged Pion Charge Exc	13.7%	9.6%
Double Pion With π^0	10.4%	19.3%
Double Pion Without π^0	1.7%	4.2%
Multi Pion With π^0	1.3%	3.2%
Multi Pion Without π^0	0.3%	1.0%
Neutral Current	0.2%	0.1%
Anti Neutrino	2.7%	1.1%
Other	8.1%	13.2%
Total	100%	100%

TABLE 6.2: Estimated percentages for backgrounds classified according to the number of pions in the final state for 1-track and 2+ tracks events.

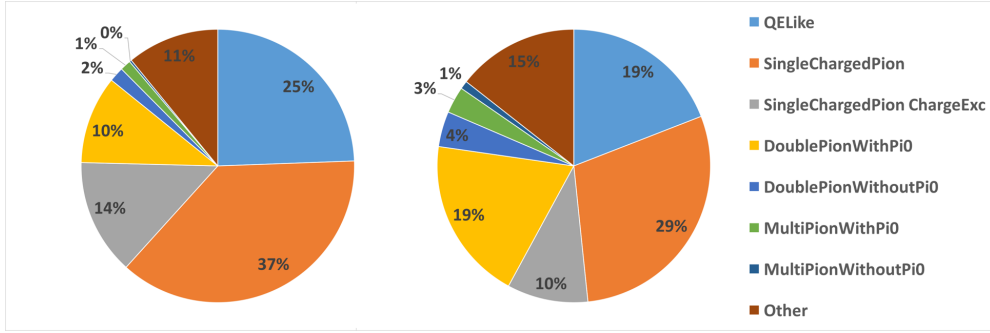


FIG. 6.2: Background percentages for events with 1-Track (left) and 2+ Tracks (right). For both 1-Track and 2+ Tracks the backgrounds of the leading categories are QE-like, single charged pion, and double pion with π^0 . The QE-like and single charged pion backgrounds for 1-Track events are higher than 2+ tracks events. However, the background events with double pion increases for events with 2+ Tracks.

6.1.2 Background classification: Neutral pion multiplicity

Background events can be classified based on the number of neutral pions in the final state. This classification does not differentiate between primary and secondary neutral pions. That is, the number of neutral pions is counted without checking whether the pion is coming from a neutrino interaction or a secondary interaction inside the detector. There are only three categories here, namely: No π^0 , single π^0 , and multi π^0 . Table 6.3 lists their percentages for each category and Fig. 6.3 shows the background percentages using pie charts. Zero π^0 production channels are

the dominant background according to this method of classification; they comprise 58.9% of the background.

Background Type	Percentages
No π^0	58.9%
Single π^0	33.7%
Multi π^0	7.4%
Total	100%

TABLE 6.3: Percentages of background events based on the number of π^0 's in the final state for selected events.

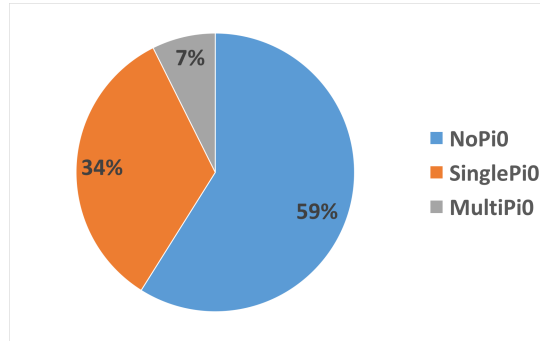


FIG. 6.3: Background percentages based on the number of neutral pions in the final state. Dividing background events according to whether or not they contain a π^0 , it is observed that 41% of background events contain at least one π^0 .

Correlations are observed with events having or not having a reconstructed short track with a high proton score in the π^0 background classification. In the case where there is no reconstructed short track, the no- π^0 background type increases. This is due to the non-tracked charge particle hits. These non-tracked hits may be mistaken as EM shower hits during neutral pion reconstruction, which increases the number of background events without π^0 . Table 6.4 lists percentages for events with 1-track (muon track only) versus 2+ tracks (muon track + short tracks) events and Fig. 6.4 shows the background percentages using pie charts.

Background Type	1-Track Percentages	2+ Tracks Percentages
No π^0	63.5%	55.5%
Single π^0	31.3%	35.5%
Multi π^0	5.2%	9.0%
Total	100%	100%

TABLE 6.4: Percentages of background events based on the number of π^0 's in the final state for events with 1-track and 2+ tracks.

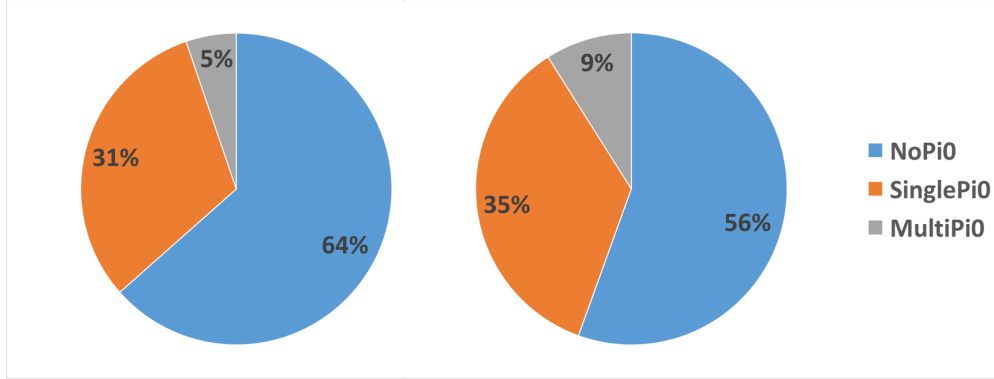


FIG. 6.4: Background percentages based on the number of neutral pions in the final state for events with 1-Track (left) and 2+ Tracks (right). For events that are either 1-Track or 2+ Tracks, the leading background type is no- π^0 .

6.1.3 Background classification: Major background sources

Background events can be classified into three categories which have comparable statistics. The largest background in this analysis consists of events that have a neutral pion in their final state. The second largest background is from events having at least one charged pion in their final state. Finally, the third background type consists of events having no mesons in the final state. If a background event does not fall into any of these categories it is classified as “Other”. For example, the neutral current events or anti-neutrino events are in the “Other” category. Also the charged current events having a particle in the final state other than nucleons and pions are classified as “Other”. Table 6.5 shows the percentages for each category and Fig. 6.5 shows the background percentages using pie charts. It is observed that, with this method of classification, backgrounds that include a π^0 in the final state are the largest contributor (39.7%), however events with charged pions and no π^0 's

give a background rate that is only modestly lower (31.2%).

Background Type	Percentages
With π^0	39.7%
Charged Pion	31.2%
QE-like	18.9%
Other	10.2%
Total	100%

TABLE 6.5: Background events and their percentage contributions.

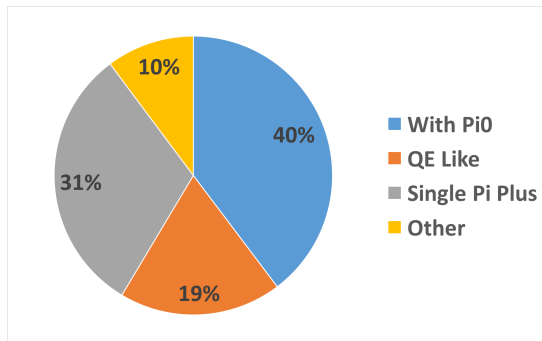


FIG. 6.5: Background percentages based on the three major background types. The leading background type is events with at least one π^0 .

As with other background classifications, the presence of a reconstructed proton track in the final state is examined. Similar behavior as with other background classifications is observed. The number of background events with π^0 decreases when there is no short track. This is due to the non-tracked charged particle hits being considered as part of EM showers during the neutral pion reconstruction. The numbers of events with a charged pion decreases when there is at least one short track. This is expected because the reconstructed tracks are required to have a high proton score, which removes the pion-like tracks. The number of QE-like events are similar in both cases. Table 6.6 lists the percentages for events with 1-track (muon track only) versus 2+ tracks(muon track + short tracks) events. Figure 6.6 shows the background content for 1-track, 2+ tracks and for all events using pie charts.

Background Type	1Track Percentages	2+ Tracks Percentages
WithPi0	34.5%	43.6%
Charged Pion	25.8%	27.8%
QE-like	21.5%	16.9%
Other	8.3%	11.7%
Total	100%	100%

TABLE 6.6: Percentage contributions of background event categories, subdivided according to the number of final-state tracks.

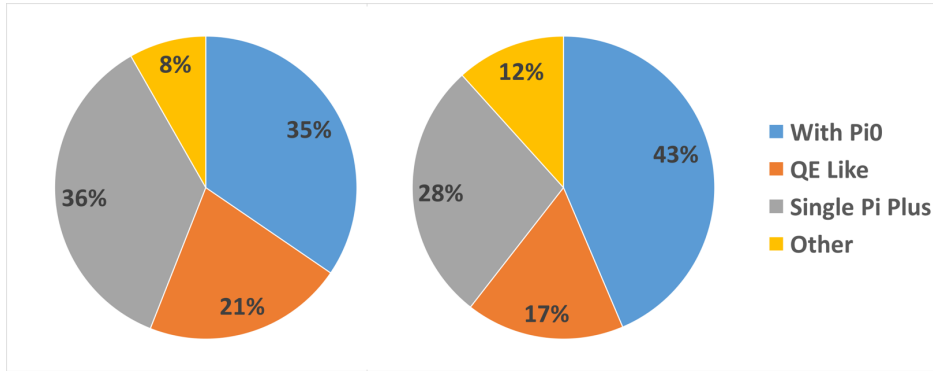


FIG. 6.6: Background percentages based on the three major background types for events with 1-Track (left) and 2+ Tracks (right). The leading background type in both 1-Track and 2+ Tracks consists of events with at least one π^0 .

6.2 Sideband fit and background constraints

Background classification based on the number of pions in the final state quantifies the relative contributions from many different interaction types. And classifying background events according to the number of neutral pions in the final state is useful for understanding the contribution of fake π^0 's in the final sample. However, neither of these classifications is appropriate for the sideband fit and background constraints. For the sideband fit and background constraints it is preferable to have similar size background groups, in order to reduce the statistical fluctuations during the sideband fit. The third method of classification described in Sec. 6.1, is the best choice for organizing the sideband fit due to the similar statistical sizes of the background categories.

After choosing the background event classification appropriately, four different

sidebands which have background rich distributions were identified. These sideband regions do not appear in the final sample; they are rejected by the event selections. For sideband fitting only the events in a specific sideband are kept.

Sideband selection is critical to obtain a reliable fit result. Ideally, each sideband should be dominated by a single background type, and the background statistics should be comparable in all sidebands. If, on the other hand, a single background type is dominant in all sidebands, the fit results will mostly depend on that specific background type and the overall background estimation may not be reliable.

In this analysis, four sidebands are used. The first sideband contains events tagged by the Michel tool as having an endpoint electron shower and is called the “Michel sideband”. This Michel sideband is enriched with events having a charged pion and also with events having a π^0 . The QE-like background events have very low statistics in the Michel sideband. The second sideband contains events having a low proton score and is called the “pID sideband”. Similar to the Michel sideband, the pID sideband is rich with events having a charged pion and events having a π^0 in the final sample. The QE-like events have very low statistics in this sideband also. The third sideband includes events having π^0 invariant mass less than 60 MeV and is called the “LowInvMass sideband”. This sideband has similar statistical contributions from each background type. The final sideband contains events having a π^0 invariant mass greater than 200 MeV and less than 500 MeV and is called the “HighInvMass sideband”. This sideband is mostly populated with events having a π^0 while the other background types have comparable statistical contributions.

The sideband fit procedure is performed on the π^0 invariant mass distribution. The π^0 invariant mass is chosen because it is one of the model-independent parameters in this analysis. The fit procedure tries to minimize the total χ^2 in all sidebands at once:

$$\chi^2 = \sum_{i=1}^{nBins} \frac{(Data_i - MC_i)^2}{Data_i}, \quad (6.1)$$

$$\chi_{Total}^2 = \chi_{Michel}^2 + \chi_{pID}^2 + \chi_{LowInvMass}^2 + \chi_{HighInvMass}^2. \quad (6.2)$$

The MC model has five different components and during the fit three of them can be varied to get the best fit result. Table 6.7 shows the MC model components and their utilization in the fit.

Event Type	Used in Fit?
Signal	No
Background: ChargedPion	Yes
Background: QELike	Yes
Background: WithPi0	Yes
Background: Other	No

TABLE 6.7: Event types of the MC components for the sideband fit.

The fit procedure varies the normalizations of the background categories to minimize the total χ^2 in all sidebands at once. During the fit, the χ^2 uses 50 bins for the Michel and pID sidebands, 30 bins for the High Invariant Mass sideband, and 6 bins for the Low Invariant Mass sideband. The total of 136 bins, each with good statistics enables an accurate fit result. Table 6.8 lists the total number of data events and simulation events in each sideband and Table 6.9 lists the number of background events in each side band. As indicated in Tables 6.8 and 6.9, the sideband with most statistics is the pID sideband, and the sideband with least statistics is the LowInvMass sideband.

Sideband	N(Data)	N(Simulation)
Michel	1803	1933.8
pID	3933	4145.0
Low Inv. Mass	1424	1701.9
High Inv. Mass	2309	2929.3

TABLE 6.8: Data and P.O.T. normalized simulation statistics for each sideband.

The fit performance as indicated by the total χ^2 and χ^2/dof , is given in Table 6.10. The degrees of freedom (dof) is defined as the number of bins minus the number of variables used in the fit. For 136 bins and 3 fit parameters, the degrees of freedom (dof) is 133. The fit category weights and their uncertainties for each background

Sideband	N(ChargedPion)	N(QELike)	N(WithPi0)
Michel	4738.5	540.8	5302.0
pID	8500.0	2091.9	10591.8
Low Inv. Mass	3227.4	3831.6	1556.6
High Inv. Mass	3194.3	5225.9	5484.8

TABLE 6.9: Statistics for background types for each sideband.

type are given in Table 6.11. The events in a specific background category are weighted, according to the fit results, by the amount given in the Table. The fit uncertainties are propagated as a systematic error on the cross-section calculations. Details are discussed in Sec. 8.

	χ^2	χ^2/dof
Before Fit	660.75	4.97
After Fit	217.91	1.64

TABLE 6.10: Fit performance represented as the total χ^2 and χ^2/dof .

	New Weight	Uncertainty on Weight
ChargedPion	1.05	0.06
QELike	0.47	0.05
WithPi0	0.83	0.05

TABLE 6.11: Background weights and their uncertainties, according to the sideband fit.

The π^0 invariant mass distribution for the data compared to the GENIE MC prediction before and after the sideband fitting is shown in Fig. 6.7. The π^0 invariant mass distribution χ^2/dof is improved from 9.05 to 1.84 by constraining the background types with the new weights found by the fit. The π^0 invariant mass distributions for data compared to GENIE MC prediction in the Michel and pID sidebands before and after the fit are given in Figs. 6.8 and 6.9. The χ^2/dof is improved for the Michel sideband from 1.61 to 1.28, and for the pID sideband from 1.59 to 1.20. The LowInvMass and HighInvMass sidebands are visible on the π^0 invariant mass distributions in Fig. 6.7 as they are the outside regions that border the signal region defined by the black lines.

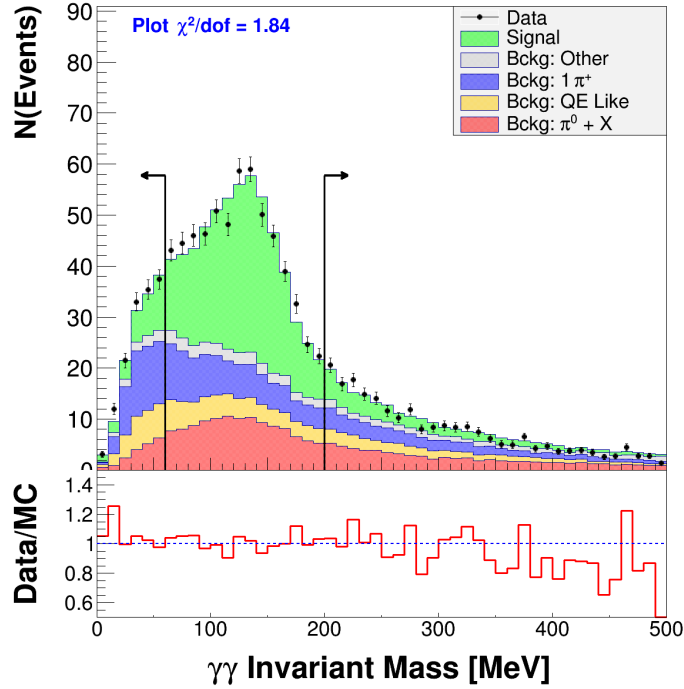
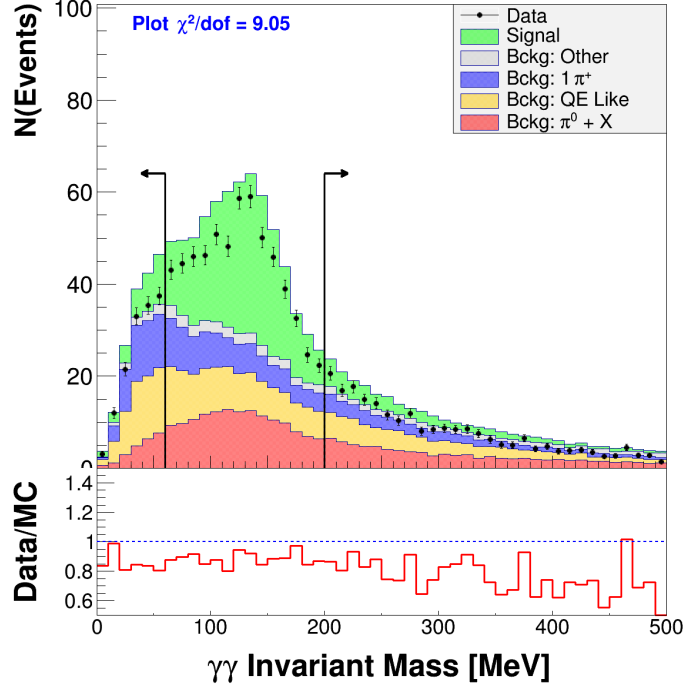


FIG. 6.7: Data and MC $\gamma\gamma$ invariant mass distributions before (top) and after (bottom) the side band fit. The LowInvMass sideband is the region to the left of the leftmost black line at 60 MeV. The HighInvMass sideband is the region to the right of the rightmost black line, at 200 MeV. The plot χ^2/dof changes from 9.05 to 1.84 after applying the fit results to the MC background model.

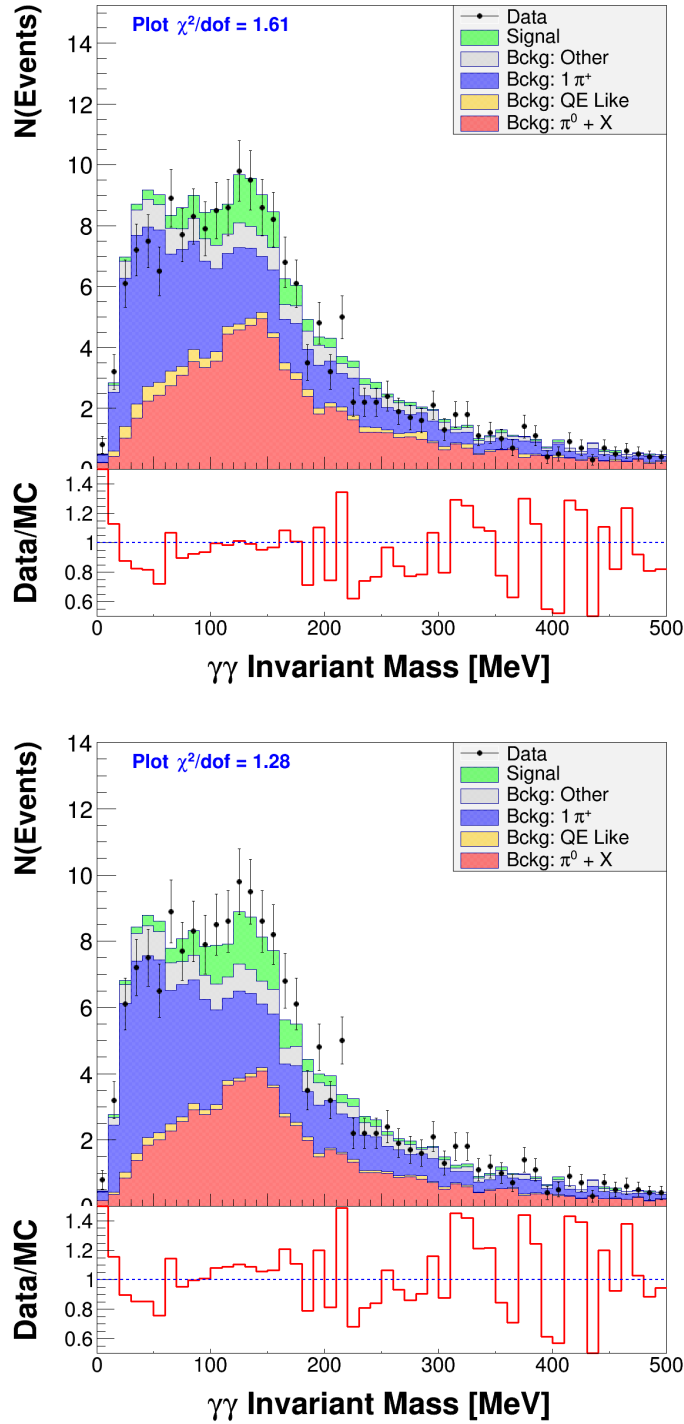


FIG. 6.8: Data and MC $\gamma\gamma$ invariant mass distributions before (top) and after (bottom) the side band fit in the Michel sideband. In the Michel sideband the QE-like events (yellow) have very small statistics compared to other two background types. Plot χ^2/dof improves after applying the fit results to the MC background model.

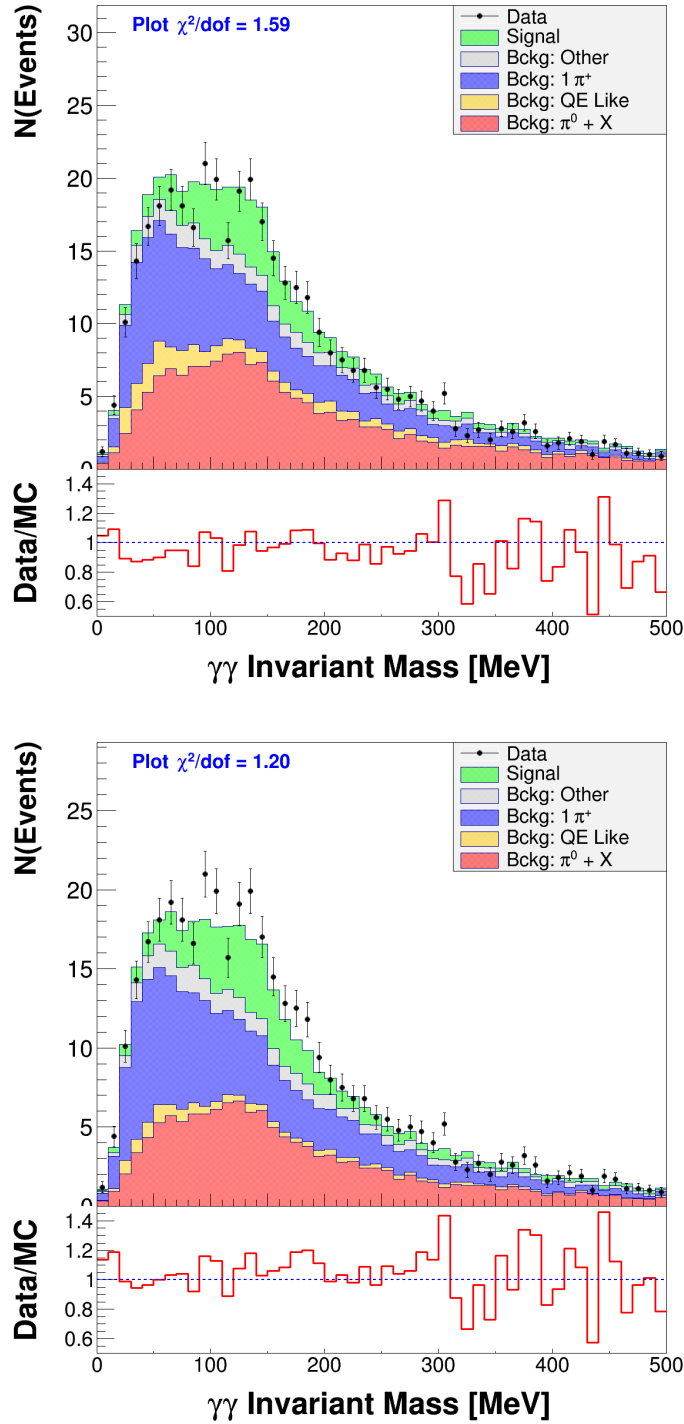


FIG. 6.9: Data and MC $\gamma\gamma$ invariant mass distributions before (top) and after (bottom) the side band fit in the pID sideband. In the pID sideband the QE-like events (yellow) have very small statistics compared to the other two background types. Plot χ^2/dof improves after applying the fit results to the MC background model.

Chapter 7

Determination of Differential Cross Sections of the Signal Channel

7.1 Differential cross-section calculation

In this Chapter the differential cross section ($\frac{d\sigma}{dX}$) is calculated for muon momentum and muon production angle; for pion momentum, kinetic energy and production angle; and for the four-momentum transfer squared. Also the cross section versus neutrino energy is calculated. The total cross section is calculated by integrating the differential cross section over neutrino energy. In general, the differential cross section for a variable X is calculated bin-by-bin in the data using the following equation:

$$\left(\frac{d\sigma}{dX}\right)_i = \frac{1}{\Phi_\nu T_n} \frac{1}{(\Delta X)_i} \frac{\sum_j U_{ij} (N_j^{data} - N_j^{bckg})}{\epsilon_i} \quad (7.1)$$

where the definition of each parameter is given in Table 7.1.

Parameter	Definition
X	Cross-section variable
Φ_ν	Integrated neutrino flux over [1.5, 20] GeV
T_n	Number of target nucleons inside the fiducial volume
ΔX	Bin width
$N_j^{data} - N_j^{bckg}$	Background subtraction
$\sum_j U_{ij}()$	Unfolding
ϵ_i	Signal event reconstruction efficiency

TABLE 7.1: Summary of variables used in the differential cross-section calculation.

Getting the background-subtracted event distribution is the first step in the calculation. The signal and background distributions in the simulation play a critical role in this stage. The predictions from the simulation are used to estimate background distributions in the data set. The second step, called “unfolding”, corrects the reconstructed quantities to the true quantities. This correction is applied to remove differences between measured and true quantities due to detector effects. The details of the unfolding method and how it works are described in Sec. 7.3. Efficiency corrections are then applied to the cross-section calculation. At the efficiency correction stage, the cross-section calculation is corrected by the ratio of reconstructed signal events to all signal events. Details of the efficiency correction stage are discussed in

Sec. 7.4. As the final step, the cross-section calculation is normalized using the integrated flux over the signal region, together with the number of nucleons inside the fiducial volume and the bin width. Normalizations for the cross-section calculation are given in Sec. 7.5.

7.2 Background subtraction

A single data event cannot be identified as a signal or a background event, consequently a background subtraction method is used to identify the signal distribution in the complete data set. First, the number of background events in the data set is estimated. For this purpose, data and POT-normalized MC distributions for the π^0 invariant mass are used. Figure 7.1 shows the data versus the simulation for the π^0 invariant mass distributions. The simulation is divided into two categories according to event type. The integral of the signal distribution for the simulation inside the signal region corresponds to the estimated number of signal events in the data. Similarly, the integral of the background distribution of the simulation inside the signal region gives the number of estimated background events in the data. The signal region in π^0 invariant mass, is defined as $60 \text{ MeV} < m_{\gamma\gamma} < 200 \text{ MeV}$. The number of estimated signal and background events in the data are given in Table 7.2.

	N(Events)	Percentage
All Events	6110	100.0%
Estimated Signal Events	3113	49.1%
Estimated Background Events	2997	50.9%

TABLE 7.2: Number of estimated signal and background events in data.

The shape of the background distribution in the cross-section variable now needs to be estimated. The shape of the background distribution from the simulation is used for this purpose. As an illustrative example, the muon momentum distribution of the data is compared to the reference simulation is shown in Fig. 7.2.

The shape of the background is obtained by normalizing the background distri-

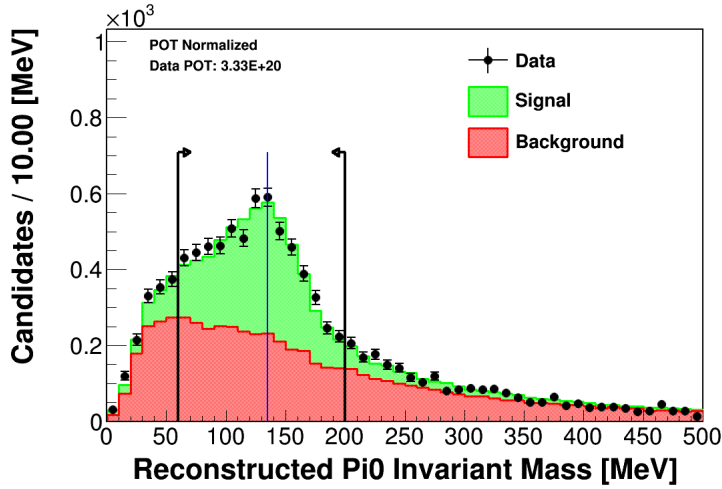


FIG. 7.1: Data and POT-normalized MC distributions for the π^0 invariant mass. The simulation is broken out by event type as signal and background (upper, lower distributions respectively). For the background estimation in the data, the events inside the signal region are used.

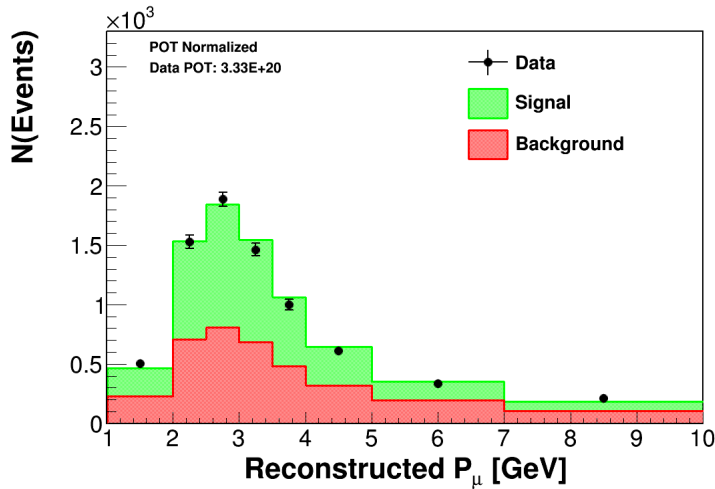


FIG. 7.2: Data (solid circles) and POT-normalized MC distributions(histograms) for muon momentum. The simulation is shown separated into signal and background events.

bution in the simulation. Then the estimated background distribution is obtained by scaling the normalized background distribution in the simulation by the estimated amount of background in the data. Finally, by subtracting the estimated background distribution from the whole data distribution, the background-subtracted data is obtained. Figure 7.3 shows the estimated background and background-subtracted

distributions for muon momentum for the data and the simulation.

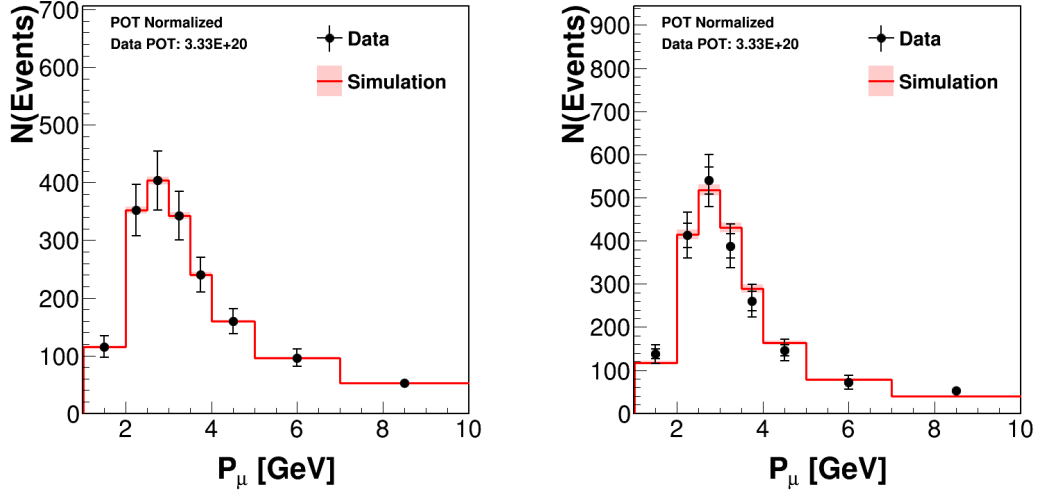


FIG. 7.3: Background-subtracted distributions of muon momentum for the data and the simulation. The plot on the left shows the estimated background distributions, the estimated background for data and simulation is exactly the same because in both cases the prediction is based on the simulation. The plot on the right shows the background-subtracted distributions in data (solid points) and in the MC (histogram), the background-subtracted distributions agree everywhere to within 1σ of the statistical plus systematic error on the data.

7.3 Unfolding

Unfolding is a method that is used to correct the measured quantities to the true quantities estimated by the simulation. This correction is applied to remove the detector resolution and reconstruction effects. For example, a measured muon momentum value may be shifted to a neighboring bin due to limited detector resolution or to a reconstruction problem. The unfolding method is designed to correct this shift by moving the event to the correct bin.

The unfolding correction is done by defining a migration matrix (U) that relates reconstructed quantities to true quantities. For the variables that are measured with good resolution, the migration matrix is nearly diagonal. The off-diagonal elements of a migration matrix are larger with a poor resolution. The migration matrices for muon momentum and muon production angle given in Fig. 7.4 are nearly diagonal

since the resolutions for muon momentum and muon angle angle have relatively small widths. The pion momentum and kinetic energy migration matrices given in Fig. 7.5 have large off-diagonal elements due to poor resolution. However, the pion angle is measured with a good resolution and has a nearly diagonal migration matrix as shown in Fig. 7.6. The migration matrices for Q^2 and neutrino energy are given in Fig. 7.7. Migration matrices for these event kinematic variables have a diagonal shape, however the neighboring off-diagonal bins are populated more than the corresponding bins for the muon variables.

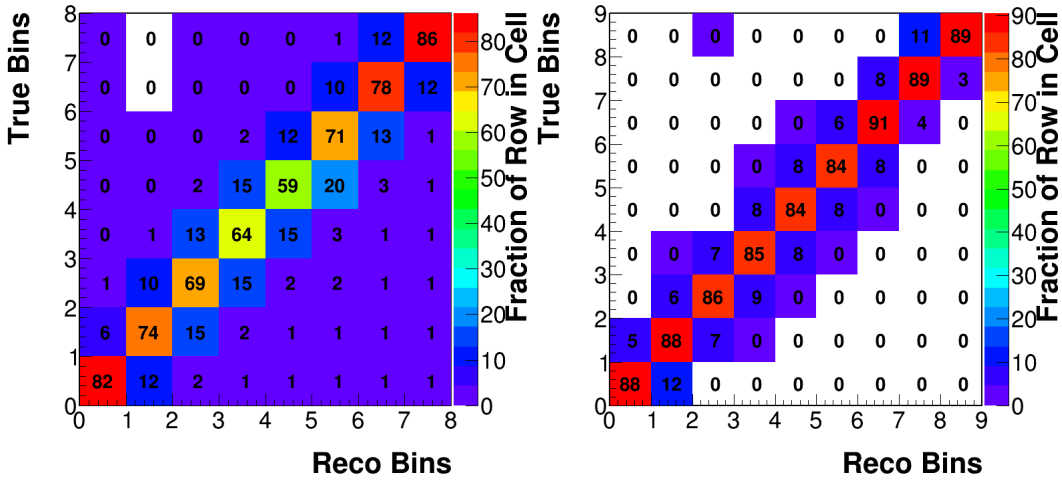


FIG. 7.4: Migration matrices for muon momentum (left) and production angle (right). The diagonal structure of the migration matrices reflects good resolutions for muon momentum and muon production angle.

An iterative unfolding method is used that is based on Bayes' theorem [71]. In statistics, Bayes' theorem provides the conditional probability of an event occurring based on an initial knowledge of conditions related to the event. An iterative algorithm using Bayes' theorem updates the initial conditions after each step and calculates the probability again with improved initial knowledge. In the analysis, the migration matrices are used as the initial probabilities, and distributions are unfolded iteratively.

The number of iterations for each variable is determined by calculating the average difference between $N(\text{Iterations})$ and $N(\text{Iterations}+1)$ using every bin. The number of iterations for each cross-section variable is given in Table 7.3. In addition to

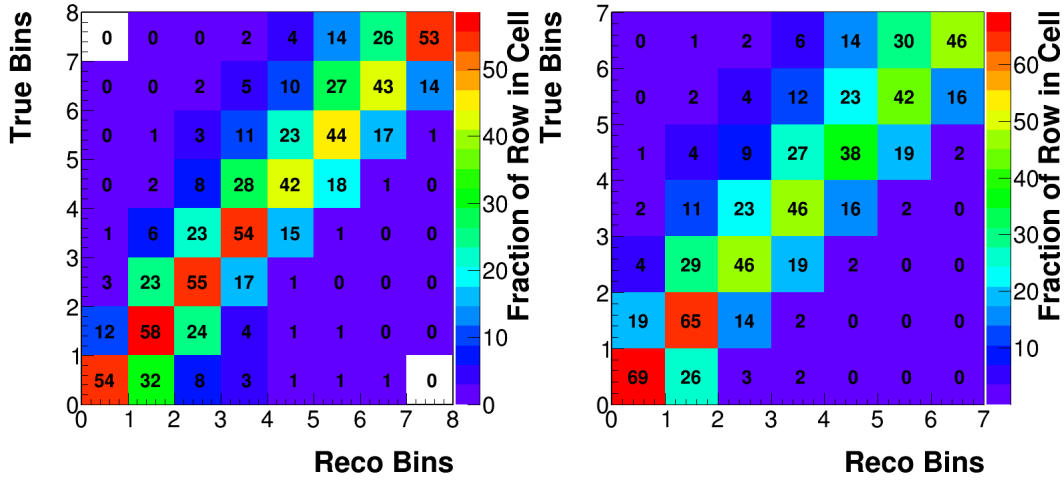


FIG. 7.5: Migration matrix for pion momentum (left) and kinetic energy (right). Off-diagonal bins in the pion momentum and kinetic energy are larger than for the muon variables. The same behavior is observed in the fractional error plots. The full width at half maximum (FWHM) of the pion momentum fraction error is 0.5, while FWHM of the muon momentum fraction error is 0.10. Both results indicate that the resolution for the pion momentum is not as good as for the muon.

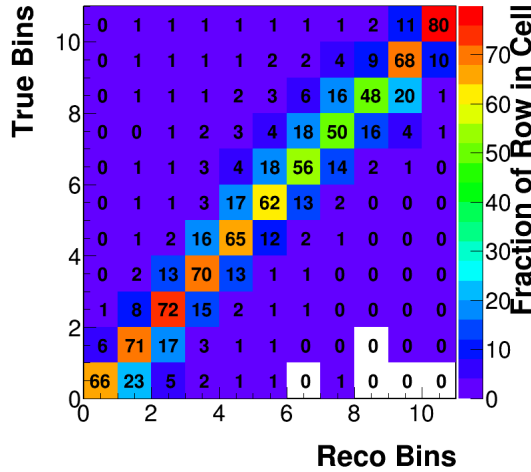


FIG. 7.6: Migration matrix for the pion production angle.

the average difference, the change in fractional residual $((N_{unfolding} - N_{true})/N_{true})$, the change in pull $((N_{unfolding} - N_{true})/\sigma_{stat})$, and the change in statistical and systematic errors in each bin after each iteration are examined. Figure 7.8 shows the unfolding-study plots for each bin after each iteration for muon momentum. As seen from the Figure, each bin behaves similarly after each iteration. Figure 7.9 shows

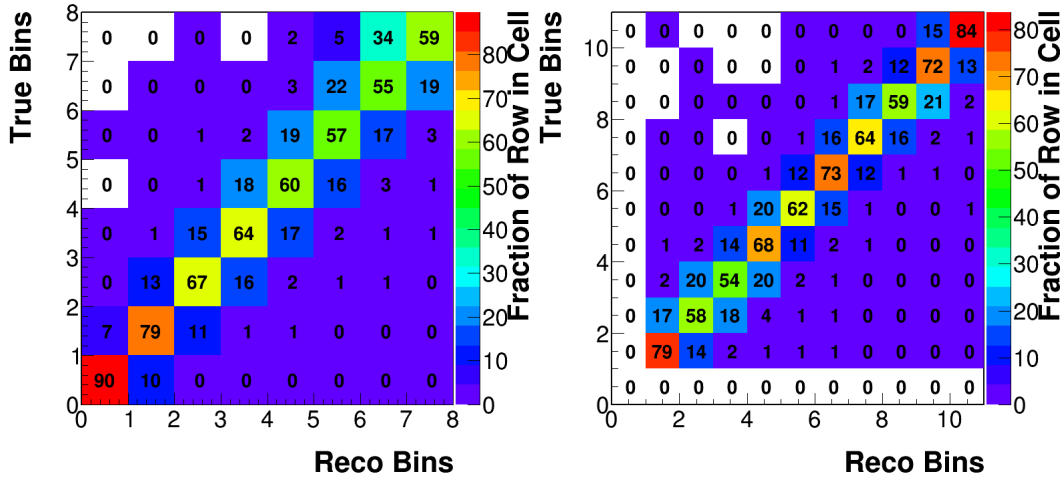


FIG. 7.7: Migration matrices for Q^2 (left) and neutrino energy (right).

the totals for the unfolding-study plots. As seen from the plots, the change in totals becomes smaller for the total fractional residual and the total pull after the first iteration. For muon momentum the average change is less than 1% after the second iteration, consequently the muon momentum is unfolded two times. For comparison the unfolding study plots for pion momentum are shown in Fig. 7.10. In the pion momentum case, the variables do not converge to a steady value as quickly as the muon momentum. The totals for the pion momentum unfolding study plots are shown in Fig. 7.11, the total fractional residual and the pull variables stabilize after the fifth iteration in the pion momentum, whereas, the stabilization in the muon momentum unfolding study variables is observed after the second iteration. For pion momentum the average change is less than 1% after the fifth iteration. Unfolding studies were applied to all cross-section variables, however only the muon momentum and pion momentum results are presented here. The unfolded distributions for the data and the simulation of muon momentum and pion momentum are shown in Fig. 7.12.

Variable	N(Iterations)
Muon Momentum	2
Muon Angle	1
Pion Momentum	5
Pion Kinetic Energy	4
Pion Angle	4
Q^2	4
Neutrino Energy	4

TABLE 7.3: Number of unfolding iterations for each cross-section variable.

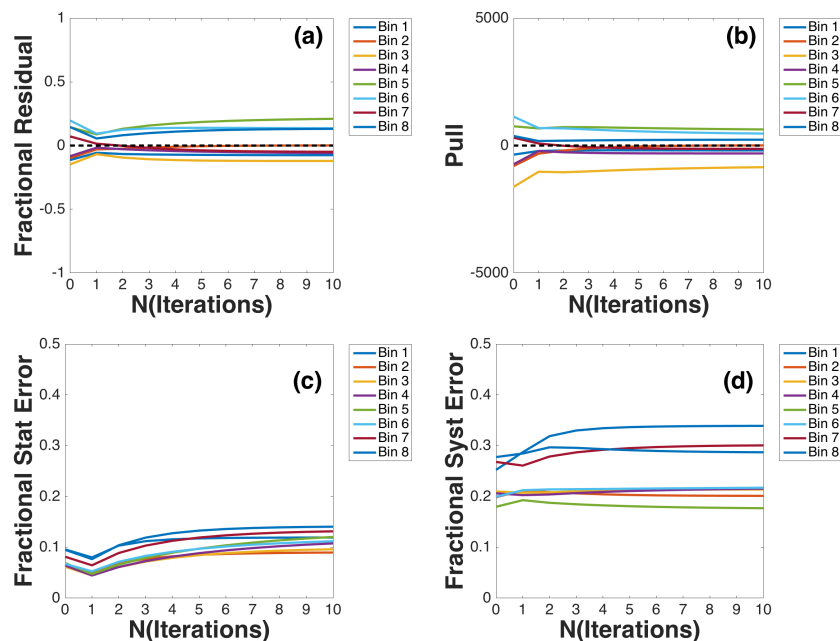


FIG. 7.8: Unfolding study plots for muon momentum for each bin after each iteration. Plot (a) is the fractional residual, plot (b) is the pull, plots (c) and (d) are the statistical and systematic errors. The unfolding procedure affects each bin in the same way.

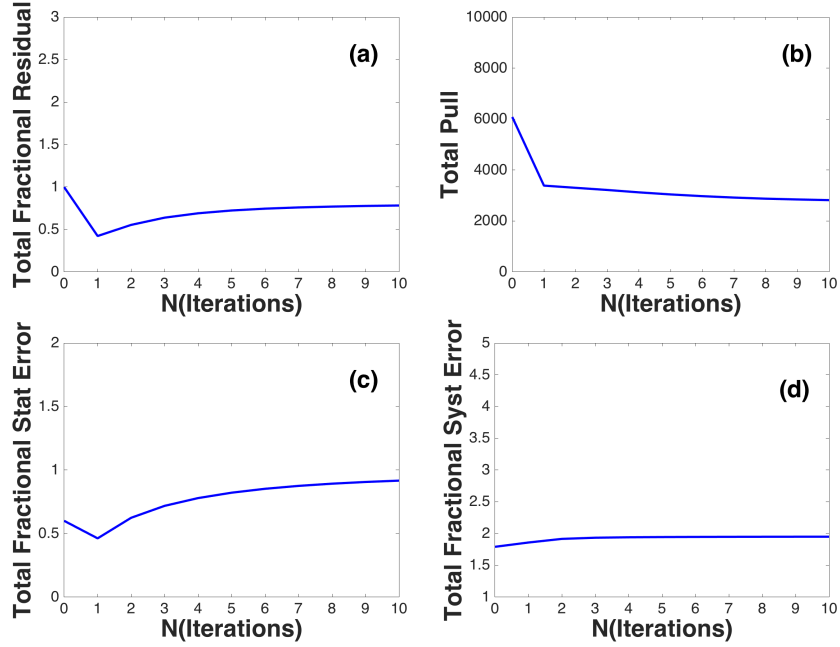


FIG. 7.9: Total unfolding study plots for muon momentum after each iteration. Totals are calculated by summing up all bins. All plots minimize in the first iteration and then slightly increases after each iteration. Unfolding uncertainty is calculated to be less than 1% for $N(\text{Iterations}) = 2$.

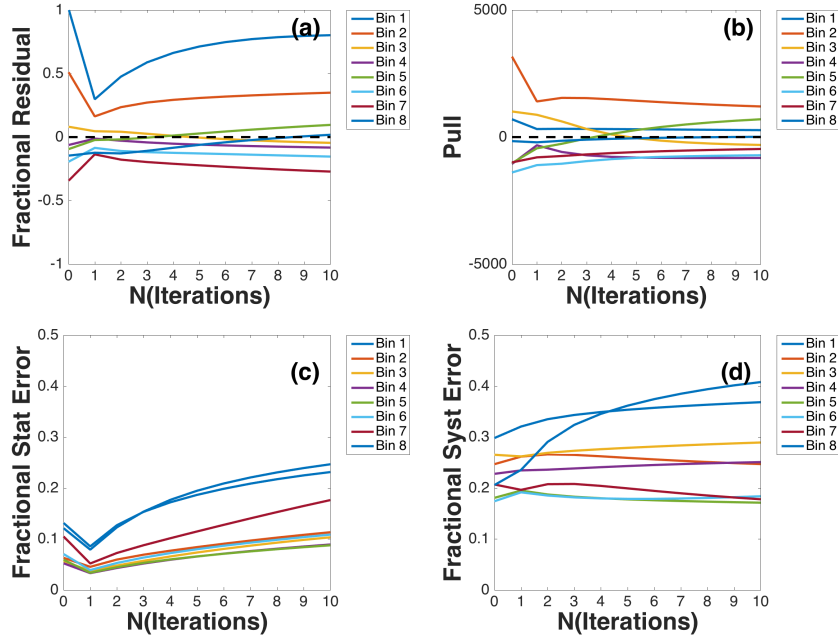


FIG. 7.10: Unfolding study plots for π^0 momentum for each bin after each iteration. Plot (a) is the fractional residual, plot (b) is the pull, plots (c) and (d) are the statistical and systematic errors. The pull variable is minimized in each bin after 4-5 iterations.

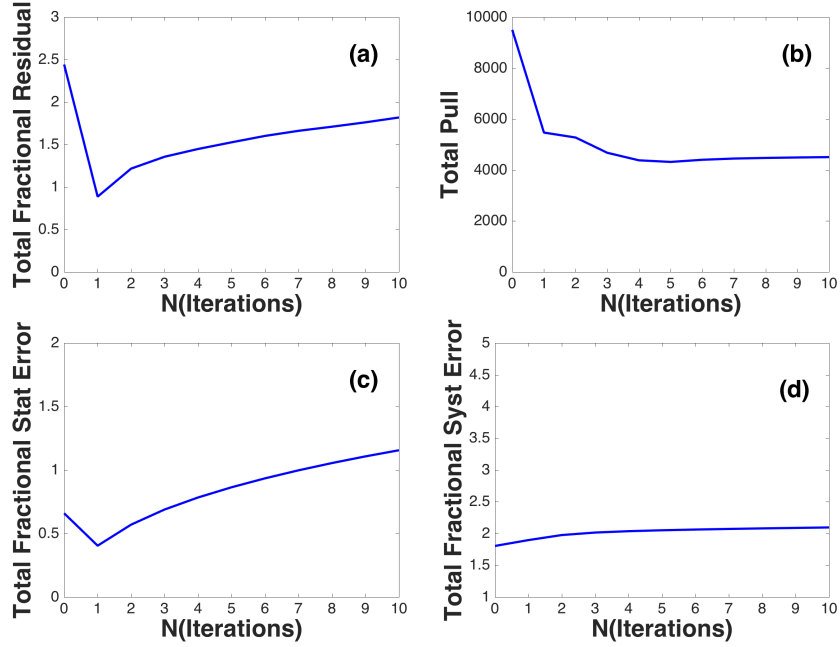


FIG. 7.11: Total unfolding study plots for π^0 momentum after each iteration. Totals are calculated by summing up all bins. For the π^0 momentum the total change becomes less than 1% after the fifth iteration.

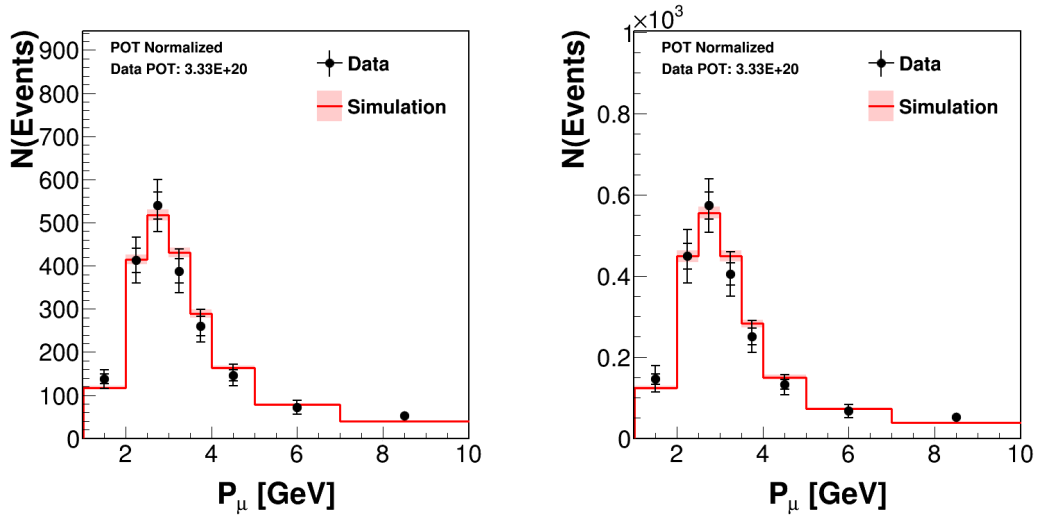


FIG. 7.12: Muon momentum distributions before (left) and after (right) unfolding. The shape of the muon momentum distribution almost does not change after the unfolding procedure due to the mostly diagonal migration matrix.

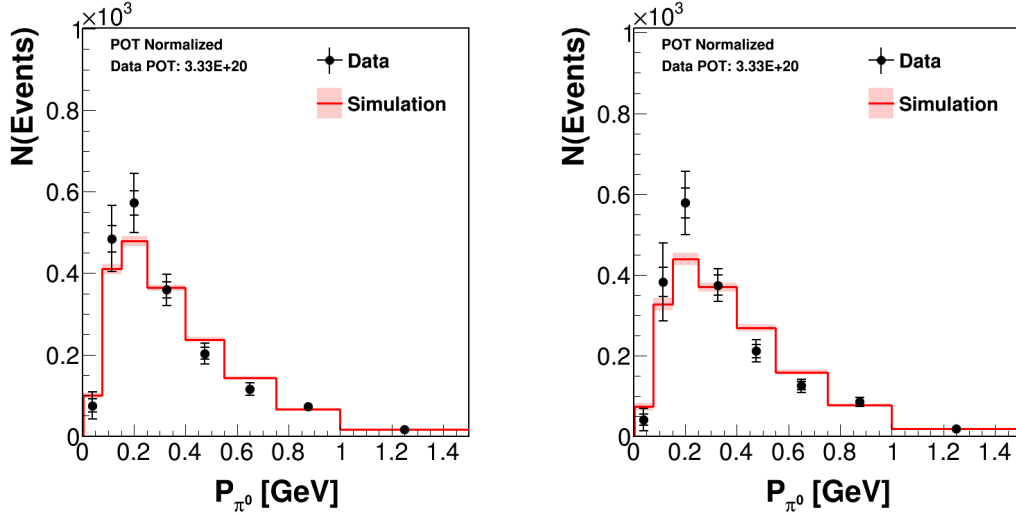


FIG. 7.13: Pion momentum distributions before (left) and after (right) unfolding. The shape of the pion momentum distribution slightly changes after the unfolding procedure. The unfolding procedure improves the measured pion momentum using the reference simulation.

7.4 Efficiency correction

The reconstruction efficiency for signal events is 8.4% in this analysis. Therefore, an efficiency correction is applied to the cross-section calculation, in order to have the distributions for 100% of the signal events. For the efficiency correction, two true signal distributions as estimated by the reference simulation are used for the cross-section variable. The first distribution is the true distribution for the reconstructed signal events and the second one is the true distribution for all the signal events. The true distribution for muon momentum is given in Fig. 7.14. As seen from the true distribution, the largest difference is in the low muon momentum bins. This difference is due to the acceptance of muon tracks. A muon track is used only if the track matches with the MINOS near detector; this criterion requires that the muon have at least 1.5 GeV momentum. The efficiency correction curve is calculated by dividing these two distributions. For example, the efficiency curve for muon momentum given in Fig. 7.15, is calculated by dividing the true distribution of reconstructed signal events to the true distribution of all signal events. The efficiency-

corrected distributions of data and simulation for muon momentum is given in Fig. 7.16.

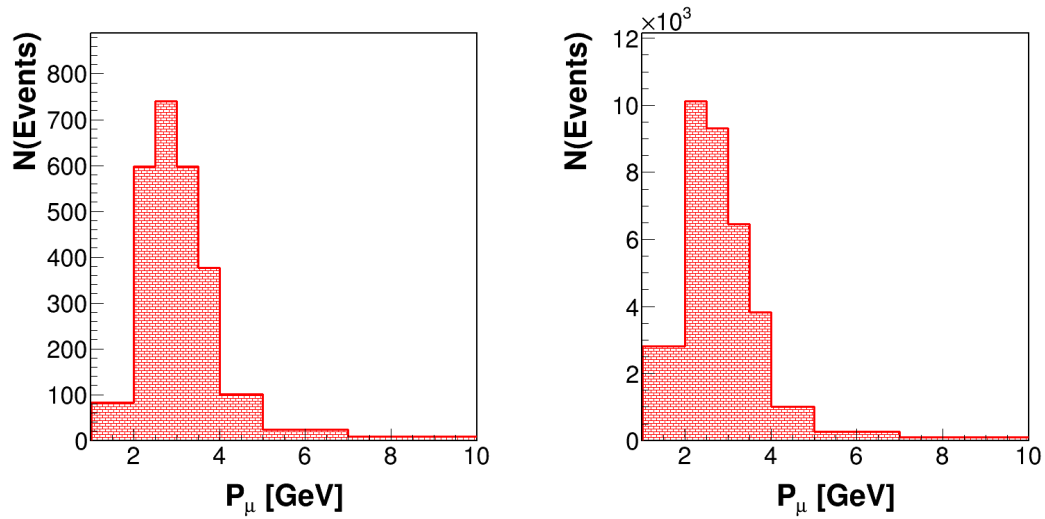


FIG. 7.14: True muon momentum distributions for signal events. The left plot is the distribution for reconstructed signal events. The right plot is the distribution for all signal events. The efficiency correction is determined by taking the ratio of reconstructed events to all signal events.

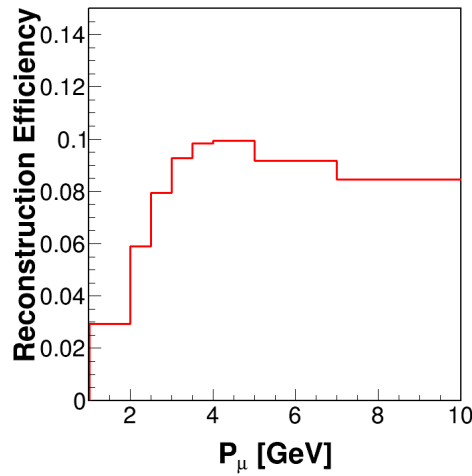


FIG. 7.15: Efficiency curve for muon momentum. The efficiency is low in the lower momentum bins due to the limited muon track acceptance in the MINOS near detector. Higher momentum bins have a roughly constant efficiency approaching 10%.

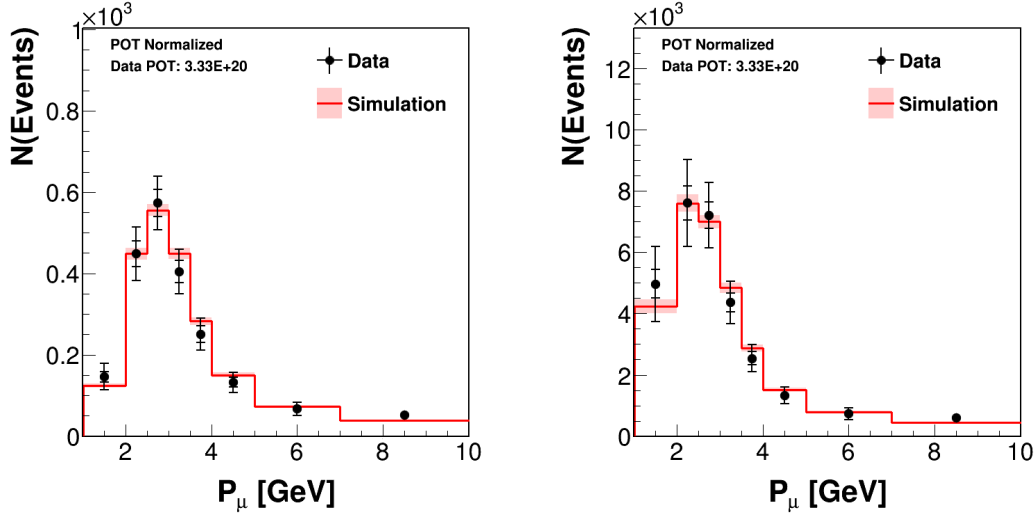


FIG. 7.16: Muon momentum distributions before (left) and after (right) the efficiency-correction. After the efficiency correction an increase in the low momentum bins is observed. The efficiency correction stage removes the detector acceptance effects from the distribution.

7.5 Flux, target number and bin width normalizations

The final step in the calculation of the cross section is the application of normalization factors. These factors appear in the denominator of Eq. (7.1) and they refer to the flux normalization, the target number normalization, and the bin width normalization.

Calculation of the differential cross section requires the integrated flux (Φ_ν) for the incoming neutrinos for the energy range 1.5 - 20 GeV. The calculation of cross section versus neutrino energy uses the flux in each E_ν bin. The flux distribution is rebinned in order to match the binning of the neutrino energy measurement. Figure 7.17 shows the flux distribution used in this analysis. The flux distribution peaks at 3.5 GeV and by 5 GeV, the flux drops to 13% of the peak. On the other hand, the CC-inclusive cross section rises linearly with energy, so that flux times cross section gives a broader distribution.

The cross-section results of this Thesis are reported per nucleon. Consequently, the cross-section calculation includes division by the number of nucleons inside the fiducial volume (T_n). The number of nucleons inside the fiducial volume is 3.17×10^{30} .

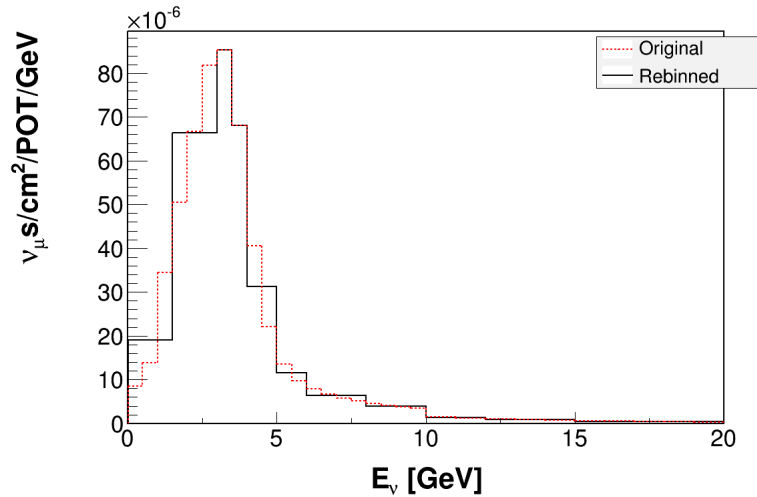


FIG. 7.17: The neutrino flux distribution used in this analysis. The flux curve is rebinned for the differential cross-section calculation to match the binning of the neutrino energy measurement.

For a differential cross-section calculation, each bin is divided by its bin width (ΔX) to express the result in the appropriate units (per GeV, per degree, etc...).

The differential cross section for the muon momentum after all normalizations is shown in Fig. 7.18.

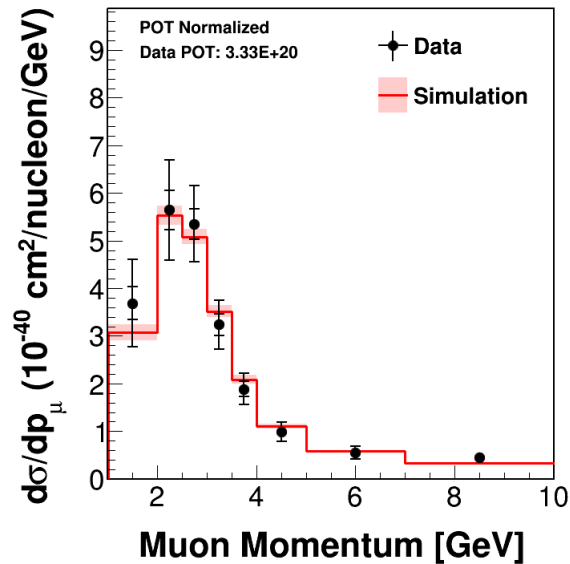


FIG. 7.18: Differential cross section of the signal channel for muon momentum. The data and simulation distributions agree everywhere to within 1σ of the statistical plus systematic error on the data.

7.6 Closure Tests

A closure test is a method to validate the data modification steps during cross-section calculations. In a closure test, MC events are used as mock data in the data modification steps, and after each step the modified mock data is compared with the truth values.

The first closure test is applied to the background estimation stage. An MC sample is used as mock data to estimate the background. Then this estimated background is compared to the true background distribution of the MC sample used. A second closure test is applied to the background subtraction stage. Again, an MC sample is used as mock data for the background subtraction and the result is compared with the true signal distribution of the MC. A third closure test is applied to the unfolding step. An MC sample is used as mock data, it is unfolded, and the result is compared to the truth distribution of selected signal events. The final closure test is applied to the efficiency correction step. An MC sample is used as mock data, it is efficiency-corrected, and the result is compared to the truth distribution of the all signal events.

All of the variables that have a reported cross section in this Thesis have been subjected to closure tests. In this section closure test plots for the muon momentum are given only as examples. These are shown in Fig. 7.19. The ratio between the mock data and the simulation is equal to one in all closure tests.

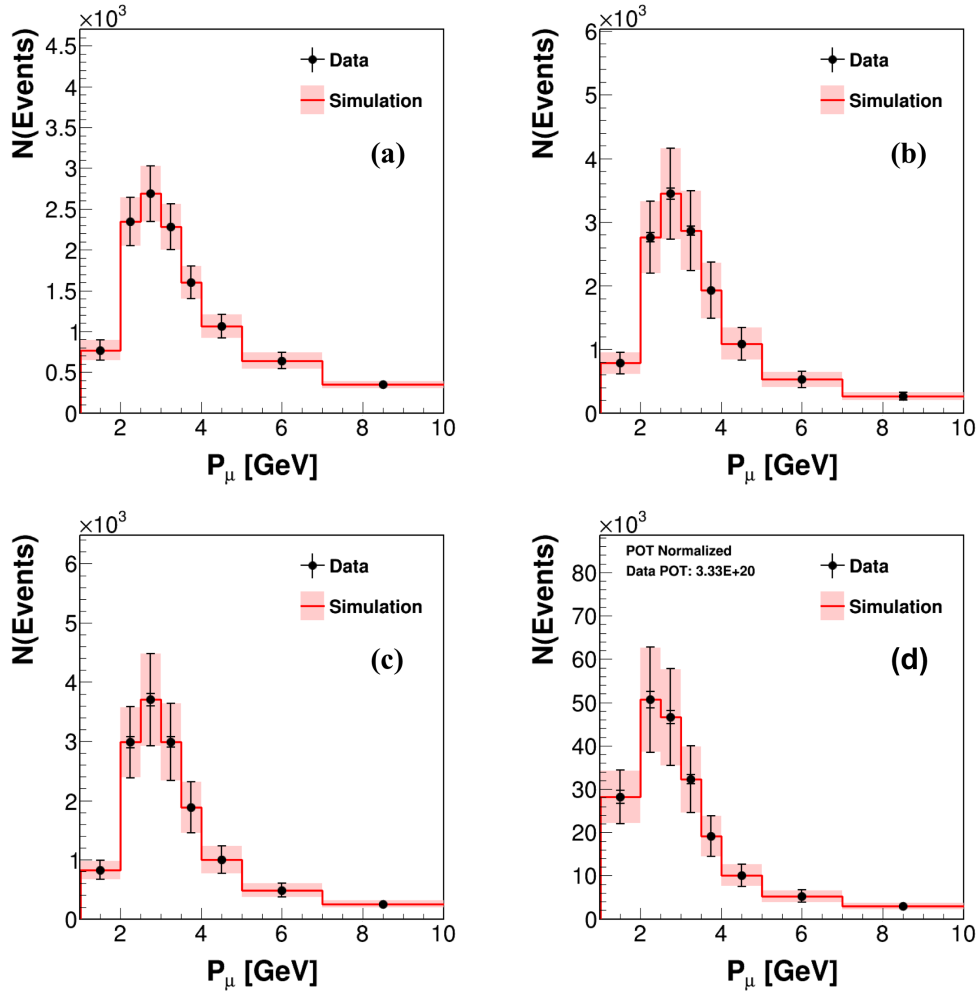


FIG. 7.19: Muon momentum closure test plots for background estimation (a), background subtraction (b), unfolding (c), and efficiency correction (d). The ratio between the mock data and the simulation is equal to one in all closure tests.

Chapter 8

Systematic Uncertainties

The cross-section measurements reported in this Thesis are sensitive to many different estimations such as the incoming neutrino flux, the neutrino simulation model, and the detector energy response. The parameters that characterize these estimations are not precisely known; each parameter has its own uncertainty. For example, the neutrino simulation model used in this analysis uses a resonant axial mass value (M_A^{RES}) that is set to 1.12 GeV with a 20% uncertainty. The simulation prediction for a measured cross section is calculated using the central value of $M_A^{RES} = 1.12$ GeV and the measurement must take into account a systematic error coming from the M_A^{RES} uncertainty. In this analysis, all the systematic errors are included using an “alternate universe” method. For instance, in a hypothetical universe, the entire analysis is repeated with a $M_A^{RES} = 1.34$ GeV (+20%) while the other parameters are kept constant. Then, the difference between the results are included as a systematic error. This alternate universe method is repeated for all other parameters that have an uncertainty.

The systematic uncertainties of this analysis are categorized into five groups. The first group contains the detector response uncertainties such as particle energy scales, particle tracking and detector mass uncertainties. The second group is populated by neutrino interaction model uncertainties, such as the M_A^{RES} uncertainty or the uncertainty associated with the strength of non-resonant single pion production. The third group contains the uncertainties for the simulated final state interactions (FSI). Examples for this group are the uncertainty on the pion charge exchange probability and on pion absorption probability inside the nucleus. The fourth group includes the uncertainties related with the incoming neutrino flux. The fifth group includes other uncertainties that do not fall in the categories describing the other groups. An example of a group-5 systematic is the uncertainty inherent to the unfolding procedure.

8.1 Detector response uncertainties

Detector response uncertainties include the uncertainties associated with the tracking and energy estimation for each final-state particle and with the secondary particle responses and the detector mass as well. Each source of systematic uncertainty in this group is explained below.

Muon momentum uncertainty

Muon momentum is measured by range and curvature using the MINOS near detector and the uncertainty has been estimated as $\pm 2\%$ by the MINOS collaboration [72].

Muon angle uncertainty

The uncertainty of the muon angle is estimated by fitting the muon track inside the MINERvA detector twice. The first fit is done from vertex to the mid-point of the muon track and the second fit is done from the mid-point to the end point of the track. Both fits provide an angle for the track, and the difference between the fit results are taken as the angle uncertainty. The angle uncertainty for the muon track was determined to be 2 mrad [55].

Muon tracking uncertainty

Muon tracking efficiency and uncertainty for the MINERvA detector and for the MINOS near detector are estimated based upon a study of events having a single track that exits from the last plane of the MINERvA detector. This study analyzed the fraction of the events having a muon track inside MINERvA to the events having a reconstructed track inside the MINOS near detector. The study analyzed the events in two samples: Low Momentum ($P_\mu < 3.0$) GeV and High Momentum ($P_\mu \geq 3.0$) GeV. Table 8.1 lists the efficiency and uncertainty obtained for each data set used in this analysis. The efficiencies are slightly lower and uncertainties slightly higher for the low momentum sample.

Data Run Period	Momentum Range	Efficiency	Uncertainty
03/22/2010 - 07/12/2010	$P_\mu < 3.0$ GeV	96.3%	0.3%
	$P_\mu \geq 3.0$ GeV	99.0%	0.1%
05/02/2011 - 05/13/2011	$P_\mu < 3.0$ GeV	97.5%	0.9%
	$P_\mu \geq 3.0$ GeV	99.5%	0.2%
06/22/2011 - 07/01/2011	$P_\mu < 3.0$ GeV	97.2%	0.6%
	$P_\mu \geq 3.0$ GeV	99.6%	0.2%
09/30/2011 - 04/30/2012	$P_\mu < 3.0$ GeV	97.1%	0.4%
	$P_\mu \geq 3.0$ GeV	99.4%	0.1%

TABLE 8.1: Muon tracking efficiency and uncertainties. From Ref. [73].

Proton tracking uncertainty

The proton tracking efficiency and uncertainty are estimated using test beam data. Data events were analyzed in two different groups according to the event topology. The first group provided efficiency and uncertainty determinations for pion production analyses; while the second group provided these determinations for QE-like analyses. Since this analysis has a topology that is similar to QE-like events; the results for the QE-like proton tracking uncertainty are used. Efficiency and uncertainty values are reported for two different cases depending on the number of planes traversed by the proton. Results of the study are summarized in Table 8.2. Uncertainties are applied according to the number of planes traversed by the proton.

Event Type	N(Planes) Traversed	Efficiency	Uncertainty
Charged Pion Production	$nPlanes < 8$	91.1%	5.5%
	$nPlanes \geq 8$	98.8%	0.7%
QE-like	$nPlanes < 8$	93.5%	4.6%
	$nPlanes \geq 8$	99.2%	0.3%

TABLE 8.2: Proton tracking efficiencies and uncertainties. In this analysis the uncertainty for the QE-like events are used. The uncertainty is higher for charged pion production analyses due to the greater vertex activity caused by additional charged pion tracks. From Ref. [74].

Proton energy uncertainties

Proton energy uncertainties are related to the total proton energy and dE/dx profile of the proton track. The uncertainties in this category are important because the

dE/dx profile of the track is used to determine whether the track is a proton or a charged pion. There are four different uncertainties associated with the dE/dx profile of the proton track.

- **Bethe-Bloch calculation uncertainty:** The Bethe-Bloch equation (Eq. (5.1)) is used to calculate the average energy loss of a particle in the MINERvA detector. Based on a study by T. Walton that compared the muon energy loss in the detector with the muon-energy range tables [75], the Bethe-Bloch calculation uncertainty is estimated to be 1% for pure materials and 3% for compounds [58, 76].
- **Detector mass model uncertainty:** The average energy loss of a particle depends on the distance in the material that the particle traverses. Estimated uncertainties of the material thicknesses inside the MINERvA detector’s tracking region are given in Table 8.3.

Plastic Scintillator	Iron	Lead
1.4%	0.5%	1.3%

TABLE 8.3: Estimated uncertainty of the material thickness inside the MINERvA detector’s tracking region. From Ref. [77].

- **Muon equivalent unit uncertainty:** The well understood muon energy loss in the active scintillators are used in MINERvA analyses as the absolute energy scale constant. The muon equivalent unit (MEU) is the factor that is used to convert number of photoelectrons in a single plane to an energy value. The uncertainty of the MEU constant is estimated to be 2.4% [35, 78].
- **Birks’ law quenching parameter uncertainty:** Birks’ law [79] is a formula given in Eq. (8.1). It estimates the light yield per path length as a function of the energy loss per path length for a particle traversing a scintillator. The GEANT4 simulation uses a Birks’ quenching parameter $k_B = 0.133$ mm/MeV, and a test beam study performed on stopping protons measured $k_B = 0.0905 \pm$

0.014 mm/MeV. The difference between the data and simulation is taken as the systematic uncertainty.

$$\frac{dS}{dx} = A \frac{\frac{dE}{dx}}{1 + k_B \frac{dE}{dx}} \quad (8.1)$$

where S is the light yield, A is the scintillation efficiency, dE/dx is the energy loss of the particle per unit path length and k_B is the Birks' quenching parameter (Birks' constant).

Electromagnetic energy scale uncertainty

The invariant mass of two EM showers is studied in the data and in the MC separately; the distributions are shown in Fig 8.1. These distributions are fitted to a double gaussian in the $0 \text{ MeV} < m_{\gamma\gamma} < 280 \text{ MeV}$ range. The peak position for the fitted data distribution is $137.8 \pm 2.6 \text{ MeV}$, while the peak position for the fitted MC distribution is $130.3 \pm 1.6 \text{ MeV}$. The EM energies are then corrected by using the π^0 mass ($m_{\pi^0} = 135.0 \text{ MeV}$) with correction factors $k_{Data} = 1.02$ and $k_{MC} = 0.97$ for data and MC respectively. The difference between the corrections for the data and MC are taken as a systematic uncertainty. The value for the uncertainty is calculated by quadrature summing the 1σ uncertainty of data and MC peak positions. The estimated uncertainty for the EM energy scale is 2.3%.

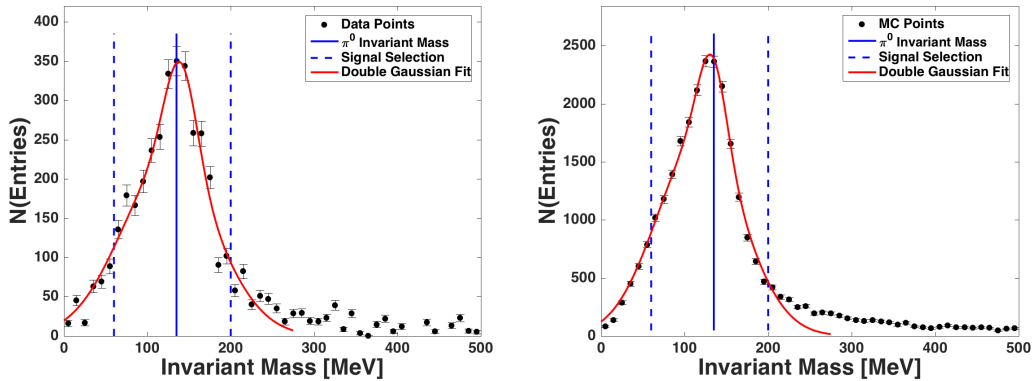


FIG. 8.1: Data (left) and Monte Carlo (right) distributions for $m_{\gamma\gamma}$. In both plots, solid blue line corresponds to the π^0 mass and dashed blue lines corresponds to the signal region selection ($60 \text{ MeV} < m_{\gamma\gamma} < 200 \text{ MeV}$).

Uncertainty in detection of Michel electrons

Michel electron detection is used to reduce the charged pion contamination in the final sample. The efficiency and the uncertainty of Michel electron detection are studied using the stopping rock muons inside the MINERvA detector’s tracking region [80]. This study reported the efficiency of the Michel electron detection algorithm for two different cases. The first case is the efficiency of correctly detecting Michel electrons and the second case describes the false identification of a no-Michel event with a Michel electron. The efficiencies and uncertainties for both cases are given in Table 8.4.

Detection Case	Efficiency	Uncertainty
True identification	70%	1.1%
False identification	1.0%	0.5%

TABLE 8.4: Michel electron detection efficiencies and uncertainties. From Ref. [81].

Uncertainty from pion charge-exchange

A charged pion can undergo charge exchange inside the MINERvA detector creating a neutral pion. D. Ashery *et al.* [82] measured the charge-exchange cross sections for pions with a 50% uncertainty. A 50% uncertainty is included in this analysis for the simulation events having a pion that undergoes a charge exchange. This uncertainty is set to zero for events that do not have a pion that undergoes a charge exchange.

Neutron response uncertainty

Within the MINERvA detector, energetic neutrons may scatter inelastically and create visible energy distant from the vertex. These distant hits created by the neutron inelastic scattering can be erroneously picked up by the neutral pion reconstruction. The uncertainty for the neutron inelastic scattering cross section was studied in another MINERvA analysis for the $\bar{\nu}_\mu + p \rightarrow \mu^+ + \pi^0 + n$ reaction and was estimated as 6% [83]. This systematic uncertainty is zero for events that do not have a final state neutron with a momentum greater than 150 MeV.

Detector mass uncertainty

The number of nucleons inside the fiducial volume is used in the differential cross-section calculation. Since the number of nucleons is directly proportional to detector mass, the uncertainty in the detector mass must be included in the systematic errors. The detector mass uncertainty is estimated to be 1.4% [77].

8.1.1 Relative contributions of the detector response uncertainties to the total systematic error

The largest uncertainty in the detector response uncertainties group is the electromagnetic energy scale uncertainty. Muon momentum and tracking uncertainties are also important sources of systematic errors for the muon variables and event kinematics. The charged pion response, neutron response, target mass, and Michel detection efficiency uncertainties have a lesser contribution to the total systematic error. The uncertainties associated with proton energy and tracking have the least contribution to the total systematic error in all of the cross-section variables.

8.2 Uncertainties inherent to the neutrino interaction model

The neutrino generator GENIE is used for the simulation of neutrino interactions. The GENIE framework provides $\pm 1\sigma$ systematic uncertainties for the parameters that are used to calculate a neutrino cross section for a specific interaction type. The default GENIE $\pm 1\sigma$ uncertainty is included in the error budget for the cross-section measurements. Table 8.5 lists the GENIE $\pm 1\sigma$ systematic uncertainties for the parameters used in cross-section models.

The neutrino interaction-model uncertainties give the largest contribution to the total systematic error in the cross-section measurements as a group. The uncertainty in the GENIE M_A^{RES} parameter is the single leading uncertainty in all the cross-section measurements. After M_A^{RES} , the uncertainties of the M_V^{RES} parameter and

GENIE Model Parameters	GENIE Variable Name	1σ
M_A (Elastic Scattering)	MaNCEL	$\pm 25\%$
Eta (Elastic Scattering)	EtaNCEL	$\pm 30\%$
M_A (CCQE Scattering)	MaCCQE	+25%
		-15%
CCQE Vector Form factor model [84]	VecFFCCQEshape	use dipole
M_A (Resonance Production)	MaRES	$\pm 20\%$
M_V (Resonance Production)	MvRES	$\pm 10\%$
1π production from $\nu p/\bar{\nu} n$ non-resonant	Rvp1pi	$\pm 50\%$
1π production from $\nu n/\bar{\nu} p$ non-resonant	Rvn1pi	$\pm 50\%$
2π production from $\nu p/\bar{\nu} n$ non-resonant	Rvp2pi	$\pm 50\%$
2π production from $\nu n/\bar{\nu} p$ non-resonant	Rvn2pi	$\pm 50\%$
Modified Pauli blocking (CCQE) at low Q^2	CCQEPauliSupViaKF	$\pm 30\%$
NC Resonance Normalization	NormNCRES	$\pm 20\%$
Bodek-Yang parameter A_{HT}	AhtBY	$\pm 25\%$
Bodek-Yang parameter B_{HT}	BhtBY	$\pm 25\%$
Bodek-Yang parameter C_{V1u}	CV1uBY	$\pm 30\%$
Bodek-Yang parameter C_{V2u}	CV2uBY	$\pm 40\%$

TABLE 8.5: GENIE $\pm 1\sigma$ systematic uncertainties for the parameters used in the cross-section models. From Ref. [85].

the non-resonant pion production normalizations (Rvn1pi and Rvn2pi) are the next largest systematic uncertainties. All the other uncertainties in this group have a very small effect on the total systematic error for the cross-section measurements.

8.3 Final state interaction model uncertainties

The GENIE generator is also used for modeling final-state interactions. For all of the GENIE parameters associated with final state interactions, the $\pm 1\sigma$ systematic uncertainty is used in the cross-section measurements. For all of the parameters, the $\pm 1\sigma$ systematic uncertainty is taken from the GENIE framework's default systematics, except the uncertainty on the anisotropy of the Δ^{++} (1232) resonance decay. For this uncertainty the result of a study by B. Eberly is used [55]. According to the study the $\pm 1\sigma$ uncertainties on anisotropy of the Δ^{++} resonance decay are taken to be half the difference between the isotropic and Rein-Sehgal anisotropic decay models. Table 8.6 lists the GENIE $\pm 1\sigma$ systematic uncertainties for the parameters used in the final state interaction model.

GENIE Model Parameters	GENIE Knob name	1σ
Pion mean free path	MFP_pi	$\pm 20\%$
Nucleon mean free path	MFP_N	$\pm 20\%$
Pion absorption	FrAbs_pi	$\pm 30\%$
Pion charge exchange	FrCEX_pi	$\pm 50\%$
Pion elastic scattering	FrElas_pi	$\pm 10\%$
Pion inelastic scattering	FrInel_pi	$\pm 40\%$
Pion - Pion production	FrPiProd_pi	$\pm 20\%$
Nucleon absorption	FrAbs_N	$\pm 20\%$
Nucleon charge exchange	FrCEX_N	$\pm 50\%$
Nucleon elastic scattering	FrElas_N	$\pm 30\%$
Nucleon inelastic scattering	FrInel_N	$\pm 40\%$
Nucleon - Pion production	FrPiProd_N	$\pm 20\%$
AGKY hadronization model	AGKYxF1pi	$\pm 20\%$
Anisotropy Δ resonance decay	Theta_Delta2Npi	$\pm 50\%$

TABLE 8.6: GENIE $\pm 1\sigma$ systematic uncertainties for the parameters used in final state interaction models. From Ref. [85].

As a group, the final-state interaction model uncertainties contribute smaller systematic errors to cross-section measurements than do the detector response or the neutrino interaction-model uncertainties. There is no single systematic that has a much larger uncertainty than others in the group; all of the systematics in this group contribute similarly to the total systematic error.

8.4 Neutrino beam flux uncertainties

A detailed neutrino beam simulation is used for this analysis. The neutrino beam is simulated by using software packages GEANT4 [43] and FLUKA [86]. A detailed neutrino beam simulation requires many different systematic uncertainties to be taken into account. The first group of uncertainties arise from the hadron interaction models, such as the uncertainties for the π^\pm and K^\pm interaction and absorption cross sections. The second group of uncertainties is associated with the beam line geometry models. For instance the largest uncertainty on the flux prediction comes from the uncertainties on the horn position relative to the target. The uncertainty on the transverse position is estimated to be ± 0.01 cm and the uncertainty on the longitudinal position is estimated to be ± 1 cm [34].

All of the individual uncertainties for the beam simulation coming from the hadron interaction models and beam line geometry models are estimated by generating 100 different alternate universes. In each universe, a single parameter is shifted and the flux prediction is calculated again with the shifted parameter. A single systematic uncertainty for the flux is calculated by quadrature summing all of the individual systematics related to the flux simulation.

Similar to the final-state interaction model uncertainties, the flux uncertainty contributes less than the detector response and neutrino interaction model uncertainties to the total systematic error on cross-section measurements.

8.5 Other uncertainties

Other individual systematic uncertainties are assigned to this group. There are three background constraint uncertainties for each background type. These uncertainties are estimated from the sideband fit. An uncertainty for the unfolding procedure is also included in this group. The unfolding uncertainty is calculated as the average difference between $N(\text{Iterations})$ and $N(\text{Iterations}+1)$. Finally, there is an uncertainty arising from the 2p2h events included in the simulation. The GENIE generator does not include 2p2h events in the simulation; and so, separate simulation files are included in the analysis. The uncertainty associated with this additional simulation is included in the “other” group. As a group, the contribution to the total systematic error on all cross-section measurements is less than 1%.

8.6 Total systematic uncertainties

As discussed in previous sections, the individual systematic uncertainties have been organized into five groups according to the source of the systematic error. In all cross-section measurements, similar trends are observed. GENIE neutrino cross-section model uncertainties are the largest contributors to the total systematic uncertainty. The second largest contributor is detector response uncertainty, while the third and fourth are the final-state interaction model uncertainties and the flux uncertainty.

The “other” category contributes least to the total systematic error. Systematic uncertainties for each variable are discussed in Ch. 9 with the cross-section measurements.

Chapter 9

Cross Section Measurements for Charged Current Single π^0 Production

Differential cross sections presented in this Chapter are calculated using Eq. (7.1). Each cross-section measurement is presented with the total (systematic + statistical) fractional uncertainties. The measurements presented in the following sections are based on GENIE v2.8.4 with additional tunings. These tunings were described in Sec. 4.3, and they can be summarized as follows: Event reweighting for Δ^{++} (1232) anisotropic decay, event reweighting for non-resonant $\nu_{\mu}n \rightarrow \mu^{-}n\pi^{+}$ interactions, and inclusion of additional simulated events with 2p2h reactions that produce QE-like final states.

9.1 Single particle differential cross sections

9.1.1 Muon momentum

Figure 9.1 shows the muon momentum differential cross section. The data and simulation distributions agree everywhere to within 1σ of the statistical plus systematic error on the data. The total fractional uncertainties for the muon momentum differential cross-section measurement are given in Fig. 9.2. The GENIE cross-section model is the leading uncertainty almost everywhere due to the large uncertainties on the M_A^{RES} and M_V^{RES} parameters and uncertainties on the non-resonant pion production normalizations (Rvn1pi and Rvn2pi). In the first bin the leading uncertainty is with the detector response due to the detector acceptance.

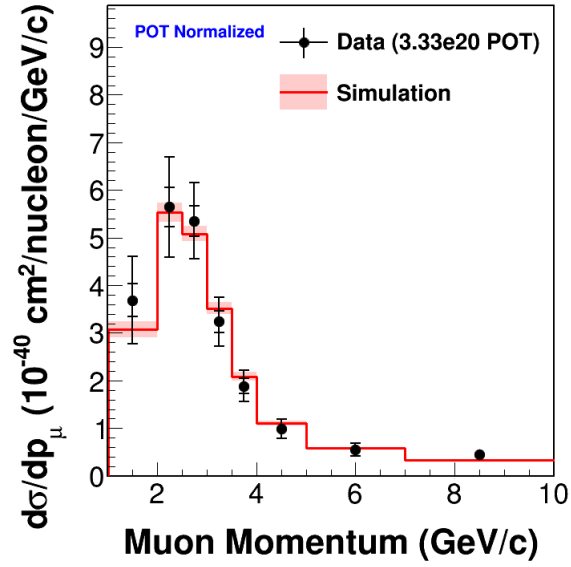


FIG. 9.1: Muon momentum differential cross-section measurement. Data and simulation agree to within 1σ in all bins.

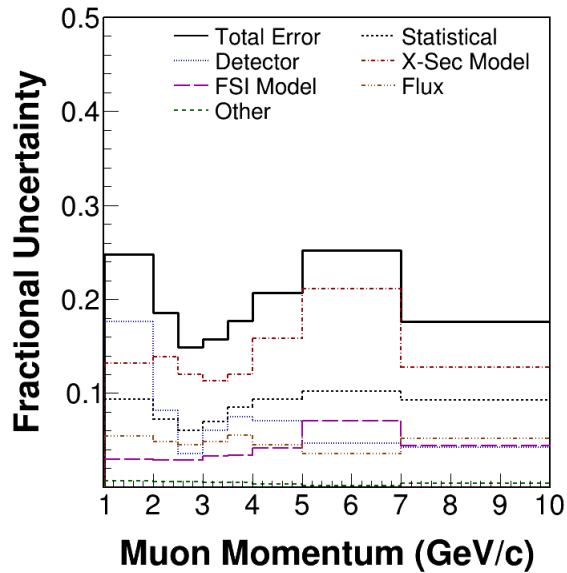


FIG. 9.2: Total fractional uncertainty on the muon momentum cross-section measurement. The leading uncertainty is the cross-section model except in the lowest-momentum bin where the detector response gives the largest uncertainty.

9.1.2 Muon production angle

Figure 9.3 shows the muon production angle differential cross section. The data and simulation distributions agree well for angles within the $5^\circ < \theta_\mu < 12^\circ$ range. The prediction of the simulation is higher than data in the forward-angle ($\theta_\mu < 5^\circ$) region. Most of these events have low Q^2 and the same trend is also observed in the Q^2 distribution presented in Sec. 9.2.1. For the angles $\theta_\mu > 12^\circ$, the simulation prediction is lower than the data. In contrast to the low-angle case, these events have high Q^2 and the same trend is also observed in the Q^2 distribution.

The total fractional uncertainties for the muon production angle differential cross-section measurement are given in Fig. 9.4. The GENIE cross-section model is the leading systematic uncertainty in all bins arising from the uncertainties in the M_A^{RES} and M_V^{RES} parameters and the non-resonant pion production normalizations (Rvn1pi and Rvn2pi). The cross-section model uncertainty is larger for low angle (low Q^2) regions and gets smaller with increasing muon angle. Total fractional uncertainty is dominated by the statistical uncertainty for angles greater than 15 degrees.

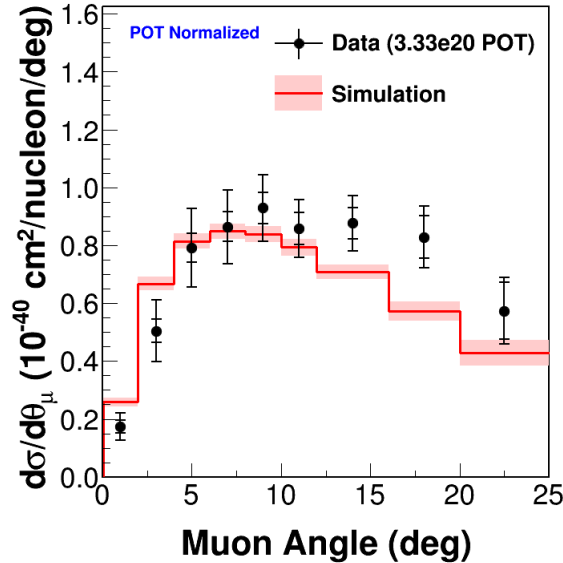


FIG. 9.3: Muon production angle differential cross-section measurement. The simulation estimation is higher than the data for low angles ($\theta_\mu < 5^\circ$) and lower than the data for angles greater than 12 degrees.

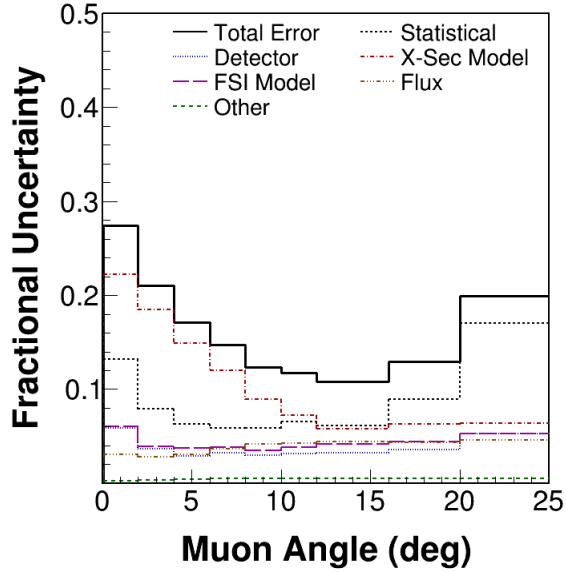


FIG. 9.4: Total fractional uncertainty on the muon production angle cross-section measurement. The leading systematic uncertainty is the cross-section model uncertainty in all bins. The first bin, corresponding to the most forward production angle, has the greatest fractional uncertainty due to the cross-section model uncertainties.

9.1.3 Pion momentum and kinetic energy

In this analysis, two electromagnetic (EM) shower three-momentum vectors (\vec{p}_{γ_1} , \vec{p}_{γ_2}) are measured. Using the EM shower three-momenta, neutral pion kinematics are calculated using the following equations:

$$\vec{p}_{\pi^0} = \vec{p}_{\gamma_1} + \vec{p}_{\gamma_2}, \quad (9.1)$$

$$E_{\pi^0} = \sqrt{|\vec{p}_{\pi^0}|^2 + m_{\pi^0}^2}, \quad (9.2)$$

$$T_{\pi^0} = E_{\pi^0} - m_{\pi^0}. \quad (9.3)$$

The differential cross sections for pion momentum (p_{π^0}) and pion kinetic energy (T_{π^0}) yield similar distributions; these are given in Fig. 9.5. The data and simulation distributions agree in most of the bins to within 1σ of the statistical plus systematic

error on the data. In both distributions the data is higher than the simulation prediction in the low momentum and low kinetic energy regions. On the other hand, in the high momentum and high kinetic energy regions, the data is less than the simulation. Overall, the data-distribution shape increases and decreases more sharply than does the simulation.

The total fractional uncertainties for the pion momentum and pion kinetic energy cross-section measurements are given in Fig. 9.6. For both variables the GENIE neutrino interaction model uncertainties are the leading uncertainty everywhere. The highest total fractional uncertainty is observed in the lowest momentum and lowest kinetic energy bins. The reason for this behavior is that the detector response and the FSI uncertainties are significantly large in the lowest kinematical region.

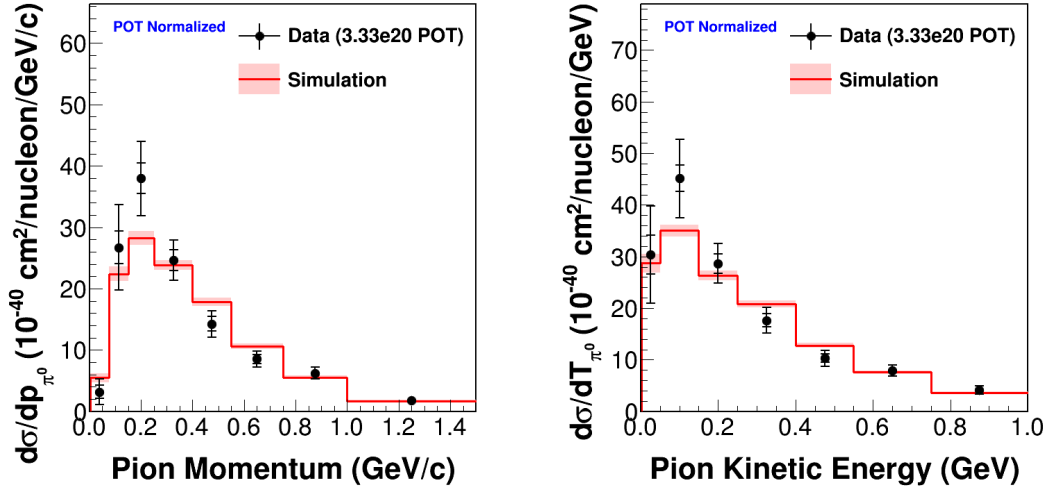


FIG. 9.5: Differential cross-section measurements for pion momentum (left) and kinetic energy (right). The data distribution shape increases and decreases more rapidly than the simulation prediction. Even with the shape difference, in most of the bins data and simulation agree to within 1σ of total error on the data.

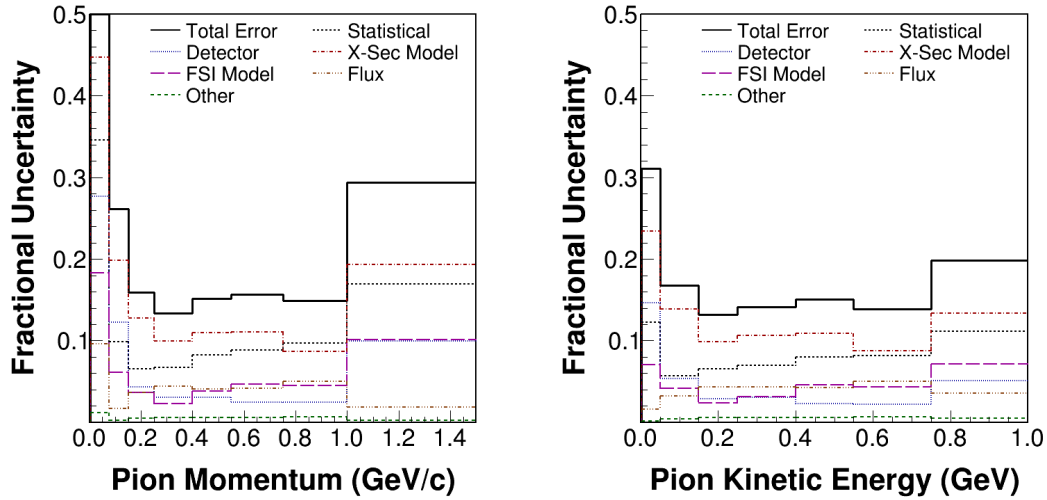


FIG. 9.6: Total fractional uncertainty on the pion momentum (left) and pion kinetic energy (right) cross-section measurements. The leading uncertainty in all of the bins is the cross-section model uncertainty. The first bin corresponding to the lowest momentum and lowest kinetic energy has the highest total fractional uncertainty. In the lowest momentum and kinetic energy bins, the detector response and the FSI model uncertainties are significantly large, in addition to cross-section model uncertainty.

9.1.4 Pion production angle

The pion production angle differential cross section is shown in Fig. 9.7. The data and simulation distributions agree everywhere to within 1σ of the statistical plus systematic error on the data. Figure 9.8 gives the total fractional uncertainties for the pion production angle differential cross-section measurement. The GENIE cross-section model is the leading uncertainty in all bins. Angles less than 10 degrees have the greatest total fractional uncertainties due to increased cross-section model uncertainties and the statistical uncertainties. Another slight increase in the total fractional uncertainty is observed for angles close to 90 degrees. This slight increase is due to the higher statistical uncertainty in that bin.

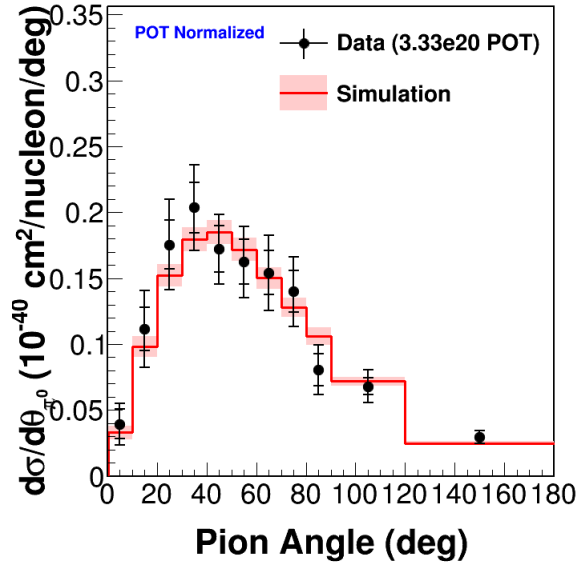


FIG. 9.7: Pion production angle differential cross-section measurement. Data and simulation agree well in all bins. There is a small disagreement between data and simulation for angles close to 90 degrees.

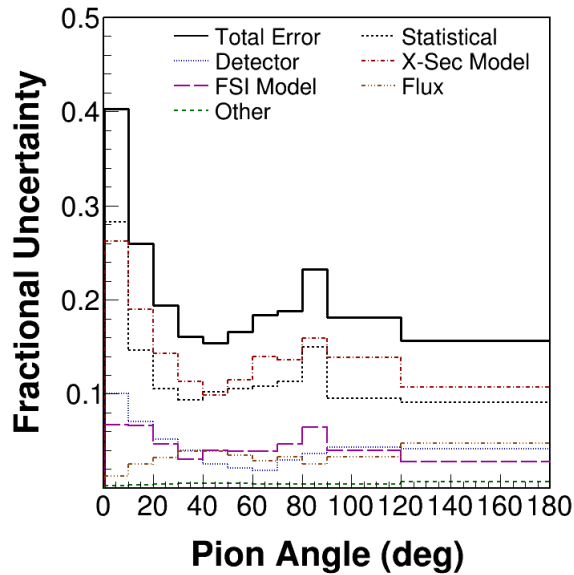


FIG. 9.8: Total fractional uncertainty on the pion production angle cross-section measurement. The leading uncertainty in all bins is the cross-section model uncertainty. The total fractional uncertainty is greatest for the first bin corresponding to the most forward production angle.

9.2 Cross-section results for interaction kinematics

9.2.1 Differential cross section for Q^2

The differential cross-section measurement for Q^2 is shown in Fig. 9.9. The simulation prediction is higher than the data in the low Q^2 region ($Q^2 < 0.3 \text{ GeV}^2$). Events having low Q^2 also have a small muon production angle and this same trend is observed in the muon production angle cross-section measurement. On the contrary, the simulation prediction is lower than the data for Q^2 values greater than 0.5 GeV^2 . This behavior is also observed in the muon production angle cross section. It is worth noting that the simulation does not include Pauli blocking for $CC(\pi)$ reactions nor does it include an RPA (random phase approximation) correction for long-range nucleon correlations. These processes may account for the observed data versus MC discrepancies.

The total fractional uncertainties for the Q^2 differential cross-section measurement are given in Fig. 9.10. The GENIE cross-section model is the leading systematic uncertainty for the low Q^2 region. However, the detector response uncertainties and the final state interaction model uncertainties become dominant for events having Q^2 greater than 1.2 GeV^2 . The statistical uncertainty is also significant for the highest Q^2 region ($Q^2 > 1.5 \text{ GeV}^2$).

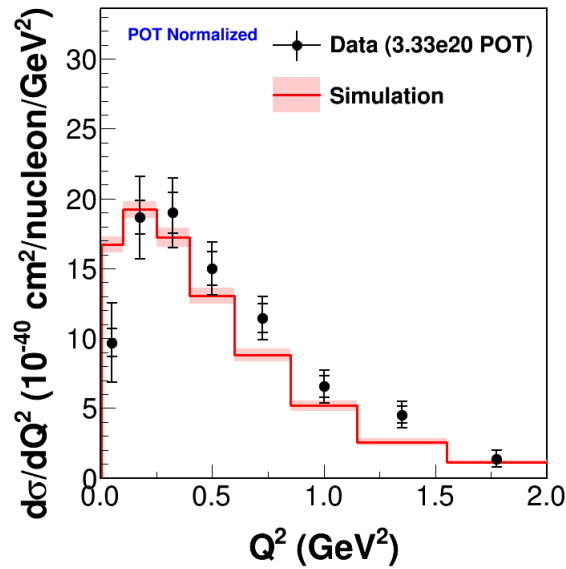


FIG. 9.9: Differential cross-section versus Q^2 for data and simulation. There is a data versus MC discrepancy at low Q^2 , which is also observed in forward going muon production angles. Data have a harder Q^2 distribution than the simulation at high Q^2 .

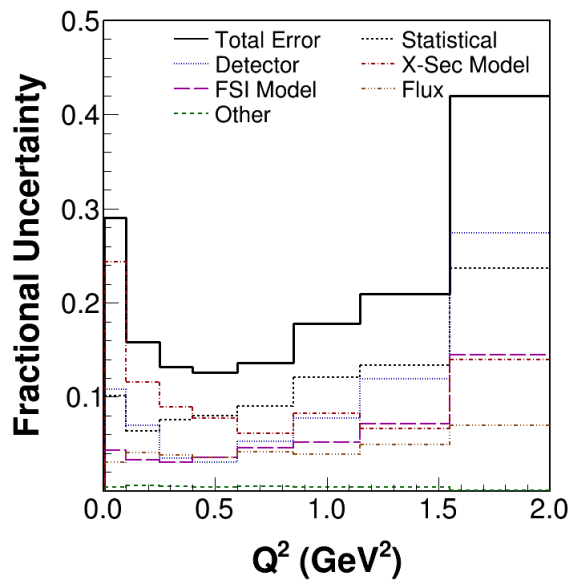


FIG. 9.10: Total fractional uncertainty on the Q^2 cross-section measurement. The leading uncertainty for the low Q^2 region is the cross-section model uncertainty. Detector response uncertainties and FSI model uncertainties becomes significant for events having Q^2 greater than 1.2 GeV².

9.2.2 Total cross section versus neutrino energy

The total cross section versus neutrino energy is calculated by integrating the differential cross section over the neutrino energy and it is shown in Fig. 9.11. The data and simulation distributions agree in most bins to within 1σ of the statistical plus systematic error on the data. There is a data excess of $\sim 1.3\sigma$ observed for the neutrino energy range $8 \text{ GeV} < E_\nu < 12 \text{ GeV}$.

Figure 9.12 shows the total fractional uncertainties for the neutrino energy cross-section measurement. GENIE cross-section model uncertainties are the leading systematic uncertainty in all bins except the first bin. For the lowest neutrino energy bin, the detector response uncertainty is the largest systematic uncertainty. The total fractional uncertainty becomes dominated by limited statistics for neutrino energies greater than 8 GeV. In most bins, flux-model uncertainties are the second leading systematic uncertainty.

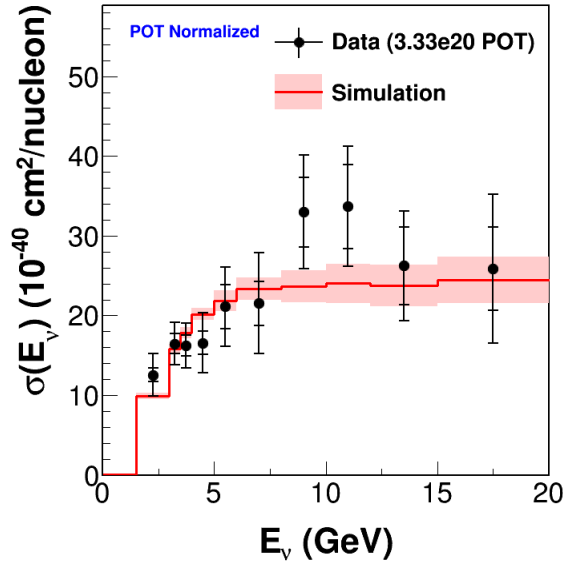


FIG. 9.11: Total cross-section measurement for neutrino energy. Data and simulation agree in everywhere except for a small data excess for neutrino energies between 8 GeV and 12 GeV.

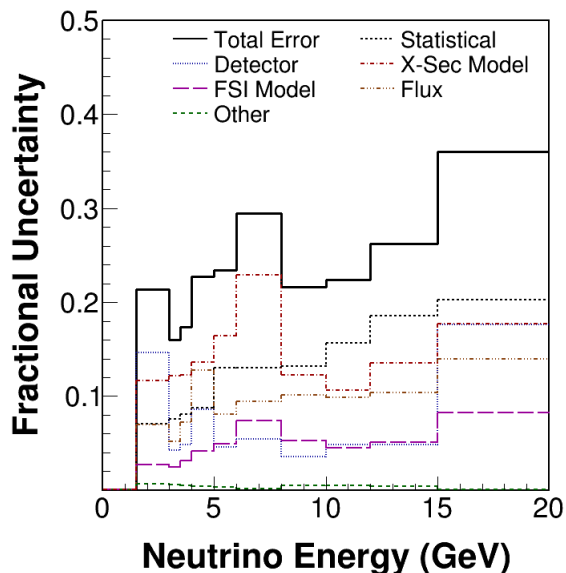


FIG. 9.12: Total fractional uncertainty on the neutrino energy cross-section measurement. GENIE cross-section model uncertainties are the leading systematic uncertainty in all bins except the first bin where the detector response is leading. Total fractional uncertainty is dominated by statistical uncertainties for neutrino energies greater than 8 GeV.

9.3 Results comparison with nominal GENIE simulations

As described in Sec. 4.3, three tunings were included to the nominal GENIE predictions: Event reweighting for Δ^{++} (1232) anisotropic decay, event reweighting for non-resonant $\nu_{\mu}n \rightarrow \mu^{-}n\pi^{+}$ interactions, and additional simulation events for 2p2h reactions in QE-like final states. All of the three tunings change the background estimation in GENIE. However, the cross-section estimation for the signal events in the simulation does not get affected by these tunings. Since the background distributions are changed in the tuned GENIE, the background subtraction method for data changes the data distributions for the signal region.

The cross-section measurements for the muon production angle and Q^2 are the only two variables that experienced a significant change from the tunings. Figure 9.13 shows the data versus reference simulations for muon production angle and Q^2 cross-section measurements. After the tunings, the data prefers higher muon

production angles and a harder Q^2 spectrum. Since Q^2 is calculated by using Eq. (4.4), larger muon angles leads to a higher Q^2 . The ratios of the data cross-sections using the tuned GENIE as reference and the data cross-sections using the nominal GENIE as reference given in Fig. 9.14. In both cases shifts toward higher values in muon production angle and Q^2 distributions are observed.

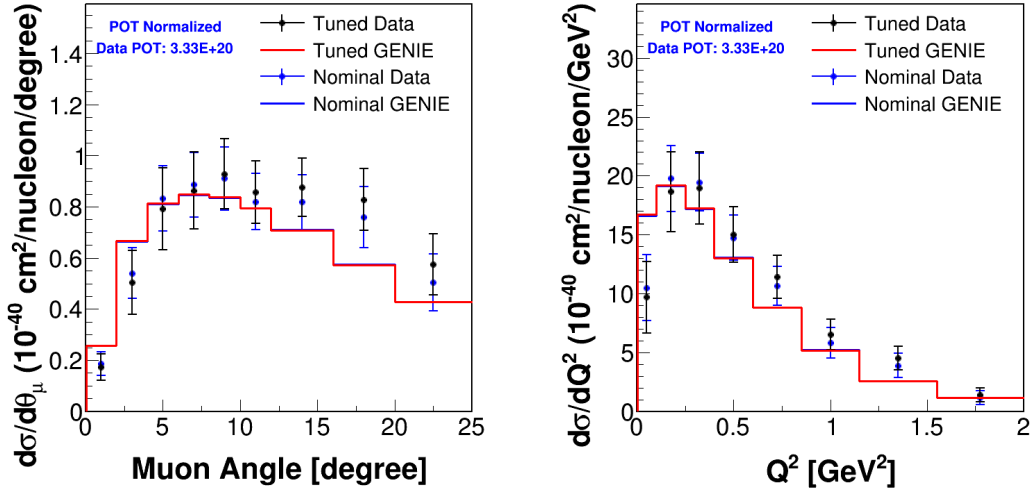


FIG. 9.13: Differential cross-section measurements for muon production angle (left) and Q^2 (right) using the tuned GENIE and the nominal GENIE. The signal prediction for GENIE is not affected by the tunings.

All of the other cross-section variables were also analyzed and minimal differences were observed between nominal GENIE and tuned GENIE. As illustrative examples the data versus reference simulations for muon momentum and pion momentum differential cross-sections are given in Fig. 9.15.

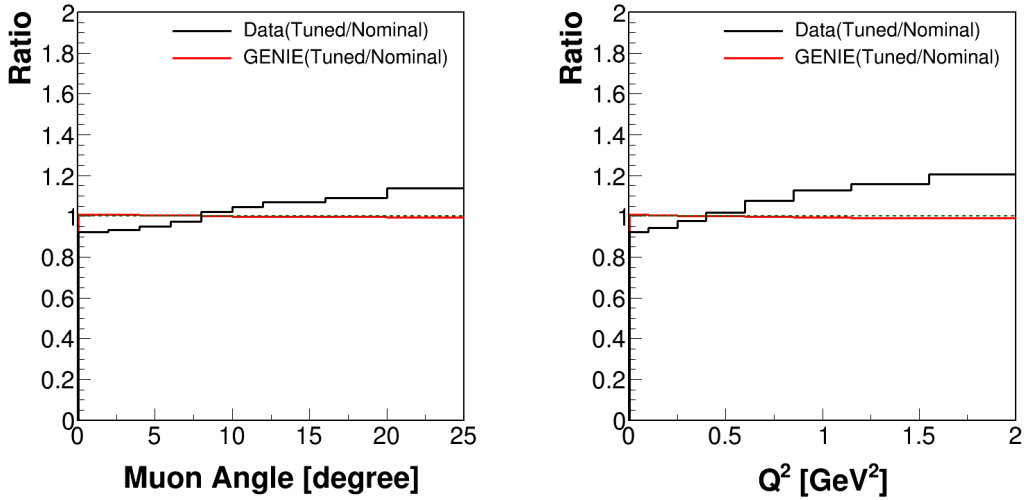


FIG. 9.14: Ratio of tuned GENIE and nominal GENIE differential cross-section measurements for muon production angle (left) and Q^2 (right). In both cases a shift towards the higher end of the spectrum is observed. As seen from the ratios for the simulation the signal prediction is not affected by the tunings.

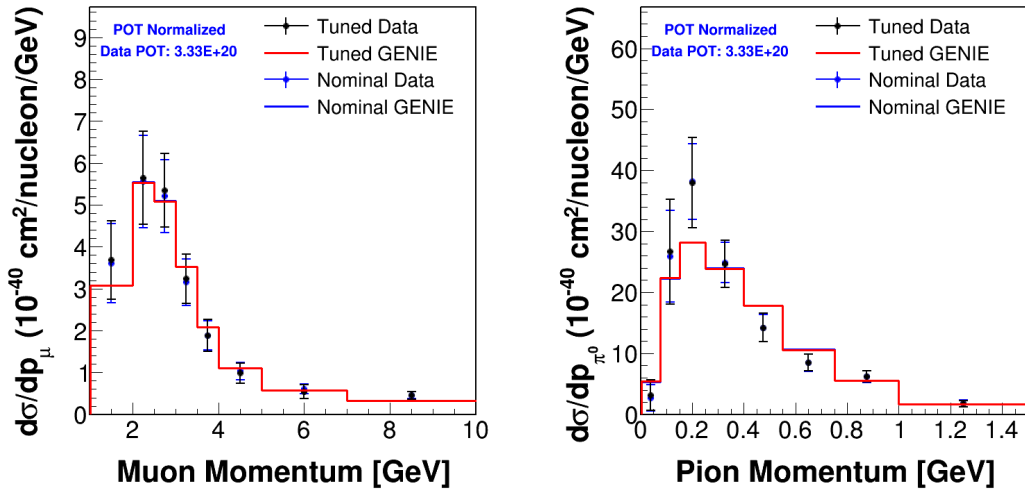


FIG. 9.15: Differential cross-section measurements for muon momentum (left) and pion momentum (right) using the tuned GENIE and the nominal GENIE. The GENIE cross-section estimations for the signal channel are not changed by the tunings. Data cross sections are changed slightly after the tunings.

9.4 Effects from pion final-state interactions

As described in Sec. 4.2, final-state interactions are important for the cross-section measurements, especially the pion final-state interactions. Pions can interact with

the nuclear medium in many different ways, which affect the cross-section measurements differently.

Some final-state interactions can obscure the original neutrino interaction. For example, a signal event can be considered as a background event (feed-out) due to final-state interactions. If the π^0 from the neutrino interaction is absorbed or undergoes a charge exchange inside the nucleus, there will be no π^0 to detect. Also, any other interaction producing additional pions or other mesons causes the event to be considered as a background event. The total feed-out according to the simulation FSI model corresponds to 24.5% of the total signal in the sample. Relative contributions of different interaction channels to the feed-out sample are shown in Fig. 9.16. Pion absorption is the leading feed-out with a 69% contribution. Interactions creating additional pions or other mesons contribute 19% to the total feed-out, and charge exchange ($\pi^0 \rightarrow \pi^\pm$) contributes 12%.

Similarly, a background event can be converted to a signal event (feed-in). There are three possible final-state interactions that can create a single π^0 inside the nucleus from a background event: 1) Pion absorption in a multi-pion event, 2) charge exchange of a single charged pion to a neutral pion, and 3) other π^0 production such as a proton interaction creating a π^0 inside the nucleus. The total feed-in due to final state interactions is 20.9% of the total signal in the sample. Figure 9.17 shows the relative contributions of different interaction channels for feed-in. Multi- $\pi \rightarrow \pi^0$ has a 47% contribution and charge exchange ($\pi^\pm \rightarrow \pi^0$) has a 44% contribution to the total feed-in sample. However, the Zero- $\pi \rightarrow \pi^0$ interactions give only a 9% contribution.

The difference between the feed-out and feed-in samples corresponds to 3.6% of the total signal events. Since both feed-out and feed-in samples have similar statistics, they mostly cancel each other and the overall normalization change in cross section variables is small.

Intranuclear scatterings of the pion from the neutrino interaction may change the pion measured quantities. For instance, a pion can scatter elastically inside the nucleus, leading to a modified angle for the pion. Another example is the inelastic

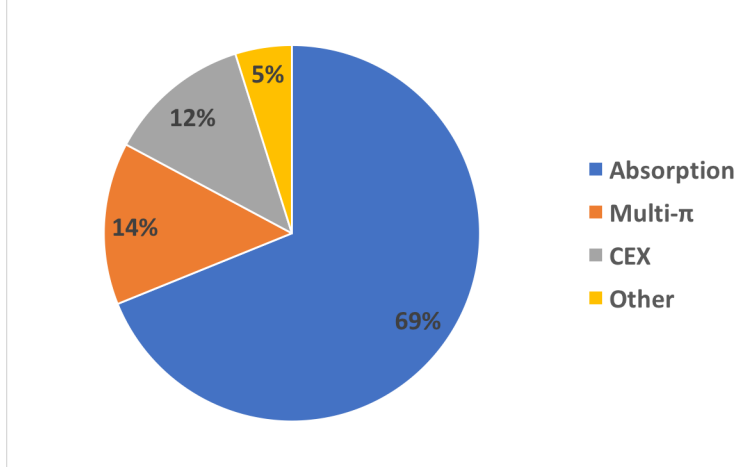


FIG. 9.16: Final state interaction types converting signal events to background events (feed-out). The leading feed-out cause is due to π^0 absorption inside the nucleus.

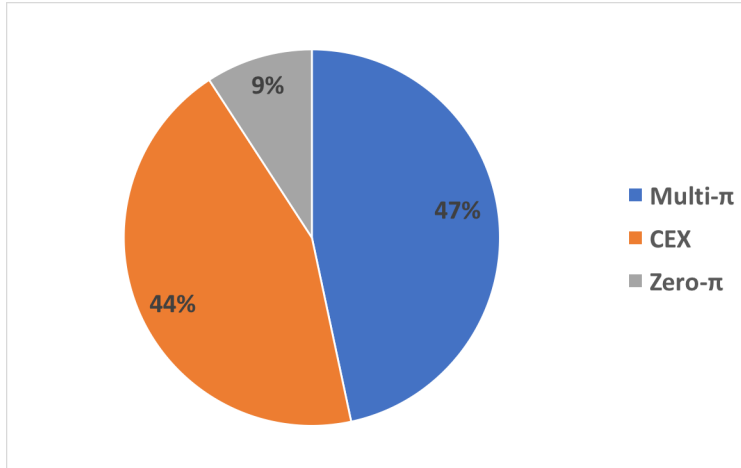


FIG. 9.17: Final state interaction types converting background events to signal events (feed-in). Both of the Multi- $\pi \rightarrow \pi^0$ and the charge exchange ($\pi^\pm \rightarrow \pi^0$) interactions have comparable contributions to the feed-in sample with $\sim 45\%$ each, and the Zero- $\pi \rightarrow \pi^0$ has a smaller contribution, around 10%.

scattering of the pions that leads to different angle and momentum outcomes.

For these reasons, the pion cross-section measurements are the most susceptible to FSI modeling. In Fig. 9.18 the top plot shows the GENIE estimation for pion momenta with and without the FSI modeling and the bottom plot shows the break-out according to FSI process. The FSI treatment in GENIE shifts the peak position to a lower momentum and improves the shape agreement of the data and the simulation. Although GENIE with the FSI estimation is better, there is still a

data excess in the low-momentum region. According to the shape comparison of data versus FSI type, the leading FSI is the π^0 inelastic scattering. One way to improve the predicted shape to the data could be to decrease the π^0 inelastic scattering rate in the momentum range above 0.4 GeV and increase the inelastic scattering rate in the low momentum region.

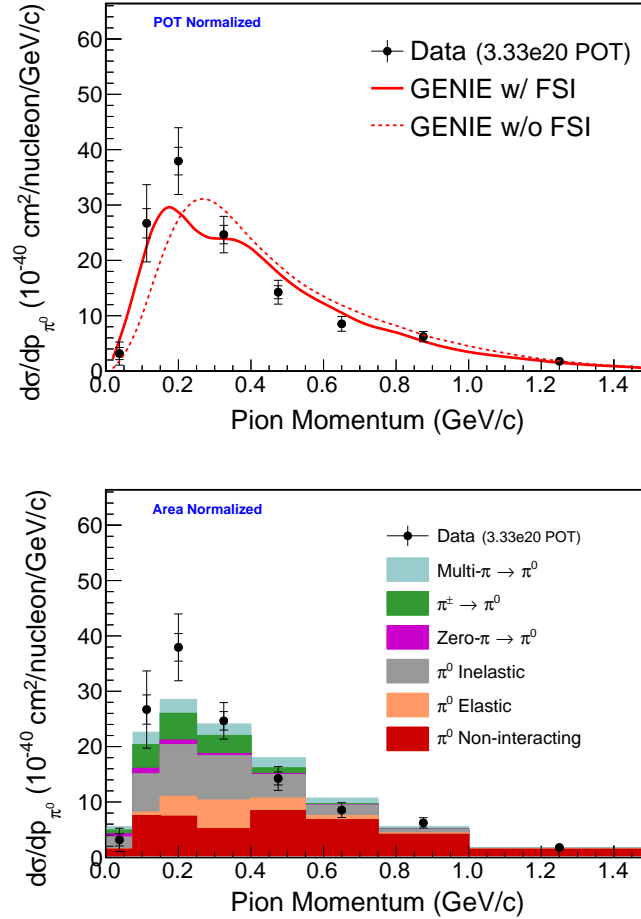


FIG. 9.18: Pion momentum differential cross section with and without FSI modeling (top), and with break-out of FSI processes (bottom). GENIE with FSI is shifting the peak position to lower values. The shape agreement between data and GENIE with FSI is much better than the case without FSI. The leading FSI is π^0 inelastic scattering. In the shape comparison the data is higher than the simulation in the low momentum region and lower than the simulation in high momentum region. This shape difference suggests a slight decrease in FSI normalization at high momentum, but a large increase at low momentum.

In Fig. 9.19 the top plot shows the GENIE estimation for the pion production angle cross-section measurement with and without the FSI modeling, and the bot-

tom plot shows the breakout by FSI processes. The final state interaction model reduces the overall normalization of the cross-section estimation. GENIE with FSI is better for matching the data distribution shape for angles greater than 40 degrees. For smaller angles, GENIE-with-FSI estimations are lower than the data whereas GENIE-without-FSI gives a better agreement. Also, for backward pions ($\theta_{\pi^0} > 90^\circ$), there is an increase in the rate estimation for the sample treated with the FSI, which improves the data versus simulation agreement for backward pions. For the distribution shape comparison, GENIE with FSI agrees to within 1σ of the total error in data everywhere.

Muons created in the neutrino interaction are not affected by the final-state interactions inside the nucleus, and so only overall normalization changes are observed in the cross-section measurements. Figure 9.20 shows the GENIE estimations for muon momentum and production angle cross-section measurements with and without FSI modeling. In both cases, the overall normalization is slightly reduced when the FSI modeling is included.

The final-state interactions have a small effect on the Q^2 and neutrino energy distributions. Figure 9.21 depicts the GENIE estimations for Q^2 and neutrino energy cross-section measurements with and without FSI modeling. A slight improvement in the low- Q^2 region is observed with the FSI modeling, but there is no major change in shape or normalization of the Q^2 distribution. In particular there is no change in the higher Q^2 region ($Q^2 > 1 \text{ GeV}^2$). The overall normalization for the neutrino energy distribution is slightly reduced with FSI modeling, but no shape difference is observed.

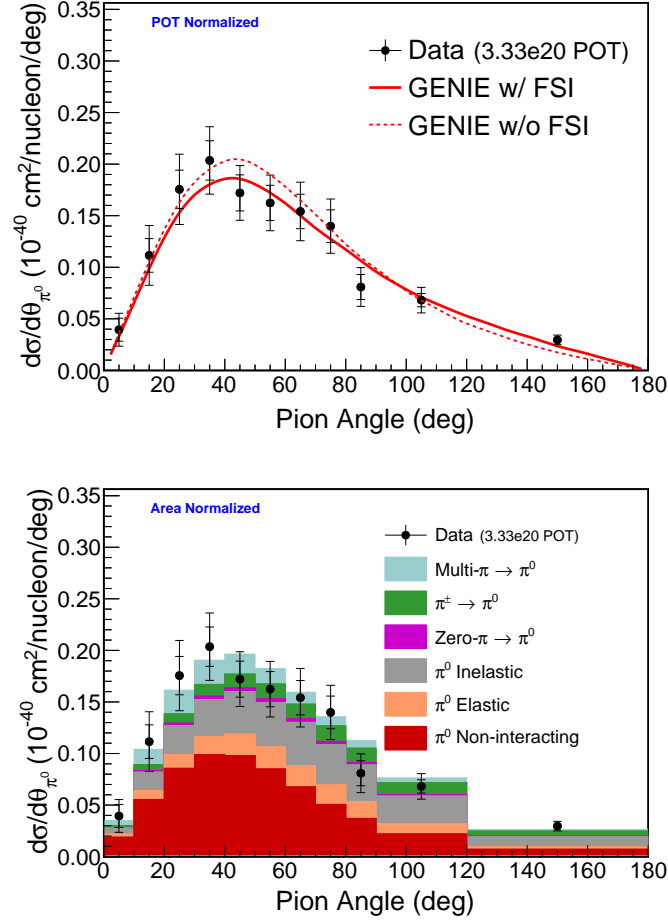


FIG. 9.19: Pion production angle differential cross section with and without FSI modeling (top), and with break-out of FSI processes (bottom). The overall normalization reduces with the inclusion of FSI modeling. GENIE with FSI matches data shape better than without FSI for angles greater than 40 degrees. For smaller angles both cases are within 1σ of the data, but GENIE without FSI gives a better agreement. The simulation with FSI matches the shape of the data very well. According to GENIE the leading FSI process is π^0 inelastic scattering.

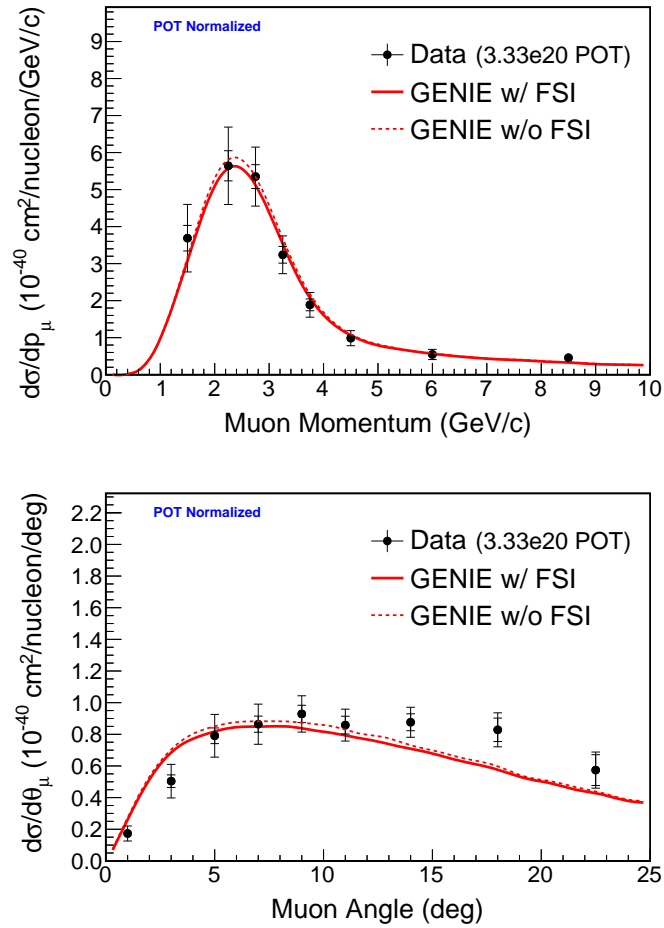


FIG. 9.20: Differential cross sections for muon momentum (top), and production angle (bottom) with and without FSI modeling. In both cases FSI modeling reduces the overall normalization but does not change the shape of the GENIE predictions.

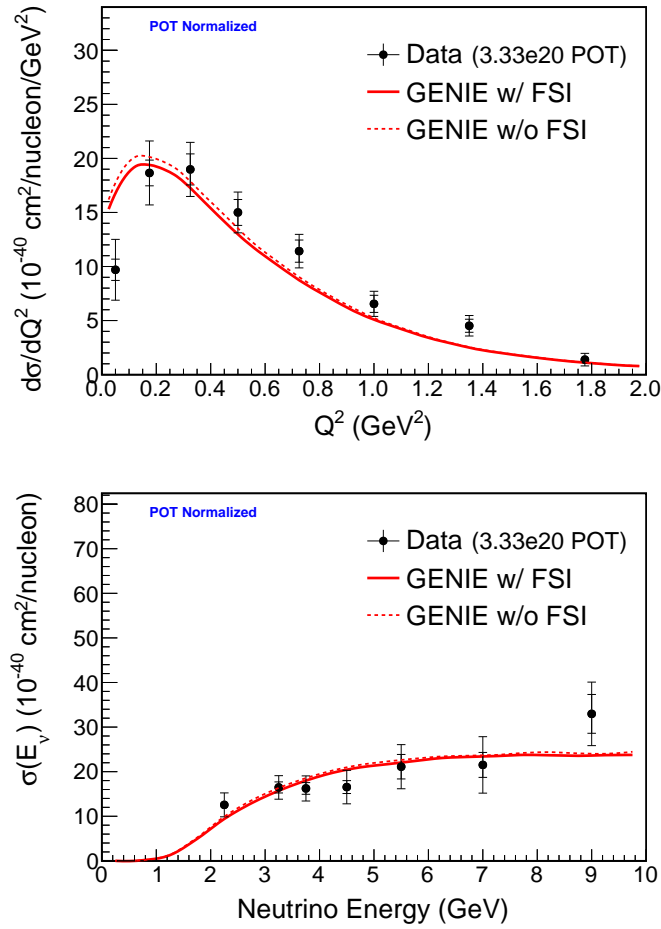


FIG. 9.21: Cross sections for Q^2 (top), and neutrino energy (bottom) with and without FSI modeling. In both cases there is a slight overall normalization reduction with the FSI modeling. The low Q^2 region is slightly improved with the FSI modeling while the neutrino energy distribution is practically unchanged.

9.5 Results comparison with MiniBooNE ν_μ -CC (π^0) measurement

The MiniBooNE experiment uses a spherical, 12 m diameter Čerenkov detector filled with mineral oil (CH_2). The detector was exposed to a neutrino beam with an energy range 0.5-2.0 GeV. The MiniBooNE collaboration reported cross sections for neutrino induced charged-current single π^0 production in 2011 [87]. In their paper, Ref. [87], the differential cross-section measurements for Q^2 , for muon kinematics, and for π^0 kinematics were reported. In this section the comparisons for $d\sigma/dQ^2$ and $d\sigma/dP_{\pi^0}$ distributions in MINERvA and MiniBooNE is provided. A study by P. Rodrigues compared the MiniBooNE data to GENIE v2.6.2 predictions in Ref. [88].

The differential cross sections for Q^2 in MINERvA and MiniBooNE are shown in Fig. 9.22. The MINERvA result is flux-averaged between $1.5 < E_\nu < 20$ GeV while the MiniBooNE result is flux-averaged between $0.5 < E_\nu < 2$ GeV. Due to the different neutrino fluxes used, MINERvA has a broader Q^2 distribution than does MiniBooNE. In both experiments, the simulation predictions (MiniBooNE uses NUANCE [89]) are lower than the data in high- Q^2 regions. Again, in both samples there is a turn-over in data in the low- Q^2 region, while both simulations fail to predict this turn-over. Comparing the discrepancies between data and simulation, GENIE appears to do a better job in matching the data in $d\sigma/dQ^2$.

Figure 9.23 shows the differential cross sections for π^0 momentum in MINERvA and MiniBooNE. Due to the different neutrino energy ranges, the $d\sigma/dP_{\pi^0}$ distribution is wider in MINERvA. Both experiments observe a data excess at low pion momentum, however GENIE manages to achieve a rough agreement with the MINERvA data, while NUANCE fails badly with predicting the MiniBooNE data for π^0 momenta below 0.3 GeV/c.

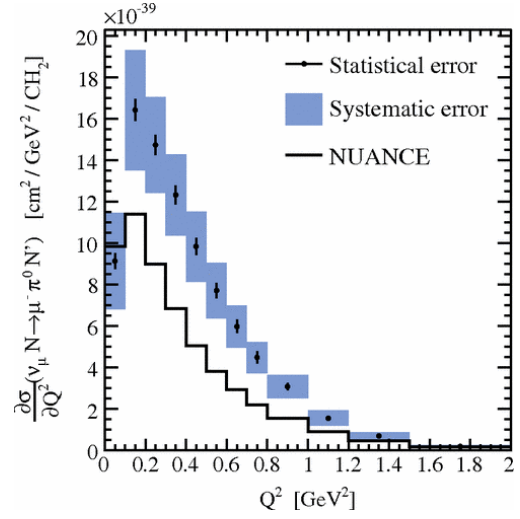
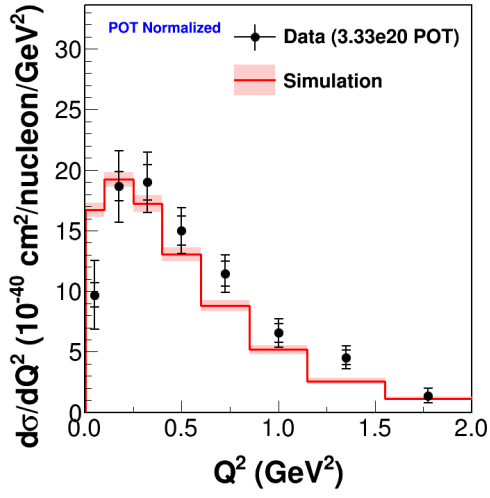


FIG. 9.22: The $d\sigma/dQ^2$ measurements for the ν_μ -CC (π^0) channel in MINERvA (left) and MiniBooNE (right). In both samples, the data is higher than the simulation prediction in the higher Q^2 region. The MiniBooNE result is from Ref. [87].

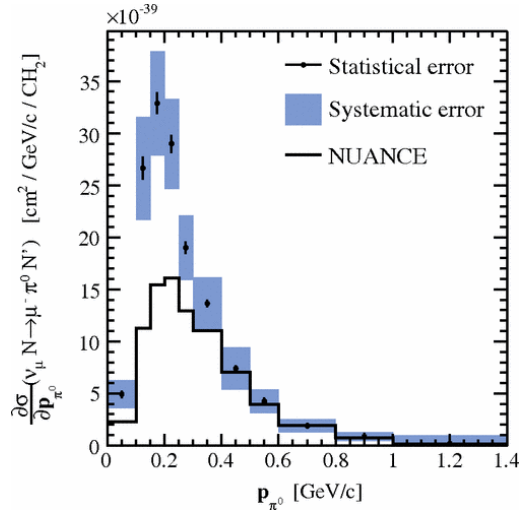
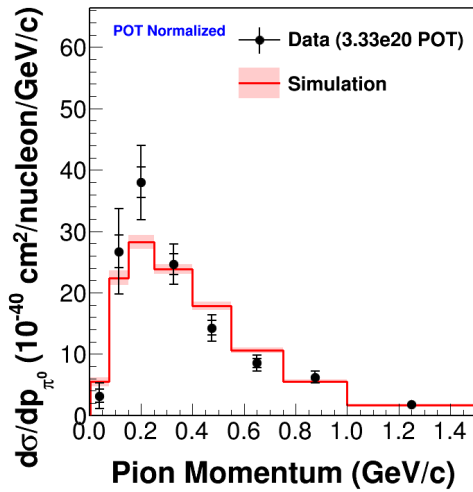


FIG. 9.23: The $d\sigma/dP_{\pi^0}$ measurements for the ν_μ -CC (π^0) channel in MINERvA (left) and MiniBooNE (right). In both samples, data is higher than the simulation prediction in the low momentum region. The MiniBooNE result is from Ref. [87].

Chapter 10

Comparisons with CC Pion Production Measurements in MINERvA

10.1 Definitions for the samples used in the comparison

The results of this analysis are compared to two different CC pion production analyses published by the MINERvA experiment [90]. The reaction equations for the latter investigations are given below.

$$\nu_\mu + \text{CH} \rightarrow \mu^- + \pi^+ + X, \quad (10.1)$$

$$\bar{\nu}_\mu + \text{CH} \rightarrow \mu^+ + \pi^0 + X'. \quad (10.2)$$

For both of these CC reactions the target is hydrocarbon (CH) and the neutrino energy is in the range $1.5 \text{ GeV} < E_\nu < 10 \text{ GeV}$. The neutrino-induced CC (π^+) sample of Eq. (10.1) is a semi-inclusive process in which X may include charged or neutral pions, as well as recoil nucleons. On the other hand, the antineutrino-induced CC (π^0) sample of Eq. (10.2) is more nearly an exclusive process that includes only single π^0 production (The X' may include recoil nucleons but no pions.). In both samples the hadronic invariant mass W is limited to 1.8 GeV. Table 10.1 summarizes the signal definitions of these two samples together with the sample obtained in this analysis.

	$\nu_\mu\text{-CC}(\pi^+)$	$\bar{\nu}_\mu\text{-CC}(\pi^0)$	$\nu_\mu\text{-CC}(\pi^0)$
Final States	$\mu^- + \pi^+ + X$	$\mu^+ + \pi^0 + X$	$\mu^- + \pi^0 + X$
X content	recoil nucleons, charged or neutral pions	recoil nucleons	recoil nucleons
W Limit	1.8 GeV	1.8 GeV	1.8 GeV
E_ν Range	1.5 - 10 GeV	1.5 - 10 GeV	1.5 - 20 GeV

TABLE 10.1: Signal definitions for samples obtained in channels $\nu_\mu\text{-CC}(\pi^+)$, $\bar{\nu}_\mu\text{-CC}(\pi^0)$, and $\nu_\mu\text{-CC}(\pi^0)$. The $\nu_\mu\text{-CC}(\pi^+)$ sample is from a semi-inclusive process that may include more than one pion in the final state. The samples $\bar{\nu}_\mu\text{-CC}(\pi^0)$ and $\nu_\mu\text{-CC}(\pi^0)$ are more nearly exclusive processes that can have only one single neutral pion. Hadronic invariant mass W is limited to 1.8 GeV in all samples. The neutrino energy range for the $\nu_\mu\text{-CC}(\pi^0)$ sample extends to 20 GeV, while the range for the other two samples extends to 10 GeV.

10.2 Model comparisons

The relative levels of agreement between the data and GENIE-based simulations are now reviewed, using all three of the CC (π) samples. In this analysis (ν_μ -CC (π^0)) GENIE v2.8.4 with additional tunings is used, whereas the ν_μ -CC (π^+) and $\bar{\nu}_\mu$ -CC (π^0) analyses used GENIE v2.6.2. For all cross-section variables the GENIE predictions with and without final-state interactions (FSI) are provided. In addition to GENIE predictions, the measurements for ν_μ -CC (π^+) and $\bar{\nu}_\mu$ -CC (π^0) also include predictions for the NuWro [91] and NEUT [92] event generators with FSI effects. All the plots for ν_μ -CC (π^+) and $\bar{\nu}_\mu$ -CC (π^0) are from Ref. [90].

The differential cross sections for muon momentum for all three samples are shown in Fig. 10.1. The peak of the differential cross section $d\sigma/dP_\mu$ for ν_μ -CC (π^0) is $\sim 27\%$ higher than the $\bar{\nu}_\mu$ -CC (π^0) cross-section peak; however, it is $\sim 74\%$ lower than the ν_μ -CC (π^+) cross-section peak. The data and GENIE with FSI agree within 1σ of the total error on the data for $\bar{\nu}_\mu$ -CC (π^0) and ν_μ -CC (π^0) samples, however the GENIE prediction is high for the ν_μ -CC (π^+) sample. In all three cases GENIE with FSI shows better agreement with data than does GENIE without FSI. The FSI model in GENIE reduces the overall normalization in ν_μ -CC (π^+) and ν_μ -CC (π^0) while it increases the normalization in $\bar{\nu}_\mu$ -CC (π^0).

Figure 10.2 shows the differential cross sections for the muon production angle for all three samples. The differential cross-section $d\sigma/d\theta_\mu$ for ν_μ -CC (π^0) lies between the other two samples; the ν_μ -CC (π^+) sample has a higher rate and $\bar{\nu}_\mu$ -CC (π^0) sample has a lower rate. The data and simulation for the $\bar{\nu}_\mu$ -CC (π^0) sample are everywhere in agreement, while the other two samples have disagreements. The simulation prediction is higher than the data for the ν_μ -CC (π^+) sample, and the data distribution is higher than the simulation for the ν_μ -CC (π^0) sample for angles greater than 12 degrees. In all three cases GENIE with FSI has better agreement with data than GENIE without FSI. As with the muon momentum cross sections, the FSI model in GENIE reduces the overall normalization in ν_μ -CC (π^+) and ν_μ -CC (π^0), while it increases the normalization in $\bar{\nu}_\mu$ -CC (π^0).

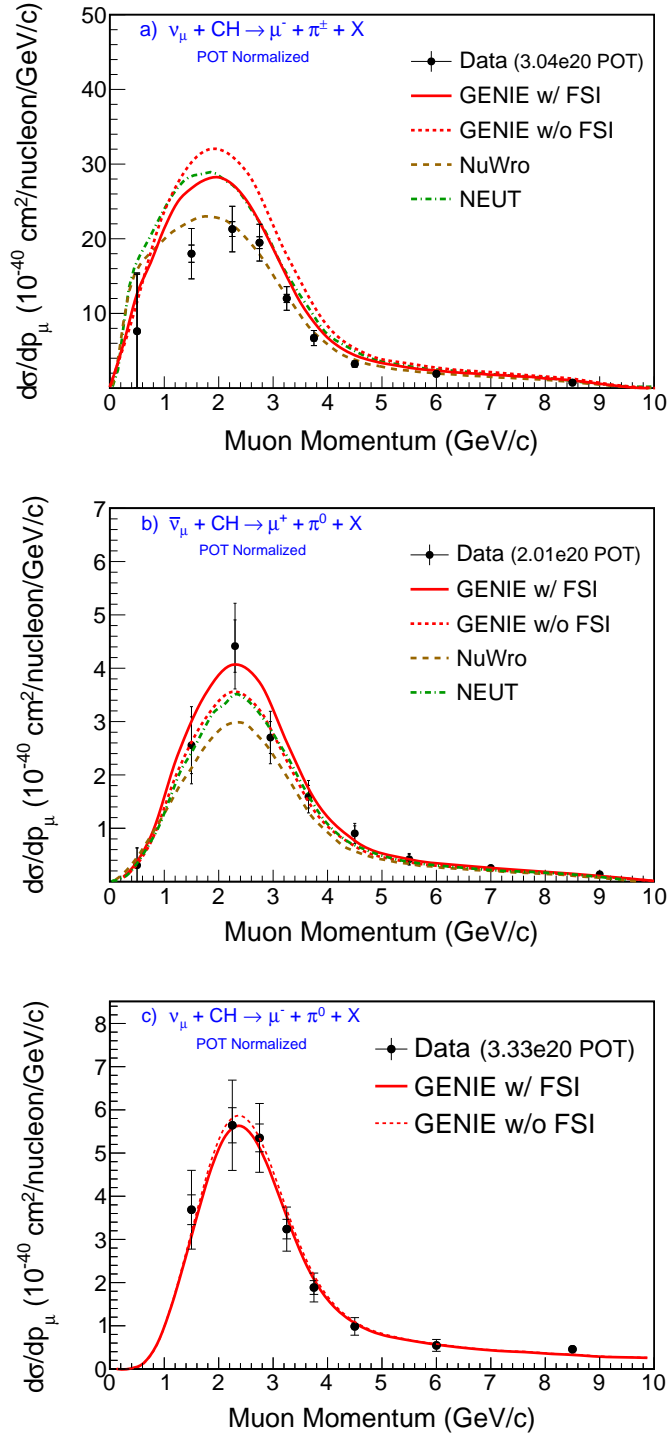


FIG. 10.1: Differential cross sections for muon momenta of the samples ν_μ -CC (π^+) (a), $\bar{\nu}_\mu$ -CC (π^0) (b), and ν_μ -CC (π^0) (c). The inner (outer) error bars on data correspond to statistical (total) uncertainties. The solid (dashed) distributions are GENIE predictions with (without) FSI. Also, (a) and (b) include predictions for NuWro and NEUT. In all three cases GENIE with FSI has a better agreement with data. The simulation prediction is higher than the data for the ν_μ -CC (π^+) sample, while in the π^0 samples it is in agreement.

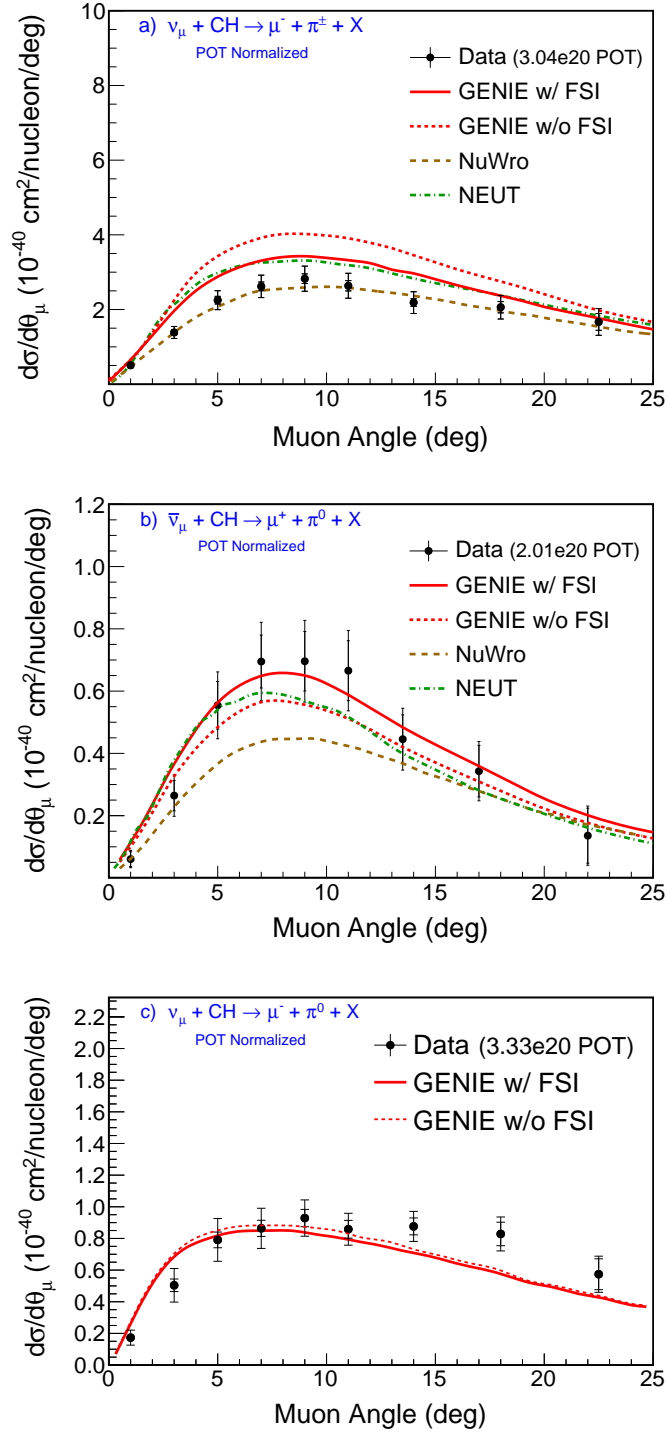


FIG. 10.2: Differential cross sections for the muon production angle for the samples ν_μ -CC (π^+) (a), $\bar{\nu}_\mu$ -CC (π^0) (b), and ν_μ -CC (π^0) (c). The inner (outer) error bars on data correspond to statistical (total) uncertainties. The simulation prediction agrees with the data everywhere in the $\bar{\nu}_\mu$ -CC (π^0) sample. The simulation prediction is higher than the data for the ν_μ -CC (π^+) sample in all bins, and there is disagreement at higher muon angles between data and the simulation for the ν_μ -CC (π^0) sample.

Figure 10.3 shows the differential cross-section measurements for the pion kinetic energy for all three samples. The kinetic energy ranges of the π^+ and π^0 are different because the charged pion tracks have a containment requirement inside the MINERvA detector which restricts the maximum pion kinetic energy to 350 MeV [49]. The FSI treatment in GENIE significantly improves the simulation prediction in all cases. As is the case for muon kinematics, the simulation estimation is higher than the data for the ν_μ -CC (π^+) sample. The data is higher than the simulation prediction for low π^0 kinetic energy and lower than the simulation for high kinetic energy, for both neutrino and anti-neutrino samples.

The differential cross sections for the pion production angle for all three samples are shown in Fig. 10.4. The simulation prediction agrees with data in the $\bar{\nu}_\mu$ -CC (π^0) and ν_μ -CC (π^0) samples, whereas the simulation prediction is higher than the data for the ν_μ -CC (π^+) sample. There is a major improvement in the simulation when the FSI effects are included for the ν_μ -CC (π^+) sample. For the samples with π^0 , GENIE with FSI has a better agreement for backward pions ($\theta_{\pi^0} > 90^\circ$).

Figure 10.5 shows the differential cross sections for the four-momentum transfer Q^2 for all three samples. The differential cross section for ν_μ -CC (π^0) is lower than the ν_μ -CC (π^+) sample, but higher than the $\bar{\nu}_\mu$ -CC (π^0) sample. In all measurements the data shows the low Q^2 turnover while the simulation fails to predict a low- Q^2 reduction. The $\bar{\nu}_\mu$ -CC (π^0) sample has the best shape and rate agreement except for the first bin. The simulation prediction for $d\sigma/dQ^2$ for the ν_μ -CC (π^+) sample is higher than the data everywhere. The data in the ν_μ -CC (π^0) sample has a “harder” (more energetic) Q^2 distribution than the simulation. The data-vs-simulation shape agreement improves with the FSI modeling in all samples, however the most significant improvement is observed in the ν_μ -CC (π^+) sample.

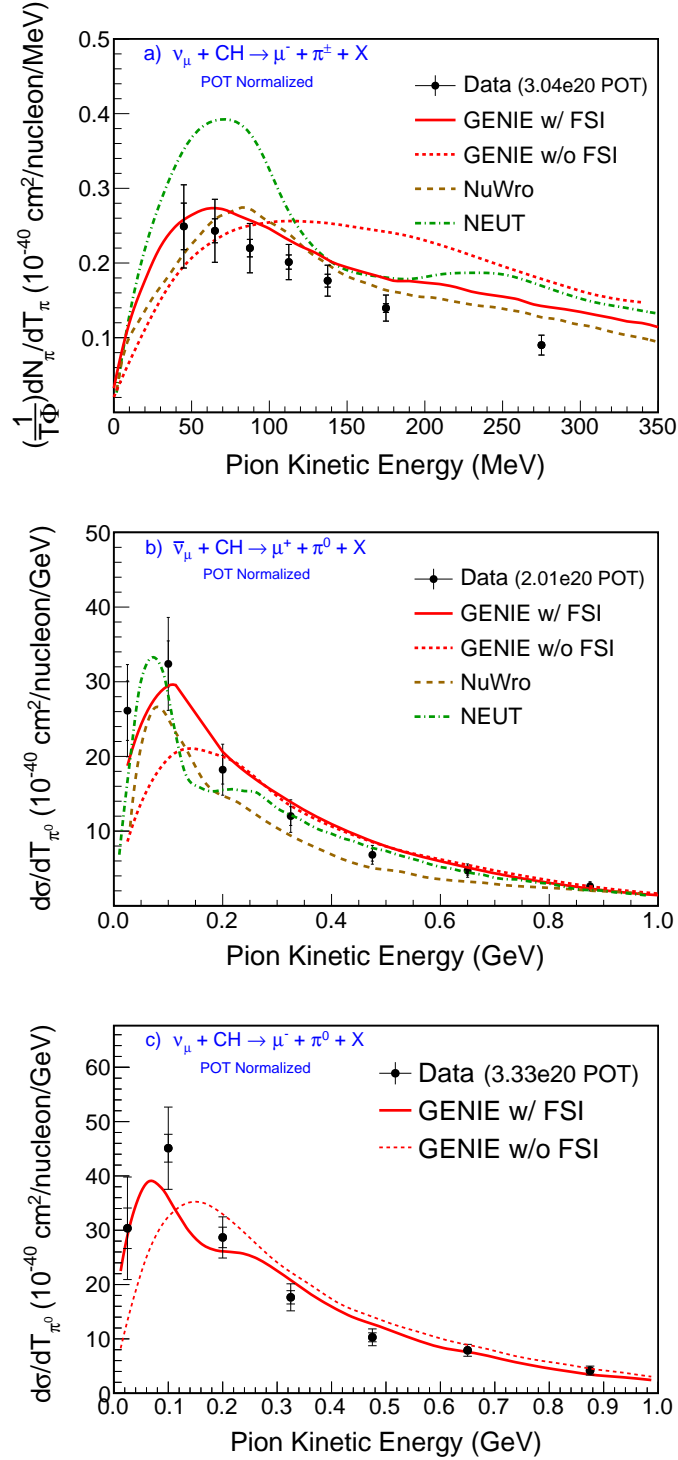


FIG. 10.3: Differential cross sections for pion kinetic energy for the samples $\nu_\mu\text{-CC}(\pi^+)$ (a), $\bar{\nu}_\mu\text{-CC}(\pi^0)$ (b), and $\nu_\mu\text{-CC}(\pi^0)$ (c). The simulation prediction is higher than the data for the $\nu_\mu\text{-CC}(\pi^+)$ sample. In all cases the shape agreement significantly improves with the FSI effects included in the simulation.

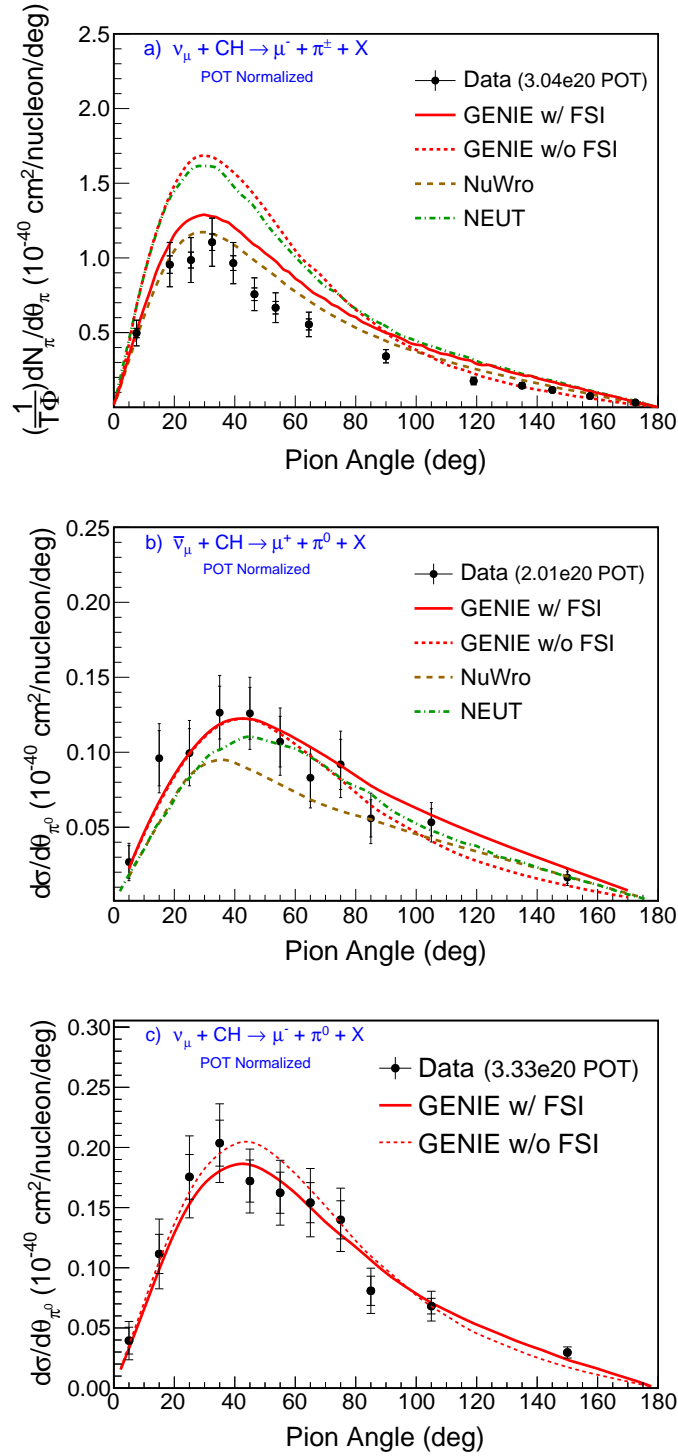


FIG. 10.4: Differential cross sections for pion production angle for the samples ν_{μ} -CC(π^{+}) (a), $\bar{\nu}_{\mu}$ -CC(π^{0}) (b), and ν_{μ} -CC(π^{0}) (c). In all cases the simulation prediction agrees with the data shape. The FSI model significantly reduces the simulation prediction and improves the data-simulation agreement for the ν_{μ} -CC(π^{+}) sample.

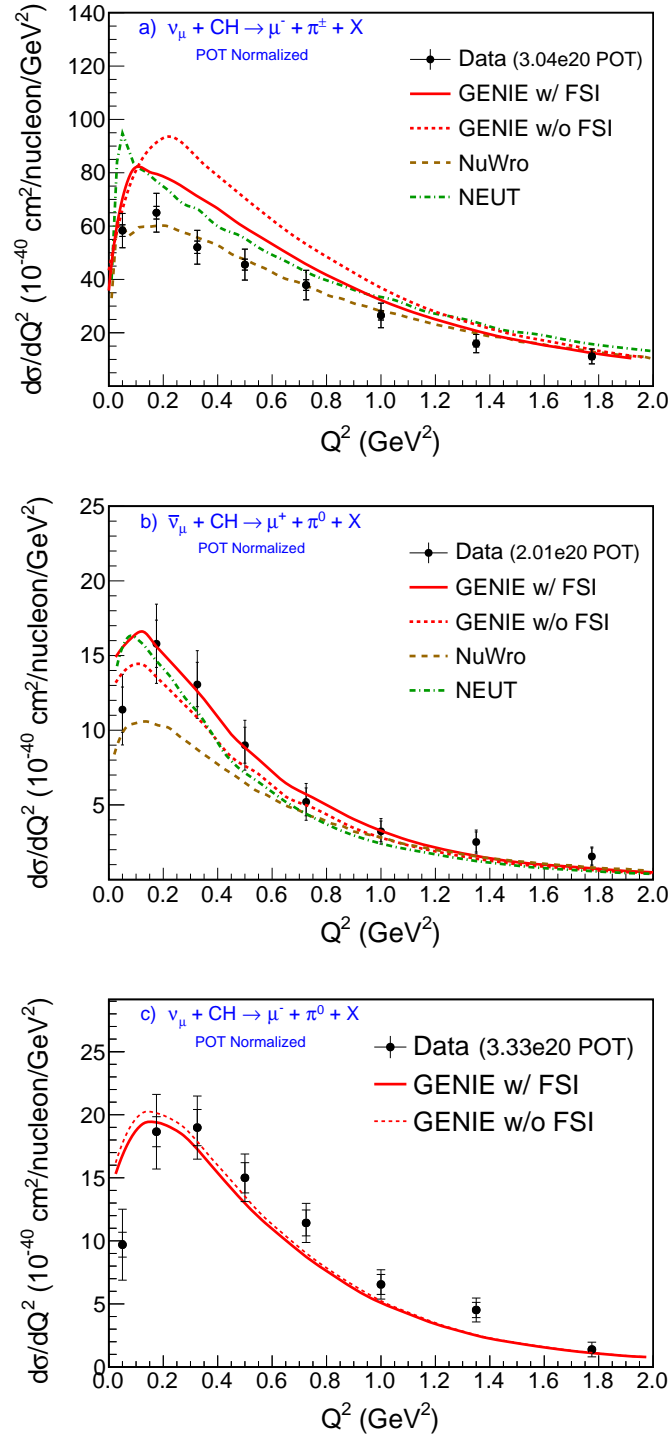


FIG. 10.5: Differential cross sections for four-momentum transfer squared Q^2 for the samples ν_μ -CC (π^+) (a), $\bar{\nu}_\mu$ -CC (π^0) (b), and ν_μ -CC (π^0) (c). FSI modeling improves the shape and rate agreement in all samples. The $\bar{\nu}_\mu$ -CC (π^0) sample has a good data-simulation agreement everywhere, while the other two samples show disagreements. The simulation prediction for ν_μ -CC (π^+) is higher than data everywhere and the simulation prediction for ν_μ -CC (π^0) is lower than the data for the high Q^2 region.

Cross sections as a function of neutrino energy E_ν for all three samples are shown in Fig. 10.6. An interesting feature of these plots is the relative cross-section rates. For the $\langle E_\nu \rangle = 7.0$ GeV bin, the cross section for the $\nu_\mu\text{-CC}(\pi^+)$ is four times higher than the other two samples. For the same bin, the measured cross section for the $\nu_\mu\text{-CC}(\pi^0)$ sample is only $\sim 16\%$ higher than $\bar{\nu}_\mu\text{-CC}(\pi^0)$ sample. A second feature of these plots is the shape difference among the distributions. The cross section for the $\nu_\mu\text{-CC}(\pi^+)$ sample reaches its plateau at $E_\nu \geq 3.0$ GeV, whereas the cross sections for the $\bar{\nu}_\mu\text{-CC}(\pi^0)$ and $\nu_\mu\text{-CC}(\pi^0)$ samples show a gradual increase through the measured region $1.5 \leq E_\nu \leq 10$ GeV. The simulation prediction for the $\nu_\mu\text{-CC}(\pi^+)$ sample is everywhere higher than the data. For the samples $\bar{\nu}_\mu\text{-CC}(\pi^0)$ and $\nu_\mu\text{-CC}(\pi^0)$, the simulation predictions agree with data nearly everywhere to within 1σ total error. GENIE with FSI versus without FSI shows major differences for the $\nu_\mu\text{-CC}(\pi^+)$ and $\bar{\nu}_\mu\text{-CC}(\pi^0)$ samples, and the FSI treatment improves the data-simulation agreement. On the other hand, small differences are observed for GENIE with FSI versus without FSI for the $\nu_\mu\text{-CC}(\pi^0)$ sample.

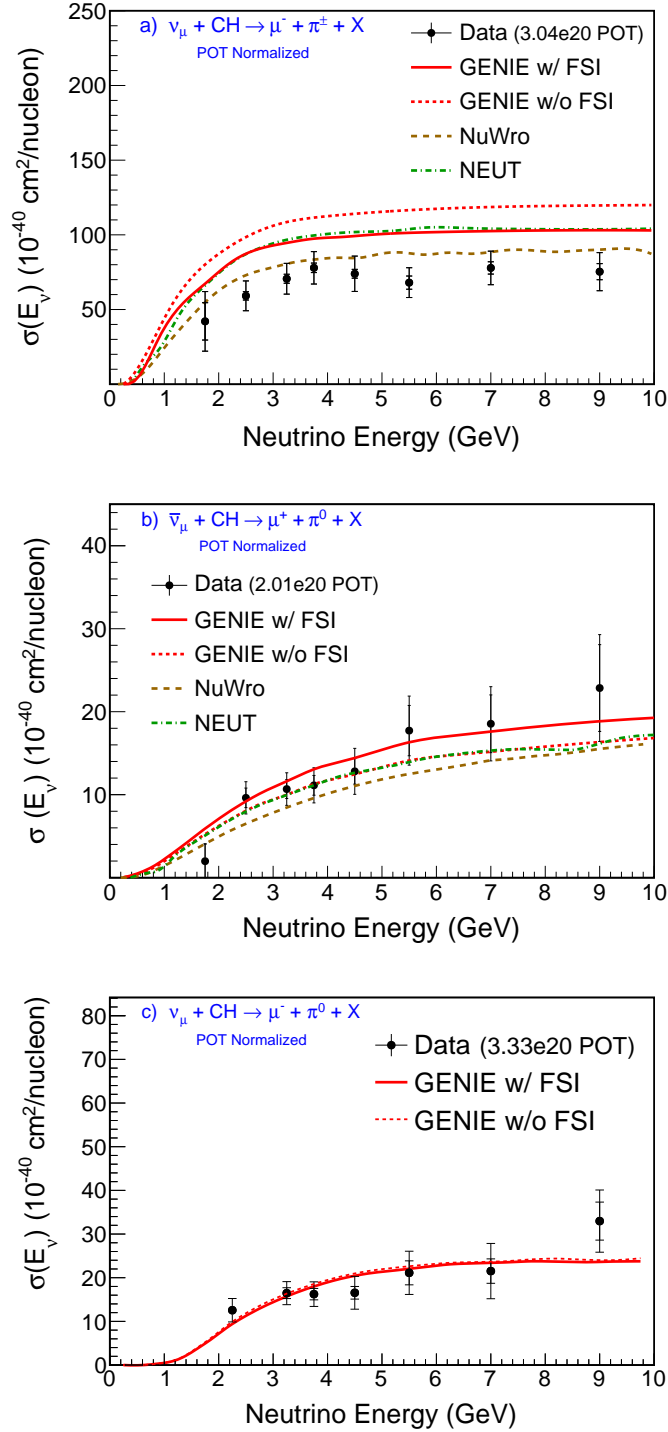


FIG. 10.6: Cross sections as a function of neutrino energy E_ν for the samples $\nu_\mu\text{-CC}(\pi^+)$ (a), $\bar{\nu}_\mu\text{-CC}(\pi^0)$ (b), and $\nu_\mu\text{-CC}(\pi^0)$ (c). The cross section for $\nu_\mu\text{-CC}(\pi^+)$ is higher than the other two samples by a factor of more than two times. The cross section for $\nu_\mu\text{-CC}(\pi^0)$ is $\sim 16\%$ higher than the $\bar{\nu}_\mu\text{-CC}(\pi^0)$ sample. The samples with π^0 exhibit a gradual increase in the cross section for the measured region, while the charged pion sample reaches its plateau around 3.5 GeV.

10.3 Comparisons of systematic uncertainties

The systematic uncertainties for all of the three samples are evaluated identically and are grouped into five categories. The first group contains the detector response uncertainties, the second is for neutrino interaction model uncertainties, the third group contains the uncertainties for the simulated final-state interactions (FSI), the fourth includes the uncertainties related to the incoming neutrino flux, and the fifth group includes other uncertainties such as uncertainties arising from the background subtraction and unfolding procedures.

Figure 10.7 shows the total fractional uncertainties for all three analyses. Overall, the lowest total fractional uncertainties are observed in the ν_μ -CC (π^+) sample, followed by the ν_μ -CC (π^0), and the highest total fractional uncertainties are observed in the $\bar{\nu}_\mu$ -CC (π^0) sample which is statistically limited. The leading systematic uncertainty group in the ν_μ -CC (π^+) sample is the detector response uncertainties, then the flux uncertainties. For the $\bar{\nu}_\mu$ -CC (π^0) sample the highest contribution to the total fractional error is from the cross-section model uncertainties followed by the Other category which contains the background normalization uncertainty. The cross-section model uncertainties are also the leading uncertainty group in the ν_μ -CC (π^0) sample followed by the detector response uncertainties. The FSI model uncertainties have similar contributions to the total fractional uncertainty in each sample.

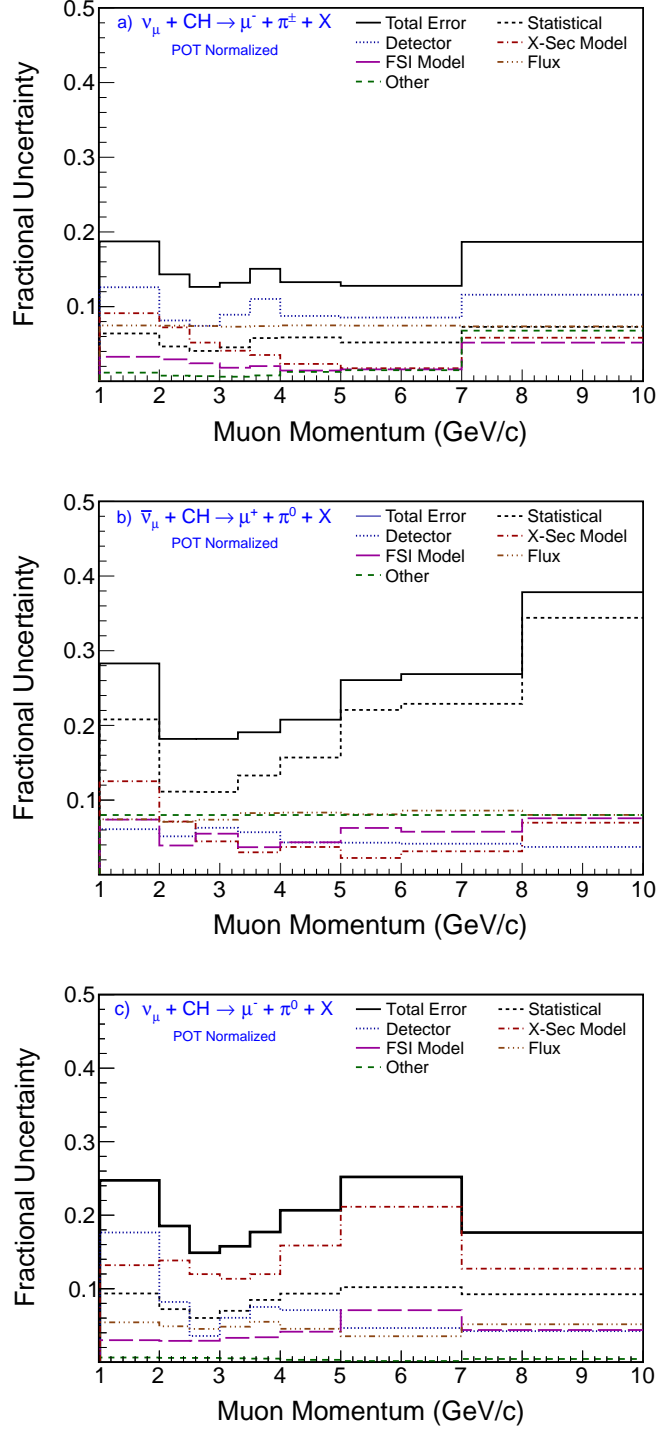


FIG. 10.7: Total fractional uncertainties for $d\sigma/dP_\mu$ for the samples ν_μ -CC (π^+) (a), $\bar{\nu}_\mu$ -CC (π^0) (b), and ν_μ -CC (π^0) (c). The leading systematic uncertainties in the ν_μ -CC (π^+) sample are the detector response uncertainties. However in $\bar{\nu}_\mu$ -CC (π^0) and ν_μ -CC (π^0), the cross-section model uncertainties are leading as a group. The anti-neutrino sample is dominated by statistical uncertainties.

10.4 Comparisons of component processes

In this Section the following processes are studied: 1) pion production via the $\Delta(1232)$ resonance, 2) pion production via other baryon resonances, and 3) Non-resonant pion production. In addition to these processes, the ν_μ -CC (π^+) sample has a small contribution from CC coherent single pion production. The charged current single π^0 final states cannot occur via CC coherent single pion production due to charge conservation.

In ν_μ -CC (π^+) the leading reactions involve the $\Delta^{+,++}$ production with a $\approx 50\%$ contribution, followed by non-resonant pion production, and higher mass N^* states. For the $\bar{\nu}_\mu$ -CC (π^0) sample, Δ^0 production is dominant, however the higher-mass baryon resonance contribution exceeds the non-resonant pion production. For the ν_μ -CC (π^0) sample, Δ^+ production is dominant with a $\approx 50\%$ contribution; non-resonant pion production has a $\approx 28\%$ contribution and the higher baryon resonances have a $\approx 22\%$ contribution.

The reaction compositions for differential cross sections in muon momentum and muon production angle for the all three samples are shown in Fig. 10.8 and Fig. 10.9 respectively. The dominant processes are distributed uniformly over $d\sigma/dP_\mu$ and $d\sigma/d\theta_\mu$ in all three samples. The CC coherent contribution in the ν_μ -CC (π^+) sample, also has a uniform distribution in momentum. However, the CC coherent contribution tends to populate lower angles in muon production angle.

The reaction compositions for differential cross sections in Q^2 for all three samples are shown in Fig. 10.10. The coherent scattering contribution in the ν_μ -CC (π^+) sample is mostly concentrated at $Q^2 < 0.4 \text{ GeV}^2$. In all samples, at high Q^2 , the non-resonant contribution is larger than the contributions from the $\Delta(1232)$ and from other baryon resonances. For all samples the $Q^2 \leq 0.1 \text{ GeV}^2$ region shows a significant rate difference between the data and the simulation. The reason could be due to long-range nucleon-nucleon correlations, usually treated with the Random Phase Approximation (RPA) [93, 94], or to Pauli blocking. In GENIE Pauli blocking and RPA are not included for any of the processes discussed in this Section. A

possible solution is to suppress the CC resonance events in the low- Q^2 region in the simulation.

Figure 10.11 shows the reaction composition of cross sections as a function of neutrino energy E_ν for all three samples. The major processes distribute uniformly over the whole neutrino energy range.

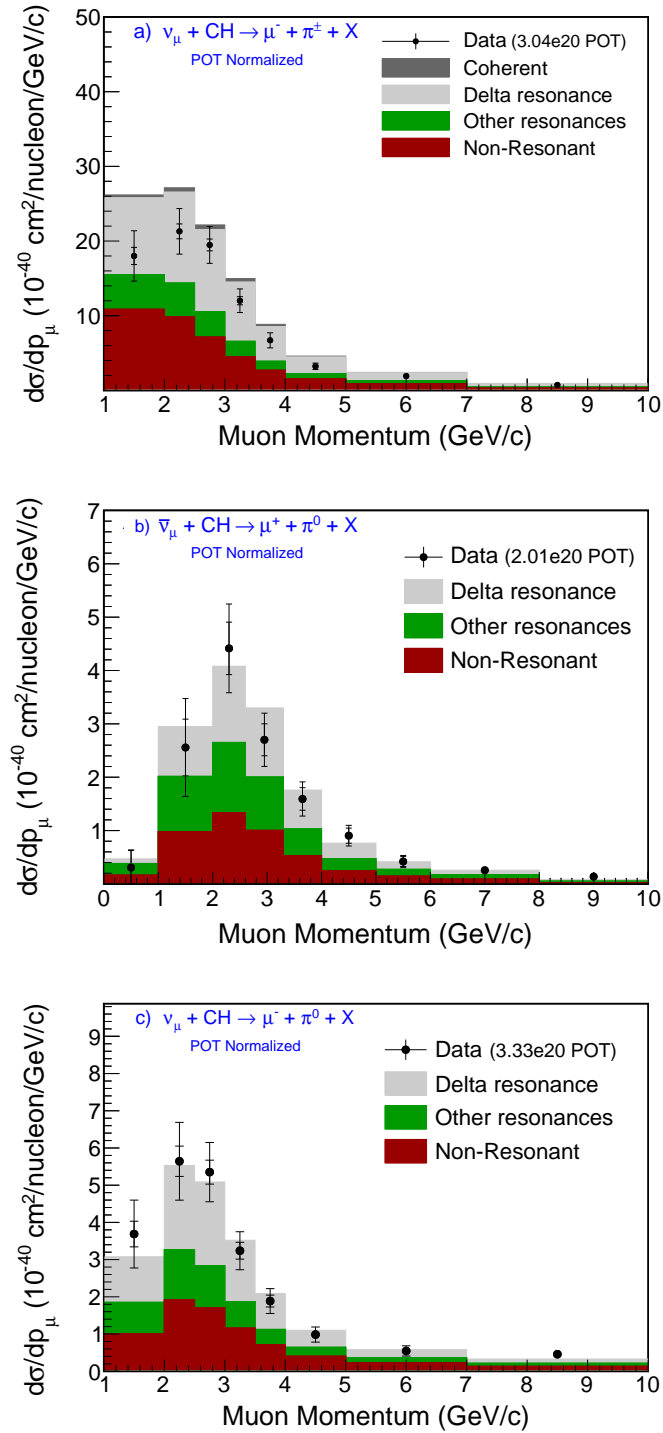


FIG. 10.8: Reaction compositions for $d\sigma/dP_\mu$ for the samples $\nu_\mu\text{-CC}(\pi^+)$ (a), $\bar{\nu}_\mu\text{-CC}(\pi^0)$ (b), and $\nu_\mu\text{-CC}(\pi^0)$ (c). The dominant processes distribute fairly uniformly in all samples.

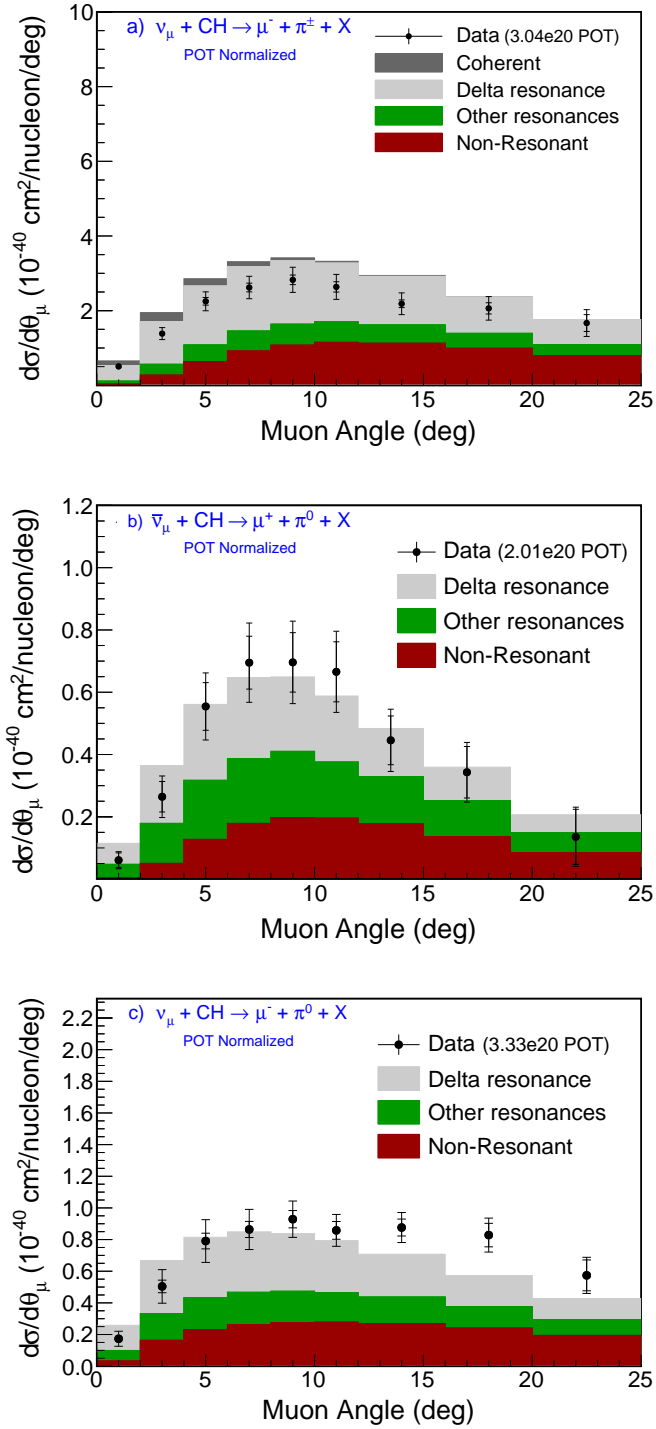


FIG. 10.9: Reaction compositions for $d\sigma/d\theta_{\mu}$ for the samples ν_{μ} -CC(π^{+}) (a), $\bar{\nu}_{\mu}$ -CC(π^{0}) (b), and ν_{μ} -CC(π^{0}) (c). The dominant processes distribute uniformly over all samples. The CC coherent pion production contribution in the ν_{μ} -CC(π^{+}) sample is observed at lower muon angles.

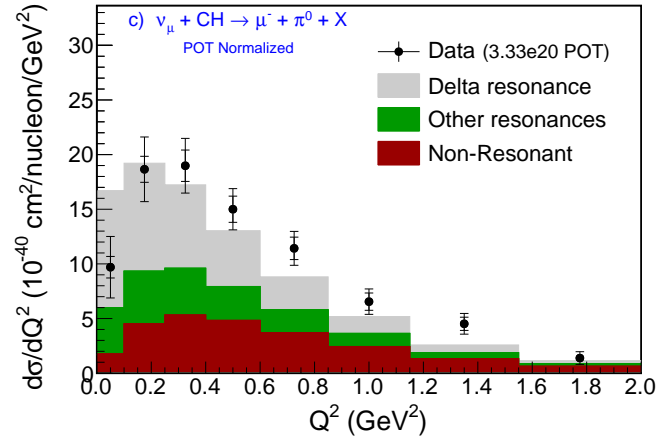
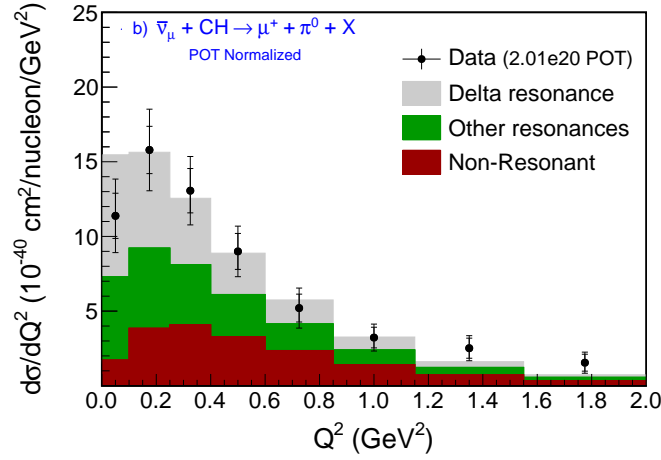
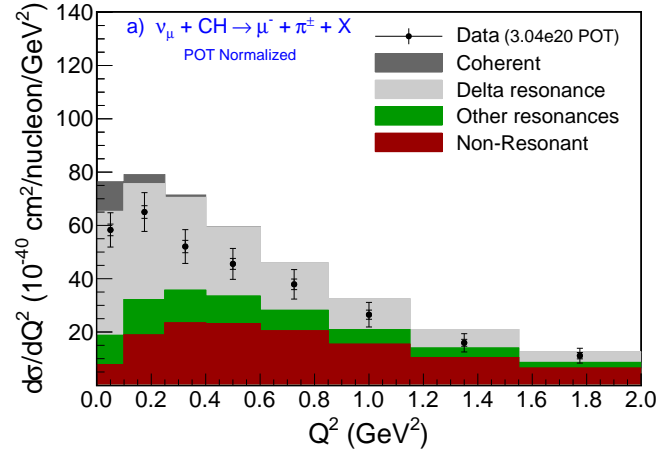


FIG. 10.10: Reaction compositions for $d\sigma/dQ^2$ for the samples ν_μ -CC(π^+) (a), $\bar{\nu}_\mu$ -CC(π^0) (b), and ν_μ -CC(π^0) (c). In all samples there is a data-simulation disagreement in the first bin. The non-resonant contribution dominates at higher Q^2 values.

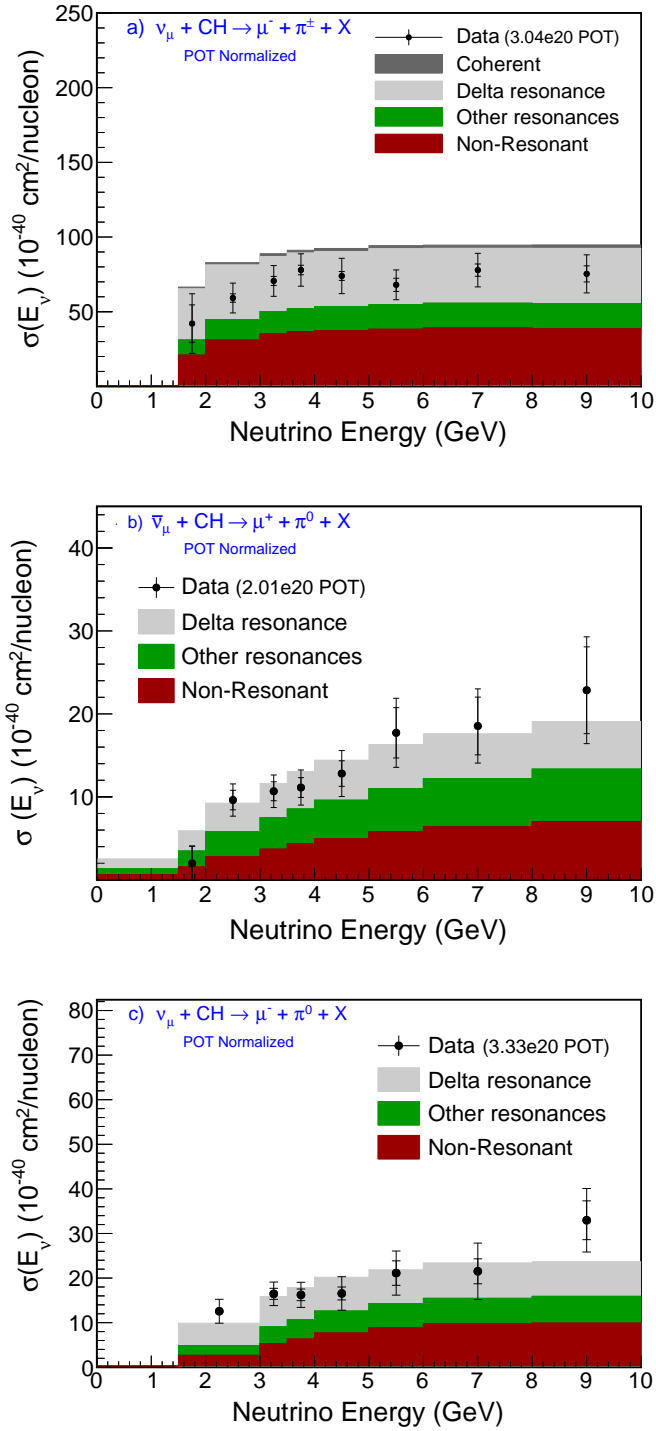


FIG. 10.11: Reaction compositions for cross section as a function of neutrino energy for the samples ν_μ -CC (π^+) (a), $\bar{\nu}_\mu$ -CC (π^0) (b), and ν_μ -CC (π^0) (c). The dominant processes distribute uniformly in all samples.

10.5 Comparisons of pion FSI channels

The FSI processes predicted by GENIE for $d\sigma/dQ^2$ for all three samples are displayed in Fig. 10.12, where the simulation has been area-normalized to the data to elicit differences in distribution shapes. The ν_μ -CC (π^+) and $\bar{\nu}_\mu$ -CC (π^0) samples show good shape agreement between the data and the GENIE prediction in the 1σ total error range. In the ν_μ -CC (π^0) sample the data is observed to be lower than the simulation prediction in the low- Q^2 region. In all samples, non-interacting pions are the leading category followed by pion inelastic scattering. All FSI processes are observed to be uniformly distributed over the whole Q^2 range.

The FSI processes for pion variables are compared with the two previous pion production results by MINERvA. The earliest measurement is for charged pion production in the MINERvA detector [49]. In that analysis the hadronic invariant mass is limited to 1.4 GeV for the charged pion kinematical distributions. Also, the neutrino energy is limited to the range $1.5 < E_\nu < 10$ GeV. The FSI decomposition for differential cross sections for pion kinetic energy is given in Fig. 10.13, where the plots are shape-normalized. As explained previously, the kinetic energy ranges for charged pions and for neutral pions are different. In both samples, the leading category is non-interacting pions followed by the inelastic pion scattering inside the nucleus. The inelastic pion scattering distributions are observed to be shifted to lower kinetic energy regions in both samples. The charge exchange process for the ν_μ -CC (π^+) sample is much lower than for the ν_μ -CC (π^0) sample.

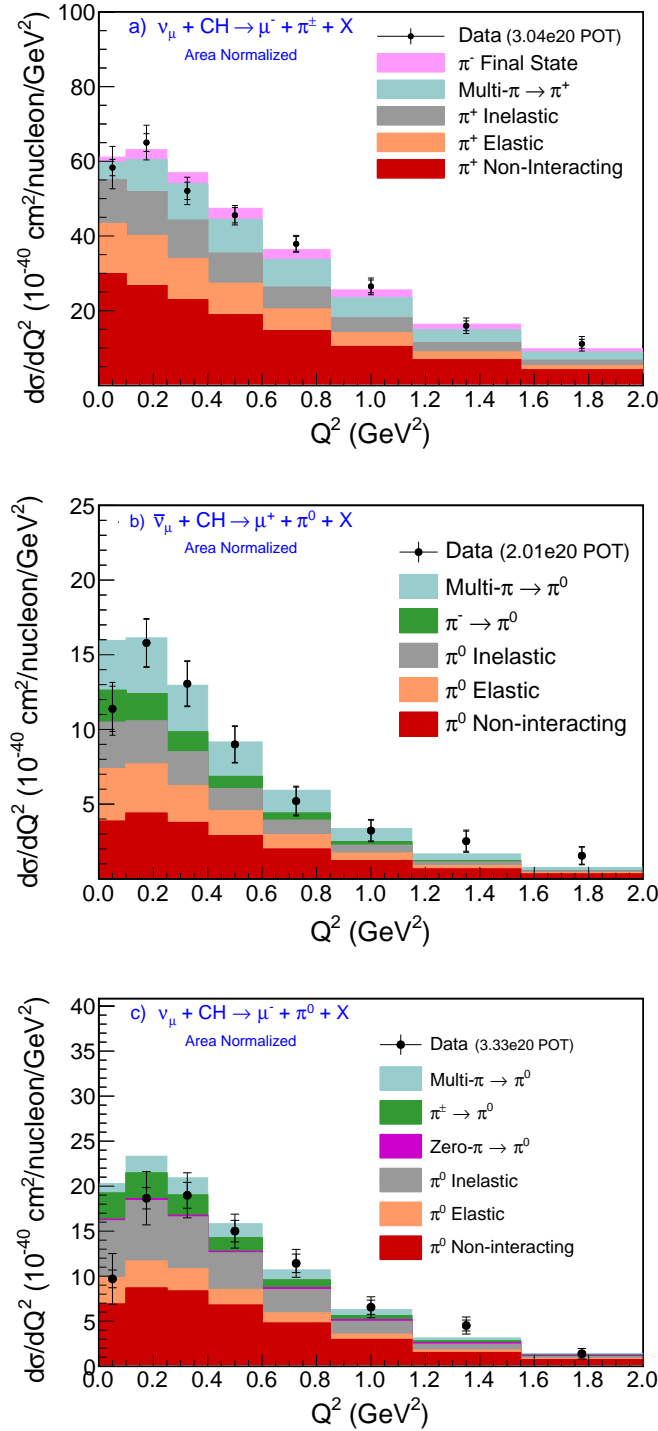


FIG. 10.12: FSI decompositions for $d\sigma/dQ^2$ for the samples ν_μ -CC(π^+) (a), $\bar{\nu}_\mu$ -CC(π^0) (b), and ν_μ -CC(π^0) (c). The simulation is area-normalized to the data in all samples. Non-interacting pions is the leading category in all samples. (Plots (a) and (b) are from Ref. [90].)

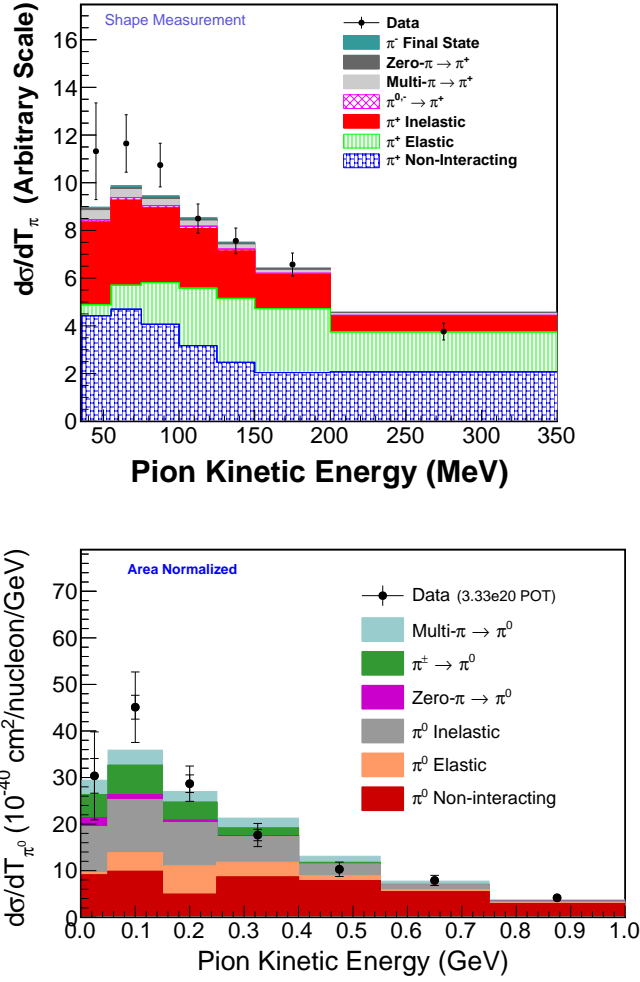


FIG. 10.13: FSI decompositions for $d\sigma/dT_\pi$ for ν_μ -CC (π^+) (top) and ν_μ -CC (π^0) (bottom). The simulation is area-normalized to the data in all samples. Pion inelastic scattering tends to populate the lower-energy bins. Charge exchange is more prevalent in the ν_μ -CC (π^0) sample than in the charged pion sample. (The top plot is from Ref. [49].)

The second pion production result obtained by MINERvA is with CC single π^0 production in the anti-neutrino beam [95]. Cross sections in that analysis are obtained without a limit on hadronic invariant mass W and with a neutrino energy range $1.5 < E_\nu < 20$ GeV. The FSI decomposition for the differential cross-section measurements for pion momentum and production angle are shown in Figs. 10.14 and 10.15 respectively. In both momentum and angle distributions, all FSI processes have similar shapes between two samples. The rates for non-interacting, elastic, and inelastic scatterings are comparable. The charge exchange processes in both samples are also very similar. The Multi- $\pi \rightarrow \pi^0$ category in the $\bar{\nu}_\mu$ -CC (π^0) sample is much higher than in the ν_μ -CC (π^0) sample. For both of the π^0 samples the inelastic scattering process is more prominent in the low momentum and higher angle regions, while the other FSI processes are distributed more uniformly.

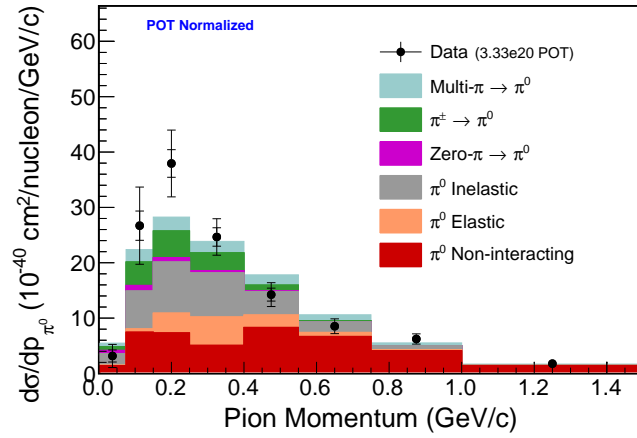
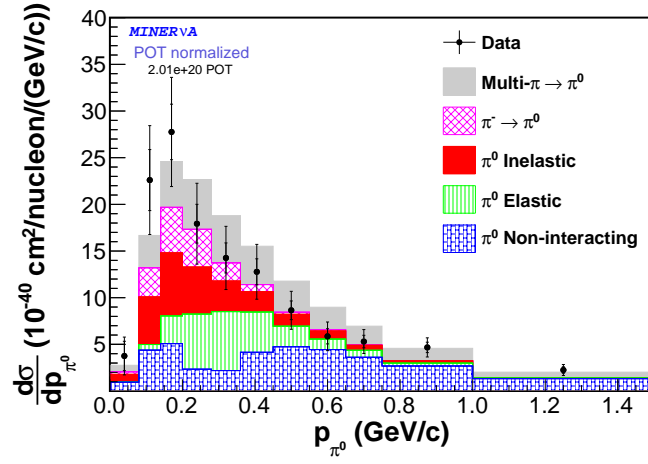


FIG. 10.14: FSI decompositions for $d\sigma/dP_{\pi^0}$ for $\bar{\nu}_\mu$ -CC (π^0) (top) and ν_μ -CC (π^0) (bottom). The rate for Multi- $\pi \rightarrow \pi^0$ is higher in the $\bar{\nu}_\mu$ -CC (π^0) sample. Other processes have similar rates and distributions in both samples. (The top plot is from Ref. [95].)

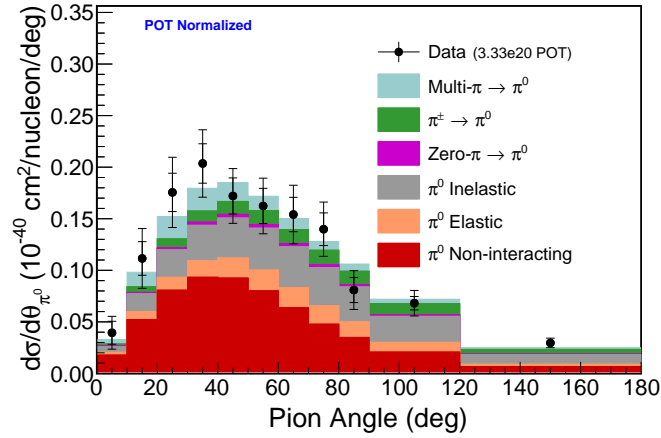
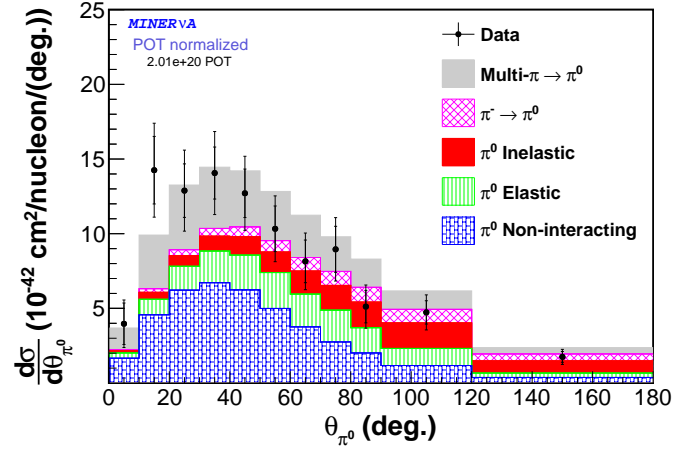


FIG. 10.15: FSI decompositions for $d\sigma/d\theta_{\pi^0}$ for $\bar{\nu}_\mu$ -CC (π^0) (top) and ν_μ -CC (π^0) (bottom). The rate for Multi- $\pi \rightarrow \pi^0$ is higher in the $\bar{\nu}_\mu$ -CC (π^0) sample. Other processes have similar rates and distributions in both samples. (The top plot is from Ref. [95].)

Chapter 11

Physics of Charged Current Single Pion Production

11.1 Suppression of baryon resonances at low Q^2

The disagreement between data and simulation at low- Q^2 can be seen in Fig. 9.9. This disagreement was reduced by applying a low- Q^2 suppression factor for resonance events in the MiniBooNE and MINOS experiments.

A low- Q^2 suppression factor for charged-current $\Delta(1232)$ resonance events was applied in analyses of the MiniBooNE data [87, 96]. The MINOS collaboration, using a sample that was enriched with baryon resonance events, fitted the Q^2 distribution over the range $0 \leq Q^2 < 0.6 \text{ GeV}^2$ in order to determine a functional form for a low- Q^2 suppression factor [97]. The data-driven low- Q^2 suppression function found by MINOS is the following:

$$f(Q^2) = A \left\{ 1 + \exp \left(1 - \frac{\sqrt{Q^2}}{Q_0} \right) \right\}^{-1} \quad (11.1)$$

In this analysis, the same functional form is used and the Q^2 cross-section measurement is fitted over the range $0 \leq Q^2 < 0.4 \text{ GeV}^2$. During the fit, the parameter A is fixed to be equal to 1.0 and the parameter Q_0 is varied. The best fit parameters for the MINOS and MINERvA experiments are given in Table 11.1. The low- Q^2 suppression function depends on the true Q^2 of the event and all the charged current baryon resonance (CC-RES) events are reweighted by this factor. The Q^2 -dependent weight functions based on MINERvA and MINOS fit results are shown in Fig. 11.1.

	MINOS	MINERvA
A	1.010	1.0
Q_0 [GeV]	0.156	0.116

TABLE 11.1: Fit parameters for the low- Q^2 suppression function. The Q_0 parameter for the MINERvA experiment is smaller than the MINOS experiment and it leads to a milder suppression. The fit parameters for the MINOS experiment are from Ref. [97].

After applying the CC-RES suppression based on the low- Q^2 fit, the most significant improvement is observed in the Q^2 and muon production angle distributions. Figure 11.2 shows the differential cross-section measurement for Q^2 and the muon production angle with and without the suppression factor. By design, the low- Q^2 dis-

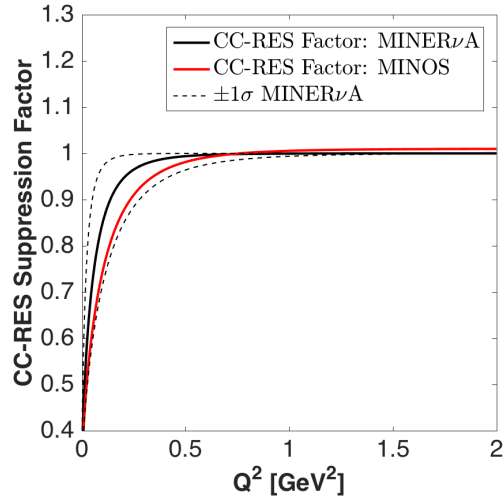


FIG. 11.1: Q^2 -dependent weight function applied to all charged CC-RES events. The MINERvA CC-RES suppression is smaller than the MINOS suppression for the same Q^2 value. The MINOS suppression factor lies within the $\pm 1\sigma$ range of the MINERvA factor.

tribution improves significantly after the suppression. The suppression also improves the muon angle distribution at small (forward) production angles.

In other cross-section variables, minimal shape differences are observed after the CC-RES suppression. An overall normalization reduction on the GENIE estimation is expected due to CC-RES event reweighting. Figures 11.3 and 11.4 show the other cross-section measurements. In all of the variables, the suppression changes the shape of the distributions slightly and reduces the overall normalization for the GENIE estimation.

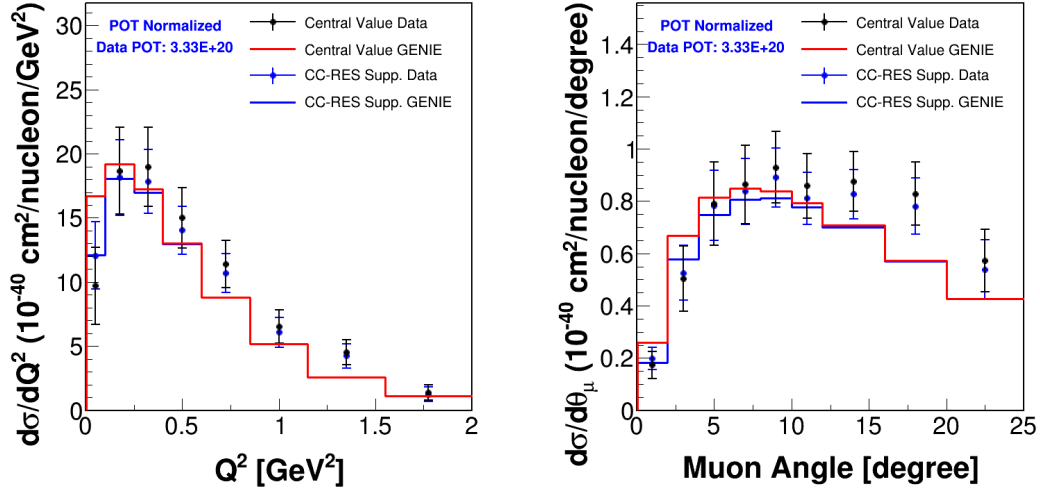


FIG. 11.2: Differential cross-section measurements for Q^2 (left) and for muon production angle (right) with and without the CC-RES suppression factor. The agreement between the data and the simulation significantly improves in the low- Q^2 region. The low- Q^2 suppression factor also improves the agreement for low muon angles.

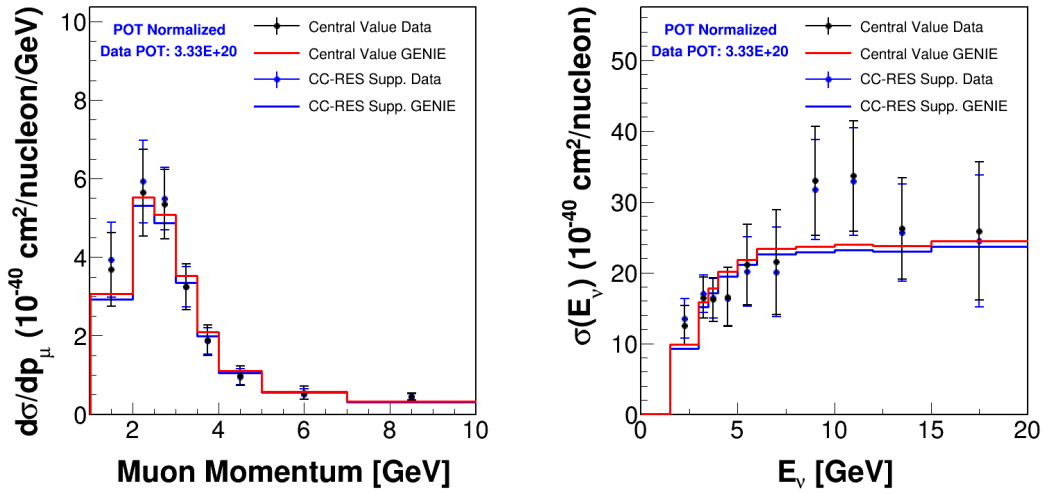


FIG. 11.3: Cross sections for muon momentum (left) and for neutrino energy (right) with and without the CC-RES suppression factor. There is a larger reduction for the GENIE estimation in the lower muon momentum range than in the higher momentum region. For the cross section versus E_ν there is no shape difference between the two samples; the overall normalization is lower for the CC-RES suppressed sample.

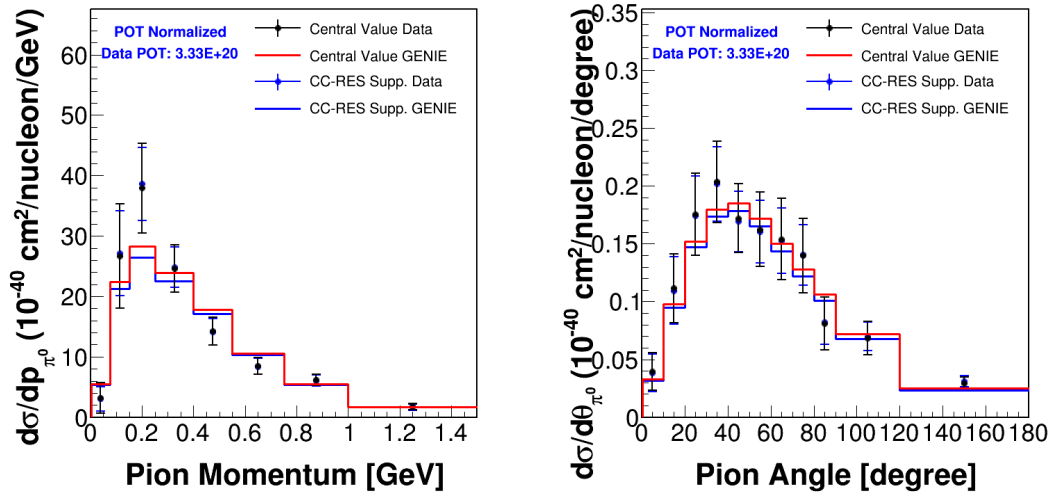


FIG. 11.4: Cross sections for pion momentum (left) and for production angle (right) with and without the CC-RES suppression factor. The CC-RES suppression is not applied in central value estimations. There is a minimal shape difference for pion momentum after the CC-RES suppression.

11.2 Q^2 distribution dependence on different E_ν ranges

This study seeks to find evidence for the interference term between vector form factors and axial-vector form factors that are used to calculate $d\sigma/dQ^2$. The form-factor contributions to $d\sigma/dQ^2$ for constant neutrino energies $E_\nu = 2$ GeV and $E_\nu = 6$ GeV are shown in Fig. 11.5. The V-A interference dependence to the neutrino energy is shown on the plots (red curve) and it is more significant in $E_\nu = 2$ GeV case. More importantly, in $d\sigma/dQ^2$ the V-A interference term is constructive for neutrinos and is destructive for antineutrinos.

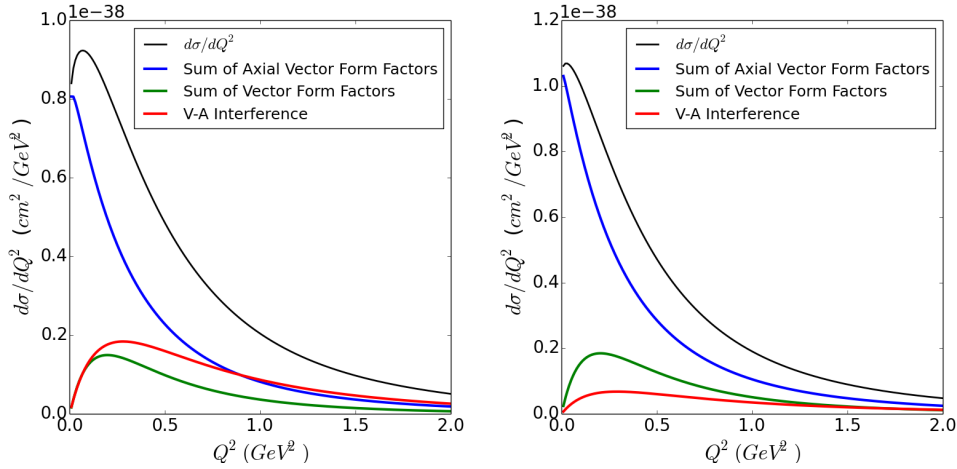


FIG. 11.5: Vector and axial-vector contributions to $d\sigma/dQ^2$ for $E_\nu = 2$ GeV (left) and $E_\nu = 6$ GeV (right). The V-A interference term strength is larger at $E_\nu = 2$ GeV than at $E_\nu = 6$ GeV. From Ref. [98].

To obtain evidence for V-A interference term, the differential cross-section measurement for the four-momentum transfer Q^2 is repeated for two different neutrino energy ranges. The first neutrino energy range is $1.5 \leq E_\nu < 4$ GeV and the second neutrino energy range is $4 \leq E_\nu < 10$ GeV. The 4 GeV cut divides the sample into subsamples of comparable statistics. The shape of the Q^2 differential cross sections are fitted to an exponential decay function ($y = a \exp(-bx)$) and the slope parameter, b , is obtained for the low- E_ν and high- E_ν ranges. The fit is performed for $Q^2 > 0.25$ GeV² to reduce the effects of low- Q^2 data-simulation disagreements in the fit.

The harder Q^2 distribution of the high- E_ν sample shown in Fig. 11.6 has a more shallow slope than does the low- E_ν sample that is shown in Fig. 11.7. The results obtained for the ν_μ -CC (π^0) sample are compared with those of the $\bar{\nu}_\mu$ -CC (π^0) sample. The slope values for both samples are given in Table 11.2. Only a small difference in the slopes is observed for the high- E_ν range for both ν_μ -CC (π^0) and $\bar{\nu}_\mu$ -CC (π^0) samples. However, the slope for the antineutrino sample is $\sim 37\%$ larger than the neutrino sample in the low- E_ν range. Since V-A interference term is constructive for neutrinos and destructive for antineutrinos, the slope difference in the low- E_ν range is expected. However, due to the large uncertainties on the antineutrino slope parameter, it is not possible to make a solid conclusion for the measurement of V-A interference term in the $d\sigma/dQ^2$ distributions.

	$1.5 \leq E_\nu < 4 \text{ GeV}$	$4 \leq E_\nu < 10 \text{ GeV}$
Slope for ν_μ -CC (π^0)	-2.7 ± 0.2	-1.0 ± 0.2
Slope for $\bar{\nu}_\mu$ -CC (π^0)	-3.7 ± 1.1	-1.1 ± 0.4

TABLE 11.2: Slopes of $d\sigma/dQ^2$ for ν_μ -CC (π^0) and $\bar{\nu}_\mu$ -CC (π^0) samples. In the high- E_ν range both samples have similar slopes on the $d\sigma/dQ^2$ curve. However, in the low- E_ν range the anti-neutrino sample has a larger slope than does the neutrino sample.

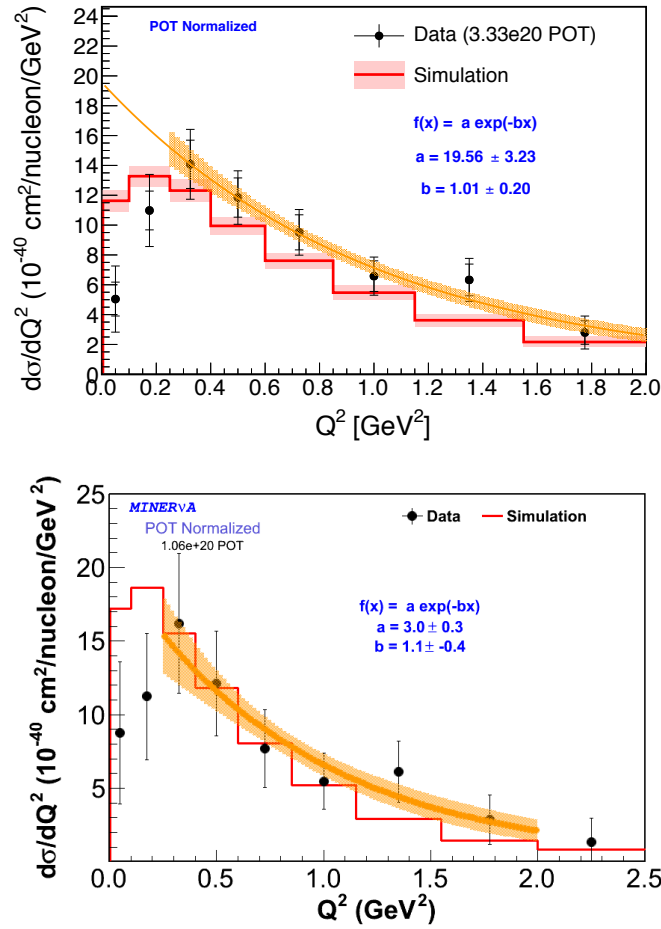


FIG. 11.6: The $d\sigma/dQ^2$ distributions for the $4 \leq E_\nu < 10$ GeV range for ν_μ -CC (π^0) (top) and $\bar{\nu}_\mu$ -CC (π^0) (bottom) samples. The distributions are fitted to an exponential decay function (orange line with error bars) and the slopes are measured. The slopes are very similar for both ν_μ -CC (π^0) and $\bar{\nu}_\mu$ -CC (π^0) samples for this high E_ν range.

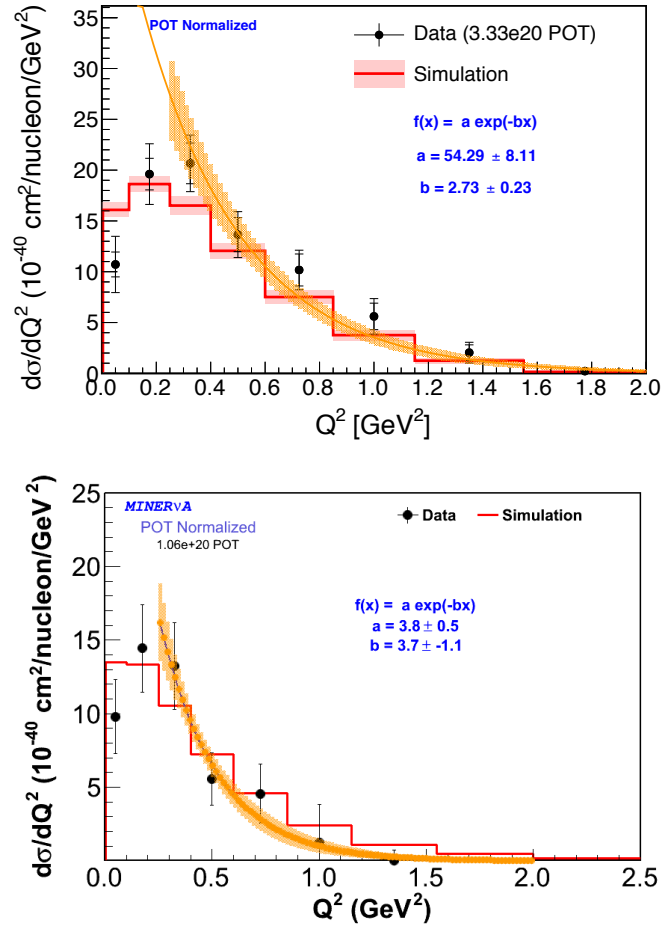


FIG. 11.7: The $d\sigma/dQ^2$ distributions for the $1.5 \leq E_\nu < 4$ GeV range for the $\nu_\mu\text{-CC}(\pi^0)$ (top) and $\bar{\nu}_\mu\text{-CC}(\pi^0)$ (bottom) samples. The distributions are fitted to an exponential function (orange line with error bars) and the slopes are measured. The $\bar{\nu}_\mu\text{-CC}(\pi^0)$ sample has a larger slope than does the $\nu_\mu\text{-CC}(\pi^0)$ sample.

11.3 Distributions for Δ^+ (1232) enriched sample

A subsample enriched in Δ^+ (1232) resonance production is obtained by limiting the maximum hadronic invariant mass W to <1.4 GeV. The selected sample is estimated to contain 65% Δ resonance, 27% non-resonant pion production and 8% of other baryon resonances. The distributions for proton-pion invariant mass and Δ^+ (1232) polarization angles are obtained for events that have a reconstructed proton in the final state. The distributions obtained for the data are unfolded to remove the detector response effects and then efficiency-corrected to remove the acceptance effects. The distributions shown in the following Sections include all data corrections.

11.3.1 Proton-Pion invariant mass distribution

The invariant mass of the proton-pion system, $M_{p\pi}$, is calculated using Eq. (11.2) and the data and the simulation distributions for the $M_{p\pi}$ are given in Fig. 11.8. The data are higher than the simulation prediction in the Δ resonance region $1.15 < M_{p\pi} < 1.30$ GeV. The excess in this particular region suggests that the data have a larger Δ^+ (1232) resonance contribution than is predicted by the simulation.

$$M_{p\pi} = \sqrt{(E_p + E_\pi)^2 - |\vec{p}_p + \vec{p}_\pi|^2}. \quad (11.2)$$

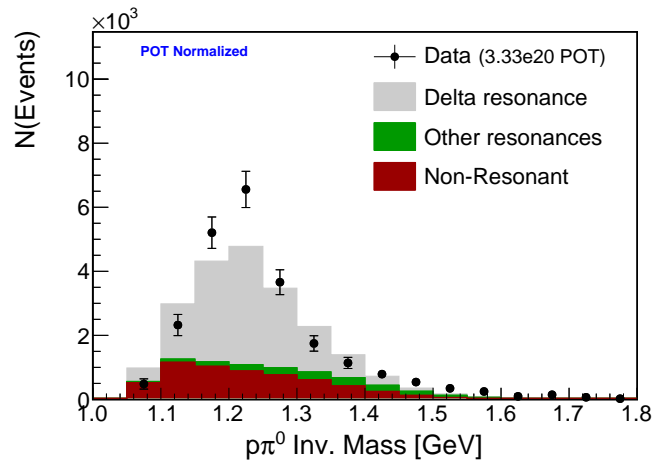


FIG. 11.8: Proton-pion invariant mass for the data and the simulation. The data lies higher than the simulation prediction in the Δ^+ (1232) resonance region.

11.3.2 Polarization in the Δ^+ (1232) region

Polarization angles for the $p\pi^0$ system are calculated using a formalism that is suited to this measurement [99, 100, 17, 21]. The coordinate system and the polarization angles are defined in the $p\pi$ rest frame. The four-momentums of the neutrino, muon, pion and proton are Lorentz boosted to the $p\pi$ rest frame for the calculation of the axes. A right-handed coordinate system is defined with the z -axis along the momentum transfer direction $(\vec{P}_\nu - \vec{P}_\mu)$, the y -axis along the production plane normal $(\vec{P}_\nu \times \vec{P}_\mu)$, and x -axis along the cross-product of the other two axes $(\vec{y} \times \vec{z})$. This coordinate system is depicted in Fig. 11.9. The angle θ is the angle between the pion momentum (\vec{P}_π) and the z -axis. The angle ϕ is the angle between the projection of pion momentum on the $x - y$ plane and x -axis.

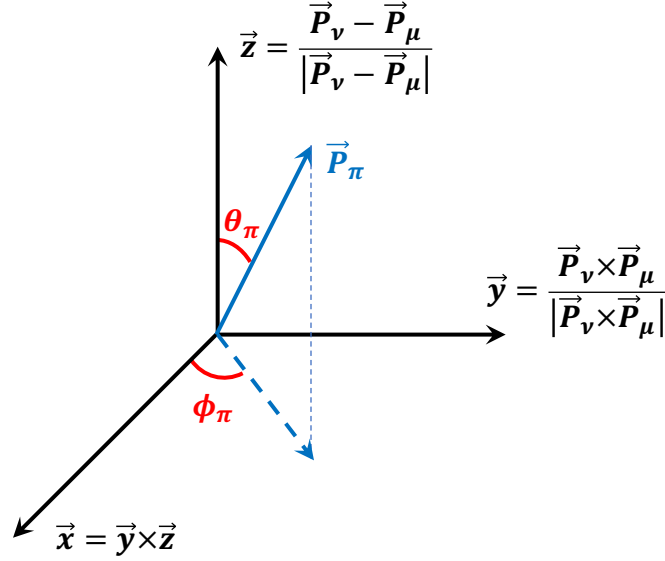


FIG. 11.9: Coordinate system used for $p\pi$ polarization calculations. The system is right-handed where the z -axis is along the momentum-transfer direction and the y -axis is along the production plane-normal. The angle θ is measured with respect to the z -axis and the angle ϕ is measured with respect to the x -axis.

The zenith-angle $\cos(\theta)$ is calculated for the data and compared with the simulation predictions for each interaction type. Figure 11.10 shows the data versus simulation predictions for $\cos(\theta)$. The contribution from each interaction type is isotropic except in the first bin where all interaction types have a modestly increased rate. Roughly speaking, the simulation prediction for $\cos(\theta)$ is isotropic. There is a slight

shape difference between the data and the simulation prediction. The data shape of $\cos(\theta)$ is fitted to three spherical harmonics ($y = a_{00} + a_{10} \cos \theta + a_{20} \cos^2 \theta$) based on the formula proposed by Rein-Sehgal paper [10]. The best fit is obtained for $a_{00} = 1931 \pm 122$, $a_{10} = 294.1 \pm 140.5$, and $a_{20} = -1081 \pm 277.4$. Figure 11.11 shows the fit result for the data. The $\chi^2/d.o.f.$ with respect to the fit result is 0.49 and with respect to the simulation prediction is 0.76. This is inconclusive evidence for anisotropy of the $\cos(\theta)$ distribution, since the difference with the simulation prediction which assumes isotropic Δ^+ decay is very small.

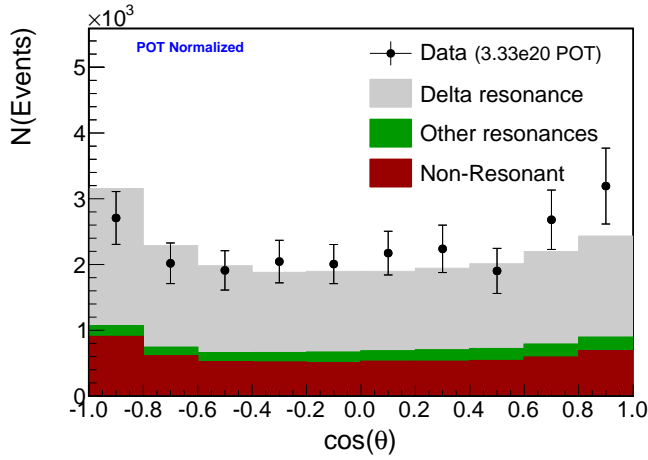


FIG. 11.10: The $\cos(\theta)$ distribution for the data and the simulation for each interaction type. All interaction types have an isotropic distribution except for the first bin.

The angle ϕ is also calculated for the data and compared with the simulation predictions for each interaction type. Figure 11.12 shows the angle ϕ distribution for the data and simulation. The simulation prediction for each interaction type is isotropic. The data distribution has a shape that suggests a negative sine curve. Consequently the data points have been fitted to the functional form $y = a + b \sin \phi$, and the best fit is obtained for $a = 2258 \pm 145$ and $b = -482.5 \pm 204.9$. The fit results for the data are shown in Fig. 11.13. The $\chi^2/d.o.f.$ with respect to the fit result is 1.19 and with respect to the simulation prediction is 1.52. Thus, the $\chi^2/d.o.f.$ difference between the shape fit and simulation prediction is not very significant.

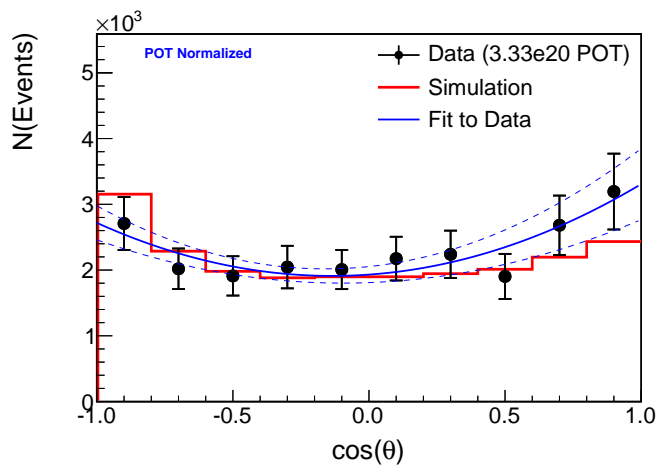


FIG. 11.11: Fitted $\cos(\theta)$ distribution for the data. The data have a slightly better agreement with the fitted curve than the simulation prediction.

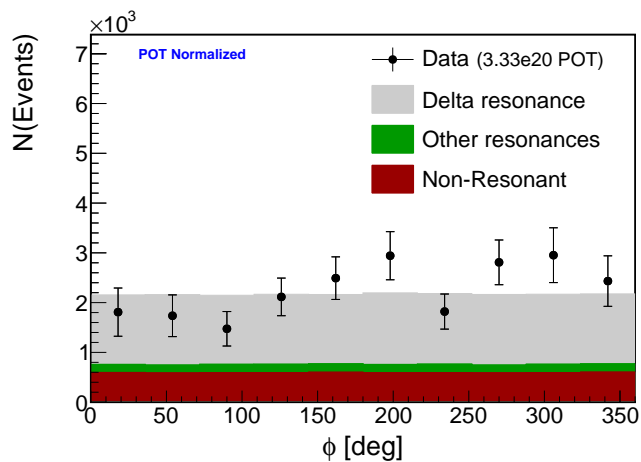


FIG. 11.12: Angle ϕ distribution for the data and the simulation. The simulation prediction is isotropic for all three interaction types.

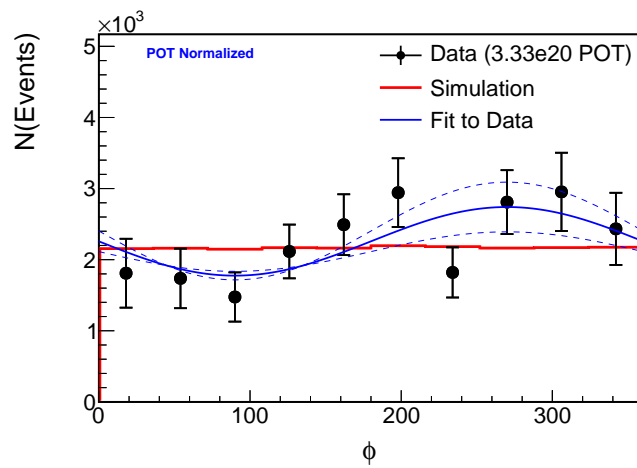


FIG. 11.13: Fitted angle ϕ distribution for the data. The data have a slightly better agreement with the fitted curve ($y = a + b \sin \phi$) than with the simulation prediction.

11.4 Distribution of hadronic invariant mass

11.4.1 Data versus Simulation disagreement

The hadronic invariant mass, W , distribution for the data and the simulation are given in Fig. 5.30. The simulation prediction fails to match the data shape in lower and higher W regions; a shift towards lower W relative to the simulation is observed in the data distribution. The amount of shift in the data is estimated by shifting the simulation prediction by different amounts and calculating the χ^2 with respect to data for each shift amount. The lowest χ^2 is obtained for the -20 MeV shift and the χ^2/dof is improved from 6.9 to 1.8. The data versus simulation agreement before and after the -20 MeV shift is shown in Fig. 11.14. The shifted simulation has a better agreement with data for the low W and high W regions. The same fitting procedure is repeated for the background subtracted data and the simulation prediction for the signal events. Again the lowest χ^2 is obtained for the -20 MeV shift and the χ^2/dof is improved from 6.6 to 1.7. The background subtracted data versus signal events before and after the -20 MeV shift is displayed in Fig. 11.15.

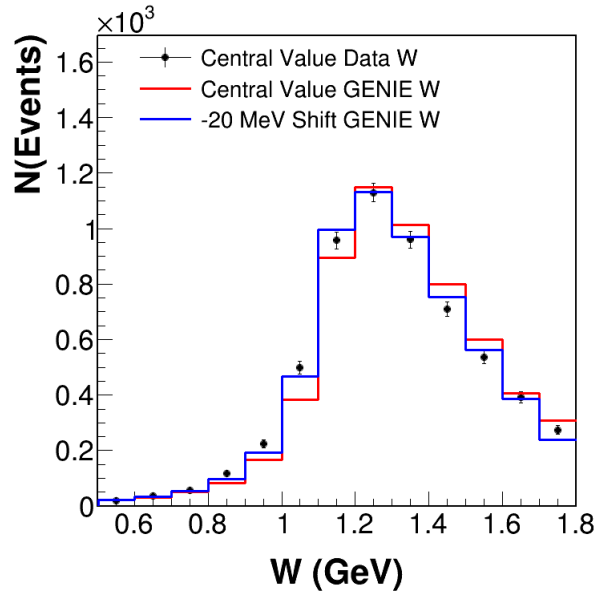


FIG. 11.14: Hadronic invariant mass W distributions for the data and for the simulation. The GENIE prediction with a -20 MeV shift (blue) has better agreement with data than does the central value prediction (red). Only statistical errors are shown for the data.

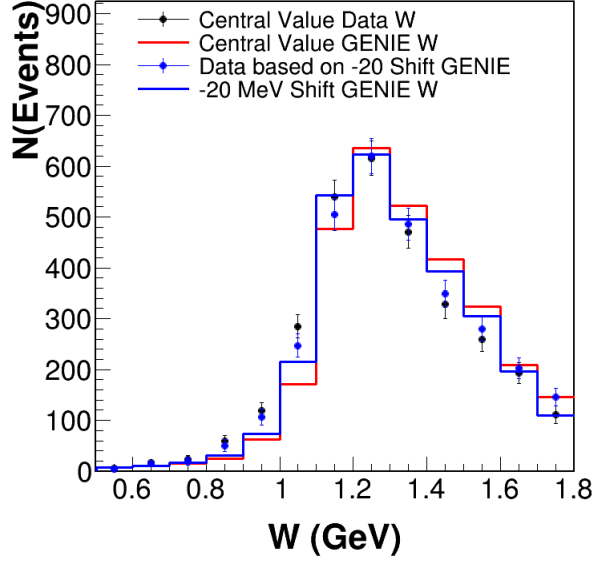


FIG. 11.15: Hadronic invariant mass W distributions for the background subtracted data and for the simulation prediction to signal events. The GENIE prediction with a -20 MeV shift (blue) has better agreement with data than does the central value prediction (red). Only statistical errors are shown for the data.

11.4.2 Decomposition of W by interaction type

In the CC single π^0 production channel, the signal events have contributions from three interaction types. The major contribution is from the Δ^+ (1232) resonance, the second leading contribution is from non-resonant pion production, and the third contribution is from other baryon resonances. The shape of each interaction type has been extracted from the simulation and fitted to different functional forms. The W range $0.8 < W < 1.8$ GeV is used for all of the shape fits.

For the Δ^+ (1232) resonance shape fit, the relativistic Breit-Wigner equation with a threshold correction is used:

$$f_{BW}(W; M_R, \Gamma_R) = A \left(\frac{W}{m_N} \right)^3 \frac{M_R \Gamma_R}{(W^2 - M_R^2)^2 + M_R^2 \Gamma_R^2} \quad (11.3)$$

where, M_R is the mass of the resonance particle, Γ_R is the full width of the distribution and m_N is the nucleon mass. The additional threshold term $(W/m_N)^3$, decreases the strength of the function for W values less than the nucleon mass. Fig-

Figure 11.16 shows the fit result for the Δ^+ (1232) resonance shape. The best fit results and the Particle Data Group (PDG) values for the Δ^+ (1232) resonance mass, M_R , and the reconstructed full width, Γ_R , are given in Table 11.3. According to the best fit, the mass of the Δ^+ particle is 15 MeV smaller than the world average and the full width of the resonance distribution is two times the PDG database value.

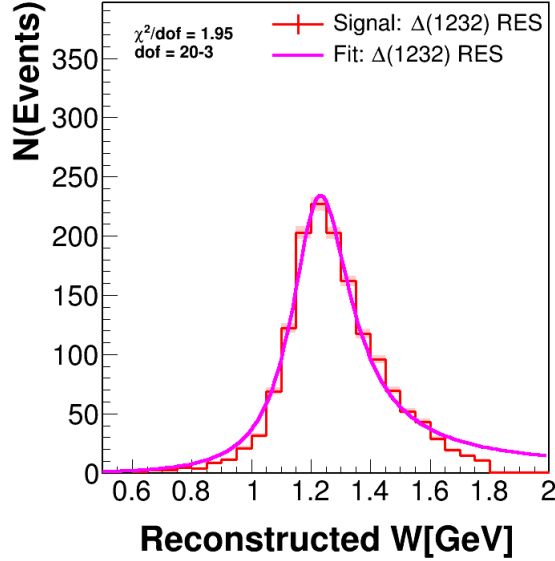


FIG. 11.16: W distribution for Δ^+ (1232) resonance events and the relativistic Breit-Wigner fit to the shape of the distribution. The best fit $\chi^2/d.o.f.$ is 1.95.

	Best Fit	PDG Database
M_R (GeV)	1.215	1.232
Γ_R (GeV)	0.246	0.117

TABLE 11.3: Mass and full width of the Δ^+ (1232) resonance. PDG values are from Ref. [101].

Best fit results for higher-mass baryon resonances are obtained by fitting the W distribution shape to a single gaussian distribution $\left(y = a \exp\left(-\frac{(x - \mu)^2}{2\sigma^2}\right)\right)$. Since these resonances consist of multiple resonance structures (e.g, $N(1440)$, $N(1520)$, and $N(1535)$) with overlapping widths, a single gaussian distribution is a pragmatic choice for the shape fit. According to the fit results the mean (μ) of the distribution is 1.47 GeV and the half width (σ) of the distribution is 0.29 GeV. The W distribution shape for the non-resonant events is fitted to a double gaussian distribution.

There is no physical motivation for this choice; a good shape fit seems to require a multiple-parameter form and a double-gaussian is found to do the job. The fit results are shown in Figs. 11.17 a) and b). The shape fits for all interaction types are then combined to get the total shape fit result for the simulation prediction for the W distribution. Figure 11.18 shows the final fit result for the simulation prediction.

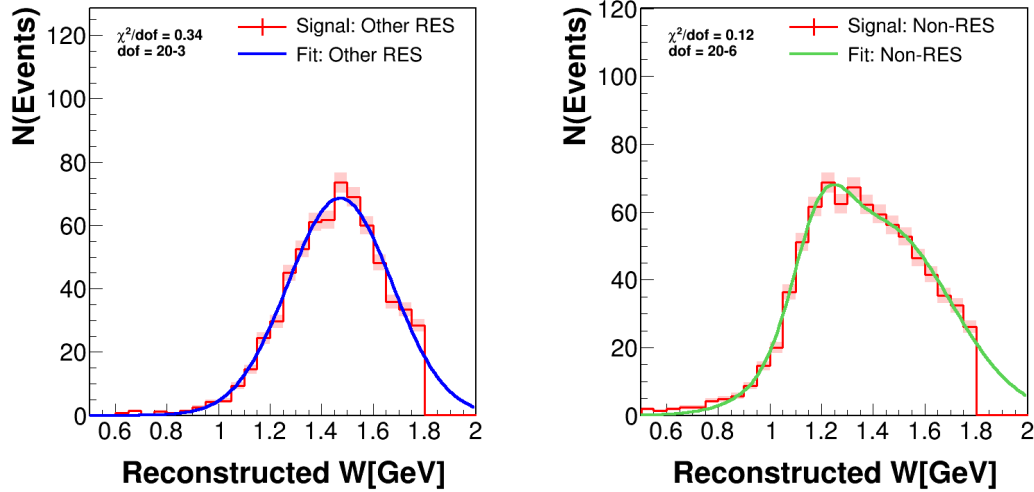


FIG. 11.17: Shape fit of the W distributions for other baryon resonances (left) and non-resonant events (right). The other baryon resonances are fitted to a single gaussian and the non-resonant contribution is fitted to a double gaussian. The best fit $\chi^2/d.o.f.$ is equal to 0.34 for baryon resonances and is equal to 0.12 for the non-resonant events.

The W distribution for the background subtracted data is also fitted. For the data shape fit, the predictions from the simulation fit results are used. For each interaction type the same functional forms are used and a total fit to the W distribution is obtained. During the shape fit, the double gaussian parameters for the non-resonant events are fixed, while the parameters for the Δ^+ (1232) resonance and other baryon resonances are varied. The result of the best total fit is shown in Fig. 11.19. The total fit for data has a $\chi^2/d.o.f. = 1.48$. Table 11.4 lists the data and simulation shape fit results for the Δ^+ (1232) resonance and other baryon resonances. According to the amplitudes, the data are estimated to have $\sim 23\%$ more Δ^+ (1232) resonance and $\sim 30\%$ less of other baryon resonances than is predicted by the simulation. The data distribution has a lower mean and a larger width for the Δ^+ (1232) shape than

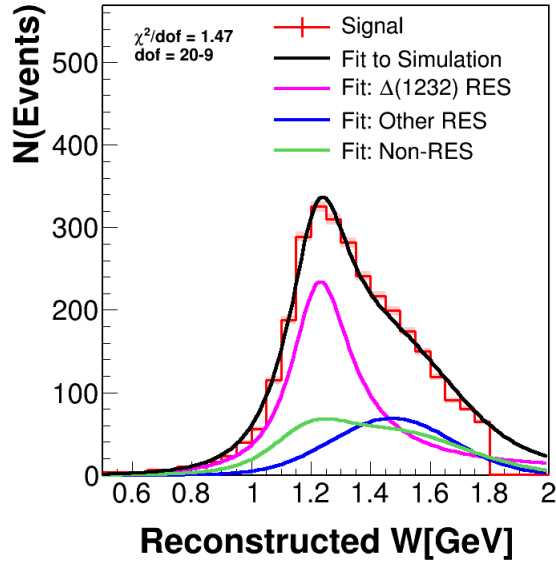


FIG. 11.18: Simulation prediction for the W distribution and the total shape fit result. The total fit $\chi^2/d.o.f.$ is equal to 1.47.

does the simulation prediction. For the other baryon resonances, the data have a lower mean and a smaller width than the simulation prediction.

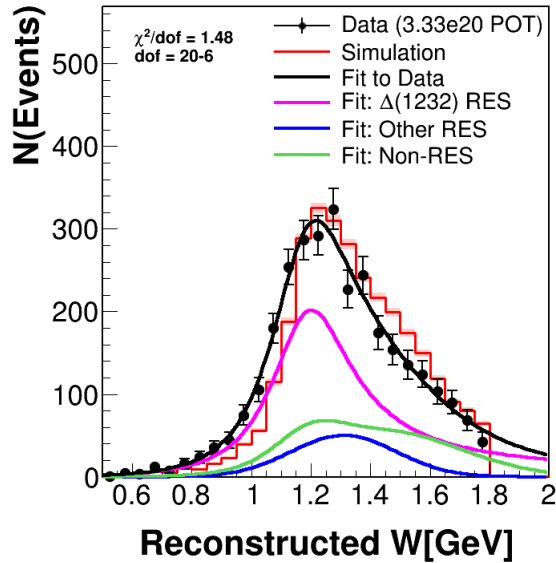


FIG. 11.19: W distribution shape fit for the data. The total fit $\chi^2/d.o.f.$ is equal to 1.48. The means for the $\Delta^+(1232)$ contribution and the other baryon resonance contributions are shifted towards lower W in the data relative to the simulation.

Interaction	Fit Parameter	Data	Simulation
Δ^+ (1232) RES	Amplitude	39.2	31.8
	Mean (M_R) [GeV]	1.17	1.21
	Full Width (Γ_R) [GeV]	0.34	0.25
Other RES	Amplitude	48.4	68.5
	Mean (μ) [GeV]	1.31	1.47
	Half Width (σ) [GeV]	0.24	0.29

TABLE 11.4: Data and simulation shape-fit results for the Δ^+ (1232) resonance and the other baryon resonances. For the Δ^+ (1232) resonance, the data distribution has a lower mean and a larger width than does the simulation prediction. For the other baryon resonances, the data have a lower mean and a smaller width than the simulation.

11.5 Search for M_A^{RES} value

There is disagreement between data and simulation in the high- Q^2 region, which can be seen in Fig. 9.9. According to the cross-section measurements, the data prefers a harder Q^2 spectrum than does the simulation. One way to reduce the disagreement is to use a higher M_A^{RES} value than the GENIE nominal ($M_A^{RES} = 1.12$ GeV) [85, 102]. In order to quantify this reduction, the measured cross section for Q^2 is fitted in the range $0.25 \text{ GeV}^2 \leq Q^2 < 2.0 \text{ GeV}^2$, using different M_A^{RES} values. The best fit result indicated that $M_A^{RES} = 1.50$ GeV. The Q^2 differential cross sections for nominal M_A^{RES} and for best fit M_A^{RES} are shown in Fig. 11.20. The best-fit result significantly improves the agreement between data and simulation in the high Q^2 region.

The uncertainty assigned by GENIE to the M_A^{RES} value is 20% [85]. The best-fit result $M_A^{RES} = 1.50$ GeV, is 34% greater than the nominal M_A^{RES} . Since the best-fit result is much higher than the expected range of M_A^{RES} , it seems likely that other physics obscures the M_A^{RES} measurement. Consequently, a measurement for the M_A^{RES} value is not being reported from this analysis.

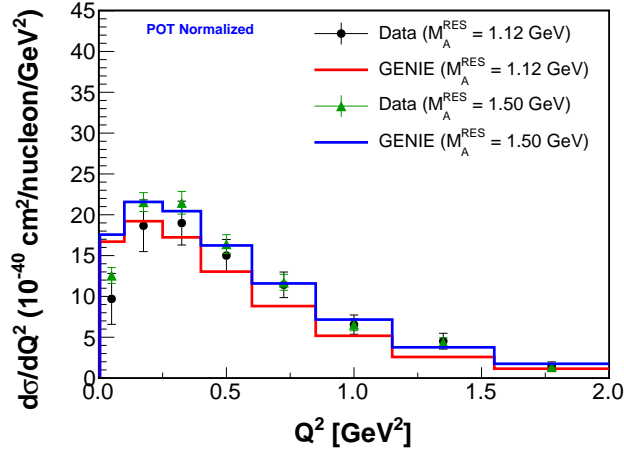


FIG. 11.20: The Q^2 differential cross sections for nominal $M_A^{RES} = 1.12$ GeV and for best fit $M_A^{RES} = 1.50$ GeV. The nominal data has statistical and systematic errors, while the data based on the best fit has only statistical errors. The best-fit result, by design, significantly improves the data-simulation agreement at high Q^2 .

11.6 Search for 2p2h contribution to single pion production

In this analysis, the QE-like 2p2h events have been included in the simulation to improve the background predictions. Evidence for 2p2h events in the pion production sector has been searched for in the signal distributions of this work. The Valencia group [53] has presented the double differential cross sections for QE-like 2p2h events for different neutrino energy ranges. Two of the distributions given in the paper are reproduced and are used to guide the search for a possible excess in data that may be associated with 2p2h.

The first 2D distribution is for muon kinetic energy versus cosine of the muon production angle. The 2p2h double differential cross section $d\sigma/dT_\mu d\cos\theta_\mu$ at $E_\nu = 3$ GeV as calculated by the Valencia group is reproduced as Fig. 11.21. The same distribution is plotted for data and simulation of this analysis, and then the difference between data and simulation is obtained. Plots in Fig. 11.22 show the data and simulation distributions and their difference. According to the QE-like 2p2h double differential cross section, the data excess should appear in the range $\cos(\theta_\mu) > 0.96$ and $T_\mu > 2.2$ GeV; however, there is no excess in that region or anywhere else in the

data plot of Fig. 11.22c.

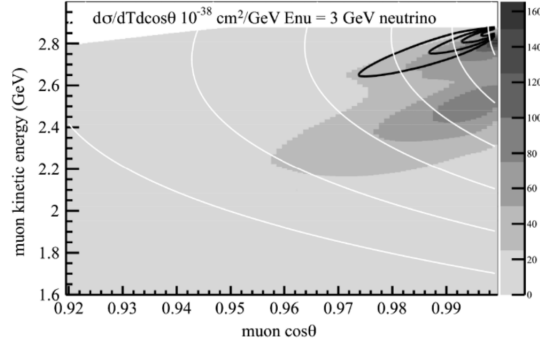


FIG. 11.21: Double differential 2p2h cross section $d\sigma/dT_\mu d\cos\theta_\mu$ at $E_\nu = 3$ GeV. The QE events are shown with the black contours. The white lines represents the constant three-momentum transfer from 0.2 to 1.2 GeV. The 2p2h cross section is high for the small angle, high kinetic energy region. From Ref. [53].

The second double differential cross section for QE-like 2p2h events is for energy transfer, q_0 , versus three-momentum transfer, q_3 . Figure 11.23 shows the $d\sigma/dq_0dq_3$ at $E_\nu = 3$ GeV as calculated for QE-like 2p2h events [53]. The same distribution has been plotted for data and simulation for this analysis, and then the difference between data and simulation is obtained. Figure 11.24 shows the data-minus-simulation distribution for q_0 versus q_3 . Using the QE-like 2p2h differential cross section as a reference, a search box in the kinematical region $0.1 < q_0 < 0.8$ GeV and $0.4 < q_3 < 1.1$ GeV is defined to look for a data excess. The search area for 2p2h contribution to CC(π) events is taken to be larger than the preferred kinematical region of the QE-like 2p2h events. A data excess of 2.0% of the data signal rate is observed in the defined search area. Since there is no data excess in the muon variables, there is no consistent evidence for the presence of a 2p2h contribution. Based upon the observed small excess in the q_0 versus q_3 distribution, an upper limit on a 2p2h contribution to the ν_μ -CC(π^0) channel can be set as 3.7% of the channel signal rate at 90% confidence level. The 3.7% upper limit is obtained by analyzing the data minus simulation difference in multiple “universes” (fully simulated measurements for which parameters of systematics are varied, one per universe). The maximum data excess is 3.7% of the signal rate for 90% of the universes.

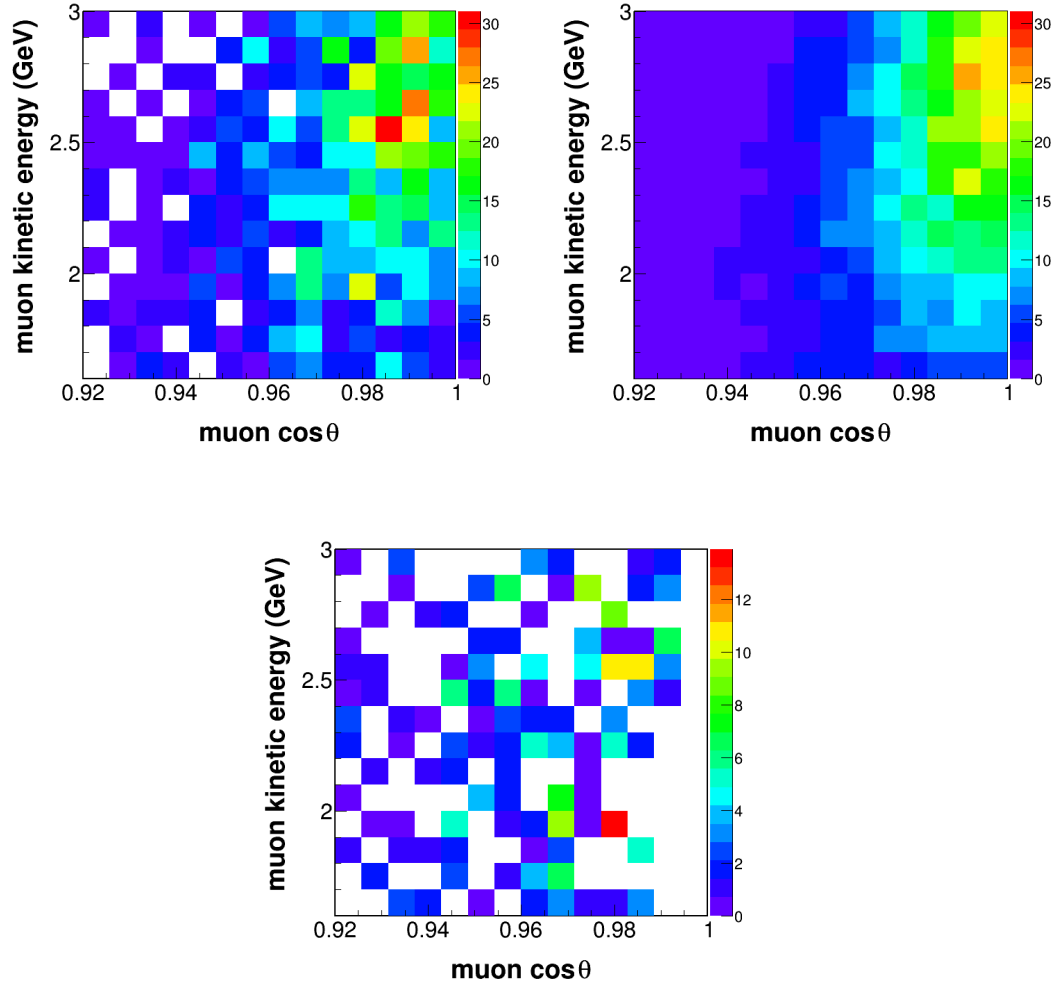


FIG. 11.22: On the top, data (left) and P.O.T. normalized simulation (right) distributions for muon kinetic energy versus cosine of the muon production angle are shown. The range of the z -axis is the same for both of the distributions. On the bottom, the distribution of positive values for data-minus-simulation is shown. No localized data excess is observed.

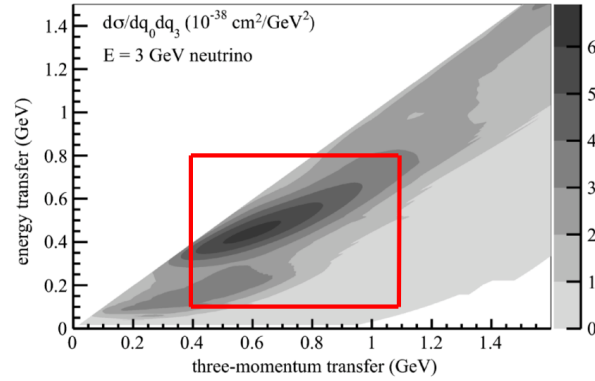


FIG. 11.23: Double differential 2p2h cross section $d\sigma/dq_0dq_3$ at $E_\nu = 3$ GeV. The QE-like 2p2h cross section is high near the kinematical region where $q_0 \approx 0.5$ GeV and $q_3 \approx 0.6$ GeV. The solid red lines shows the search area for a 2p2h contribution in the ν_μ -CC (π^0) channel. From Ref. [53].

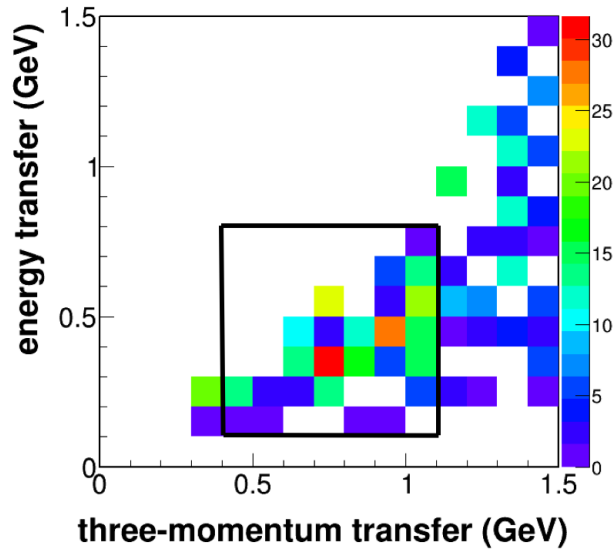


FIG. 11.24: Data-minus-simulation distribution for energy transfer versus three-momentum transfer. There is a small excess in the search area defined with solid black lines, amounting to $\sim 2.0\%$ of the data signal rate.

Chapter 12

Conclusions

12.1 Cross-section measurements for ν_μ -CC (π^0)

In this thesis, new differential cross-section measurements are reported for single particle kinematics: Muon momentum, muon production angle, pion momentum, pion kinetic energy, and pion production angle. The differential cross section for four-momentum transfer squared Q^2 and the cross section versus neutrino energy are also reported. The GENIE neutrino event generator is the basis for the simulation in this analysis. The simulation enables improvements of the data measurements and provides predictions for the measured quantities. The simulation is tuned for better predictions by using event reweighting for Δ^{++} (1232) anisotropic decay, event reweighting for non-resonant $\nu_\mu n \rightarrow \mu^- n \pi^+$ interactions, and by simulating events for 2p2h reactions in QE-like final states.

The simulation prediction for the muon momentum agrees with data everywhere. However, some discrepancies are observed in comparison with the muon production angle measurement. The data is lower than the simulation prediction for forward-going muons (small production angle), however it exceeds the simulation prediction for large angles. In both of the measurements, the leading systematic uncertainty is the cross-section model uncertainty.

Data and simulation in pion momentum and in pion kinetic energy have small disagreements. The simulation prediction needs to be tuned to estimate slightly higher rates for lower momentum and kinetic energy regions. The simulation prediction for the pion production angle agrees with data everywhere. As is the case for muon momentum and angle cross-section measurements, the leading systematic uncertainty in pion kinematics cross-section measurements is the cross-section model uncertainty.

Discrepancies in simulation predictions are observed in the Q^2 cross-section measurement. The largest disagreement between the data and the simulation is in the lowest Q^2 bin, probably because of missing physical models in the simulation. The low- Q^2 discrepancy may be explained due to the absence of Pauli Exclusion and RPA models in GENIE for CC (π) production. A further discrepancy is observed

in the high- Q^2 region where the data has a harder spectrum than the simulation prediction. The leading systematic uncertainties are the cross-section model uncertainties for low- Q^2 region, and the detector response uncertainties for high- Q^2 region ($Q^2 > 1.2 \text{ GeV}^2$).

The simulation prediction for the cross section versus neutrino energy agrees with data almost everywhere. The cross section reaches a nearly constant value for $E_\nu > 5 \text{ GeV}$. The leading systematic uncertainties are the cross-section model uncertainties.

12.2 Comparisons with $\nu_\mu\text{-CC}(\pi^+)$ and $\bar{\nu}_\mu\text{-CC}(\pi^0)$

The cross-section results for the $\nu_\mu\text{-CC}(\pi^0)$ channel are compared with two different published MINERvA analyses in Ch. 10. The latter analyses are for the neutrino induced single charged pion production, $\nu_\mu\text{-CC}(\pi^+)$, and for the antineutrino induced neutral pion production, $\bar{\nu}_\mu\text{-CC}(\pi^0)$. In all measured quantities the rates for $\nu_\mu\text{-CC}(\pi^+)$ is four times higher than the neutrino and antineutrino $CC(\pi^0)$ samples. The $\nu_\mu\text{-CC}(\pi^0)$ production rates are 16% higher than the $\bar{\nu}_\mu\text{-CC}(\pi^0)$ production rates. There is a simulation prediction problem in $\nu_\mu\text{-CC}(\pi^+)$ in which the simulation prediction is higher than the data measurement everywhere in all variables, while this problem is not observed in the $CC(\pi^0)$ samples.

The CC single pion production reactions for all three samples are decomposed in terms of the $\Delta(1232)$ resonance, other baryon resonances, and non-resonant pion production. In all three samples, $\Delta(1232)$ production is the leading reaction channel with a $\sim 50\%$ contribution. In $\nu_\mu\text{-CC}(\pi^+)$ and $\nu_\mu\text{-CC}(\pi^0)$ the second leading channel is non-resonant pion production, however in the $\bar{\nu}_\mu\text{-CC}(\pi^0)$ the other baryon resonances have larger contributions than the non-resonant pion production.

The final state interactions are studied for all three samples. The shape of the π^0 final state interactions are similar in $\nu_\mu\text{-CC}(\pi^0)$ and $\bar{\nu}_\mu\text{-CC}(\pi^0)$ samples. However, shape and normalization differences are observed between π^0 and π^+ final state interactions in $\nu_\mu\text{-CC}(\pi^0)$ and $\nu_\mu\text{-CC}(\pi^+)$ samples.

The leading systematic uncertainties in ν_μ -CC (π^0) and $\bar{\nu}_\mu$ -CC (π^0) are the cross-section model uncertainties, while in the ν_μ -CC (π^+) sample the detector response uncertainties are leading.

12.3 Physics of ν_μ -CC (π^0) sample

In addition to cross section measurements, the final sample is used for different physics explorations and the results are reported in Ch. 11.

The final sample is studied to find an effective treatment for the observed low- Q^2 data versus simulation disagreement. An approach used in the MINOS experiment is repeated for MINERvA data, and a low- Q^2 suppression factor for all CC-RES events has been found. It is shown that, a data-driven functional form can be used to suppress CC-RES events in low- Q^2 to reduce the data versus simulation disagreements in both Q^2 and muon angle distributions.

Differential cross sections for Q^2 are obtained for different neutrino energy ranges, and the distributions are compared with antineutrino counterparts. In the low- E_ν region, an expected difference in slope parameter due to V-A interference term is observed. However, due to the measured slope parameter in antineutrino sample has large uncertainties, a strong conclusion cannot be given.

A sub-sample enriched with Δ^+ (1232) events is obtained by limiting the hadronic invariant mass $W \leq 1.4$ GeV and requiring a visible proton track in the event. Using the sub-sample, the proton- π^0 invariant mass is studied. Data versus simulation disagreements for the $p\pi^0$ invariant mass distribution are observed at the expected Δ^+ (1232) region ($1.1 < m_{p\pi^0} < 1.3$ GeV). The data has a higher and narrower distribution in the Δ^+ (1232) region than the simulation prediction. Polarization angles for the $p\pi^0$ system are also studied using the Δ^+ (1232) enriched sub-sample. Data distributions have anisotropic shapes for $\cos\theta$, and angle ϕ , however the simulation predicts near-isotropy for the both polarization angles. The best fit to the shape of the data distribution is compared with the isotropic prediction from the simulation, and it is concluded that the differences between the best fit results and the isotropic

predictions are not significant. The simulation is successful in describing $\cos\theta$, and angle ϕ based upon isotropic decay of the Δ^+ (1232) resonance.

Distributions of the hadronic invariant mass, W , are studied for data and simulation and a small energy shift in the simulation is observed. According to the study, the data and GENIE prediction for the W have a 20 MeV energy difference. The source of this extra energy is unknown, but it may be due to Fermi motion or to another nuclear effect, or it may be due to the absence of interference in the GENIE baryon resonance model.

The shapes of the W distributions for resonant and non-resonant pion production interactions in data are identified by using the simulation as a reference. According to the shape fit, the data has $\sim 23\%$ more Δ^+ (1232) resonance content than does the simulation prediction. This result agrees with the conclusion based on the $p\pi^0$ invariant mass distribution.

The harder data distribution in $d\sigma/dQ^2$ for the high- Q^2 region can be explained with an increased value of M_A^{RES} . A range of different M_A^{RES} values are fitted to the $d\sigma/dQ^2$ distribution. The best fit is obtained for $M_A^{RES} = 1.50$ GeV, which is 34% greater than the nominal M_A^{RES} value. Since the best fit result is much larger than the expected M_A^{RES} range, it seems that other physics must be involved in the data versus simulation disagreement in high- Q^2 region.

Finally, a 2p2h contribution on ν_μ -CC (π^0) channel has been searched for using the 2D distributions for muon angle versus muon kinetic energy and for three-momentum transfer versus energy transfer. After comparisons with predicted 2p2h cross sections in these 2D histograms, no evidence for 2p2h contribution in this sample is observed. However, an upper limit of 3.7% of the signal rate can be set for the 2p2h contribution on ν_μ -CC (π^0) channel. The method for obtaining the upper limit for the 2p2h contribution is described in Sec. 11.6.

Appendix A

MINERvA Collaboration

O. Altinok,¹ L. Aliaga,^{4,5} L. Bellantoni,⁶ A. Bercellie,⁷ M. Betancourt,⁶ A. Bodek,⁷
A. Bravar,⁸ H. Budd,⁷ T. Cai,⁷ M. F. Carneiro,⁹ M. E. Christy,¹⁰ H. da Motta,⁹ S.
A. Dytman,² G. A. Díaz,^{7,5} B. Eberly,² E. Endress,⁵ J. Felix,¹¹ L. Fields,^{6,12} R.
Fine,⁷ R. Galindo,¹³ H. Gallagher,¹ T. Golan,^{7,6} R. Gran,¹⁴ D. A. Harris,⁶ A.
Higuera,^{7,11}, K. Hurtado,^{9,15} M. Kiveni,⁶ J. Kleykamp,⁷ M. Kordosky,⁴ T. Le,^{1,3} E.
Maher,¹⁶ S. Manly,⁷ W. A. Mann,¹ C. M. Marshall,⁷ D. A. Martinez Caicedo,⁹, K.
S. McFarland,^{7,6} C. L. McGivern,² A. M. McGowan,⁷ B. Messerly,² J. Miller,¹³ A.
Mislivec,⁷ J. G. Morfín,⁶ J. Mousseau,¹⁷ D. Naples,² J. K. Nelson,⁴ A. Norrick,⁴
Nuruzzaman,^{3,13} V. Paolone,² J. Park,⁷ C. E. Patrick,¹² G. N. Perdue,^{6,7} L.
Rakotondravohitra,⁶ M. A. Ramirez,¹¹ R. D. Ransome,³ H. Ray,¹⁷ L. Ren,² D.
Rimal,¹⁷ P. A. Rodrigues,⁷ D. Ruterbories,⁷ H. Schellman,^{18,12} D. W. Schmitz,^{19,6}
C. Simon,²⁰ C. J. Solano Salinas,¹⁵ S. Sánchez Falero,⁵ B. G. Tice,³ E. Valencia,¹¹
T. Walton,¹⁰ J. Wolcott,^{7,1} M. Wospakrik,¹⁷ and D. Zhang⁴

¹*Physics Department, Tufts University, Medford, Massachusetts 02155,
USA*

²*Department of Physics and Astronomy, University of Pittsburgh, Pittsburgh,
Pennsylvania 15260, USA*

³*Rutgers, The State University of New Jersey, Piscataway, New Jersey 08854,
USA*

⁴*Department of Physics, College of William & Mary, Williamsburg, Virginia
23187, USA*

⁵*Sección Física, Departamento de Ciencias, Pontificia Universidad Católica del Perú, Apartado 1761, Lima, Perú*

⁶*Fermi National Accelerator Laboratory, Batavia, Illinois 60510, USA*

⁷*University of Rochester, Rochester, New York 14627, USA*

⁸*University of Geneva, 1211 Geneva 4, Switzerland*

⁹*Centro Brasileiro de Pesquisas Físicas, Rua Dr. Xavier Sigaud 150, Urca, Rio de Janeiro, Rio de Janeiro 22290-180, Brazil*

¹⁰*Hampton University, Department of Physics, Hampton, Virginia 23668, USA*

¹¹*Campus León y Campus Guanajuato, Universidad de Guanajuato, Lascurain de Retana No. 5, Colonia Centro, Guanajuato 36000, Guanajuato México*

¹²*Northwestern University, Evanston, Illinois 60208, USA*

¹³*Departamento de Física, Universidad Técnica Federico Santa María, Avenida España 1680 Casilla 110-V, Valparaíso, Chile*

¹⁴*Department of Physics, University of Minnesota-Duluth, Duluth, Minnesota 55812, USA*

¹⁵*Universidad Nacional de Ingeniería, Apartado 31139, Lima, Perú*

¹⁶*Massachusetts College of Liberal Arts, 375 Church Street, North Adams, Massachusetts 01247, USA*

¹⁷*University of Florida, Department of Physics, Gainesville, Florida 32611, USA*

¹⁸*Department of Physics, Oregon State University, Corvallis, Oregon 97331, USA*

¹⁹*Enrico Fermi Institute, University of Chicago, Chicago, Illinois 60637, USA*

²⁰*Department of Physics and Astronomy, University of California, Irvine, Irvine, California 92697-4575, USA*

Appendix B

Tables for the Cross-Section Measurements

This Appendix provides tabulated results for the cross-section measurements for all variables. Three cross-section results based on different reference simulations are provided for each variable. The first cross-section measurement is based on the Nominal GENIE v2.8.4. The second cross-section measurement is based on the tuned GENIE which includes the following tunings: Event reweighting for Δ^{++} (1232) anisotropic decay, event reweighting for non-resonant $\nu_{\mu}n \rightarrow \mu^{-}n\pi^{+}$ interactions, and additional simulation events for 2p2h reactions in QE-like final states. The third cross-section measurement is based on the GENIE version which includes the CC-RES suppression for low Q^2 in addition to the default tunings. Systematic uncertainties for each cross-section measurement based on the “Tuned GENIE” are given as percentages of the measured value.

B.1 Muon momentum

Bin Range [GeV/c]	Nominal GENIE	Tuned GENIE	Tuned GENIE + CC-RES Suppression
1.0 - 2.0	3.61	3.69	3.93
2.0 - 2.5	5.56	5.64	5.92
2.5 - 3.0	5.21	5.35	5.48
3.0 - 3.5	3.16	3.24	3.25
3.5 - 4.0	1.88	1.89	1.87
4.0 - 5.0	1.03	0.986	0.953
5.0 - 7.0	0.614	0.546	0.513
7.0 - 10.0	0.462	0.457	0.439

TABLE B.1: Results for the muon momentum differential cross-section measurement. GENIE v2.8.4 is used in the analysis. The unit of the cross-section measurement is $10^{-40}\text{cm}^2/\text{nucleon}/\text{GeV}/\text{c}$.

Bin Range [GeV/c]	(I) Detector Response	(II) Neutrino Int. Model	(III) FSI Model	(IV) Flux	(V) Other	Total
1.0 - 2.0	17.65%	13.20%	2.99%	5.42%	0.63%	22.90%
2.0 - 2.5	8.20%	13.84%	2.90%	4.88%	0.59%	17.07%
2.5 - 3.0	3.57%	11.98%	2.91%	4.53%	0.58%	13.62%
3.0 - 3.5	6.04%	11.34%	3.31%	4.83%	0.53%	14.13%
3.5 - 4.0	7.51%	11.98%	3.39%	5.50%	0.49%	15.55%
4.0 - 5.0	7.08%	15.87%	4.15%	4.54%	0.32%	18.44%
5.0 - 7.0	4.65%	21.14%	7.07%	3.53%	0.13%	23.05%
7.0 - 10.0	4.23%	12.72%	4.38%	5.16%	0.44%	15.02%

TABLE B.2: Bin-by-bin systematic uncertainties on muon momentum differential cross-section measurement, expressed as percentages of the measured value.

B.2 Muon production angle

Bin Range [deg]	Nominal GENIE	Tuned GENIE	Tuned GENIE + CC-RES Suppression
0.0 - 2.0	0.187	0.173	0.199
2.0 - 4.0	0.541	0.504	0.526
4.0 - 6.0	0.833	0.791	0.784
6.0 - 8.0	0.886	0.864	0.838
8.0 - 10.0	0.910	0.929	0.89
10.0 - 12.0	0.820	0.858	0.812
12.0 - 16.0	0.819	0.876	0.827
16.0 - 20.0	0.759	0.828	0.781
20.0 - 25.0	0.504	0.574	0.539

TABLE B.3: Results for the muon production angle differential cross-section measurement. GENIE v2.8.4 is used in the analysis. The unit of the cross section measurement is $10^{-40} \text{cm}^2/\text{nucleon}/\text{deg}$.

Bin Range [deg]	(I) Detector Response	(II) Neutrino Int. Model	(III) FSI Model	(IV) Flux	(V) Other	Total
0.0 - 2.0	6.18%	22.22%	6.04%	3.06%	0.24%	24.04%
2.0 - 4.0	3.95%	18.49%	3.94%	2.79%	0.30%	19.52%
4.0 - 6.0	2.84%	14.87%	3.75%	3.03%	0.40%	15.89%
6.0 - 8.0	3.19%	11.96%	3.80%	3.61%	0.48%	13.45%
8.0 - 10.0	2.95%	8.92%	3.45%	4.18%	0.53%	10.86%
10.0 - 12.0	3.12%	7.26%	3.82%	4.21%	0.52%	9.75%
12.0 - 16.0	3.14%	5.77%	4.16%	4.40%	0.54%	8.95%
16.0 - 20.0	3.17%	6.26%	4.39%	4.33%	0.52%	9.35%
20.0 - 25.0	4.13%	6.36%	5.25%	4.62%	0.53%	10.33%

TABLE B.4: Bin-by-bin systematic uncertainties on muon production angle differential cross-section measurement, expressed as percentages of the measured value.

B.3 Pion momentum

Bin Range [GeV/c]	Nominal GENIE	Tuned GENIE	Tuned GENIE + CC-RES Suppression
0.0 - 0.075	2.71	3.16	3.04
0.075 - 0.15	25.9	26.7	27.2
0.15 - 0.25	38.2	37.9	38.6
0.25 - 0.40	24.9	24.7	24.8
0.40 - 0.55	14.1	14.2	14.1
0.55 - 0.75	8.45	8.53	8.4
0.75 - 1.00	6.21	6.23	6.12
1.00 - 1.50	1.79	1.77	1.68

TABLE B.5: Results for the pion momentum differential cross-section measurement. GENIE v2.8.4 is used in the analysis. The unit of the cross section measurement is $10^{-40}\text{cm}^2/\text{nucleon}/\text{GeV}/c$.

Bin Range [GeV/c]	(I) Detector Response	(II) Neutrino Int. Model	(III) FSI Model	(IV) Flux	(V) Other	Total
0.0 - 0.075	27.65%	44.67%	18.33%	9.60%	1.14%	56.48%
0.075 - 0.15	12.28%	19.84%	6.11%	1.66%	0.24%	24.18%
0.15 - 0.25	4.36%	12.79%	3.66%	3.67%	0.49%	14.48%
0.25 - 0.40	3.08%	9.92%	2.30%	4.43%	0.60%	11.54%
0.40 - 0.55	3.05%	10.98%	3.83%	4.04%	0.54%	12.69%
0.55 - 0.75	2.44%	11.05%	4.70%	4.16%	0.55%	12.96%
0.75 - 1.00	2.46%	8.69%	4.47%	5.03%	0.66%	11.28%
1.00 - 1.50	9.96%	19.31%	10.15%	1.90%	0.27%	24.06%

TABLE B.6: Bin-by-bin systematic uncertainties on pion momentum differential cross-section measurement, expressed as percentages of the measured value.

B.4 Pion kinetic energy

Bin Range [GeV]	Nominal GENIE	Tuned GENIE	Tuned GENIE + CC-RES Suppression
0.0 - 0.05	29.0	30.4	30.7
0.05 - 0.15	45.1	45.1	45.8
0.15 - 0.25	28.9	28.7	28.9
0.25 - 0.40	17.6	17.6	17.6
0.40 - 0.55	10.2	10.3	10.2
0.55 - 0.75	7.83	7.89	7.78
0.75 - 1.0	4.18	4.16	4.04

TABLE B.7: Results for the pion kinetic energy differential cross-section measurement. GENIE v2.8.4 is used in the analysis. The unit of the cross section measurement is $10^{-40}\text{cm}^2/\text{nucleon}/\text{GeV}$.

Bin Range [GeV]	(I) Detector Response	(II) Neutrino Int. Model	(III) FSI Model	(IV) Flux	(V) Other	Total
0.0 - 0.05	14.65%	23.43%	7.03%	1.58%	0.18%	28.56%
0.05 - 0.15	5.35%	13.89%	4.19%	3.23%	0.43%	15.80%
0.15 - 0.25	2.92%	9.90%	2.37%	4.36%	0.59%	11.46%
0.25 - 0.40	3.07%	10.62%	3.13%	4.30%	0.58%	12.28%
0.40 - 0.55	2.27%	10.85%	4.57%	4.23%	0.56%	12.73%
0.55 - 0.75	2.18%	8.77%	4.32%	4.98%	0.66%	11.20%
0.75 - 1.0	5.07%	13.37%	7.13%	3.54%	0.48%	16.37%

TABLE B.8: Bin-by-bin systematic uncertainties on pion kinetic energy differential cross-section measurement, expressed as percentages of the measured value.

B.5 Pion production angle

Bin Range [deg]	Nominal GENIE	Tuned GENIE	Tuned GENIE + CC-RES Suppression
0 - 10	0.0386	0.0395	0.0384
10 - 20	0.108	0.112	0.109
20 - 30	0.172	0.176	0.174
30 - 40	0.199	0.204	0.202
40 - 50	0.168	0.172	0.169
50 - 60	0.161	0.162	0.160
60 - 70	0.159	0.154	0.153
70 - 80	0.144	0.140	0.140
80 - 90	0.0834	0.0809	0.0821
90 - 120	0.0692	0.0681	0.0698
120 - 180	0.0291	0.0296	0.0312

TABLE B.9: Results for the pion production angle differential cross-section measurement. GENIE v2.8.4 is used in the analysis. The unit of the cross section measurement is $10^{-40}\text{cm}^2/\text{nucleon}/\text{deg}$.

Bin Range [deg]	(I) Detector Response	(II) Neutrino Int. Model	(III) FSI Model	(IV) Flux	(V) Other	Total
0 - 10	9.62%	26.25%	6.69%	1.22%	0.28%	28.78%
10 - 20	7.19%	18.98%	6.62%	2.51%	0.32%	21.50%
20 - 30	5.31%	14.28%	4.67%	3.25%	0.43%	16.27%
30 - 40	3.97%	11.35%	3.09%	3.92%	0.52%	13.03%
40 - 50	2.49%	9.83%	4.01%	3.90%	0.52%	11.59%
50 - 60	2.15%	11.50%	3.94%	3.52%	0.47%	12.84%
60 - 70	1.84%	13.98%	3.86%	2.88%	0.39%	14.91%
70 - 80	2.95%	13.58%	4.67%	3.27%	0.45%	15.02%
80 - 90	3.63%	15.93%	6.47%	2.56%	0.39%	17.77%
90 - 120	4.35%	13.91%	3.98%	3.31%	0.45%	15.48%
120 - 180	4.15%	10.68%	2.77%	4.79%	0.65%	12.74%

TABLE B.10: Bin-by-bin systematic uncertainties on pion production angle differential cross-section measurement, expressed as percentages of the measured value.

B.6 Four-momentum transfer square Q^2

Bin Range [GeV ²]	Nominal GENIE	Tuned GENIE	Tuned GENIE + CC-RES Suppression
0.00 - 0.10	10.5	9.7	12.1
0.10 - 0.25	19.8	18.7	18.1
0.25 - 0.40	19.5	19.0	17.8
0.40 - 0.60	14.7	15.0	14.0
0.60 - 0.85	10.6	11.4	10.7
0.85 - 1.15	5.81	6.55	6.08
1.15 - 1.55	3.9	4.52	4.24
1.55 - 2.00	1.15	1.38	1.24

TABLE B.11: Results for the four-momentum transfer square Q^2 differential cross-section measurement. GENIE v2.8.4 is used in the analysis. The unit of the cross section measurement is $10^{-40}\text{cm}^2/\text{nucleon}/\text{GeV}^2$.

Bin Range [GeV ²]	(I) Detector Response	(II) Neutrino Int. Model	(III) FSI Model	(IV) Flux	(V) Other	Total
0.00 - 0.10	10.80%	24.36%	4.36%	3.06%	0.38%	27.18%
0.10 - 0.25	6.99%	11.58%	3.27%	4.11%	0.56%	14.52%
0.25 - 0.40	3.49%	8.94%	3.06%	3.85%	0.53%	10.80%
0.40 - 0.60	3.06%	7.71%	3.57%	3.54%	0.45%	9.71%
0.60 - 0.85	5.29%	6.10%	4.58%	4.14%	0.51%	10.18%
0.85 - 1.15	7.72%	8.21%	5.18%	3.89%	0.43%	13.01%
1.15 - 1.55	11.90%	6.66%	7.14%	4.92%	0.43%	16.16%
1.55 - 2.00	27.41%	13.97%	14.45%	6.98%	0.06%	34.70%

TABLE B.12: Bin-by-bin systematic uncertainties on four-momentum transfer squared Q^2 differential cross-section measurement, expressed as percentages of the measured value.

B.7 Neutrino energy

Bin Range [GeV ²]	Nominal GENIE	Tuned GENIE	Tuned GENIE + CC-RES Suppression
0.0 - 1.5	N/A	N/A	N/A
1.5 - 3.0	12.2	12.6	13.5
3.0 - 3.5	16.1	16.5	17.0
3.5 - 4.0	15.8	16.2	16.4
4.0 - 5.0	16.5	16.5	16.3
5.0 - 6.0	22.6	21.1	20.2
6.0 - 8.0	24.7	21.5	20.1
8.0 - 10.0	32.9	33.0	31.7
10.0 - 12.0	32.1	33.7	32.9
12.0 - 15.0	24.3	26.2	25.6
15.0 - 20.0	24.0	25.9	24.5

TABLE B.13: Results for the neutrino energy cross-section measurement. GE-
NIE v2.8.4 is used in the analysis. The unit of the cross section measurement is $10^{-40}\text{cm}^2/\text{nucleon}$.

Bin Range [GeV]	(I) Detector Response	(II) Neutrino Int. Model	(III) FSI Model	(IV) Flux	(V) Other	Total
0.0 - 1.5	N/A	N/A	N/A	N/A	N/A	N/A
1.5 - 3.0	14.62%	11.64%	2.73%	7.01%	0.68%	20.16%
3.0 - 3.5	4.23%	12.20%	2.49%	5.17%	0.60%	14.15%
3.5 - 4.0	4.87%	12.23%	3.12%	7.26%	0.53%	15.36%
4.0 - 5.0	8.61%	13.57%	4.16%	12.77%	0.41%	20.95%
5.0 - 6.0	4.60%	16.42%	4.91%	8.08%	0.35%	19.50%
6.0 - 8.0	5.45%	22.86%	7.41%	9.45%	0.15%	26.40%
8.0 - 10.0	3.60%	12.22%	5.23%	10.13%	0.46%	17.10%
10.0 - 12.0	4.85%	10.60%	4.47%	9.90%	0.51%	15.94%
12.0 - 15.0	4.89%	13.54%	5.10%	10.38%	0.39%	18.47%
15.0 - 20.0	17.61%	17.74%	8.27%	13.92%	0.10%	29.78%

TABLE B.14: Bin-by-bin systematic uncertainties on neutrino energy cross-section
measurement, expressed as percentages of the measured value.

Appendix C

Brief History of Neutrinos

Neutrinos are extremely weakly interacting particles with very small masses. Their existence was postulated by Wolfgang Pauli in 1930 after the observation of unexpected electron kinetic energy distributions in beta decays. Before the hypothesis of neutrinos, beta decay was known as a form of radioactive decay in which a nucleus of atomic number Z transforms to atomic number $Z+1$ (or $Z-1$) and an electron (or positron) is emitted. Beta decay is energetically possible because the daughter nucleus has less mass than the parent. Using Einstein's $E = mc^2$ and two-body kinematics, early nuclear physicists expected that the electron (or positron) would carry off the difference in masses in the form of kinetic energy. However, it turned out that the electron always carried off less energy than expected; rather than all electrons having the same energy, a continuous distribution was observed, as illustrated for ^{14}C in Fig. C.1.

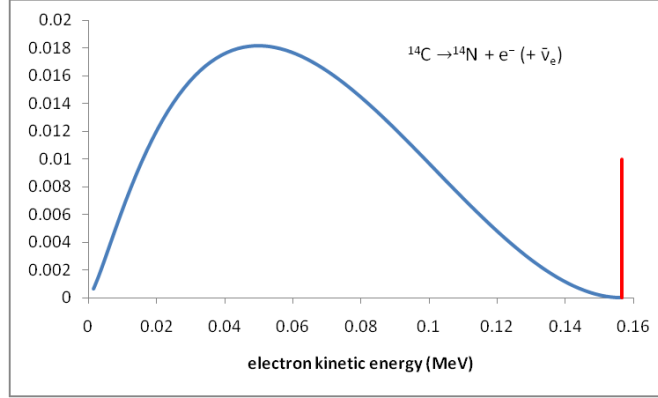


FIG. C.1: Electron energy spectrum for beta decay of carbon-14. The red line marks the expected electron kinetic energy corresponding the difference in masses of parent and daughter nucleus in the absence of a final-state neutrino. The blue line shows the observed electron energies. From Ref. [103]

According to energy conservation this was an unexpected result. Some physicists including Niels Bohr questioned the validity of the principle of energy conservation. However, Pauli offered a pioneering hypothesis to explain the missing energy in beta decay. He proposed that during beta decay, in addition to the electron, an electrically neutral particle is also emitted, in such a way that the sum of the energies of both particles is constant.

Pauli originally called his particle the “neutron”, but when this name was given to the particle neutron (the proton-like neutral hadron discovered by James Chadwick[104]), Fermi formalized Pauli’s idea with his four-fermion theory of beta decay [105] and renamed the particle as “neutrino” (Italian for “little neutral one”). The success of Fermi’s theory provided strong evidence for the existence of neutrinos. However, due to the weakly interacting nature of the neutrinos, experimental detection did not take place until 25 years later.

As of 2016 there are three neutrino flavors; they have been experimentally detected in the following order:

1956 Discovery of the electron neutrino by Cowan et al. [106]. The experiment used the antineutrino flux from a nuclear reactor to detect the inverse beta decay reaction ($\bar{\nu}_e + p \rightarrow e^+ + n$) with a detector containing many target protons in a hydrogenous liquid scintillator.

1962 Discovery of the muon neutrino at Brookhaven by Danby et al. [107]. The experiment used a neutrino beam generated by decay in flight pions according to the reaction: $\pi^\pm \rightarrow \mu^\pm + (\nu/\bar{\nu})$. The neutrino flavor was determined by counting the relative rates for the following interactions in the detector: $\nu + n \rightarrow p + e^-$, $\bar{\nu} + p \rightarrow p + e^+$, $\nu + n \rightarrow p + \mu^-$, and $\bar{\nu} + p \rightarrow p + \mu^+$. If there is only one neutrino flavor, one expects to get the same rates for electron and muon production. However, only muons were detected which proves the existence of muon neutrinos.

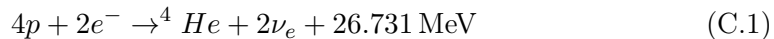
2001 First direct observation of the tau neutrino at Fermilab by the DONUT Collaboration [108]. The DONUT experiment was designed to observe the charged current interactions of the ν_τ by identifying the τ lepton as the only lepton created at the interaction vertex of neutrino induced events.

C.1 Neutrino oscillation experiments

Neutrino oscillation experiments can be classified according to the neutrino source. There are four main neutrino sources used by oscillation experiments.

Solar neutrinos

Stars are an excellent source of neutrinos because of their nuclear reactions in the core. The main source of energy in hydrogen-burning stars (like the Sun) is through the proton-proton chain mechanism:



where 2% of the energy (0.6 MeV) is carried by the neutrinos according to the standard solar model [109]. It is known that the luminosity of the Sun equals 3.92×10^{26} Watts or 2.4×10^{39} MeV/s. According to the standard solar model, the Sun should emit 2×10^{38} electron neutrinos (ν_e) per second. If the neutrino flux on Earth is calculated using these numbers, the flux is:

$$\Phi_{\nu_e} = 6.5 \times 10^{14} \text{ m}^{-2}\text{s}^{-1} \quad (\text{C.2})$$

Due to this natural high flux, the Sun is a good neutrino source and it is possible with a solar neutrino experiment to measure the neutrino mixing angle θ_{12} and solar mass difference $\Delta m_{\odot}^2 = \Delta m_{21}^2$ [110]. Global fit results for θ_{12} and Δm_{21}^2 are given in Table 1.1.

Atmospheric neutrinos

Very high energy particles (cosmic rays) arrive to Earth from different parts of the Universe. Most cosmic rays are atomic nuclei: most of these are hydrogen nuclei, some are helium nuclei, and the rest heavier elements. Once these particles enter into the Earth's atmosphere, they interact with the nuclei in the air. Typically, in these interactions, π and K mesons are produced. These mesons are unstable, and they decay to other particles. For example, a π^+ decays to an anti-muon (μ^+) and a muon neutrino (ν_{μ}). Then the produced anti-muon (μ^+) decays to a positron (e^+), an electron neutrino (ν_e), and a muon anti-neutrino ($\bar{\nu}_{\mu}$). There are many other similar interactions for π^- and K^{\pm} . Figure C.2 shows the production of atmospheric neutrinos [111].

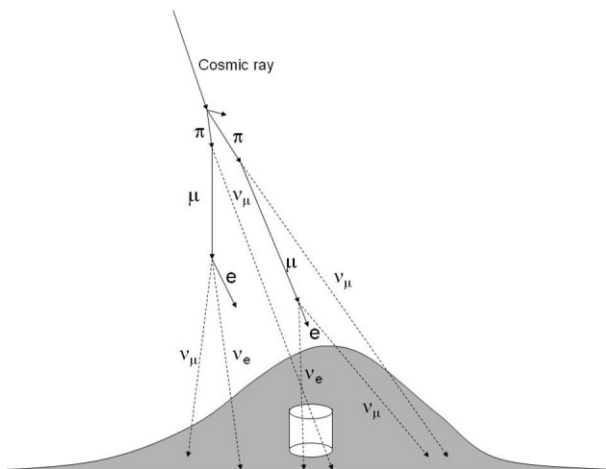


FIG. C.2: Production of atmospheric neutrinos by cosmic-ray interactions. The typical height of the neutrino production is 15 km above the ground. From Ref. [111]

Using atmospheric neutrinos, oscillation experiments managed to constrain the neutrino mixing angle θ_{23} and atmospheric mass difference $\Delta m_{atm}^2 = \Delta m_{32}^2$ [112].

Reactor neutrinos

Nuclear power plants are the one of the main sources of electricity for humanity. In reactor cores, electron antineutrinos ($\bar{\nu}_e$) are emitted isotropically from fission products of four primary isotopes: ^{235}U , ^{238}U , ^{239}Pu , and ^{241}Pu . Reactor antineutrinos have played a key role in measuring the nonzero neutrino mixing angles θ_{12} and θ_{13} [113, 114, 115]. Global fit results for θ_{13} are given in Table 1.1.

Accelerator neutrinos

Focused high-intensity neutrino beams are highly useful for the study of neutrino interactions and oscillations. There are three laboratories in the world which can create a high intensity neutrino beam: Japan Proton Accelerator Research Complex (J-PARC) in Japan, the European Organization for Nuclear Research (CERN) in Europe, and Fermi National Accelerator Laboratory (Fermilab) in the United States. Details of The Neutrinos at the Main Injector (NuMI) neutrino beam in Fermilab are given in Chapter 2. Accelerator neutrinos in conjunction with long baseline beams and far versus near detector configurations are used to measure neutrino mixing angles and mass-square differences. Existing and future accelerator neutrino oscillation experiments are specifically designed to measure the CP-Violating phase (δ_{CP}) and to determine the neutrino mass hierarchy [116].

Bibliography

- [1] Y. Fukuda *et al.* (Super-Kamiokande Collaboration), Phys. Rev. Lett. **81**, 1562 (1998).
- [2] Q. R. Ahmad *et al.* (SNO Collaboration), Phys. Rev. Lett. **87**, 071301 (2001).
- [3] K. Abe *et al.* (T2K Collaboration), arXiv:1609.04111 (2016).
- [4] D. Ayres, Report No: FERMILAB-PROPOSAL-0929, Technical report, NOvA Collaboration (2004).
- [5] M. A. Leigui de Oliveira *et al.* (DUNE Collaboration), Report No: 150608 CERN single phase prototype, Technical report, DUNE Collaboration (2015).
- [6] J. A. Formaggio and G. P. Zeller, Rev. Mod. Phys. **84**, 1307 (2012).
- [7] M. Betancourt, Neutrino Cross Sections, Presented at NPC Neutrino University (2016).
- [8] U. Mosel, GIBUU - A Theory and Method for Neutrino-Nucleus Interactions, Presented at Fermilab (2017).
- [9] M.V. Diwan, V. Galymov, X. Qian, and A. Rubbia, Ann. Rev. Nucl. Part. Sci. **66** (2016).
- [10] D. Rein and L. M. Sehgal, Ann. Phys. (N.Y.) **133**, 79 (1981).
- [11] R. P. Feynman, M. Kislinger, and F. Ravndal, Phys. Rev. D **3**, 2706 (1971).
- [12] A. Mann, MINERvA Internal Note DocDB-13000-v1, Technical report, MINERvA Collaboration (2017).

- [13] U. K. Yang and A. Bodek, Phys. Rev. Lett. **82**, 2467 (1999).
- [14] U. Yang and A. Bodek, Eur. Phys. J. C **13**, 2, 241 (2000).
- [15] A. Bodek and U. K. Yang, J. Phys. G **29**, 8, 1899 (2003).
- [16] S. J. Barish *et al.*, Phys. Rev. Lett. **36**, 179 (1976).
- [17] G. M. Radecky *et al.*, Phys. Rev. D **25**, 1161 (1982).
- [18] G. M. Radecky *et al.*, Phys. Rev. D **26**, 3297 (1982).
- [19] T. Kitagaki *et al.* (BNL Collaboration), Phys. Rev. D **34**, 2554 (1986).
- [20] H. J. Grabosch *et al.* (SKAT Collaboration), Zeitschrift für Physik C Particles and Fields **41**, 4, 527 (1989).
- [21] D. Allasia *et al.* (Amsterdam-Berge-Bologna-Padov-Pisa-Saclay-Torino Collaboration), Nucl. Phys. B **343**, 2, 285 (1990).
- [22] N. Agafonova *et al.* (OPERA Collaboration), Phys. Lett. B **691**, 3, 138 (2010).
- [23] D. Griffiths, *Introduction to Elementary Particles*, Wiley-VCH (2010).
- [24] E. W. Otten and C. Weinheimer, Reports on Progress in Physics **71**, 8, 086201 (2008).
- [25] I. Esteban, M. C. Gonzalez-Garcia, M. Maltoni, I. Martinez-Soler, and T. Schwetz, J. High Energy Phys. **2017**, 1, 87 (2017).
- [26] M. C. Gonzalez-Garcia, M. Maltoni, and T. Schwetz, NuFIT 3.0 (2016), www.nu-fit.org (2016).
- [27] D. Crane, Report No: FERMILAB-DESIGN-1995-03, Technical report, NuMI Beam Group (2002).
- [28] E. Ables, Report No: FERMILAB-PROPOSAL-0875, Technical report, MINOS Collaboration (1995).

- [29] G. Tzanankos, Report No: FERMILAB-PROPOSAL-1016, Technical report, MINOS+ Collaboration (2011).
- [30] D. Drakoulakos, Report No: FERMILAB-PROPOSAL-0938, Technical report, MINERvA Collaboration (2004).
- [31] C. Anderson *et al.* (ArgoNeuT Collaboration), J. Instrum. **7**, 10, P10019 (2012).
- [32] P. Adamson, K. Anderson, and M. Andrews, Nucl. Instrum. Meth. **A806**, 279 (2016).
- [33] D. Martinez, The MINERvA Experiment, Presented at New Perspectives Conference Fermilab (2014).
- [34] L. Aliaga *et al.* (MINERvA Collaboration), Phys. Rev. D **94**, 092005 (2016).
- [35] L. Aliaga *et al.* (MINERvA Collaboration), Nucl. Instrum. Methods Phys. Res., Sect. A **743**, 130 (2014).
- [36] MINERvA Collaboration, MINERvA Detector Conventions, https://cdcv.sfnal.gov/redmine/projects/minerva-ops/wiki/Plane_Views (2016).
- [37] D.G. Michaele *et al.* (MINOS Collaboration), Nucl. Instrum. Methods Phys. Res., Sect. A **596**, 2, 190 (2008).
- [38] E. Gallas and J. Li, Report No: FERMILAB-TM-2062, Technical report (1998).
- [39] N. Tagg *et al.*, Nucl. Instrum. Methods Phys. Res., Sect. A **539**, 3, 668 (2005).
- [40] P. Adamson *et al.* (MINOS Collaboration), Phys. Rev. D **81**, 072002 (2010).
- [41] K.A. Olive *et al.* (Particle Data Group), Chin. Phys. C **C38**, 090001 (2014).
- [42] C. Andreopoulos *et al.* (GENIE Collaboration), Nucl. Instrum. Methods Phys. Res., Sect. A **614**, 1, 87 (2010).

- [43] S. Agostinelli, J. Allison, K. Amako, J. Apostolakis, H. Araujo *et al.*, Nucl. Instrum. Methods Phys. Res., Sect. A **506**, 3, 250 (2003).
- [44] GENIE Collaboration, GENIE Release Notes, <http://releases.genie-mc.org>.
- [45] Geant4 Collaboration, Geant4 Release Notes, <http://geant4.cern.ch/support/ReleaseNotes4.9.4.html>.
- [46] A. Bodek and J. L. Ritchie, Phys. Rev. D **24**, 1400 (1981).
- [47] S. A. Dytman and A. S. Meyer, AIP Conference Proceedings **1405**, 1, 213 (2011).
- [48] R. Brun, F. Bruyant, M. Maire, A. C. McPherson, and P. Zancarini, *GEANT 3: user's guide Geant 3.10, Geant 3.11; rev. version*, CERN, Geneva (1987).
- [49] B. Eberly *et al.* (MINERvA Collaboration), Phys. Rev. D **92**, 092008 (2015).
- [50] P. Rodrigues, C. Wilkinson, and K. McFarland, Eur. Phys. J. C **76**, 8, 474 (2016).
- [51] C. Wilkinson, P. Rodrigues, S. Cartwright, L. Thompson, and K. McFarland, Phys. Rev. D **90**, 112017 (2014).
- [52] J. Nieves, I. R. Simo, and M. J. V. Vacas, Phys. Rev. C **83**, 045501 (2011).
- [53] R. Gran, J. Nieves, F. Sanchez, and M. J. V. Vacas, Phys. Rev. D **88**, 113007 (2013).
- [54] P.A. Rodrigues *et al.* (MINERvA Collaboration), Phys. Rev. Lett. **116**, 071802 (2016).
- [55] B. M. Eberly, Report No: FERMILAB-THESIS-2014-18, Ph.D. thesis, University of Pittsburgh (2014).
- [56] P. Rodrigues, MINERvA Internal Note DocDB-12529, Technical report, MINERvA Collaboration (2014).

- [57] B. Eberly and T. Walton, MINERvA Internal Note DocDB-8190-v1, Technical report, MINERvA Collaboration (2013).
- [58] T. Walton, Report No: FERMILAB-THESIS-2014-11, Ph.D. thesis, Graduate College of Hampton University (2014).
- [59] G. N. Perdue, MINERvA Internal Note DocDB-10017-v2, Technical report, MINERvA Collaboration (2015).
- [60] R. Luchsinger and C. Grab, *Comp. Phys. Comm.* **76**, 3, 263 (1993).
- [61] E. Wolin and L. Ho, *Nucl. Instrum. Methods Phys. Res., Sect. A* **329**, 3, 493 (1993).
- [62] R. Ospanov, Report No: FERMILAB-THESIS-2008-04, Ph.D. thesis, The University of Texas at Austin (2008).
- [63] D. E. Groom, N. V. Mokhov, and S. I. Striganov, *At. Data Nucl. Data* **78**, 2, 183 (2001).
- [64] A. P. D.T.J. Thomas, MINOS Internal Note 301, Technical report, MINOS Collaboration (1997).
- [65] C. Patrignani *et al.* (Particle Data Group), *Chin. Phys. C* (2016).
- [66] J. Neyman and E. S. Pearson, *Phil. Trans. R. Soc. A* **231**, 694-706, 289 (1933).
- [67] R. Fernow, *Introduction to Experimental Particle Physics*, Cambridge University Press (1990).
- [68] J. L. P. Gallo, Report No: FERMILAB-THESIS-2012-56, Ph.D. thesis, Centro Brasileiro de Pesquisas Fisicas (2012).
- [69] J. Park, MINERvA Internal Note DocDB-9407-v5, Technical report, MINERvA Collaboration (2014).
- [70] J. Park, Report No: FERMILAB-THESIS-2013-36, Ph.D. thesis, University of Rochester (2013).

- [71] G. D'Agostini, Nucl. Instrum. Methods Phys. Res., Sect. A **362**, 2, 487 (1995).
- [72] D.G. Michael *et al.* (MINOS Collaboration), Nucl. Instrum. Methods Phys. Res., Sect. A **596**, 2, 190 (2008).
- [73] M. Betancourt, MINERvA Internal Note DocDB-11367-v8, Technical report, MINERvA Collaboration (2015).
- [74] C. McGivern, MINERvA Internal Note DocDB-10367, Technical report, MINERvA Collaboration (2014).
- [75] D. E. Groom, N. V. Mokhov, and S. I. Striganov, At. Data Nucl. Data **78**, 2, 183 (2001).
- [76] T. Walton, MINERvA Internal Note DocDB-7595-v3, Technical report, MINERvA Collaboration (2012).
- [77] R. Ransome, MINERvA Internal Note DocDB-6016-v7, Technical report, MINERvA Collaboration (2012).
- [78] A. R. Mislivec, MINERvA Internal Note DocDB-7571-v3, Technical report, MINERvA Collaboration (2012).
- [79] J. B. Birks, Proceedings of the Physical Society. Section A **64**, 10, 874 (1951).
- [80] D. Zhang, MINERvA Internal Note DocDB-10064, Technical report, MINERvA Collaboration (2014).
- [81] D. Zhang, MINERvA Internal Note DocDB-11443, Technical report, MINERvA Collaboration (2015).
- [82] D. Ashery, I. Navon, G. Azuelos, H. K. Walter, H. J. Pfeiffer *et al.*, Phys. Rev. C **23**, 2173 (1981).
- [83] T. Le, MINERvA Internal Note DocDB-10423-v2, Technical report, MINERvA Collaboration (2014).

- [84] R. Bradford, A. Bodek, H. Budd, and J. Arrington, Nucl. Phys. B (Proc. Suppl.) **159**, 127 (2006).
- [85] H. Gallagher, MINERvA Internal Note DocDB-7578-v3, Technical report, MINERvA Collaboration (2012).
- [86] T. Bohlen, F. Cerutti, and M. Chin, Nuclear Data Sheets **120**, 211 (2014).
- [87] A. A. Aguilar-Arevalo *et al.* (MiniBooNE Collaboration), Phys. Rev. D **83**, 052009 (2011).
- [88] P. A. Rodrigues, AIP Conference Proceedings **1663**, 1, 030006 (2015).
- [89] D. Casper, Nucl. Phys. B (Proc. Suppl.) **112**, 1, 161 (2002).
- [90] C. L. McGivern, T. Le, B. Eberly *et al.* (MINERvA Collaboration), Phys. Rev. D **94**, 052005 (2016).
- [91] T. Golan, C. Juszczak, and J. T. Sobczyk, Phys. Rev. C **86**, 015505 (2012).
- [92] Y. Hayato, Acta Phys. Polon. **B40**, 2477 (2009).
- [93] M. Martini, M. Ericson, G. Chanfray, and J. Marteau, Phys. Rev. C **80**, 065501 (2009).
- [94] J. Nieves, I. R. Simo, and M. V. Vacas, Phys. Lett. B **721**, 1-3, 90 (2013).
- [95] T. Le *et al.* (MINERvA Collaboration), Phys. Lett. B **749**, 130 (2015).
- [96] A. A. Aguilar-Arevalo *et al.* (MiniBooNE Collaboration), Phys. Rev. D **83**, 052007 (2011).
- [97] P. Adamson *et al.* (MINOS Collaboration), Phys. Rev. D **91**, 012005 (2015).
- [98] D. Norman, Tufts Senior Thesis ID: sd.0000389, Technical report, Tufts University (2016).
- [99] P. A. Schreiner and F. Von Hippel, Nucl. Phys. **B58**, 333 (1973).

- [100] S. L. Adler, *Annals of Physics* **50**, 2, 189 (1968).
- [101] K.A. Olive *et al.* (Particle Data Group), *Particle Physics Booklet* (2014).
- [102] K. S. Kuzmin, V. V. Lyubushkin, and V. A. Naumov, *Acta Phys. Polon.* **B37**, 2337 (2006).
- [103] T2K Collaboration, A Brief History Of Neutrinos, <http://t2k-experiment.org/neutrinos/a-brief-history/> (2016).
- [104] J. Chadwick, *Nature* **129**, 312 (1932).
- [105] F. L. Wilson, *Am. J. Phys.* **36**, 12, 1150 (1968).
- [106] C. L. Cowan, F. Reines, F. B. Harrison, H. W. Kruse, and A. D. McGuire, *Science* **124**, 3212, 103 (1956).
- [107] G. Danby, J.-M. Gaillard, K. Goulianos, L. M. Lederman, N. Mistry *et al.*, *Phys. Rev. Lett.* **9**, 36 (1962).
- [108] K. Kodama *et al.* (DONUT Collaboration), *Phys. Lett. B* **504**, 3, 218 (2001).
- [109] A. G. Lars Bergstrom, *Cosmology and Particle Astrophysics*, Springer-Verlag Berlin Heidelberg (2004).
- [110] K. Abe *et al.* (Super-Kamiokande Collaboration), *Phys. Rev. D* **83**, 052010 (2011).
- [111] T. Kajita, *Proc. Jpn. Acad., Ser. B, Phys. Biol. Sci.* (2010).
- [112] R. Wendell *et al.* (Super-Kamiokande Collaboration), *Phys. Rev. D* **81**, 092004 (2010).
- [113] K. Eguchi *et al.* (KamLAND Collaboration), *Phys. Rev. Lett.* **90**, 021802 (2003).
- [114] F. P. An *et al.* (Daya Bay Collaboration), *Phys. Rev. Lett.* **108**, 171803 (2012).
- [115] J. K. Ahn *et al.* (RENO Collaboration), *Phys. Rev. Lett.* **108**, 191802 (2012).

- [116] K. N. Deepthi, C. Soumya, and R. Mohanta, *New J. Phys.* **17**, 2, 023035 (2015).